Electro-thermal optimization of an energy storage system based on li-ion batteries

PhD student:

UNAI IRAOLA IRIONDO

Supervisor:

ANDER ETXEBERRIA LARRAZABAL

Mondragon Goi Eskola Politeknikoa

2014/04/30

ACKNOWLEDGEMENTS

First of all, I would like to thank Ander Etxeberria for his help during these years conducting the thesis work as my director. I would like to thank Jose María Canales for his technical advices and for helping me when there were problems to go ahead. I want to specially thank Ibon Ajuria for his help with the mechanical issues during the work. I wouldn´t like to forget Eneko Unamuno and Lorea Gorrotxategi for their work with the experimental tests. Finally I want to show my gratitude to my colleagues Iosu Aizpuru and Unai San Andres because they have always been ready to help me even if they had to work more for that reason.

I can´t forget many other people, people from Orona room at university, Iratxo, Sergio, Aritz when he was there...other workmates from the department, Igor, Aitor, Alain, Manex, Mazu, Gaizka, Gaizka, Ander, David, Jonan, Gonzalo, Iosu, Javi, Urtzi, Patxi...thank you because it is so nice being with you every day.

I want to acknowledge Orona company for their support during this work and for the opportunity to collaborate with them, it has been a pleasure for me.

I would also like to express my gratitude to Kempten University and especially to the people working in the department conducted by professor Biechl; I felt part of the team since the first day and I had very good experiences working there and learning from their researches.

Finally, I want to thank each member of the jury for coming to this event and for giving me their point of view about the developed work.

No me puedo olvidar de mis amigos, que son lo mejor que hay y que consiguen que un día malo en el que todo ha salido mal termine de la mejor manera posible, riendo sin parar y sin ganas de ir a casa.

Para acabar, me gustaría agradecer a mi familia, hermanos, amama, a mi tía, y a mi sobrino Ibai que pronto le tendré corriendo por aquí, pero sobre todo a mis padres por permitirme llegar hasta aquí y porque siempre han creído que lo podía hacer. Y gracias por haberme enseñado siempre a esforzarme para conseguir las cosas.

Ta eskerrik asko zuri rubia, zelan ahaztuko naiz zutaz; beti nere albuan egon zaralako eta egun txarretan beti hitz onak euki ditxuzulako neretzat. Badakit batzutan humore txarrez bueltau naizela etxera baina zurekin errezaua izan da amaierara heltzea.

Eskerrik asko guztioi

RESUMEN

Los avances en el ámbito de la energía han contribuido notablemente al desarrollo de nuestra sociedad. El incremento del consumo energético unido a la posible extinción de los combustibles fósiles obliga a buscar la máxima eficiencia energética en todas las aplicaciones además de exigir fuentes de energía alternativas, como pueden ser las renovables, para abastecer estos consumos. Además, existen otras soluciones como los sistemas de almacenamiento de energía que permitirían almacenar energía durante momentos de bajo consumo energético, y entregarla durante los momentos de máximo consumo.

Este trabajo se centra en los sistemas de almacenamiento basados en células electroquímicas, concretamente en las baterías de litio, ya que su alta densidad de energía y su vida útil las hace adecuadas para aplicaciones de potencia. Sin embargo, la temperatura de trabajo es un factor clave ya que influye en las prestaciones de este tipo de batería y además afecta a su envejecimiento. Por tanto, esta tesis se centra en la optimización electro-térmica de sistemas de almacenamiento basados en baterías de litio con el fin de alargar la vida útil de los mismos aprovechando al máximo sus prestaciones.

LABURPENA

Energiaren arloan izandako aurrerapenek gure gizartearen garapenean izugarri lagundu dute. Energi kontsumoaren igoera eta erregai fosilen desagerpena direla eta gaur egungo erronka nagusia sistemen efizientzia energetikoan eta ordezko energia iturrien bilaketan datza. Bestalde, energia metatzeko sistemak agertzen dira kontsumo hauei aurre egiteko aukera modura, eguneko kontsumoak bajuak direnean energia metatu ahal dutelako, eta kontsumoak maximoak direnean entregatzeko.

Lan hau energia metatzeko sistema elektrokimikoetan oinarritzen da, konkretuki litio-ioiez osatutako baterietan, beraien energia dentsitate altua eta bizitza luzea egokiak baitira potentzia aplikazioetan erabiltzeko. Hala ere, tenperaturak influentzia inportantea dauka bateria hauen errendimenduan eta bizitzan. Beraz, tesi hau litio-ioiez osatutako energia metatze sistemetan eta hauen optimizazio elektro-termikoan oinarritzen da, beraien bizitza ahalik eta gehien luzatzeko helburuarekin.

ABSTRACT

Advances in the field of energy have contributed significantly to the development of our society. The increase of the energy consumption joined to the possible extinction of fossil fuels requires finding the maximum efficiency possible in all the applications, and demands alternative energy sources, for instance renewable ones, to support this consumption. Besides, energy storage systems are considered another solution, due to the possibility of storing energy during low consumption periods and release it during maximum demand ones.

This work will focus on energy storage systems based on electrochemical devices, particularly in lithium-ion batteries, which are presented as a suitable alternative for power applications due to their high energy density and large cycle life. However, these batteries are very sensitive to their working temperature because it affects their performance and reduces their cycle life. With this scenario, this thesis is oriented to the electro-thermal optimization of lithium ion battery based energy storage systems with the target of maximizing their cycle life taking advantage of their optimum performance.

TABLE OF CONTENTS

LIST OF FIGURES

LIST OF TABLES

NOMENCLATURE

SOC	State of charge
SOH	State of health
CFD	Computational fluid dynamics
DOD	Depth of discharge
EIS	Electrochemical impedance spectroscopy
EOL	End of life
EV	Electric vehicle
HEV	Hybrid electric vehicle
Li-ion	Lithium-ion
OCV	Open circuit voltage
CC	Constant current
CV	Constant voltage
TIM	Thermal interface material
$LiFePO_4$	Lithium iron phosphate
BTMS	Battery thermal management system
BMS	Battery management system
PWM	Pulse width modulation
PCM	Phase change material
LTI	Linear Time Invariant

Chapter 1. INTRODUCTION

The introduction chapter is divided in three main parts: first of all the framework in which this work is focused will be presented; after that the objectives of the work will be explained; there is a main objective and some partial ones; finally, the structure followed in this document will be shown to conclude the introduction chapter. The aim of this chapter is to explain the current situation regarding to the use of batteries in real applications and justify the use of these devices for power applications. Besides, the consequences of utilizing li-ion cells at different working temperatures are presented in this chapter.

1.1 Framework

Advances in the field of energy have contributed significantly to the development of society up to the present situation, and its consumption is increasing day by day. The lack of natural resources joined to the high consumption requires looking for the highest possible efficiency and adding alternatives to support the energy demand; renewable energies are a real alternative to support energy production, but there are other alternatives to improve the present situation. Energy storage systems are presented as an important option because they present important advantages: the ability to work without a grid connection and make autonomous systems; the capacity to accumulate energy from different energy sources and use it to support the grid when the energy demand is higher; and in some applications, accumulate energy that otherwise is going to be lost to use it later. There are different ways to accumulate energy; mechanically with flywheels, electrically with ultracapacitors or thermally with steam accumulators... However, nowadays, energy storage systems based on electrochemical devices, also called batteries, are commonly used in several applications.

a) b)

Figure 1.1: a) Low power electronic equipment applications; b) High power *EV* application.

Different battery technologies have been grown up since the first battery appeared; lead-acid, nickel metal hydride, nickel cadmium and lithium-ion (li-ion) batteries are the most representative ones. However, li-ion technology is mostly used today in portable applications, and there is increasing interest in using this technology for power applications. High power applications require high voltage and current levels and thus, large battery packs. The high energy and power density of li-ion batteries is then an important advantage against other technologies when large battery packs are needed.

High power demands increase Joule effect power losses and temperature can reach undesirable values. This hot ambient directly affects the cycle life of the battery [1] and can be dangerous if temperature is not under control above 70 ºC because *thermal runaway* phenomenon can be triggered [2]. Conversely, cold climates (0-10ºC) also worsen the performance of the li-ion battery because of the increase in their internal resistance under cold environments; besides, charging the battery in very cold climates (<10ºC) can damage the battery irreversibly and reduce its capacity under 80% in a few

cycles [1], [3]. Thus, it is important to keep battery module temperatures within a safe range (commonly 20-40 ºC) for any working condition [4].

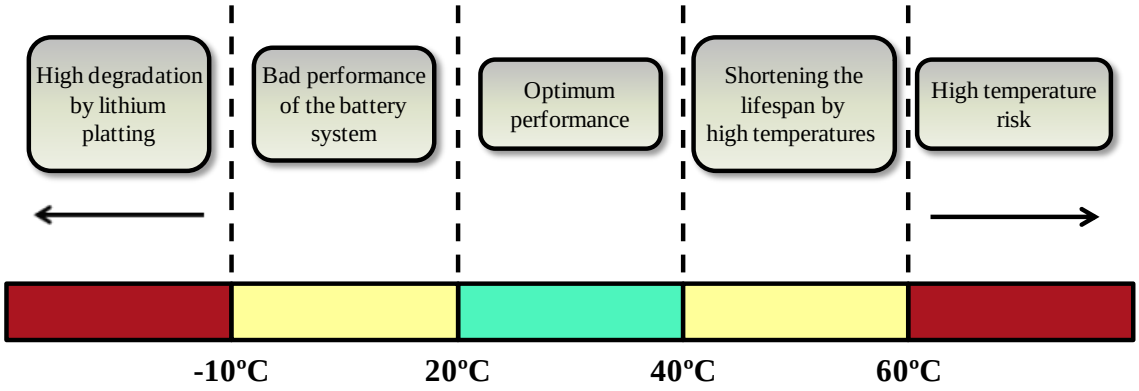

Figure 1.2: Different working temperature ranges for lithium-ion batteries and their consequences.

Apart from the maximum temperatures of the battery module, there is another critical parameter to take into account when thermal design is done: it is the temperature distribution within the battery module. If this distribution is not uniform the aging of each cell because of temperature will be different and the power capability and available capacity of the battery module will decrease because the weakest cell will limit its performance. Therefore, it is important to keep the temperatures of the different zones of a battery close to their optimum working temperature, but also to have a distribution as uniform as possible when battery modules are thermally designed.

1.2 Objectives

Taking into account the previous lines, the main objective of this thesis is to define a methodology to design thermally optimized lithium-ion battery modules for power applications with the aim of maximizing their lifespan and taking advantage of their performance.

In order to reach the main objective, some partial objectives are considered: first of all an internal heat generation model of each cell is required to simulate different applications current profiles and obtain the heat generated by the cells within a module. Besides, a thermal model able to predict an average temperature of a single cell will be developed; second partial objective is to develop different strategies to minimize the maximum temperature gradient of a li-ion battery module to avoid uneven aging processes; third partial objective is to develop a simulation tool able to predict an average temperature for each cell within a battery module for different working conditions, ambient temperatures, or battery layouts; another partial objective is to evaluate the advantages and disadvantages of using different lithium-ion cell formats for battery modules. Thus, three different 8 cell battery modules (prismatic, cylindrical and pouch) are going to be evaluated in this work; finally, as this work is only focused on the cooling of the modules, different forced air cooling strategies will be analyzed for the different battery modules.

1.3 Structure of the document

The structure followed in this thesis document is summarized in Figure 1.3; in chapter 2 the state of the art is done regarding to the li-ion batteries and the effects of temperature in their degradation. First of all, different li-ion battery technologies will be analyzed and the advantages and disadvantages of each technology will be explained.

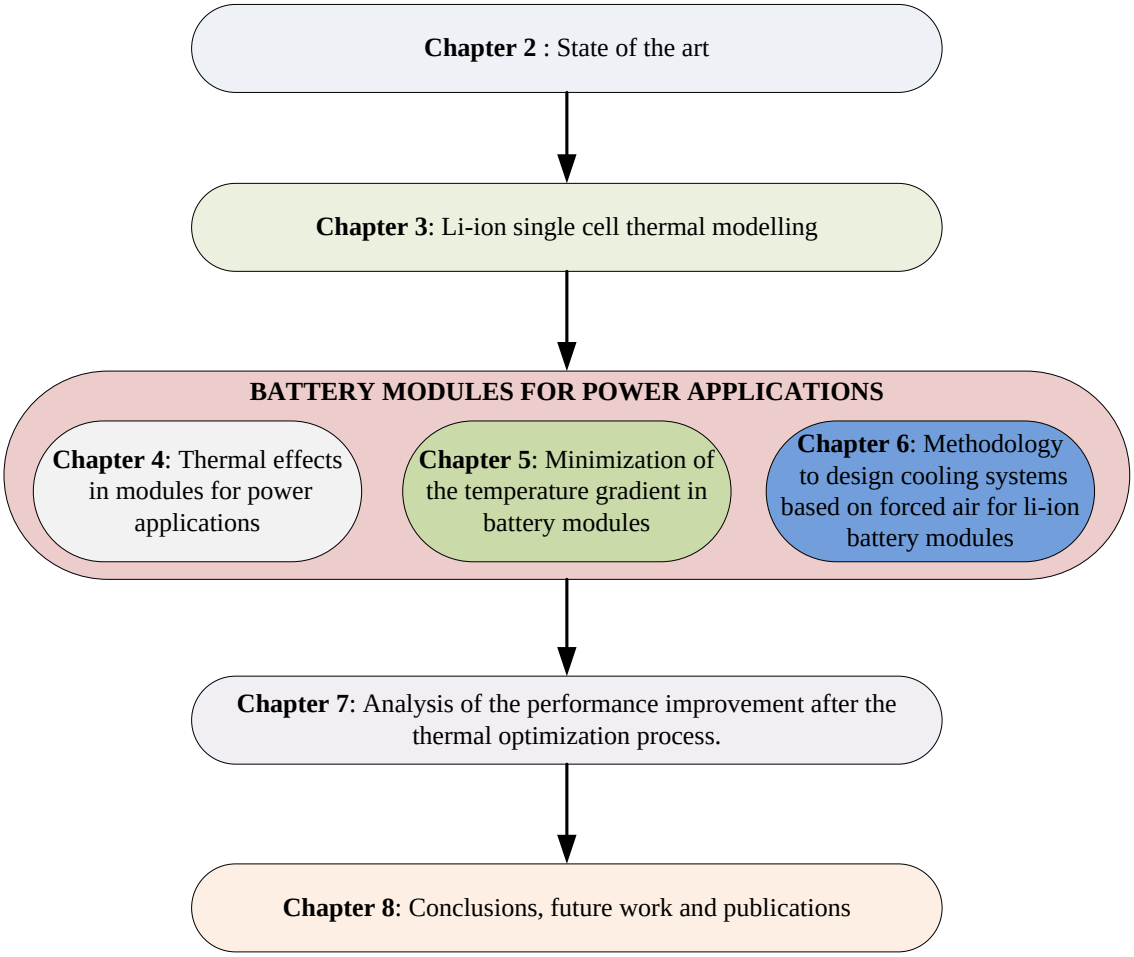

Figure 1.3: Overview of the structure followed in the document.

Chapter 3 is focused on the thermal modelling of li-ion single cells. A methodology to obtain a thermal model is explained step by step since the new batteries are acquired by the user until the model of the li-ion module is obtained. This methodology will be validated comparing experimental results for different current profiles with the simulation results.

After analyzing and modelling li-ion single cells thermal behaviour, next chapters are focused on li-ion battery modules for power applications. In chapter 4, the consequences of delivering high powers in li-ion battery modules will be explained to understand why is necessary to thermally manage these devices. After that, in chapter 5, the proposed techniques to avoid uneven temperature distributions will be described as the first step

to improve the thermal behaviour of the battery. In chapter 6 the second step to improve it is defined; a methodology to design *BTMS* systems for li-ion battery modules is proposed. In this work forced air cooling systems have been selected to cool down the battery modules.

Finally, chapter 7 presents the results obtained for the battery modules developed under a power application profile. Modules without cooling systems are compared to the ones with cooling system. The maximum average temperature and maximum temperature gradients are analyzed. Besides, the Arrhenius law is used to estimate the energy delivered by each module during their whole life depending on an average working temperature of the cells within the module.

At the end of the document the most important conclusions, future lines and the publications obtained during this work will be presented.

Chapter 2. STATE OF THE ART

The state of the art is composed by three main sections. First of all, a general overview about lithium-ion batteries will be done; a general description of a cell, followed by an explanation of the chemical reaction of this kind of batteries. Finally the advantages and disadvantages of different cells will be analyzed depending on their cathode materials.

Following, aging mechanisms of this type of cells are going to be explained; causes and consequences of this aging will be pointed out and the bad contribution of some parameters like temperature or voltage will be analyzed.

After that, lithium-ion cells failure modes are going to be explained; voltage and temperature related failures but also separator shutdown failures will be analyzed.

After analyzing general aging mechanisms and safety issues in lithium-ion batteries, special attention will be paid in temperature effects both in aging and in safety concerns during the summary of the chapter. The aim of this summary is to justify the thesis work and show the importance of researching temperature issues in li-ion batteries.

2.1 Lithium-ion cells

Lithium-ion cells store the energy by means of a chemical reaction and convert it into electrical energy; this is common for each battery or cell technology but, in this case, li-ion cells use lithium as the reactive element. Lithium is the lightest metallic element and has the highest electrochemical potential, thus, li-ion cells are adequate for energy storage applications.

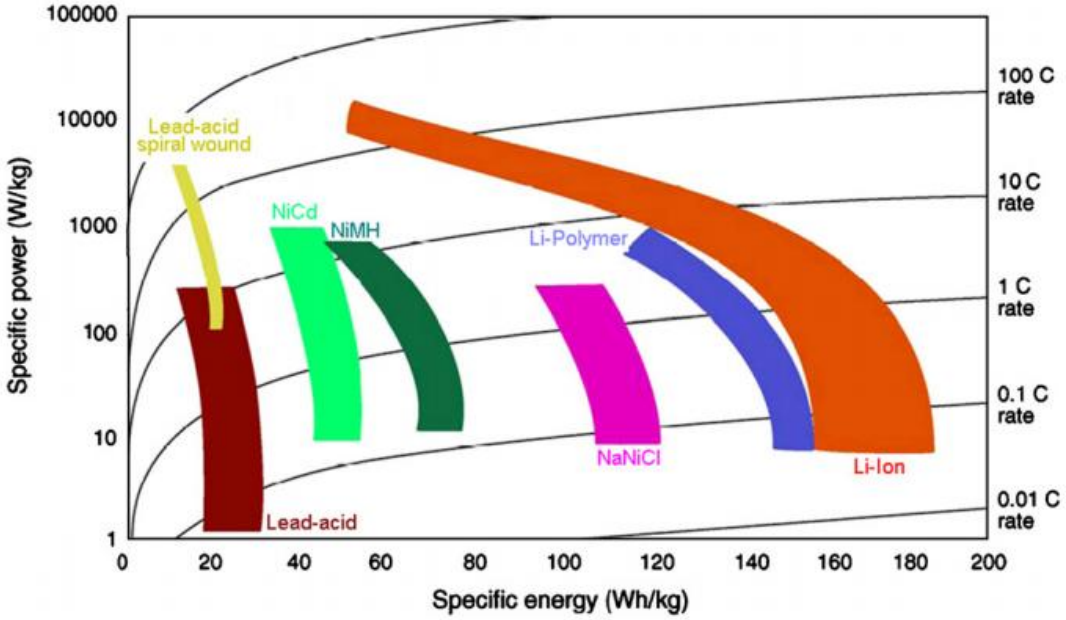

Figure 2.1: Ragone plot of electrochemical energy storage systems [5].

Besides, as it can be seen in Figure 2.1, li-ion batteries are suitable for a wide range of applications because they present good features in terms of specific energy and power. These are the most important advantage of this technology; however, some disadvantages have to be considered when working with li-ion batteries (TABLE 2.1).

TABLE 2.1 MOST IMPORTANT ADVANTAGES AND DISADVANTAGES OF LI-ION TECHNOLOGY [6]

ADVANTAGES	No maintenance required
	Long cycle life
	Wide temperature range operation
	Low self discharge
	Rapid charge possibility
	High rate and high power discharge
	High efficiency
	No memory effect
DISADVANTAGES	High cost
	Degradation with high temperatures
	Thermal runaway

Apart from the energy and power density advantage, their long cycle life, wide temperature range operation, low self-discharge and high efficiency appear as important benefits of this technology. The most important drawbacks are the high cost, the possible degradation of these batteries with quite high temperatures (over 35ºC) and some safety issues related to high temperatures.

Figure 2.2: Commonly used geometries for li-ion cells, prismatic, pouch and cylindrical cells in the figure.

Lithium-ion cells are divided into two main groups: primary and secondary cells. The secondary ones are rechargeable while the primary ones can only be discharged once. The most common geometries are the prismatic, the cylindrical, and the pouch ones Figure 2.2. The casing of the cylindrical and prismatic cells makes them more robust than the pouch cell, however, the energy/space ratio is excellent in pouch cells comparing it with the other geometries. Cylindrical cells are presented as the cells with the worst thermal behaviour against pouch cells, which are considered the best ones. The most elemental unit when talking about energy storage systems based on electrochemical devices are cells. These cells can be connected in series and/or in parallel to reach a battery module. Battery modules, at the same time, can be connected in series and/or in parallel to obtain a battery pack.

2.1.1 General description of a cell

The main parts of a li-ion cell are the two electrodes (cathode and anode), the electrolyte and the separator. These main components are located in the container to be inaccessible. Following a brief explanation about these cell components is presented. Figure 2.3 shows a simplified structure of a li-ion cell.

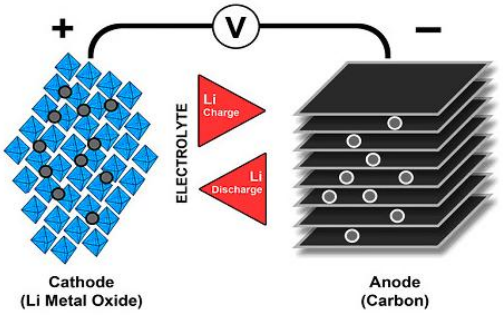

Figure 2.3: Li-ion cell structure general picture [7].

- ***Cathode***: It is the positive electrode and it is commonly a metal oxide, (with a layered structure) combination of lithium with a metal oxide like cobalt,

manganese, nickel... Different cathode materials will be analyzed following. The current collector is used to be made of aluminium.

- ***Anode***: It is the negative electrode and it is usually composed by carbon or graphite layers, with a current collector made of copper.
- ***Electrolyte***: It permits the lithium ions flow inside the cell. It usually is non aqueous electrolyte with a separator for electrically insulate the electrodes, but the polymeric solid matrix electrolyte is another possibility. In this case, no separator is needed.
- ***Separator*** (in case of non aqueous electrolyte): There are different types of separators according to their material; polypropylene, polyethylene, polyethylene terephthalate etc. Some separators have the shutdown property. This property allows them to acquire a high impedance value when the temperature of the cell is reaching a dangerous value. By this way, the current is diminished in order to get a reduction of temperature.

2.1.2 Electrochemical reaction

Some electrochemical cells like lead acid and nickel cadmium batteries are based on *REDOX* oxidation reduction chemistry. However, nickel metal hydride and lithium-ion batteries involve an ion transfer mechanism called intercalation, which is the insertion and extraction of ions into and out of the crystalline lattice of an electrode, without chemically altering its crystal structure [8]. When charging/discharging a lithium-ion cell, there are two aspects to take into account: first one is the movement of electrons by the external circuit, and the second one, the transmission of lithium ions between electrodes internally.

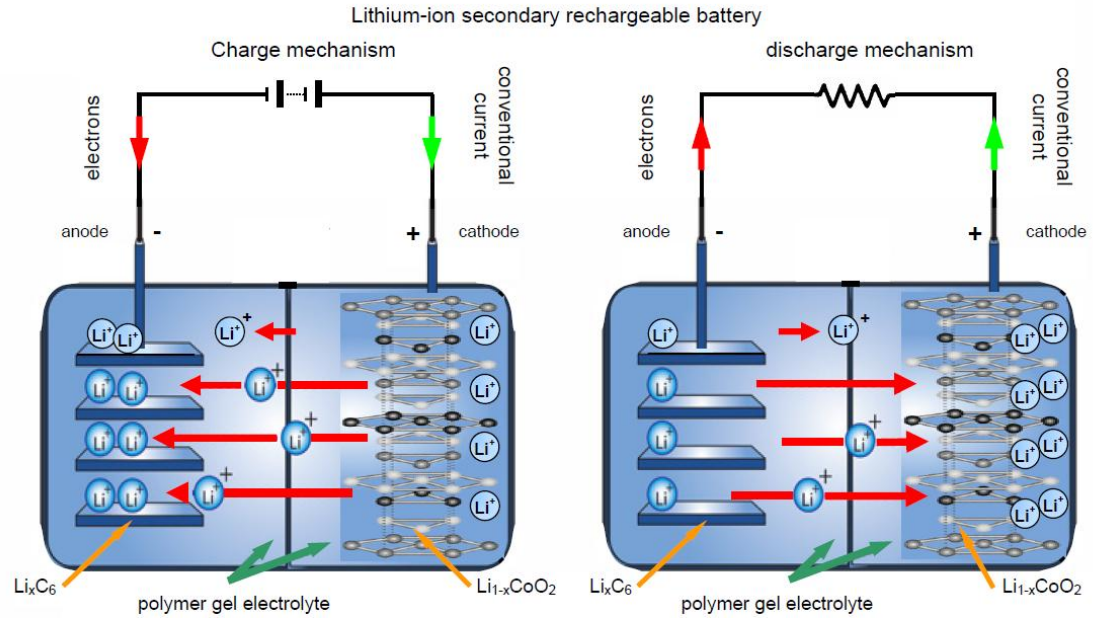

Figure 2.4: Lithium-ion cells charge and discharge process. [8].

When discharging, both electrons and lithium-ions move from the negative (anode) to the positive electrode (cathode). The reaction is reversible, so, when charging, both

electrons and lithium-ions move from the cathode to the anode. Figure 2.4 shows the process mentioned previously in detail.

2.1.3 Different cathodes in lithium-ion cells

There is a large amount of different li-ion cells available depending on the material used in the cathode. Although there can be differences in the electrolyte or the anode, this part of the document is going to be focused on different cathodes. At the end of this chapter there is a comparison between the most important technologies in li-ion cells. The data summarized in TABLE 2.2 has been obtained from the bibliography [9], [10], [7], [11], [12] and [2].

2.1.3.1 $LiCoO_2$

It is the most conventional of cathode materials. These kind of cells are very used in portable devices.

1. Advantages

- High energy density makes them adequate to use them in portable applications.

2. Disadvantages

- The price of cobalt is higher than the price of other metals used in cathodes.
- Lower thermal stability than other materials.
- Limitation in charge/discharge current (1C limitation).
- Limited charge/discharge number of cycles.

2.1.3.2 $LiMn_2O_4$

1. Advantages

- Price
- Safety. Good thermal stability.
- Low internal resistance, consequently, high charge/discharge current rate.
- This technology is usually used in power applications.

2. Disadvantages

- Lower energy density than LiCoO2.

2.1.3.3 $LiFePO_4$

1. Advantages

- Good thermal stability, good performance in abuse conditions.
- High discharge current rate permitted.
- Cycle life.

2. Disadvantages

- Relatively low terminal voltage, consequently lower specific energy.

2.1.3.4 Li(Ni, Co, Mn)O_2

Due to the problems with the $LiNiO_2$ another interesting variant is usually used as cathode material, it is the $Li(NiCoMn)O_2$ or NCM.

1. ***Advantages***

- High nominal capacity.
- High discharge currents permitted.

2. ***Disadvantages***

- It suffers degradation because of the dissolution of manganese.

2.1.3.5 Li(Ni, Co, Al)O_2

It is similar to $LiCoO_2$. It is commonly called NCA.

1. ***Advantages***

- High energy density and power.

2. ***Disadvantages***

- Price.
- Safety, low thermal stability.

Finally, Figure 2.5 and TABLE 2.2 summarize the most important features of the previously analyzed li-ion technologies and compare them with spider charts. In power applications $LiFePO_4$ batteries are considered a good option due to their thermal stability, high charge and discharge rates and cycle life.

TABLE 2.2 COMPARISON BETWEEN DIFFERENT LI-ION CELL TECHNOLOGIES.

	NCM	NCA	$LiMn_2O_4$	$LiFePO_4$	$LiCoO_2$
Voltage [V]	3.6	3.6	3.8	3.2	3.7
Energy density [Wh/Kg]	170	170	100	>110	114
Power density [W/Kg]			2000	1000	285
Cycle life [number of cycles]	>1300		400	>1200	400
Safety [5 is the most safe]	3	3	4	5	3
Operating temperature range [8] **[ºC]**	-20-60				
Self discharge [%/month @ 20ºC] [8]	<10				
Cool storage	Not required				
Better SOC to storage [%] [8]	40				

In this thesis $LiFePO_4$ cells have been selected from the different cathode materials explained above to do the experimental single cell and module tests. Their large lifespan and high safety level have been determinant for this selection because are considered the most important features of the energy storage system for power applications.

Moreover, as mentioned in the objectives chapter, the main concern in this thesis is to enlarge as much as possible the lifespan of energy storage systems based on lithium-ion batteries, improving their thermal behaviour. Following, lithium-ion cells degradation mechanisms and failure modes will be analyzed.

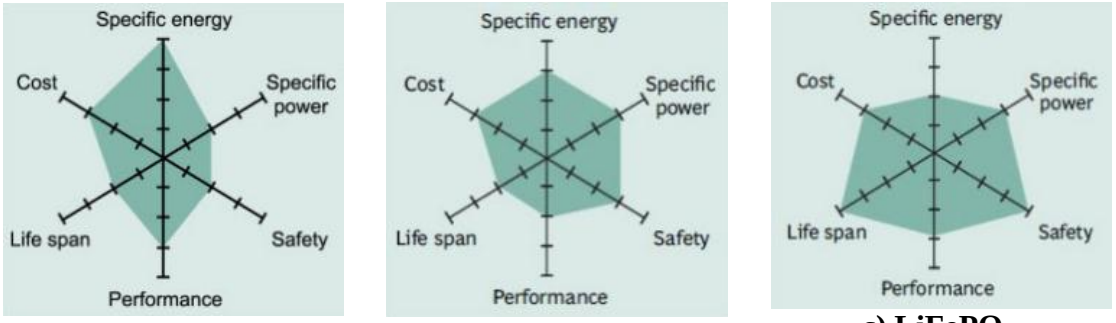

a) $LiCoO_2$ **b) $LiMn_2O_4$** **c) $LiFePO_4$**

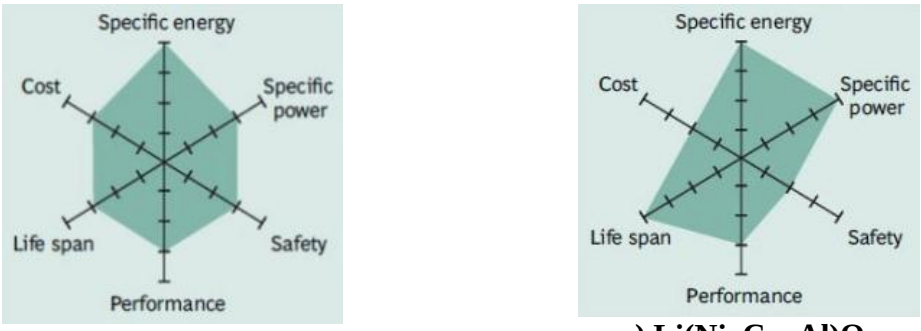

d) Li(Ni, Co, Mn)O_2 **e) Li(Ni, Co, Al)O_2**

Figure 2.5: Comparison of different li-ion technologies with spider charts [7]**.**

2.2 Ageing mechanisms in lithium-ion batteries

As mentioned before, there are lots of applications where batteries can be found nowadays and other ones where batteries are thought to be present in the future. For example, lithium-ion batteries appear as a possible solution for applications like *EV* or *HEV*. Apart from the aforementioned safety, battery lifetime, peak power capability and specific energy become of increasing interest. Long-term cycling with reliable performance and storage behaviour is demanded. Unfortunately, battery performance becomes worse as cell is cycled, an ageing effect appears. These ageing effects depend on the cycling conditions during the whole life of the battery. Issues like charging/discharging rates, temperatures, *DOD* or number of cycles have to be taken into account because of their influence in cycling aging. Besides, when a li-ion cell is not cycled but is storing energy for long times an aging effect has to be considered due to the calendar aging.

Nominal capacity and power capability suffer a reduction on their values as the aging increases making the battery arrive to the end of life (*EOL*). A battery gets the end of life when it is not able to deliver the 75%-80% of the nominal capacity during a full discharge cycle. The aim of this chapter is to make a review of the ageing mechanisms in lithium-ion batteries in general, and pay special attention in the ones related to temperature effects. J. Vetter et al. in [13] say that the main ageing effects take place in the interface between the electrodes and the electrolyte but they analyze each electrode interface separately. This document will follow the same structure.

2.2.1 Ageing of anodes

There are three main reasons for the ageing of the anode in lithium-ion batteries. First one is pointed out to be the most important reason of ageing in [13] and is hardly examined during their work.

- Changes of the electrode at the electrolyte interface and in the electrolyte.
- Changes of the active material.
- Changes of the composite electrode.

The most important anode ageing effect appears in the interface between anode and electrolyte, called solid electrolyte interface (*SEI*). *SEI* layer is a protective layer for the anode built during the first charge/discharge cycles. It is permeable for lithium cations but not for other electrolyte components and electrons. The target of the *SEI* layer is to protect electrolyte compounds from further reduction and the electrode from corrosion [13].

Figure 2.6 shows the principle changes in the anode/electrolyte interface. *SEI* layer is composed by electrolyte decomposition products and as mentioned before, it is principally generated during the first cycles of the cell. However, the electrolyte decomposition and *SEI* growth continues during next cycles. This growth carries some bad consequences for the anode. *SEI* penetrates into pores of the electrode and changes

the morphology of the anode. The anode accessible surface area is decreased, hence the impedance raises and there is a power capability fade in the cell. It is important to mention that aspects like impedance increase or safety of the cell depend on the thermal behaviour of the *SEI* layer. Although high temperatures enhance the kinetics of the chemical reaction, they contribute to the aforementioned changes in the *SEI* layer. When *SEI* breaks down because of temperature, more *SEI* layer can be generated to solve the break down by the electrolyte decomposition. Consequently lithium is again lost and hence, there is a capacity loss in the cell. If the *SEI* is not regenerated, the anode surface is exposed to electrolyte reactions.

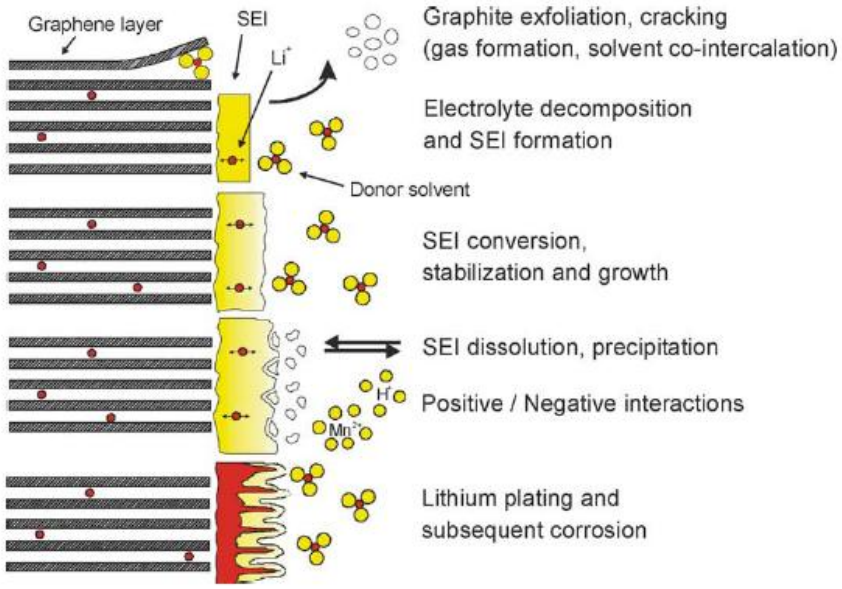

Figure 2.6: Possible changes in the anode/electrolyte interface [10]**.**

Previous ageing effects are related to high temperatures, next one is the slow lithium-ion diffusion at low temperatures. Metallic lithium platting effect and lithium dendrite could appear. Metallic lithium reacts with the electrolyte and accelerates ageing. Again, lithium is lost when metallic lithium is generated and there is a capacity fade in the cell.

The second ageing effect in anodes is considered to happen due to changes in the active material of the chemical reaction but is said to be a minor contributor in the overall ageing of li-ion batteries; actually, this effect is considered to be less than 10% of the total ageing. Most important changes in active material are graphite volume changes. It has a small impact in the reversibility of the material. Besides J. Vetter et al. in [13] point out solvent co-intercalation, gas evolution and cracking formation as an ageing effect.

Finally, ageing due to changes at the composite electrode; the loss of contact in different parts of the composite electrode implies an increasing impedance of the cell. The power capability will decrease. Contact loss between current collector and carbon, between carbon particles and between binder and current collector are the main reasons to enhance the ageing process. The reason is the inevitable volume changing of active anode material during cycling. The last ageing effect is the corrosion of the anode because of possible reactions with the electrolyte. Degradation of the different parts of

the composite electrode occurs. Following, a summary of the previous ageing effects is presented in TABLE 2.3.

TABLE 2.3 SUMMARY OF THE AGEING EFFECTS IN THE ANODE OF LI-ION CELLS [13]

Cause	Effect	Consequences	Bad contribution
Electrolyte decomposition	Loss of lithium Impedance rise	Capacity fade Power fade	High temperatures High *SOC*
Decrease of accessible surface in the anode	Impedance rise	Power fade	High temperatures High *SOC*
Change in porosity of anode	Impedance rise Overpotentials	Power fade	High cycling rate High *SOC*
Metallic lithium platting	Loss of lithium	Capacity fade	Low temperature High cycling rate Overcharge
Solvent co-intercalation Gas evolution and cracking formation	Loss of active material	Capacity fade	Overcharge
Contact loss of active material	Loss of active material	Capacity fade	High cycling rate High *DOD*
Decomposition of binder	Loss of lithium and mechanical stability	Capacity fade	High temperatures High *SOC*
Current collector corrosion	Impedance rise Overpotentials Inhomogeneous distribution of current and potential	Power fade Enhance other ageing mechanisms	Overdischarge Low *SOC*

2.2.2 Ageing of cathodes

As shown during chapter 2, there are a lot of different cathode materials available for lithium-ion cells. Depending on the material of the cathode, performance of the cell, as well as cycle life can be modified, that is why ageing effects in cathodes are also material dependant. In this work, the aim is to give the most important ageing effects in cathodes, and not to examine each cathode material. The ageing effects and their prevention are of increasing interest nowadays but there is not a complete knowledge about the topic. There are some publications focused on this issue. J. Vetter et al in [13] and M. Wohlfahrt-Mehrens et al in [14] made a review of the general ageing effects related to changes in cathodes. In [14] three main principles are pointed out as the reasons of capacity fading at positive electrodes.

- Structural changes during cycling.
- Chemical decomposition/dissolution reaction.
- Surface modification.

Two cathode materials are analyzed in [14], lithium-nickel-cobalt oxides and lithium manganese spinel. Most of the cathode materials presented in this document in chapter 2.1.3 have similar characteristics to these ones.

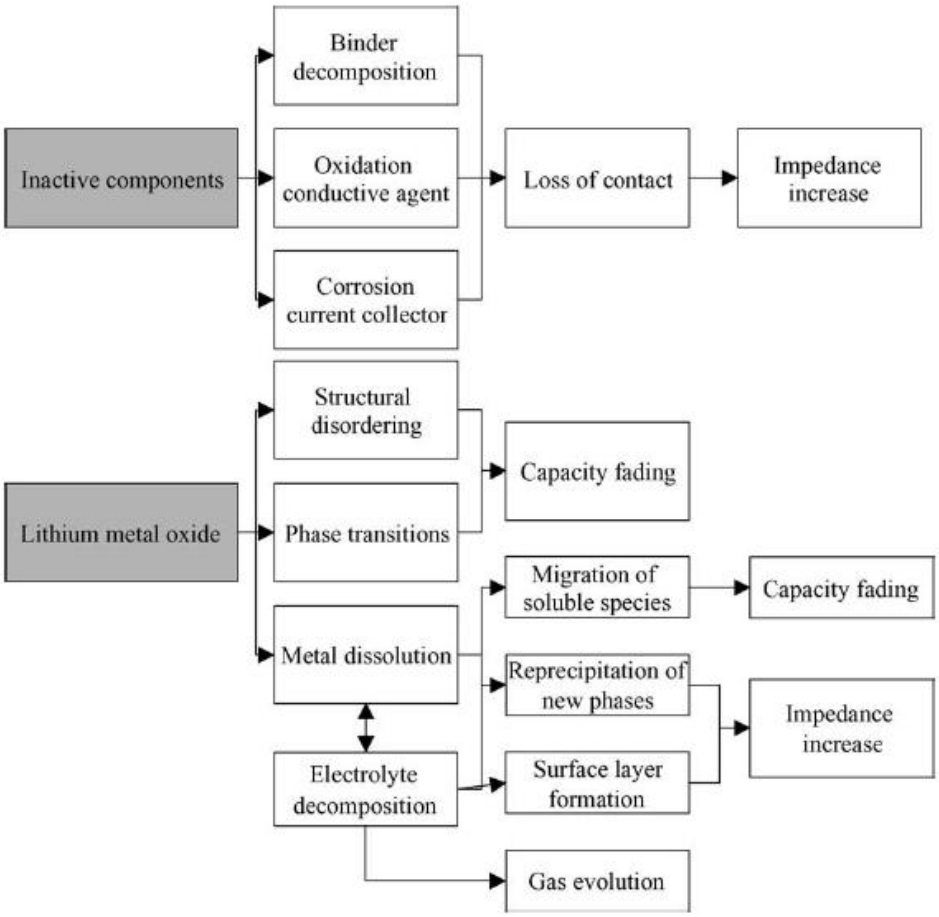

Figure 2.7: Causes and effects of ageing mechanisms in cathodes [14]**.**

Figure 2.7 shows different degradation causes and effects in the cathodes of li-ion batteries. These causes are divided into inactive components and the ones related to lithium metal oxide. The inactive components degradation provokes a loss of contact between the different layers inside the cell and the consequence is the increase of the internal impedance. According to the causes related to the lithium metal oxide, the structural changes suffered can provoke several consequences in the behaviour of the cell like capacity fading, impedance increase or gas evolution.

2.3 Failure modes

Lithium-ion batteries safety limits are specified with their working temperature and terminal voltage levels. Outside the green box, Figure 2.8 shows temperature and voltage related failures. In the worst case, when very high temperatures are reached the thermal runaway can be triggered and the irreversible destruction of the li-ion cell can happen. This effect is considered to happen at high temperatures; however, other temperature related failures happen at lower temperatures like breakdown of *SEI* layer, exothermic breakdown of electrolyte or cathode active material breakdown. Low temperatures are also damaging since lithium platting effect limits the capacity hugely.

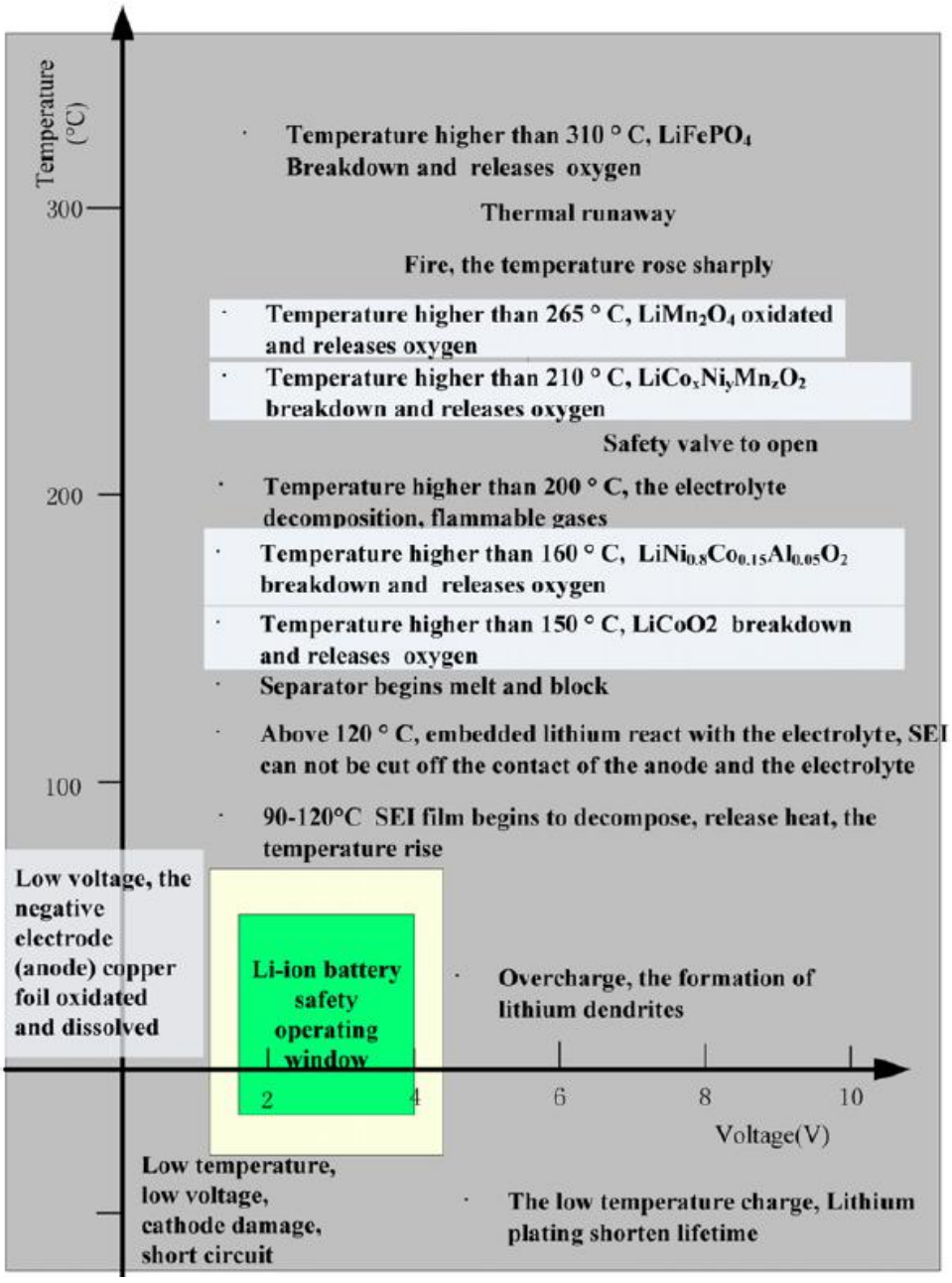

Figure 2.8: Lithium ion cells failure modes [15]**.**

2.3.1 Voltage related failures

Li-ion cells operating voltage must be between certain values in each kind of li-ion cell in order to work properly. If the operating voltage goes beyond the upper limit, the overvoltage causes the generation of the metallic lithium and reduces the capacity of the cell. The operating voltage increase produces an excess of current flowing through the li-ion cell. This excess of current makes the lithium ions not to be able to accommodate quickly enough between the intercalation layers, and they are finally accumulated on the anode surface as metallic lithium. This metallic lithium does not take part in next cycles; it is an irreversible loss of lithium. During the next cycles the capacity loss because of this reason will be appreciable.

Allowing operating voltage to fall below end of discharge voltage for large periods could result in breakdown of the electrode materials. The copper in the anode current collector is dissolved in the electrolyte. This phenomenon could result in a higher self discharge of the cell and finally in a shortcut between the two electrodes. On the other hand, the cathode could suffer a gradual breakdown. Cycling could continue but after some cycles oxygen from the cathode material could be released and result in the capacity loss of the li-ion cell.

2.3.2 Separator shutdown related failure

This property found in some separators is very interesting to protect single cells or cell packs consisting of a few cells connected in series. However, E.P. Roth in [16] validated that if the shutdown occurs in a cell connected in series with high voltages, the thermal runaway could be reached even earlier than without shutdown protection. In this case, the cell in shutdown would increase its impedance and all the voltage would be applied on it. In this case the separator breakdown occurs because of the high voltage applied to the cell.

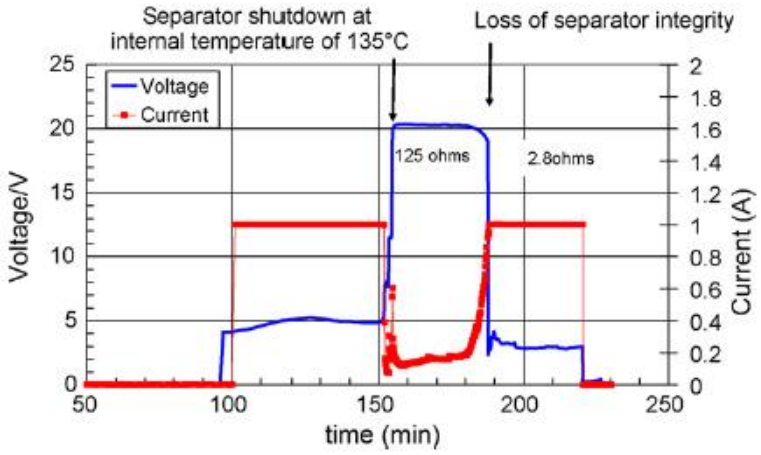

Figure 2.9: Cell voltage and current profile during overcharge situation [16]**.**

Figure 2.9 shows how the voltage is supplied to the measured cell. Around 35 minutes passed since the shutdown of the separator until the separator lost its integrity and failed. The next step was to increase the voltage supplied to the cell to 30 volts. The results are shown in Figure 2.10.

The separator reached its breakdown very quickly resulting in cell thermal runaway. Finally, a comparison between a separator with shutdown protection and another without shutdown protection was done. Figure 2.11 shows the cell with shutdown in the separator resulted in thermal runaway earlier than the cell without shutdown protection.

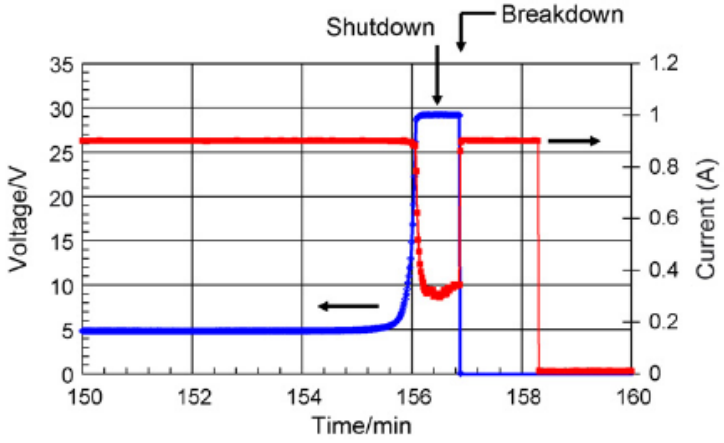

Figure 2.10: Overcharge using higher power supply voltage (30 V) [16].

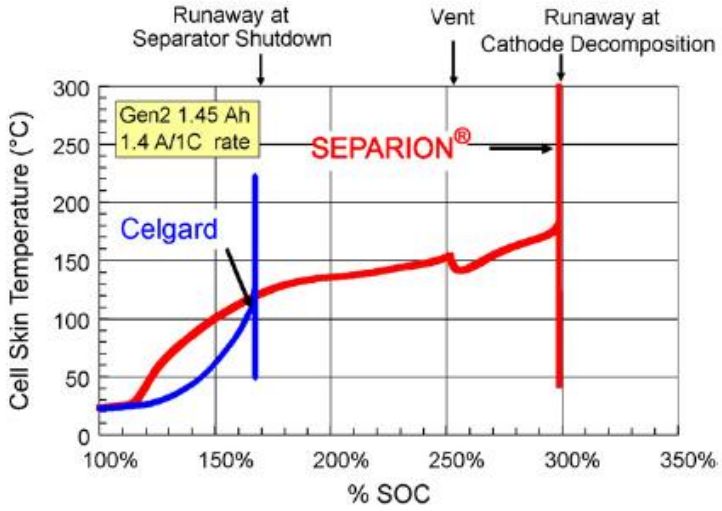

Figure 2.11: Comparison between separators with shutdown and without shutdown protection [16].

2.3.3 Temperature related failures

Temperature related failures will be analyzed in detail during the state of the art of next chapters during this document, however, a brief introduction to these failure modes will be done in this section; there are two failure modes due to temperature in li-ion cells: low temperature failure mode and high temperature failure mode. Working at low temperatures is damaging for li-ion cells because of the lithium platting effect; if this

phenomenon occurs some lithium is lost for the chemical reaction and the capacity of the cell is reduced. In extreme conditions, under -20ºC the situation is critical because the cell can reach the *EOL* in a few cycles.

Working at very high temperatures thermal runaway phenomenon can be triggered. The working temperature has to be very high for this to happen, above 70ºC but if this phenomenon is triggered the cell can explode or even burn.

2.4 Summary and justification of the work

Temperature is one of the key factors regarding to performance and lifespan in lithium-ion batteries as mentioned during Chapter 1; high temperatures can reduce the lifespan of a lithium-ion cell and when very high temperatures are reached (above 70ºC) the *thermal runaway* phenomenon can be triggered, bringing the cell even to its destruction. Low temperatures are also damaging for lithium-ion cells due to the lithium platting effect; lithium is accumulated on the anode surface as metallic lithium and this lithium will be unusable for future reactions. The consequence is a reduction in the available capacity.

There are some ageing effects related to temperature in both electrodes, thus temperature is clearly one of the reasons of cell ageing. This is the reason of doing the whole following work, in order to minimize the impact of temperature in cell ageing without forgetting safety. The information given before is quite general and can be completed with the work of Arora et al. in [12], it is a more extensive work. Different authors have worked on the topic of temperature and cell ageing; following, some of these works and their conclusions are presented. There are some experimental works where temperature effects in capacity and power fading are presented. In literature the long term cycling (more than 4000 cycles) of $LiFePO_4$ cells has been demonstrated being this one of the advantages of this technology. However, Zhang et al. in [13] showed how capacity fading in $LiFePO_4$ cells was critical depending on temperature. They cycled the cell at elevated temperatures (50ºC); after 600 cycles the capacity was the 74% of the initial. Each 300 cycles they made capacity and power fade characterizations at different temperatures (-10, 0, 25 and 45ºC) to measure the remaining capacity and power. They attributed the capacity fading to the growth of the *SEI* layer in the anode and the subsequent loss of lithium. Figure 2.12 shows these results. During the first 300 cycles capacity fading is not so hard. However, there is an abrupt fall of the capacity during the second 300 cycles. They also studied the power fade of the battery and saw that the most critical working temperatures are the low ones. There was an impedance rise because of the iron deposition in the anode. The discharge pulse power capability at 45ºC does not decrease during the cycle life. However, at low temperatures, 0 or -10ºC the power fade after 600 cycles is 61.6% and 77,2% respectively.

Dubarry et al. in [14] talked about the loss of lithium because of the growth of *SEI* layer as the main reason of capacity degradation, in addition to the loss of active materials. They used a dynamic stress test (*DST*) cycle aging and obtained some results comparing the Peukert coefficient along the cycle life of the $LiFePO_4$ cell.

Broussely et al. in [15] differentiate between aging during cycling and during resting, The main aging effects when cycling are the growth of the *SEI* and the electrode porosity or surface reduction in the electrode. Talking about aging on rest they say that only thermodynamical stability of the components in presence will govern the aging. In addition, they mention that any defect in the *SEI* will result in lithium corrosion because cycling is needed to repair the *SEI*. In reality, the *SEI* layer is never totally perfect and a low rate of corrosion can always be suffered on rest.

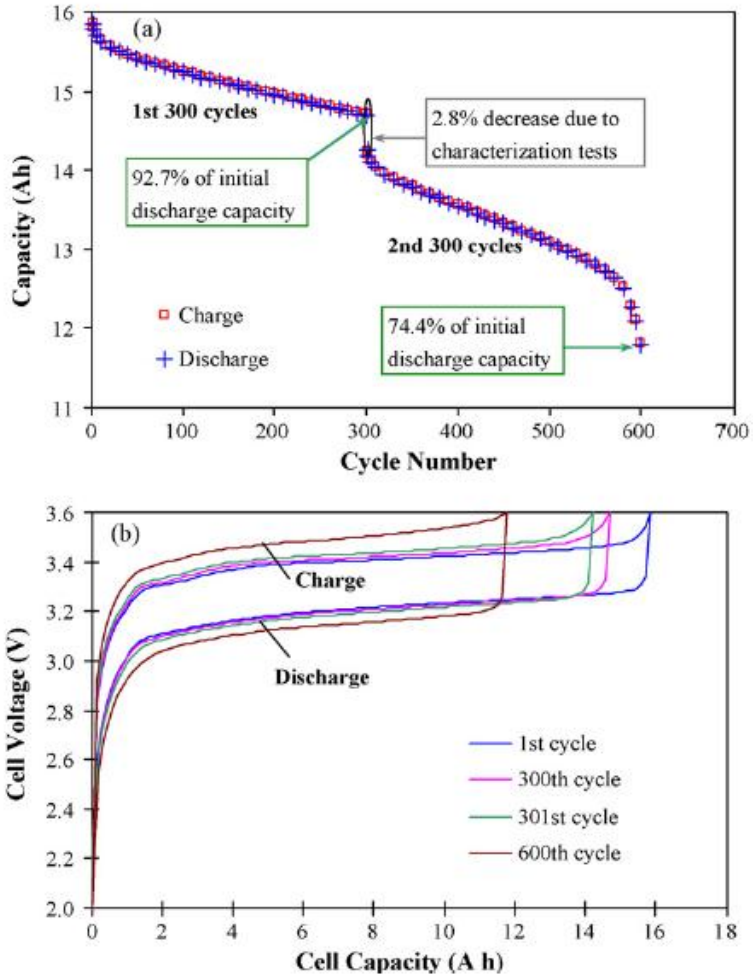

Figure 2.12: Cycling performance of a LiFePO4 cell at 3C rate and 50ºC, from 3,6 to 2 volts. a) Capacity vs cycle life; b) Charge/discharge loops in different points of their cycle life [13]**.**

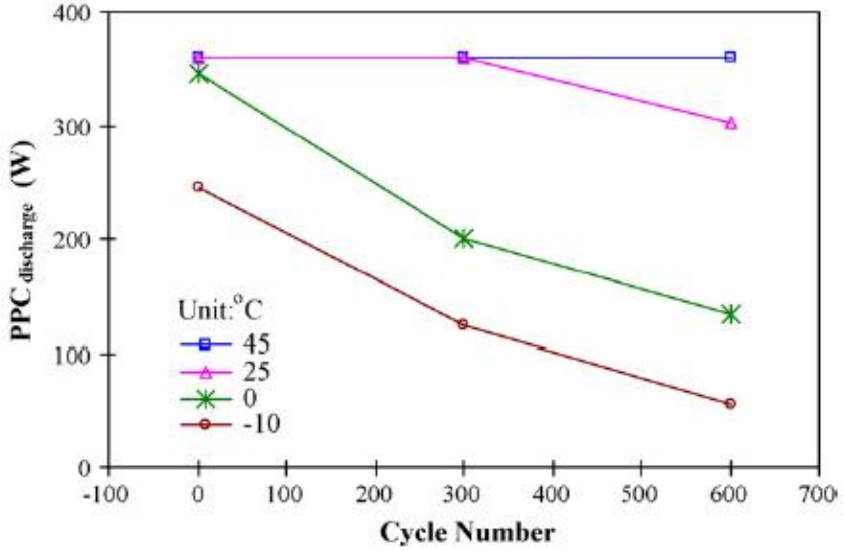

Figure 2.13: Discharge pulse power capability of a $LiFePO_4$ cell during its cycle life at different temperatures [13]**.**

Wang et al. in [16] pointed out the loss of active lithium associated to anodes again as the main reason of cell ageing. They made a large amount of essays at different temperatures, *DOD* and C-rates to evaluate the cycle life and calendar life of a $LiFePO_4$ cell. Their results are partially shown in the following three figures.

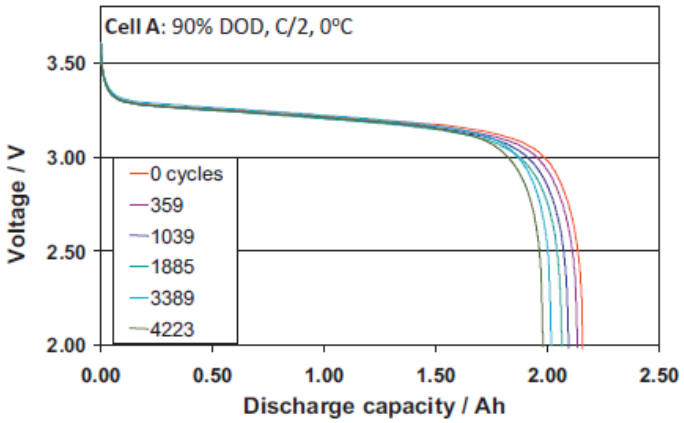

Figure 2.14: Discharge curves of a $LiFePO_4$ cell at 0ºC during its cycle life [16].

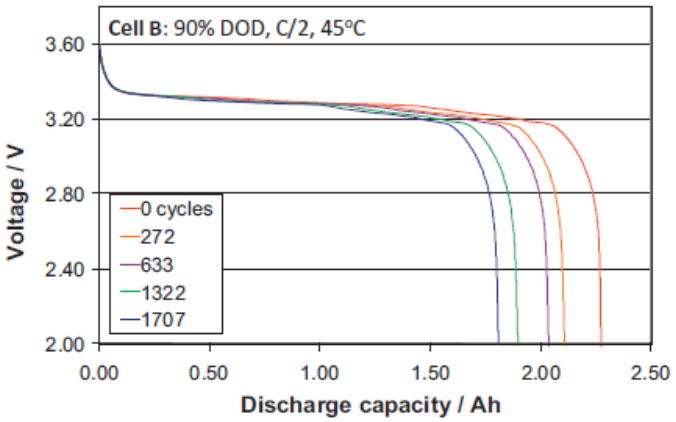

Figure 2.15: Discharge curves of a $LiFePO_4$ cell at 45ºC during its cycle life [16].

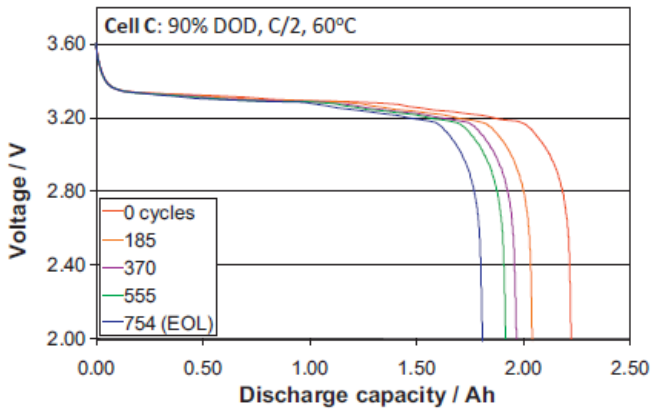

Figure 2.16: Discharge curves of a $LiFePO_4$ cell at 60ºC during its cycle life [16].

Although higher temperatures improve cell performance in terms of capacity, the cycle life is hardly reduced in comparison with lower temperatures. The conclusion of the

work was that the capacity is strongly affected by temperature and time while the effect of *DOD* was less important in low C-rates.

Belt et al. in [17] tested six 12 Ah cells to evaluate cycle life performance as a power assist vehicle battery. They did different essays following the *PNGV* Battery Test Manual, Revision 3. They had to probe that the six cells were able to get some power and capacity goals. Figure 2.17 shows that the initial amount of capacity is stable for the six Saft America HP-12 (12 Ah) cells. Besides, the amount of capacity is reduced at low temperatures (10ºC) and increased at higher temperatures (45ºC). Although the skills of the cells were improved working at elevated temperatures, Belt et al. thought the cycle life was going to be reduced because of the temperature.

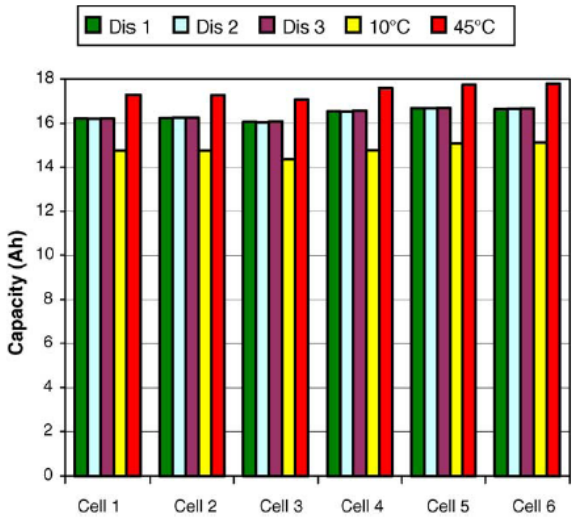

Figure 2.17: Capacity initial characterization of the cells [17]**.**

However, the results obtained showed that cells cycled at 50ºC had a larger amount of capacity after 300,000 cycles that the ones cycled at 30ºC. They said that this was an unexpected result shown in Figure 2.18. *RPT0* corresponds to the initial state of the cycle life, and *RPT11* to the end of life. The same happened with the power results. Cells cycled at high temperatures (50ºC) were thought to suffer a severe power fade against the ones cycled at lower temperatures (30 or 40ºC) but the difference only was evident in one of the cells cycled at 50ºC, in the other one there was much power available at the end of the test. Figure 2.18 is showing the power results.

Another important ageing aspect shown in Figure 2.19 and proved in the bibliography is the depth of discharge (*DOD*). High *DODs* during the life of li-ion cells have important consequences in their cycle life. They cause a loss of contact in the active material with the subsequent loss of active lithium involved in the chemical reaction. The capacity of the cell is reduced due to this effect, so the cell will reach its end of life (*EOL*) earlier than with a smaller *DOD*. Wang et al. in [16] analyzed this phenomenon doing a capacity test to different $LiFePO_4$ cells under different *DODs* and temperatures. As it is shown in Figure 2.19 in each temperature, the cell cycled more times was the one cycled with the lower rate of *DOD*.

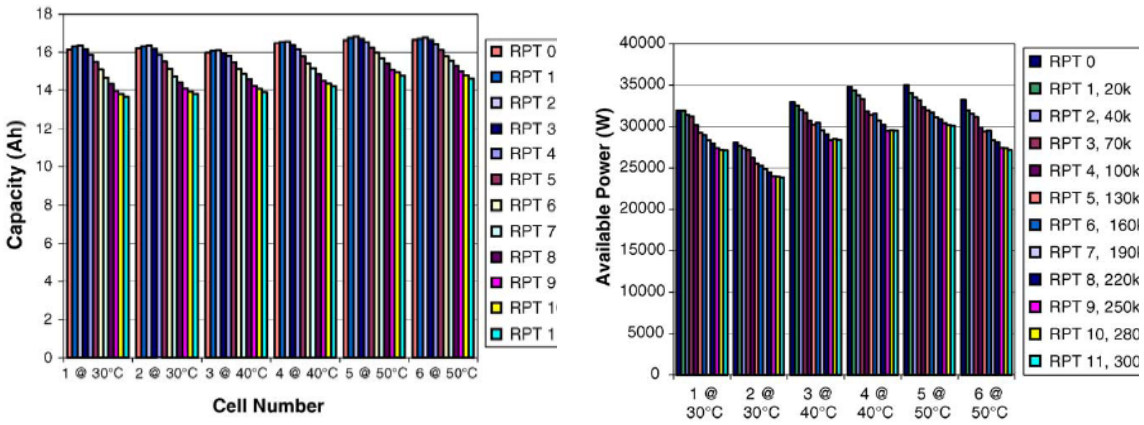

Figure 2.18: Available capacity and power capability vs cycle life for six Saft America HP cells [17]**.**

If the *DOD* is too much high, the overdischarge can be reached. The overdischarge is a very high *DOD*, so the bad contributions of the *DOD* are enhanced. In some works current collector corrosion is pointed out because of the overdischarge. The effects of corrosion are an impedance rise, and inhomogeneous distribution of current and potentials. The same happens with high states of charge (*SOC*) and overcharges. High *SOCs* have bad contributions in terms of porosity changes in the anode, electrolyte decomposition and decreasing the accessible surface in the anode. Overcharge enhances these problems and adds another one, the lithium platting and the subsequent loss of capacity.

Finally, high cycling rate also has bad contributions to cells. Some works point out lithium platting and contact loss of active material as two important causes of cycling the cell with high cycling rates. Capacity loss is unavoidable under these conditions [1].

	Temperature °C												
DOD (%)	-30		0		15		25		45		60		C-rate
90	1	1	2242	2240	2144	2130			1796	1661	754	518	
80	1	1	2520	2520	2390		2439	563	2120	2123	1011	1006	
50	13	15	3976	3965	3827	3804			3387	3317	3355	3963	
20	2662	4979	9625	9652	9234		4711	2211 2204	8374	8379	9801	9821	C/2
10	9678	12082	18579	18534	18067	17940			16235	16571	19098	19385	

Figure 2.19: Degradation of the cell due to the DOD and temperature [1]**.**

As a conclusion of the chapter, we can say that temperature managing in lithium batteries is important in terms of safety, performance and cycle life. Lots of authors talk about this topic in their works. However, it is important to know the ideal working point of the cell working with. Although temperature is critical for ageing, another aspects like high *DOD* and *SOC*, high cycling rate, overcharge and overdischarge are important aspects also. Taking them into account as much as possible when using the cell, the ageing effects could be minimized and consequently extend the cycle and calendar life of the cell.

Chapter 3. THERMAL CHARACTERIZATION AND MODELLING OF LITHIUM ION SINGLE CELLS

The main topics of the chapter are thermal characterization of lithium ion cells and the steps followed to develop thermal models of these devices. A brief introduction and the state of the art about these topics will lead to the methodology applied since the li-ion cell is acquired until the thermal model is reached.

This methodology is divided in three parts: firstly, the calculation of the internal heat generation of the device; two experimental tests are required to calculate the internal heat generation; after that, thermal characterization experimental tests where some thermal properties of the li-ion cell are estimated; and finally the developed thermal models are presented and validated comparing them with real charge/discharge cycles. At the end of the chapter the main conclusions will be explained in detail and possible improvements will be also proposed.

3.1 Introduction

Although li-ion batteries are nowadays integrated in many low power systems, power applications are the main target related to these systems since they can be useful in grid applications supporting the main grid, or in electro-mobility making autonomous systems without grid connection.

There are several parameters that are specific for each li-ion cell depending on the technology used, the size of the cell, manufacturer or format; hence, it is usual to characterize the cell both electrically and thermally. The aforementioned parameters are the internal resistance, the open circuit voltage, internal heat generation or heat capacity, for instance. In this work some experimental tests are conducted to measure these parameters and to evaluate the thermal behaviour of the device under different working conditions.

Besides, designing energy storage systems for power applications requires testing single cells and battery packs under real power applications requirements to ensure their reliability. During these tests, the energy storage system is exposed to very important thermal and electrical stresses. Besides, testing the behaviour of these devices under real conditions is very time consuming; in this context it is interesting to have a simulation tool able to model the electrical and thermal behaviour of the energy storage system without exposing it to electrical and thermal stress, and wasting less time. Therefore, first step to reach this simulation tool is the li-ion single cell model.

The objective of this chapter is to implement a methodology to thermally characterize li-ion single cells and to develop a model able to simulate the behaviour of these devices for different current profiles.

3.2 State of the art

According to the thermal characterization and modelling of li-ion single cells, there are two main aspects analyzed in this document, as shown in Figure 3.1: the internal heat generation models and the temperature distribution ones. The internal heat generation models represent the heat generated inside li-ion cells due to chemical and electrical processes; analyzing the bibliography these models can be divided into coupled and decoupled models. In coupled ones an electrochemical model calculates the internal heat generation of the li-ion cell and a thermal model calculates the influence of this heat generation into chemical and physical parameters within the cell. Decoupled models do not take into account this influence for the calculation of the internal heat generation.

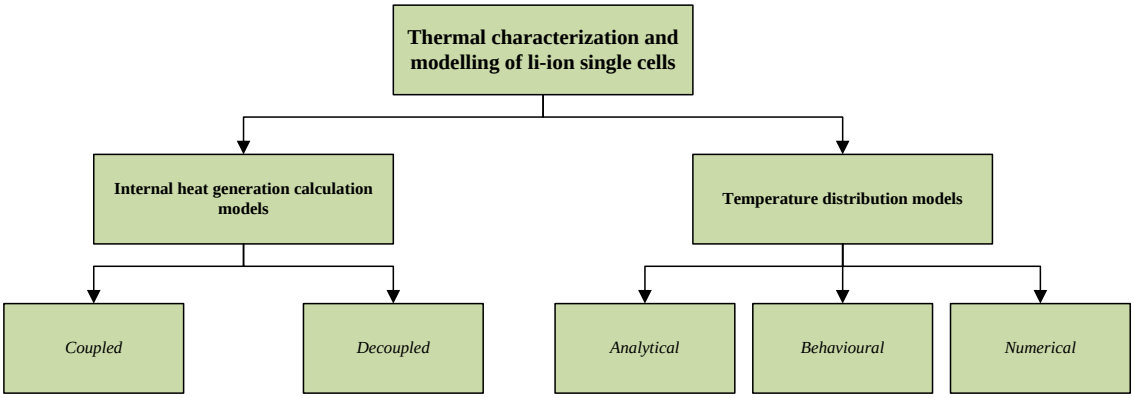

Figure 3.1: Summary of the state of the art in this chapter.

Temperature distribution models instead can be divided into three main groups: analytical, behavioural and numerical models. Analytical models use mathematical equations to calculate the temperature distribution of the cell; in the case of li-ion cells, the electrical and chemical processes can be difficult to implement analytically. Behavioural ones approximate the heat transfer problem to an electrical problem taking advantage of electrical equivalent circuits. Finally, numerical models calculate the heat transfer problem in different points across the cell to reach an accurate temperature distribution using specialized finite element simulation tools.

3.2.1 Internal heat generation models

Temperature distribution within li-ion cells depends on the amount of heat generated per unit volume in it, and how this heat is distributed inside the cell. Lithium-ion cells in general are complex systems where chemistry, thermodynamics and electricity take part in charge and discharge processes. Bandhauer et al. in [2] mentioned three principle sources of heat in lithium-ion cells.

- Interfacial kinetics. Heat is produced due to changes in the concentration of the reactants in the chemical reaction; the amount of heat generated by the chemical reaction depends on the activation and relaxation reaction rate in the chemical process.

- Species transport. Heat produced due to the movement of active materials inside the battery.
- Ohmic losses. Heat produced due to the Joule effect.

There are four principle terms when calculating the internal heat generation (q) inside a li-ion cell; the enthalpy of the reaction, the enthalpy of mixing of active materials, the enthalpy of the phase change of materials and side reactions. Depending on the assumptions made by the author, the complete equation (3.1) can be modified.

$$q = Enthalpy\ of\ reaction \begin{Bmatrix} Irreversible\ heat\ rate[I^2 \cdot Rint(SOC)] \\ entropic\ heat\ rate(SOC) \end{Bmatrix} + \\ + Enthalpy\ of\ mixing + Enthalpy\ of\ phase\ change \\ + side\ reactions \tag{3.1}$$

The enthalpy of the reaction is the sum of the irreversible and entropic heating; the irreversible heat rate is the term caused by Joule effect. The internal resistance (R_{int}) value increases when a low *SOC* is reached, thus, for the same charge or discharge current, power losses due to Joule effect are higher for low values of *SOC*. The entropic heat rate reflects how incremental addition of lithium atoms affects ordering of lithium on the host lattice. This term is reversible depending on the *SOC* value; the reversibility of this term makes the process to be endothermic or exothermic when low current rates are applied (less than *C/1*). However, under higher currents, irreversible heat rate makes the overall heat rate to be exothermic.

The enthalpy of mixing heat rate is related to the concentration and relaxation gradients in the active materials inside the cell during the chemical process. These reaction rates are not uniform during the whole charge and discharge process. When the current is cut off the concentrations gradients inside the cell relax and cause heat opposite in sign but equal in magnitude to the one produced due to concentration gradients. This term is usually negligible because it will only be significant if the enthalpy of the mixture as a function of concentration is nonlinear. Phase change term is the heat produced due to phase changes in active materials within the cell and is usually negligible also.

Side reactions term is referred to the heat produced by degradation due to charge and discharge cycling, and because of the effects derived of this degradation, capacity fading and changes in composition of active materials inside the cell. There is another heat rate source that appears sometimes in bibliography: Joule heating produced from bulk electron movement in the current collectors. Bandhauer et al. in [2] mentioned that this term is insignificant in small cells but it is important in large ones. Kim et al. in [17] have researched the thermal behaviour of current collectors in li-ion pouch cell with a mathematical procedure. They concluded that it is important to model the heat rate from bulk electron movement in the current collectors when large size pouch cell batteries are used.

3.2.1.1 Decoupled models

Bernardi et al. in [18] determined an expression for the calculation of heat generation inside a battery cell using a thermodynamic energy balance for the whole cell volume; this equation uses an average temperature for the cell and applying the first law of thermodynamics around it, the following expression is achieved:

$$q = IV + \sum_l \left[I_l T^2 \frac{d\frac{OCV_{l,avg}}{T}}{dT} \right] - \quad \text{entalphy of reaction}$$

$$- \sum_j \frac{d}{dt} \left[\int_{v_j} \sum_i c_{i,j} RT^2 \frac{\partial}{\partial T} \ln \left(\frac{\gamma_{i,j}}{\gamma_{i,j}^{avg}} \right) dv_j \right] - \quad \text{entalphy of mixing} \qquad \textbf{(3.2)}$$

$$- \sum_{j\,,j \neq m} \sum_i \left[\left(\Delta H_{ij \to m}^0 - RT^2 \frac{d}{dT} \ln \frac{\gamma_{i,m}^{avg}}{\gamma_{i,j}^{avg}} \right) \frac{dn_{i,j}}{dt} \right] \quad \text{phase change}$$

First term corresponds to the electrical power and the second one is the sum of reversible work and entropic heating; third term corresponds to the power losses by mixing of active materials and the last one to the heat produced by phase changes of the materials within the cell. This expression and several variants of it are commonly used in bibliography for the calculation of the internal heat generation due to its compromise between accuracy and simplicity. Several authors used this equation in a simplified version (3.3), where mixing and phase change heat sources are neglected.

$$q = I\left(OCV_{avg} - V\right) - I\left(T \frac{\partial OCV_{avg}}{\partial T}\right) \qquad \textbf{(3.3)}$$

OCV_{avg} *[V]*	Average open circuit voltage (OCV)
V [V]	Cell voltage
I [A]	Current through the cell
T [K]	Temperature of cell

First term on the right side is the overpotential due to ohmic losses, charge transfer overpotentials at the interface and mass transfer limitations; the electrode potential is determined to be average. The second one is the entropic heat, and the derivative of the open circuit voltage respect to temperature is called entropic heat coefficient. TABLE 3.1 is showing four different researches where internal heat generation is calculated with decoupled models and concretely with equation (3.3).

TABLE 3.1 SUMMARY OF THE RESEARCHES USING DECOUPLED MODELS FOR INTERNAL HEAT GENERATION

Author	Equation used to model *q*	Temperature dependency	Cell voltage and OCV calculation
Al Hallaj et al.[19]	(3.3)	Entropic	Experimentally
Chen et al. [20]	(3.3)	Entropic	Experimentally
Onda et al.[21]	(3.3)	Entropic and current distribution	Experimentally
Wang et al.[22]	(3.3)	Entropic	Experimentally

3.2.1.2 Coupled models

An alternative for the experimental calculation of internal heat generation are coupled models. An electrochemical model interacts with a thermal model to predict the temperature distribution of the cell. Figure 3.2 shows a diagram with the interconnection of both models; q is used in the calculation of temperature distribution and this temperature is the feedback for the electrochemical model.

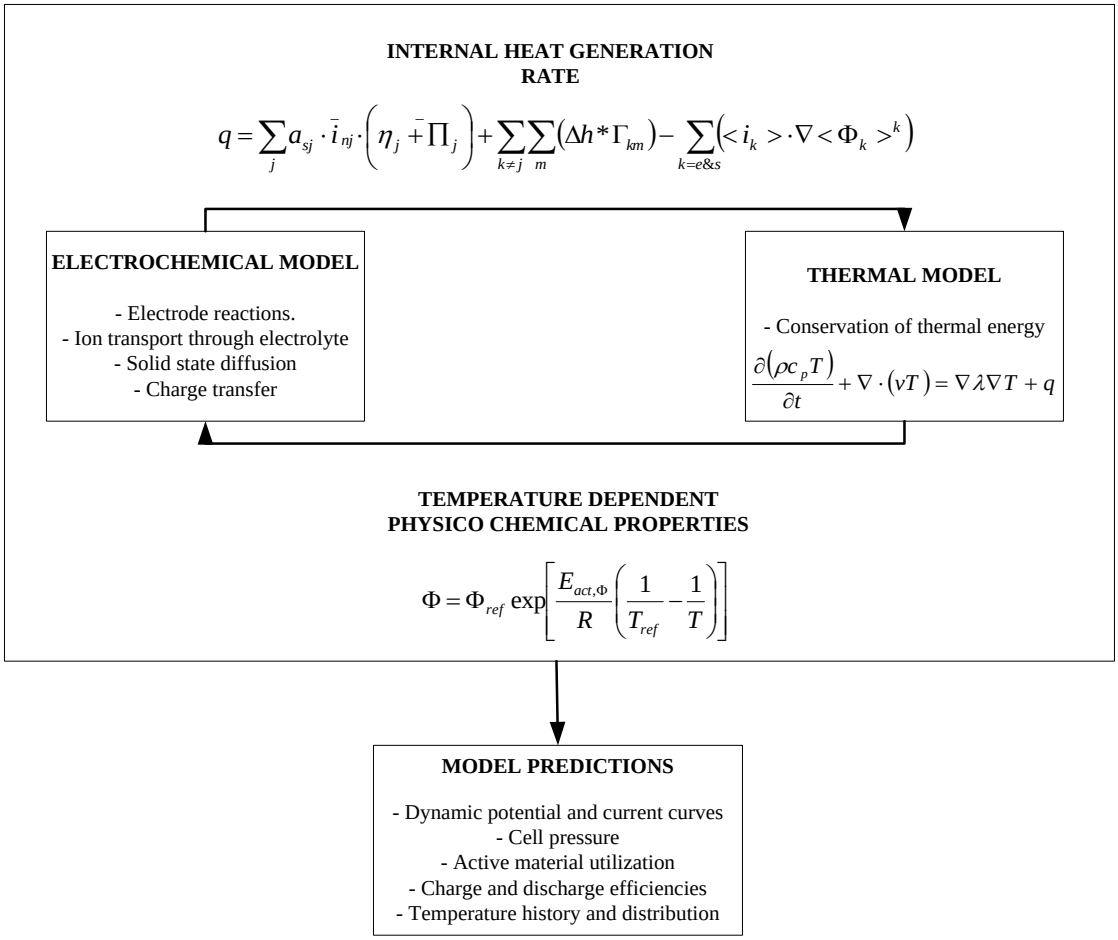

Figure 3.2: Coupled electrochemical and thermal model [23]**.**

This diagram was presented by Gu et al. in [23]; in this case the calculation of q is much more complex because electrochemical aspects are taken into account; besides, information about the internal composition of the cell is required and this information is hardly provided by the battery manufacturers. Equation (3.4) shows the equation they used to model the internal heat generation of a li-ion battery cell.

$$q = -\sum_j a_{sj} \cdot \bar{\imath}_{nj} \left(U_j - T \frac{\partial U_j}{\partial T} \right) + \sum_j a_{sj} \cdot \bar{\imath}_{nj} \left(\bar{\Phi}_{se} - \bar{\Phi}_{es} \right) + \\ + \sum_{k \neq m} \sum_m (\Delta h * \Gamma_{\mathrm{km}}) - \sum_{k=e\&s} \left(< i_k > \cdot \nabla < \Phi_k >^k \right) \quad \textbf{(3.4)}$$

First two terms on the right side of equation (3.4) refer to the enthalpy of the chemical reaction; third term refers to the heat generated due to phase change of materials and the last one is the heat generated due to Joule effect. Each term in this equation is temperature dependent and more terms are included in the equation, hence, the calculation of the internal heat generation is more accurate than in equation (3.3).

TABLE 3.2 shows different studies with electrochemical models coupled with thermal models; the most common electrochemical model used in bibliography is the one presented by Doyle et al. [24], and different equations are used to model the thermal model. Dependency of temperature in overpotentials and ohmic losses are included in the internal heat generation calculation.

TABLE 3.2 SUMMARY OF RESEARCHES APPLYING AN ELECTROCHEMICAL-THERMAL COUPLED MODEL [2]

Author	Electrochemical model	Equation used to model q	Temperature dependency	OCV
Pals and Newman	Doyle et al.	(3.3)	Overpotential	Not given
Botte et al.[25]	Fuller et al.	Rao and Newman equation plus negative electrode decomposition	Decomposition reaction rate	Dahn et al. and Doyle
Thomas and Newman [26]	Doyle et al.	Given formulation with or without mixing or reaction rate	Overpotential and entropic	Thomas et al.
Gomadam et al.[27]	Doyle et al.	Gu and Wang	Overpotential, ohmic and entropic	Not given
Kumaresan et al.[28]	Doyle et al.	Gu and Wang	Overpotential, ohmic and entropic	Measured in paper
Verbrugge [29]	Applied voltage	(3.3)	Overpotential, ohmic and entropic	Data given in paper
Song and Evans [30]	Doyle et al.	Complete model	Overpotential, ohmic and entropic	Doyle et al.

To sum up, electrochemical-thermal coupled models are more accurate than the decoupled ones although they need to know the internal composition of the cell in addition to the chemical and thermal properties of the materials taking part in the chemical process. Thus, the simplicity is the most important advantage of the decoupled models.

3.2.2 Temperature distribution models

Temperature distribution for a single li-ion cell is an important aspect to keep under control; a non uniform temperature distribution can lead to a faster aging process of the cell and decrease its benefits. Besides, achieving the temperature distribution of a cell can help in the design of the thermal management system if this cell is used within a battery pack. Modeling this aspect for different working conditions without the need of experimental tests is important to avoid aging and also to reduce time consumption of these experimental tests with simulations. Each application will demand a different current profile, and the model must be able to calculate the temperature distribution for any current profile demanded. The evaluation of the model is commonly made with the superficial temperature of the cell because normally it is impossible to measure temperature inside the cell without special equipment.

Achieving the temperature distribution of the cell consists of having a concrete value of temperature for each infinitesimal of the battery cell; obviously it is not possible to calculate numerically one temperature for each infinitesimal. The infinite order model is reduced to a finite order one limiting the number of points for the calculation. Sometimes, when small cells are used, no spatial accuracy is needed and the cell itself can be defined as the less significant element of the model; an average temperature for the entire cell will be achieved. Spatial accuracy is lost but computational time is saved. According to bibliography there are 1D, 2D and 3D temperature distribution models depending on the shape of the cell analyzed and also depending on the accuracy required and the complexity permitted. Three different groups of models can be found in bibliography: analytical models, behavioral models and numerical models.

3.2.2.1 Analytical models

Analytical models solve the energy balance in equation (3.5) to calculate the temperature distribution across the li-ion cell. The term on the left side in equation is the heat stored by the cell; first term on the right side represents the conduction for the three Cartesian axes and q represents the internal heat generation of the cell. Muratori et al. in [31] use an analytical model for the calculation of the temperature distribution in a pouch cell.

$$\frac{\partial\left(\rho c_p T\right)}{\partial t} = \nabla k \nabla T + q \qquad \textbf{(3.5)}$$

3.2.2.2 Behavioural models

Based on the analogy principle, the physical variables are represented by electrical equivalent variables working with behavioural models. The most common equivalent thermal circuits in bibliography are *continued fraction circuits* or *Cauer networks*, and *partial fraction circuits* or *Foster networks* [32]. *Cauer models* reflect the real physical setup of the battery, with thermal capacities with intermediary thermal resistances representing each layer of the cell. *Foster models* nodes instead, do not represent

physically the li-ion cell [33]; Figure 3.3 presents these two different thermal equivalent circuits.

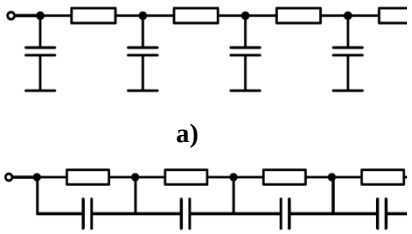

a)

b)

Figure 3.3: Thermal equivalent circuits. a) *Cauer model*; b) *Foster model* [32]**.**

Figure 3.4 shows the equivalent *Cauer model* used by Forgez et al. in [34]; C_{th} and R_{th} represent the thermal capacity and thermal conductivity of the cell respectively. T_{in} is the temperature inside the cell and T_s is the temperature on the surface of the cell. Finally, q models the internal volumetric heat generation of the cell.

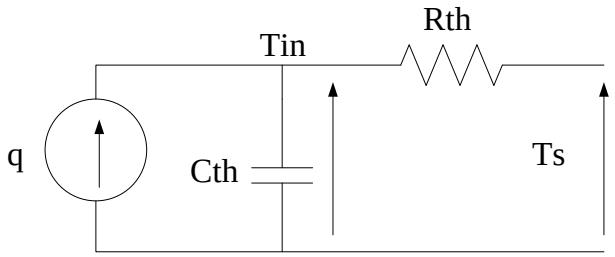

Figure 3.4: *1st order Cauer model* for a li-ion single cell [34]**.**

Forgez et al. measured temperature inside a cylindrical cell and on the surface of it. Then, they calculated R_{th} in a steady state situation, and C_{th} applying a step at the input q and doing a transient analysis of the system. They concluded that it was necessary to have thermal models in li-ion cells to be able to predict the inside temperature; the validation of their model showed an error less than 1.5ºC. *Foster networks* are also used by other authors as Xiao et al.[33].

In other cases the interior of the cell is not accessible for the user to measure the inside temperature of the cell; in this cases *electrothermal impedance spectroscopy* techniques are used to estimate the parameters of the equivalent electrical circuit. Schmidt et al. in [35] presented two procedures to estimate the parameters of the equivalent electrical circuit in Figure 3.4 for a li-ion pouch cell.

3.2.2.3 Numerical models

Numerical models take advantage of powerful numerical tools to calculate the temperature distribution of the cell with higher order models than in the previous cases. Finite element simulation tools are commonly used for this purpose; internal heat generation is applied in the different points of the model and a conduction problem is solved for the whole li-ion cell to calculate the temperature distribution. The internal heat generation can be defined as a constant for the whole cell or spatially dependent.

The heat capacity of the materials within the cell or an equivalent heat capacity for the entire cell must be known. Besides, the thermal conductivity in each Cartesian axes or an average value of it have to be known to solve the problem with numerical models.

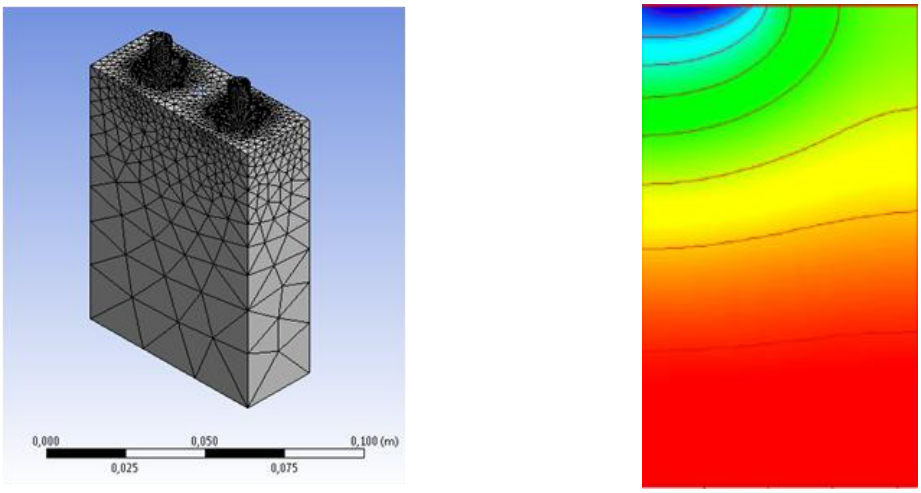

a) **b)**

Figure 3.5: a) Meshing of a cell with a finite element simulation tool; b) Temperature distribution of a li-ion cell [36]**.**

Figure 3.5 shows a prismatic li-ion cell meshed by a finite element simulation tool and a temperature distribution obtained for another pouch cell for a concrete current profile. The infinite order problem is converted into a finite high order model and then the temperature profile is calculated and the possible hot spots of the cell are detected. These models are normally very time consuming comparing them with the previous ones but a better accuracy is reached.

3.2.3 Conclusions of the state of the art

According to the internal heat generation model, it is considered a decoupled model to be the best option for this work. Coupled models require knowing the chemical processes occurring inside the cell and information about the properties of the materials within it. This information is hardly provided by manufacturers, so a decoupled model is selected in this work for the internal heat generation model. The advantages are the simplicity of the model and the amount of works where such models are used; as a drawback, the accuracy is the most important one.

For the temperature distribution issue, three different models will be developed: 1st order and 2nd order behavioural models, and a numerical 3D thermal model. Behavioural models are adequate for single cell level because of their simplicity. Numerical models are considered a good option if battery modules and packs are going to be modelled and a single cell numerical 3D model is the first step to get this kind of simulation tool. Besides, battery thermal management systems will be designed during this work and numerical simulation tools can be suitable for this purpose.

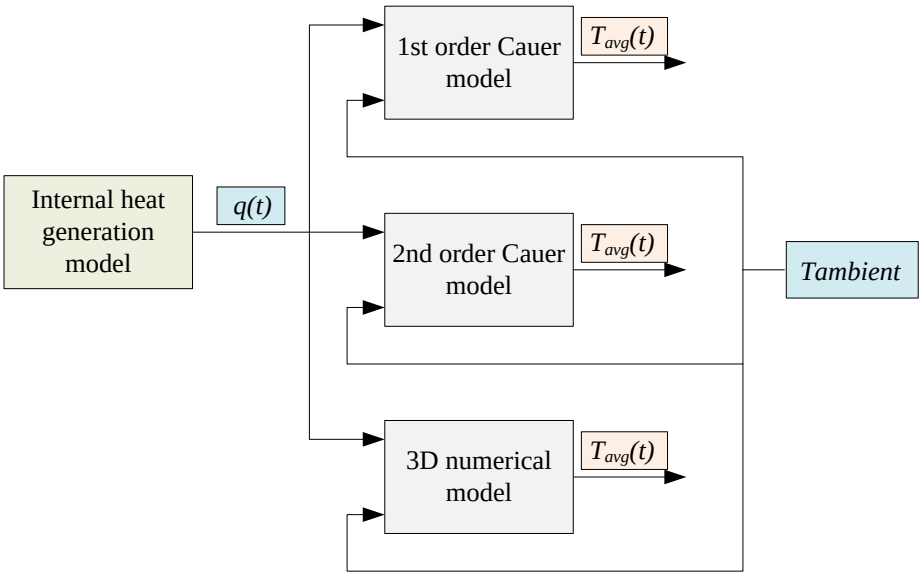

Figure 3.6: Overall diagram of the thermal models developed in this work.

Figure 3.6 shows an overall diagram of the thermal models developed in this thesis work after analyzing the state of the art. An internal heat generation model will estimate the heat generated within the cell; this internal heat generation will be one of the inputs for the three models previously mentioned. The other input will be the ambient temperature; as the experimental tests will be done in this work in a controlled chamber, this input will be constant. The thermal properties of the cell under test will be estimated with experimental thermal characterization tests to configure each thermal model. Finally, the output of the thermal models will be an average surface temperature of the cell. Following, the internal heat generation model proposal, the thermal characterization process developed and the thermal model proposals are going to be explained in detail.

3.3 Internal heat generation model proposal

The internal heat generation model in this work is based on the equation of Bernardi et al. [18], equation (3.6) in this document. The *q* value calculated is an average value of the whole cell, it is not spatially dependent. The main drawback of this equation is the lack of accuracy during the transients; during the transients all the current is not generating heat losses inside the cell but this equation does not take it into account. However, the error committed is assumable for the applications analyzed during this work.

$$q = I\left(OCV_{avg}(SOC) - V\right) - I\left(T\left(\frac{\partial OCV_{avg}}{\partial T}(SOC)\right)\right) \quad \textbf{(3.6)}$$

Figure 3.7 shows the internal heat generation model used in this work. The *OCV* and the $\partial OCV_{avg}/\partial T$ are *SOC* dependent; the instantaneous values of these parameters are calculated using look up tables. Equation (3.6) also requires the instantaneous value of the terminal voltage *(V)*, the charge or discharge current *(I)*, and cell temperature *(T)*.

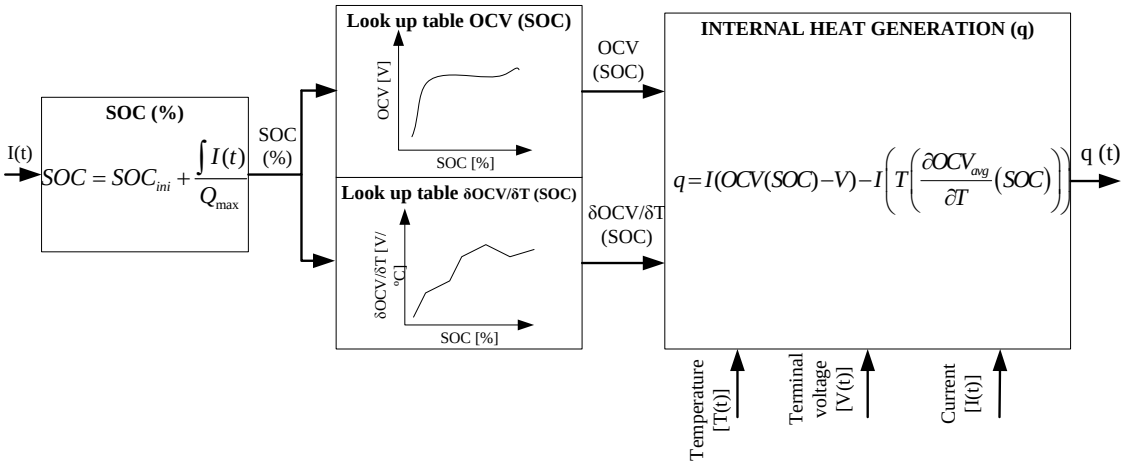

Figure 3.7: Internal heat generation model proposal.

3.3.1 *OCV* determination

In this thesis work a *linear interpolation method* [37] has been developed to determine the *OCV*. The *linear interpolation method* consists of doing a complete charge and discharge with a very low current rate *(C/20)*; the overpotential effect is neglected and the *OCV* is considered equal to the terminal voltage. Resulting *OCV* curves for the cell under test are shown in Figure 3.8.

TABLE 3.3 THE STEPS FOLLOWED DURING THE *LINEAR INTERPOLATION METHOD*

	Process	Test current[A]	End of process	Temperature[ºC]
1	Discharge	I=C/20	V=2 v	25
2	Relaxation	I=0	time = 3600 s	25
3	Charge	I=C/20	V=3.65 v	25

TABLE 3.3 shows the procedure followed to reach the results presented. First a complete discharge is done until the end of discharge voltage of the cell. After a relaxation time of 3600 seconds the charging process is begun at the same current rate after the nominal voltage is reached to finish the experimental test.

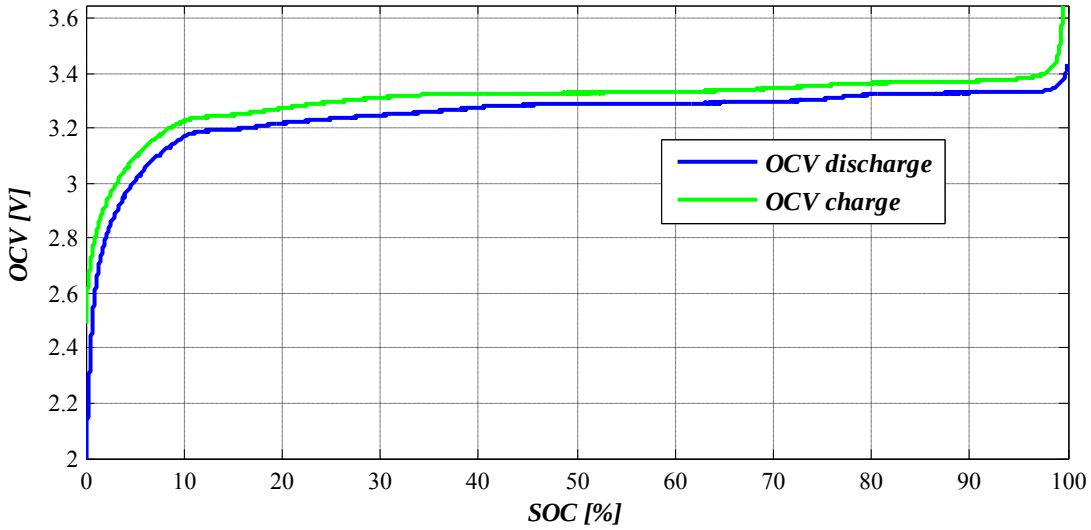

Figure 3.8: *OCV* results during charge and discharge process for a li-ion cell.

3.3.2 Entropic heat coefficient determination

There are several papers concerning the analysis of the entropy of reaction in li-ion cells; Viswanathan et al. in [38] researched the effect of entropy change of lithium intercalation in cathodes and anodes on Li-ion battery thermal management. Thomas et al in [39] explain the whole procedure followed in this work. Hallaj et al in [40] also explain the reasons for the entropy change due to structural changes in the li-ion cell.

The entropy of the reaction is calculated here as the $\partial OCV_{avg}/\partial T\ (SOC,\ T)$, second term on the right side in equation (3.6) and it depends on the state of charge of the cell and also, on the working temperature. However, the dependency on temperature is neglected in this work for a temperature range from 20ºC to 40ºC, the expected working temperature range. This experimental test consists of varying the temperature of the cell, changing the ambient temperature inside a temperature box, to provoke a variation in the *OCV* voltage quantifying this variation for different *SOC* values.

The procedure followed during this test is the one in Figure 3.9; the cell is charged with the common *CC+CV* technique and is considered fully charged. Then, the cell is discharged at *1C* rate in small decrements of *0.7 Ah* until the voltage of the cell reaches the end of discharge voltage (*2V*). After each partial discharge a relaxation period is applied; the relaxation period varies from *3600 seconds* for high *SOC* to *24 hours* for low *SOC* [37] and after it, the cell is considered to be relaxed. The discharging current has to be low enough to create no temperature change in the cell and is commonly lower than the one selected in this work; however, with the cells used in this work, the variation of temperature was small enough and the duration of the entire test was reduced considerably.

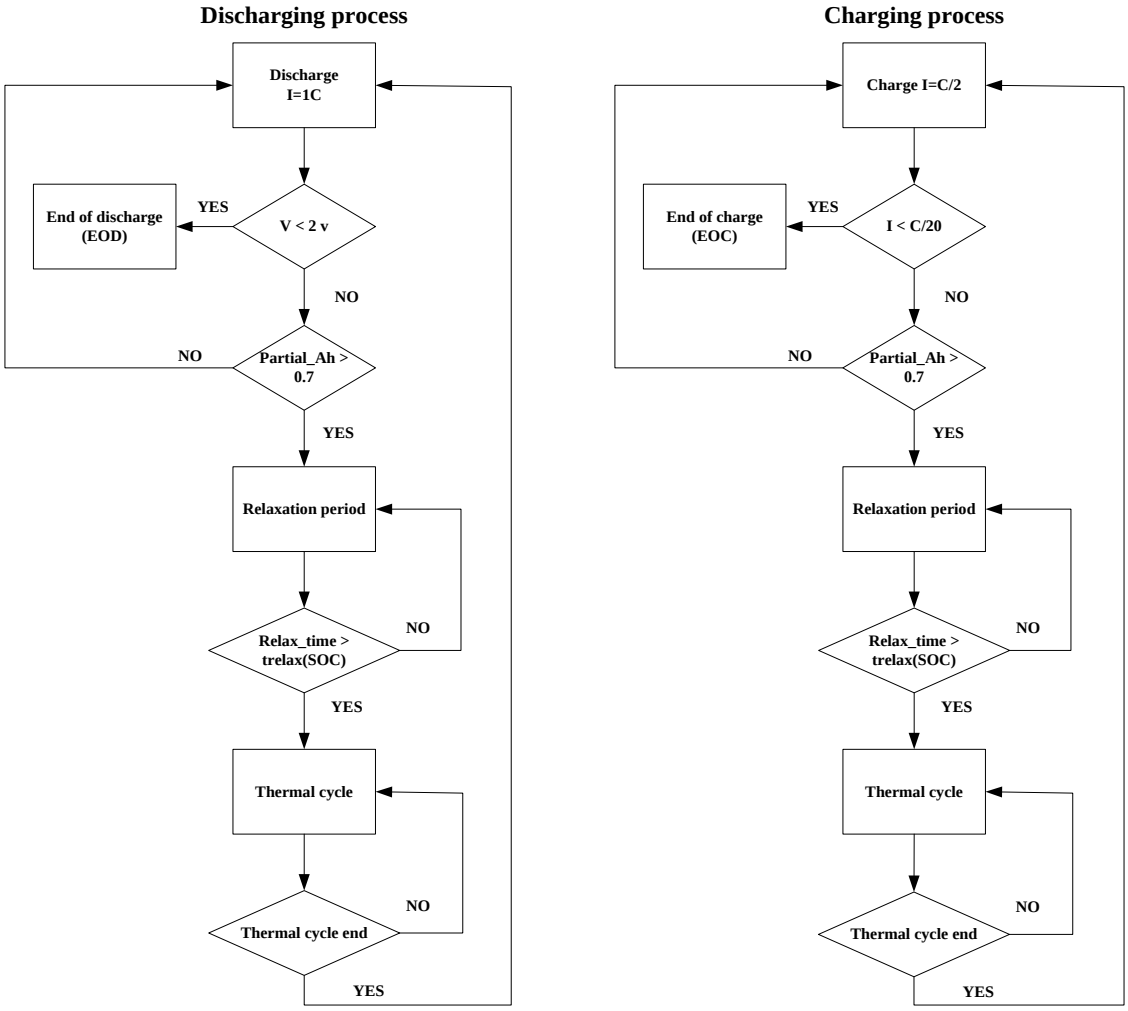

Figure 3.9: Procedure followed to estimate the entropy of the reaction.

After that, the same process is followed for a *C/2* rate to charge the cell with a *CC+CV* process until the charging current is less than *C/20* amperes. The same criterion as with discharge was followed during the charging process to select this rate.

After the relaxation period, both in charge and discharge, the temperature cycle shown in Figure 3.10 b) is applied. Starting at an ambient temperature of 25ºC, temperature is reduced until 18ºC and then increased to 32ºC; during the last raise of temperature, the entropy of the reaction is quantified with (3.7), and after that, temperature is reduced until 25ºC again to follow with the test. The values of 18ºC and 32ºC are selected depending on the variation of the *OCV*. If this range is not wide enough a higher resolution is needed to quantify the variation of the voltage.

Relaxation time before applying the temperature cycle is crucial during this experimental test; if the cell has not reached its equilibrium the measurement of the *OCV* variation due to the variation of temperature can be distorted. At 25ºC, the terminal voltage of the cell must be the same before and after applying the temperature cycle. Otherwise, variations in the *OCV* will be quantified because of the relaxation time, and not only because the temperature change.

$$\frac{\partial OCV_{avg}}{\partial T}(SOC) = \frac{OCV_{avg}(T_{max}) - OCV_{avg}(T_{min})}{T_{max} - T_{min}} \quad \textbf{(3.7)}$$

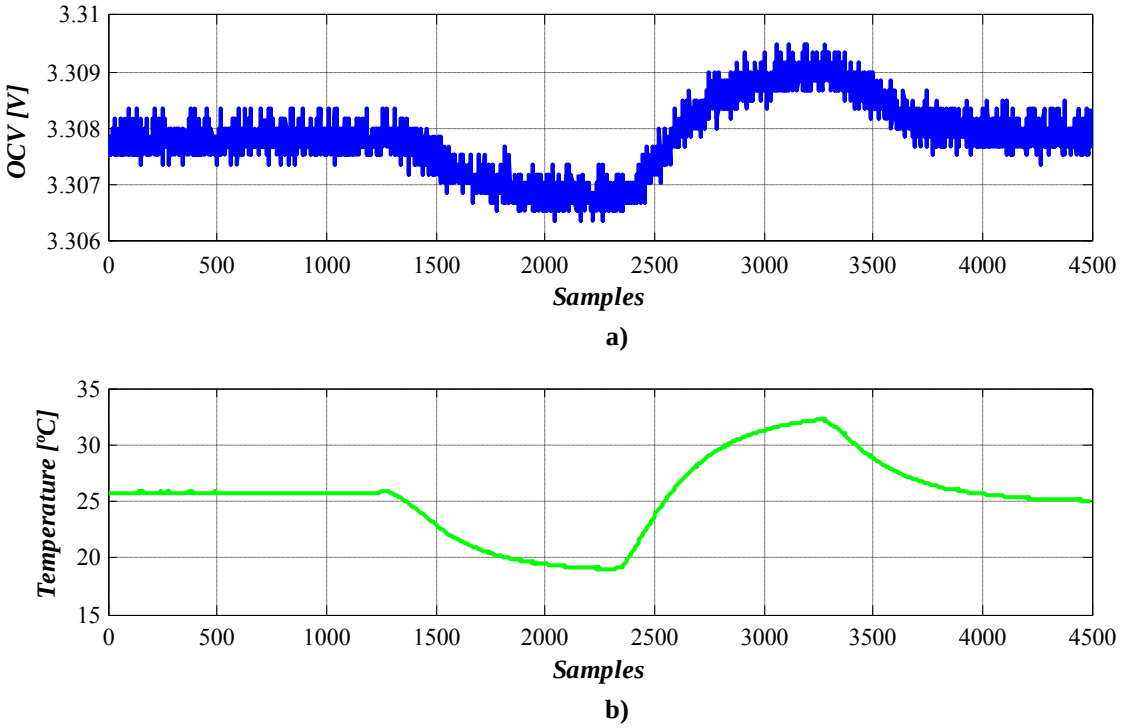

Figure 3.10: a) *OCV* due to temperature variation for a 70% of *SOC*; b) Ambient temperature change inside temperature box.

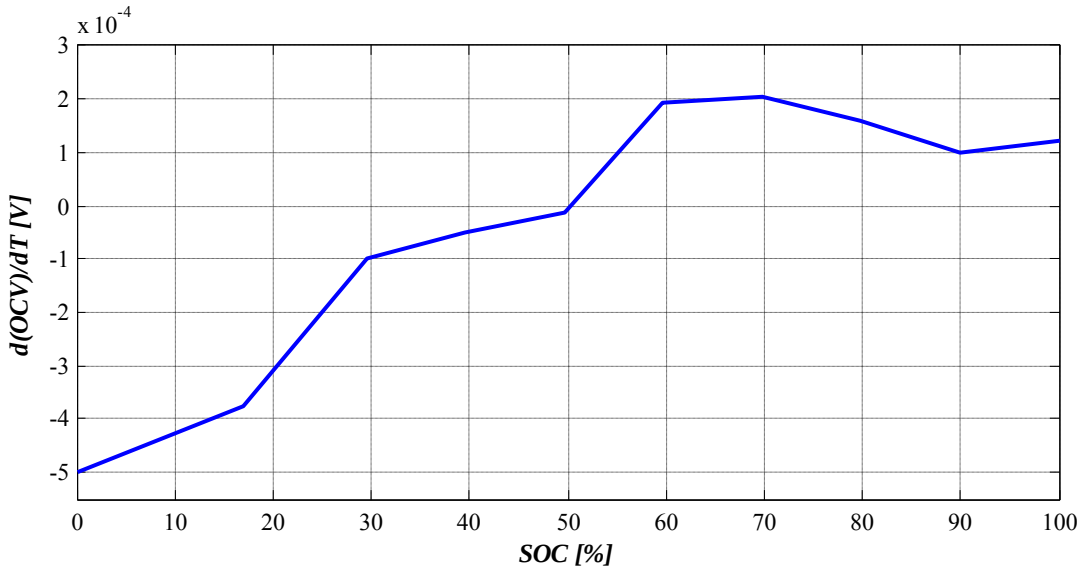

Figure 3.11: Entropy of the reaction depending on the state of charge of a cell.

Figure 3.10 shows the change in *OCV* due to temperature change for a 70% of SOC; when temperature is reduced until 18ºC voltage is also reduced and when temperature is increased until 32ºC *OCV* also increases, so the sign of the entropic heat coefficient is positive. However, this sign can be negative for other *SOC* values; Figure 3.11 shows the evolution of this parameter with the *SOC*, and the change of the sign is clearly seen

below 50%. The consequence of this effect is that if a very low current is applied to the cell and Joule effect losses are very low, the entropic term will cause an endothermic or an exothermic thermal behaviour depending on the *SOC*. This is the reason because the entropic term is also called reversible in bibliography [18].

The calculation of the entropic heat coefficient with experimental tests is very time consuming because of the large relaxation times and the large thermal cycle periods. Besides, the influence of this entropic term in the overall power losses of the li-ion cell is very small for power applications. In this work the working current rates are considered to be normally higher than *1C*; with this scenario, the influence of the entropic heat coefficient can be neglected.

3.3.3 Validation of the internal heat generation model

In order to do the validation of the model some information from an experimental test is required. The instantaneous values of the cell current, terminal voltage and average temperature are measured during a 7.69C constant current discharge and included in the model presented in Figure 3.7.

This data is used to estimate the evolution of the internal heat generation profile during the same discharge process; Figure 3.12 b shows the resulting profile for this discharge rate. In this work is not possible to compare the obtained profile with experimentally obtained data because special calorimetry equipment is required to measure the generated heat and it is not available at this moment. Calorimeters are able to measure with high precision the amount of heat released by a device in a temperature controlled ambient. An excess of heat generated is expected because during transients a percentage of the applied current is not generating losses and this model does not take it into account. Besides, both terms in the internal heat generation equation are multiplied by the current provoking an instantaneous cancellation of the heat generation when no current is flowing throughout the cell. However, internal heat decreases with a lower dynamic [41] and thus, an error is committed.

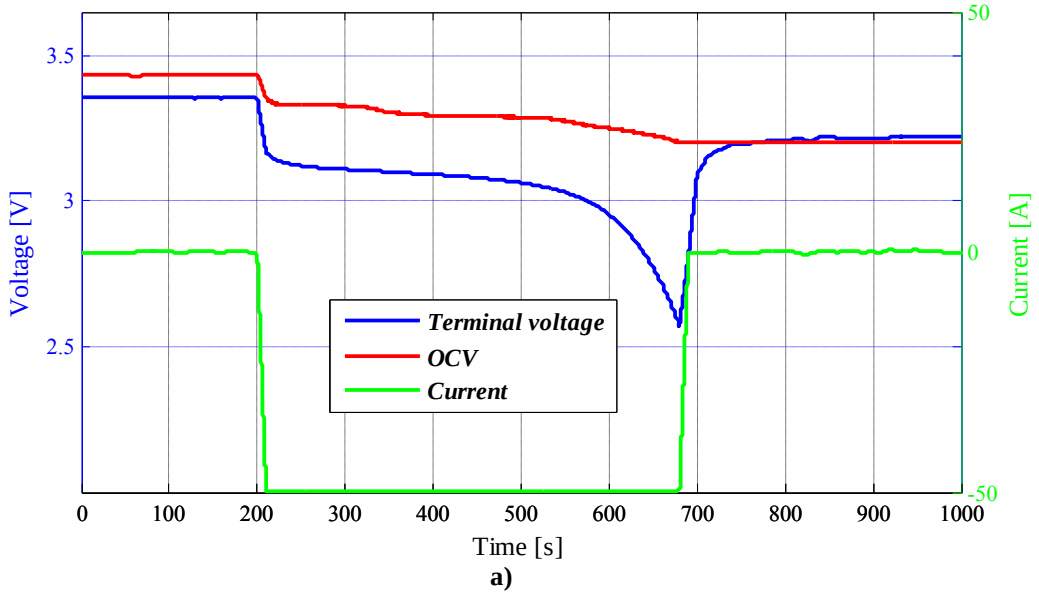

a)

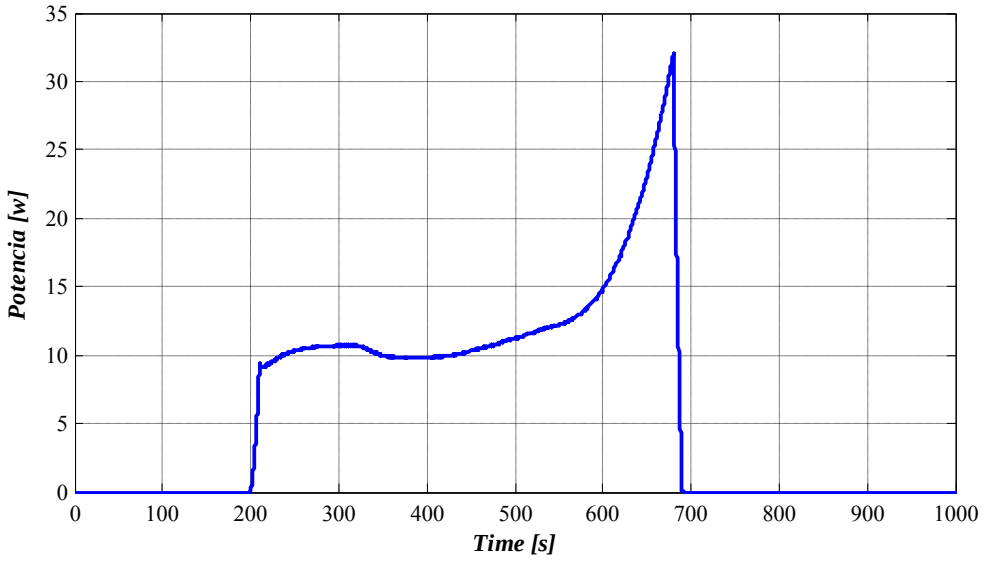

b)

Figure 3.12: Model results during a 7.69C constant current discharge process; a) Terminal voltage, *OCV* and current results; b) Estimated internal heat generation profile.

3.4 Developed thermal characterization process for li-ion cells

During the thermal characterization of the li-ion cells several experimental tests are conducted in order to achieve thermal parameters:

- EIS test to obtain the internal impedance of the cell for different frequencies.
- Heat capacity test for the average thermal capacity of the cell.
- Power pulse test to achieve the thermal response of the surface temperature of the cell.

3.4.1 Electrochemical impedance spectroscopy test (EIS)

The electrochemical impedance spectroscopy (*EIS*) test is a standard test and consists of applying a sinusoidal current to the cell under test at different frequencies and measuring the value of the internal impedance. The range of frequencies for this analysis is from 6.5kHz to 1Hz; the same procedure is repeated for different *SOC* values. The goal of this test is to find the value of the frequency at which the impedance of the cell is purely resistive R_0 for a concrete *SOC*. This frequency value (f_0) will be used during the following two experimental tests in this chapter; Figure 3.13 shows the result of this test for a state of charge of 50%. For the cell under test R_0 at 50% of *SOC* is around 1mΩ.

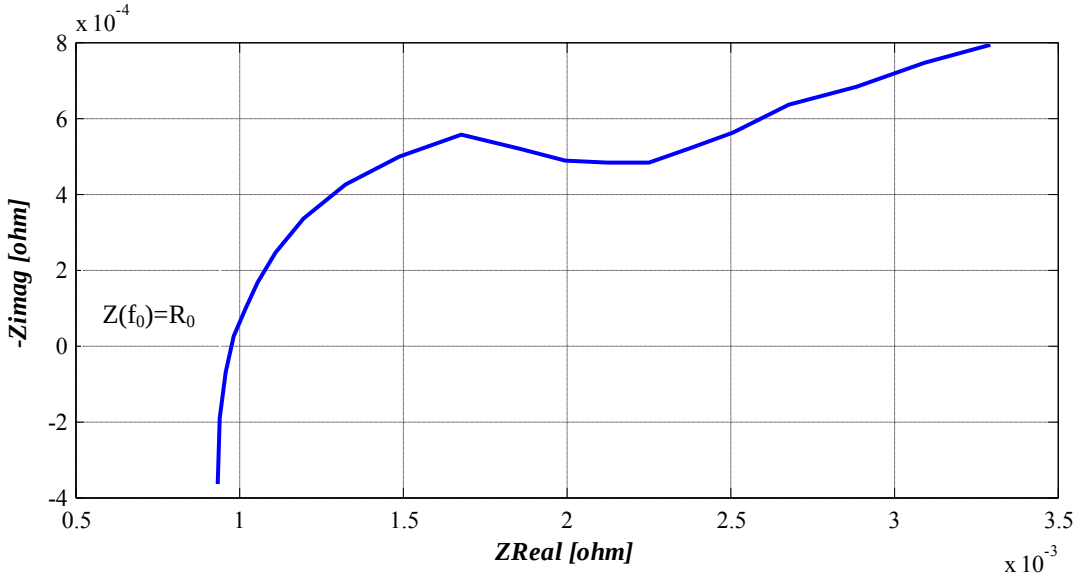

Figure 3.13: EIS measurement at 50% of the *SOC*.

3.4.2 Heat capacity test

An important parameter to be able to predict the thermal behaviour of the li-ion cell is the heat capacity C_{th}. In this work an average value of the heat capacity for the overall cell has been calculated conducting an experimental test [42]. Other authors estimate it from the heat capacities of each material within the li-ion cell; however, this data about

the materials and their thermal properties is not usually accessible and experimental estimations are conducted with calorimeters in some studies.

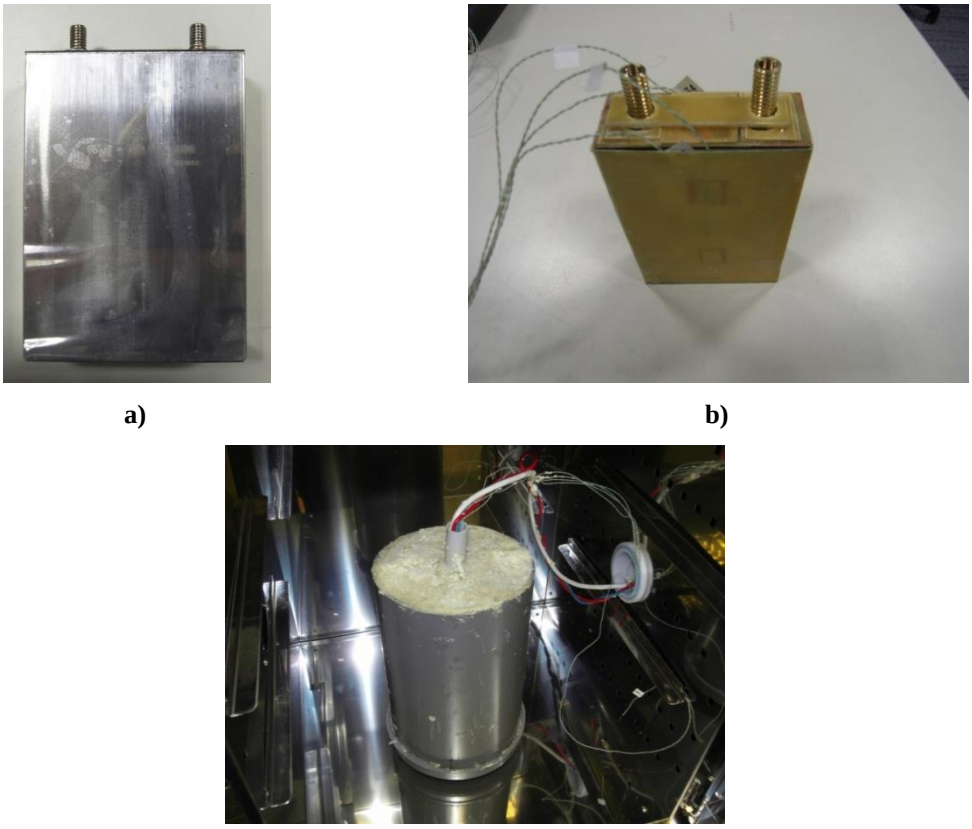

a) **b)**

c)

Figure 3.14: Example of the setup of the heat capacity test with a prismatic cell. a) Cell; b) Cell covered with the protection layer; c) Final assembly.

Due to the absence of such equipment, another experimental test has been conducted to estimate C_{th}. Four thermocouples are placed on the surface of a single cell under test, and the cell is covered by a protection layer; then the cell and the protection layer are inserted in a tube and this tube is filled with a thermal insulation material. This material solidifies and the cell is trapped in it with the connection and measurement wires out from the structure; Figure 3.14 shows the final assembly of the experimental test. With this assembly heat cannot be evacuated to the environment and all the heat generated inside the cell is accumulated in the equivalent capacitor in Figure 3.15.

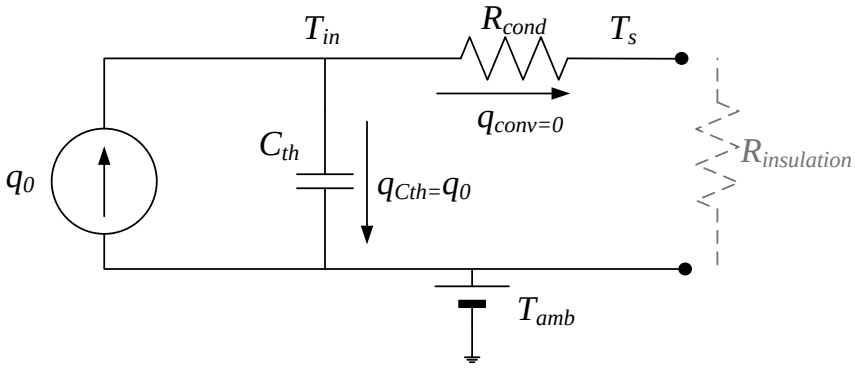

Figure 3.15: Equivalent thermal circuit with insulation material.

The target of this setup is to avoid heat transfer by convection to the ambient; Figure 3.15 shows the equivalent thermal circuit of the cell with an insulated material covering the battery. The insulation material adds a big thermal resistance in the resistor branch, avoiding heat transfer by convection, thus, the whole amount of heat generated inside the cell goes for the thermal capacity C_{th}. If the internal heat generation of the cell is constant, T_{in} should increase linearly.

$$q_0 = R_0 \left(\frac{I_A}{\sqrt{2}}\right)^2 \quad \textbf{(3.8)}$$

This constant power pulse is generated inside the cell following the procedure presented by Schmidt et al. in [35]; a sinusoidal current of frequency f_0 is applied to the cell for a concrete *SOC*. In the case of li-ion power cells the amplitude of this current must be high because the internal impedance of these cells is small. The sinusoidal current permits to keep a constant *SOC* during the test and generates a constant power pulse inside the cell; the amplitude of the power pulse can be obtained with equation (3.8). I_A is the amplitude of the sinusoidal current and R_0 is the value of the impedance of the cell at f_0 frequency obtained during the *EIS* test.

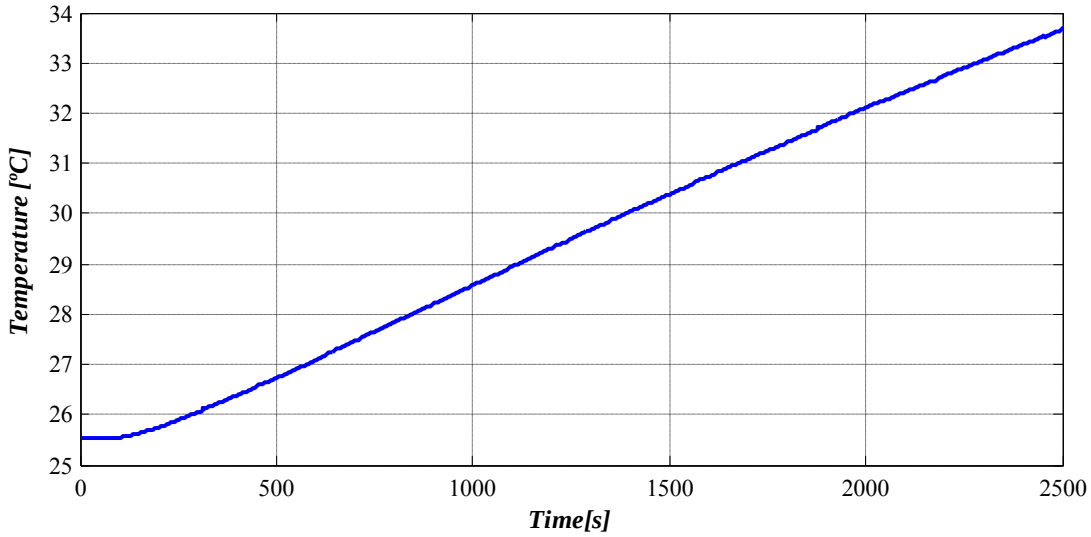

Figure 3.16: Evolution of surface temperature during the heat capacity test.

Figure 3.16 shows the evolution of the cell surface temperature during this test. Results show a linear evolution on the temperature of the cell; this result was expected since the thermal capacitor of the cell is supplied by a constant power pulse and ideally no power is lost by convection. The average heat capacity is then calculated from equation (3.9). Although C_{th} will change depending on the working temperature, in this thesis work it is considered constant for the battery working temperature range (25-45ºC).

$$C_{th} = \frac{q_0 \Delta t}{\Delta T} \quad \textbf{(3.9)}$$

The absolute value of Δt/ΔT is calculated for all the combinations between the different samples of the signal in Figure 3.16 building a matrix like the one represented in

TABLE 3.4. After building the matrix, the median of all the values in it is calculated and substituted in (3.9) to calculate the average value of C_{th}.

TABLE 3.4 SLOPE MATRIX FOR N DIFFERENT TEMPERATURE/TIME POINTS.

t \ T	1	2	3	. . .	N
1	$\frac{\Delta t_{1,1}}{\Delta T_{1,1}}$	$\frac{\Delta t_{1,2}}{\Delta T_{1,2}}$	$\frac{\Delta t_{1,3}}{\Delta T_{1,3}}$	. . .	$\frac{\Delta t_{1,N}}{\Delta T_{1,N}}$
2	$\frac{\Delta t_{2,1}}{\Delta T_{2,1}}$	$\frac{\Delta t_{2,2}}{\Delta T_{2,2}}$	$\frac{\Delta t_{2,3}}{\Delta T_{2,3}}$	. . .	$\frac{\Delta t_{2,N}}{\Delta T_{2,N}}$
3	$\frac{\Delta t_{3,1}}{\Delta T_{3,1}}$	$\frac{\Delta t_{3,2}}{\Delta T_{3,2}}$	$\frac{\Delta t_{3,3}}{\Delta T_{3,3}}$	. . .	$\frac{\Delta t_{3,N}}{\Delta T_{3,N}}$
.	.	.	.	.	.
.	.	.	.	.	.
.	.	.	.	.	.
N	$\frac{\Delta t_{N,1}}{\Delta T_{N,1}}$	$\frac{\Delta t_{N,2}}{\Delta T_{N,2}}$	$\frac{\Delta t_{N,3}}{\Delta T_{N,3}}$	. . .	$\frac{\Delta t_{N,N}}{\Delta T_{N,N}}$

3.4.3 Power pulse thermal characterization test

Last test during the thermal characterization process is the power pulse test; this test consists of generating constant heat losses inside the cell under test and measuring the thermal response on the surface of the cell. In order to generate constant power losses the procedure is the same as during heat capacity test, the procedure obtained from Schmidt et al. work [35]. In this case no insulation material is covering the cell and heat is evacuated by natural convection to the controlled ambient. Before applying the sinusoidal current to the battery four thermocouples are located at different points of the surface of the li-ion cell. The objective is to identify different behaviours of the surface temperatures depending on their location. Finally, the power pulse is applied and the response of the thermocouples is measured during around 2.5 hours until temperatures reach the steady state Figure 3.17.

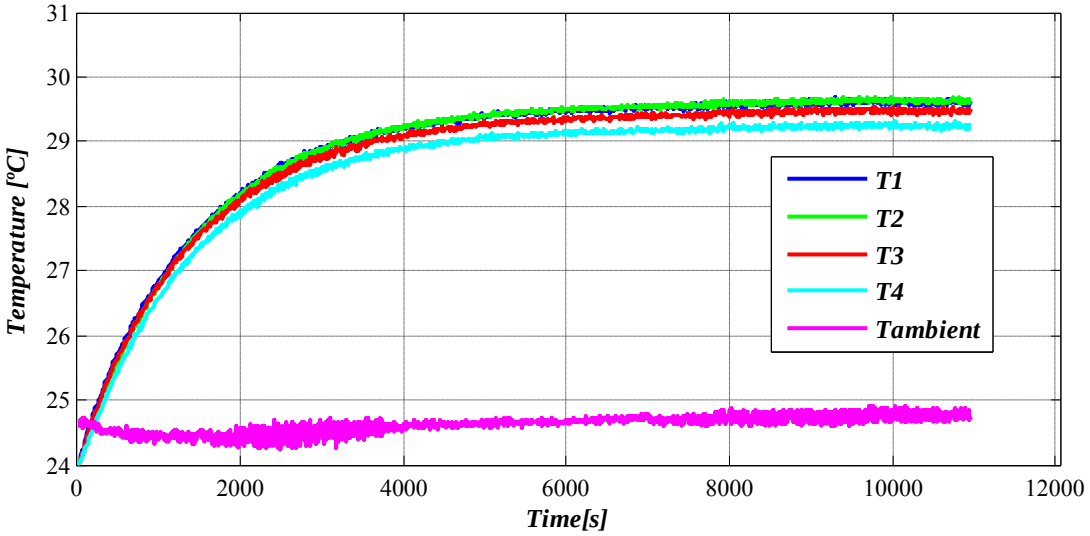

Figure 3.17 Response of the surface thermocouples to the power pulse.

Results show that in small size cells the thermal behaviour of all the thermocouples is similar. However, if bigger cells are thermally characterized it is possible to obtain higher dispersions between thermal measurements for the same experimental test. The reason is that in bigger cells the spatial internal heat generation dispersion is higher and also that the heterogeneous current distribution throughout the current collectors is more appreciable. As a consequence zones with different thermal behaviour can be found in the same li-ion cell. The results for this test are used in 3.5.3 to obtain the parameters of the behavioural models.

3.5 Behavioural temperature distribution models

Following, the procedure to develop a thermal behavioural model for a li-ion cell is going to be explained; in this work *Cauer networks* have been selected for this purpose and two different equivalent circuits will be analyzed; 1st order and 2nd order *Cauer networks*. Figure 3.18 shows the inputs and the output of the behavioural model; internal heat generation and ambient temperature are the inputs of the thermal equivalent circuit and the average surface temperature is the output.

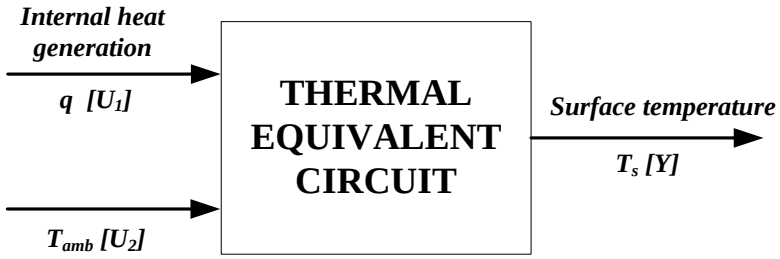

Figure 3.18: Overall thermal model.

The assumptions made for these behavioural models are the following ones:

- Ambient temperature is considered a constant since all the experimental tests are conducted in a controlled temperature chamber.
- Temperature on the surface of the cell is considered uniform, so a single output temperature will be achieved by the model.
- The internal heat generated within the cell is uniform for the whole cell.

3.5.1 First order Cauer network

The thermal equivalent circuit in Figure 3.19 is a *Cauer 1st order model* consisting of an internal heat generation inside the cell q_0 *(W)*, a thermal capacity C_{th} *(J/ºC)*, a resistor modelling the conduction R_{cond} *(ºC/W)*, and a resistor modelling the convection R_{conv}*(ºC/W)*. T_s*(ºC)* is the temperature on the surface of the cell, $T_{ambient}$*(ºC)* is the ambient temperature and T_{in}*(ºC)* is the temperature inside the cell. The value of the conduction resistor determines the temperature difference between inside and the surface of the cell. The convective resistor instead, the temperature difference between the surface and the ambient. Heat capacity determines the dynamics of the temperature inside and on the surface of the cell.

In order to achieve the differential equation governing the model, the state space theory is applied for a power pulse q_0 constant input; initial conditions are equal to zero and the resulting equations are (3.10) and (3.11).

$$\frac{dT_{in}(t)}{dt} = \frac{q_{Cth}(t)}{C_{th}} = \frac{(R_{cond} + R_{conv})q(t) - T_{in}(t)}{(R_{cond} + R_{conv})C_{th}} \quad \textbf{(3.10)}$$

$$T_s(t) = \frac{(R_{cond} + R_{conv})T_{amb}(t) + R_{conv}T_{in}(t)}{(R_{cond} + R_{conv})} \quad \textbf{(3.11)}$$

From these two equations the state space model is obtained:

$$[\dot{T}_{in}(t)] = \left[\frac{-1}{(R_{cond} + R_{conv}) \cdot C_{th}}\right][T_{in}(t)] + \left[\frac{1}{C_{th}} \quad 0\right]\begin{bmatrix} q(t) \\ T_{amb}(t) \end{bmatrix} \tag{3.12}$$

$$[T_s(t)] = \left[\frac{R_{conv}}{(R_{cond} + R_{conv})}\right][T_{in}(t)] + [0 \quad 1]\begin{bmatrix} q(t) \\ T_{amb}(t) \end{bmatrix} \tag{3.13}$$

The general equation of the output for a *LTI* system with two inputs and one output can be written like (3.14), where *Y(s)* is the output of the system in Laplace domain, $T_s(s)$, U_1(s) corresponds to the internal heat generation input in Laplace domain, *q(s)*, U_2(s) is the ambient temperature input in Laplace domain, T_{amb}(s), and *G1(s)* and *G2(s)* are the transfer functions relating the inputs and the output.

$$Y(s) = G_1(s)U_1(s) + G_2(s)U_2(s) \tag{3.14}$$

From equations (3.12) and (3.13) the final equation for the output (T_s) is achieved in Laplace domain:

$$T_s(s) = \left[\frac{R_{conv}}{\left(C_{th}(R_{cond} + R_{conv})\left(\frac{s+1}{C_{th}(R_{cond} + R_{conv})}\right)\right)}\right] q(s) + T_{amb}(s) \tag{3.15}$$

Equation (3.15) is the general equation governing the output of the equivalent thermal model in Figure 3.19; in this equation the transfer function relating the ambient temperature and the cell surface temperature is equal to one.

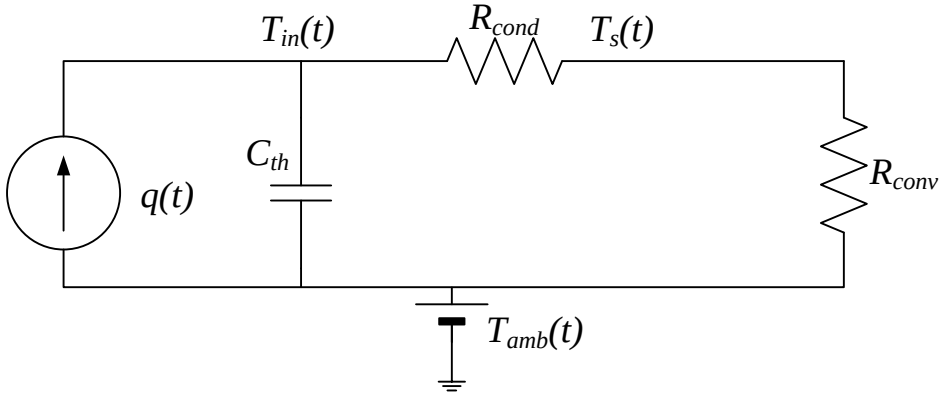

Figure 3.19: *1st order Cauer network* for a li-ion cell.

3.5.2 Second order Cauer network

Figure 3.20 shows a two node *Cauer network*; it is similar to the one node one but in this case two conduction resistors (R_{cond1} and R_{cond2}) and two thermal capacitors (C_{th1} and C_{th2}) model the behavior of the li-ion battery. The other resistor (R_{conv}) models again the thermal convection phenomenon in this equivalent thermal model. Ambient temperature (T_{amb}) and heat generation (q_0) input are the same as in one node model. T_{in1}

and T_{in2} represent the internal temperatures of the cell in the different layers modeled and T_s represents the surface temperature of the cell.

After applying the state space equations theory for a constant power pulse q_0 with the initial conditions equal to zero, the resulting equations are (3.16), (3.17) and (3.18).

$$\frac{dT_{in1}(t)}{dt} = \frac{R_{cond\,1}q_0 - T_{in1}(t) - T_{in2}(t)}{R_{cond\,1}C_{th1}} \tag{3.16}$$

$$\frac{dT_{in2}(t)}{dt} = \frac{(R_{cond\,2} + R_{conv})T_{in1}(t) - (R_{cond\,1} + R_{cond\,2} + R_{conv})T_{in2}(t)}{(R_{cond\,2} + R_{conv})C_{th2}R_{cond\,1}} \tag{3.17}$$

$$T_s(t) = \frac{(R_{cond\,2} + R_{conv})T_{amb}\,(t) + R_{conv}\,T_{in2}(t)}{(R_{cond\,2} + R_{conv})} \tag{3.18}$$

From these three equations the state space model is:

$$\begin{bmatrix}\dot{T}_{in1}(t)\\ \dot{T}_{in2}(t)\end{bmatrix} = \begin{bmatrix}\frac{-1}{R_{cond\,1}C_{th1}} & \frac{1}{R_{cond\,1}C_{th1}}\\ \frac{1}{R_{cond\,1}C_{th2}} & \frac{-(R_{cond\,1} + R_{cond\,2} + R_{conv})}{(R_{cond\,2} + R_{conv})R_{cond\,1}C_{th2}}\end{bmatrix}\begin{bmatrix}T_{in1}(t)\\ T_{in2}(t)\end{bmatrix} + \cdots + \begin{bmatrix}\frac{1}{C_{th1}} & 0\\ 0 & 0\end{bmatrix}\begin{bmatrix}q_0\\ T_{amb}\,(t)\end{bmatrix} \tag{3.19}$$

$$[T_s(t)] = \begin{bmatrix}0 & \frac{R_{conv}}{R_{cond\,2} + R_{conv}}\end{bmatrix}\begin{bmatrix}T_{in1}(t)\\ T_{in2}(t)\end{bmatrix} + [0 \quad 1]\begin{bmatrix}q_0\\ T_{amb}\,(t)\end{bmatrix} \tag{3.20}$$

As in the case of the first order network the equation governing the output of the thermal equivalent circuit in Figure 3.20 is presented in equation (3.21):

$$T_s(s) = \left[\frac{R_{conv}}{\left(C_{th1}s(R_{cond\,1} + R_{cond\,2} + R_{conv}) + C_{th2}s(R_{cond\,2} + R_{conv})\right)} + \cdots + \frac{R_{conv}}{(s^2C_{th1}C_{th2}R_{cond\,1}(R_{cond\,2} + R_{conv}) + 1)}\right]q(s) + T_{amb}\,(s) \tag{3.21}$$

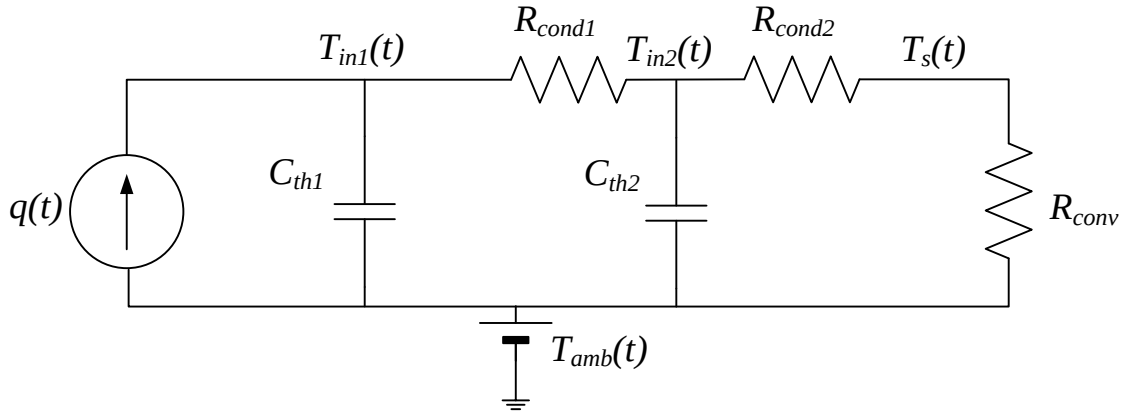

Figure 3.20: *2nd order Cauer network* for a li-ion cell.

3.5.3 Fitting the parameters of both Cauer networks

Finally, the values of the parameters of the equivalent *Cauer networks* have to be estimated; the parameters are fitted to the curve obtained from the power pulse test in 3.4.3 taking advantage of a least square method. As the internal heat generation input was constant during the power pulse test the general equations for the *Cauer networks* (3.15) and (3.21) are adapted for this kind of input, equation (3.22) for the first order *Cauer network* and equation (3.23) for the second order one:

$$T_s(s) = \frac{T_{amb}\,(s)(C_{th}(R_{cond}\ + R_{conv})s + 1) + q_0(s)R_{conv}}{(C_{th}(R_{cond}\ + R_{conv})s + 1)s} \tag{3.22}$$

$$T_s(s) = \frac{T_{amb}\,(s)}{s} + \frac{q_0 R_{conv}}{s} + \frac{q_0 R_{conv}}{s(C_{th1}C_{th2}R_{cond\,1}(R_{cond\,2} + R_{conv})s^2)} + \cdots$$
$$\cdots + \frac{q_0 R_{conv}}{s\big(s(C_{th1}R_{cond\,1} + C_{th1}R_{cond\,2} + C_{th1}R_{conv}\ + C_{th2}R_{cond\,2} + C_{th2}R_{conv}\,)\big)} \tag{3.23}$$

Figure 3.21 shows one of the fitting results obtained for the 1st order network; results show good agreement between the two signals. The error between the two signals is also shown in this figure and is always less than *0.3ºC* in this case.

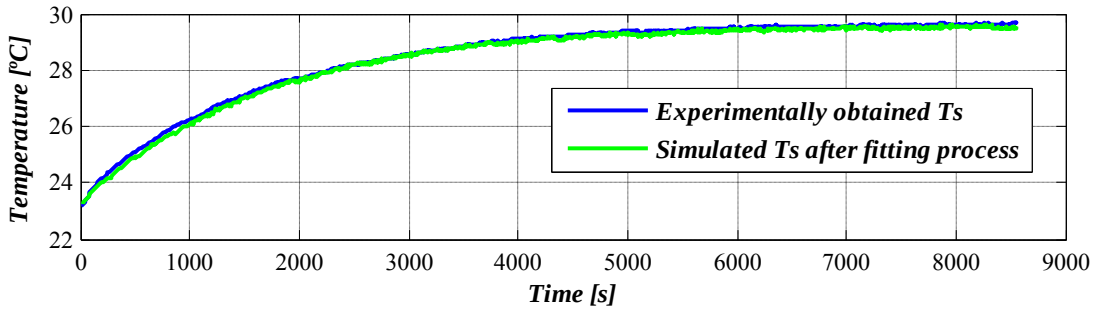

a)

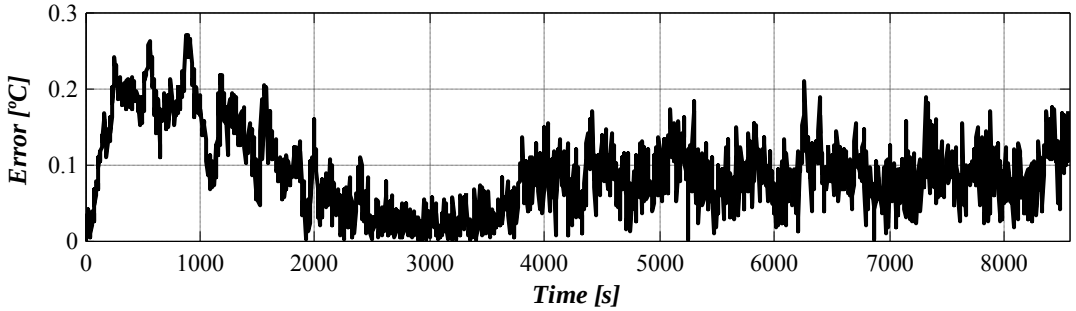

b)

Figure 3.21 Example of the fitting results for a 1st order *Cauer network*.

However, there are infinite suitable *RC* combinations to do the fitting for both networks. In order to choose the solution that fits the parameters but also represents the physical properties of the li-ion cell some parameters are imposed before the fitting process. In the case of the 1st order network, the value of C_{th} is imposed to the value obtained during the heat capacity test in 3.4.2; in the case of 2nd order network it is not possible

to do this because there are two capacitors in the equivalent circuit and during the heat capacity test an average value of the heat capacity is obtained, thus, the values of the capacitors have no physical sense in this case.

R_{conv} value can be calculated when the steady state is reached during the experimental test in Figure 3.17 for both *Cauer networks*. The following equation (3.24) has been used for the estimation.

$$R_{conv} = \frac{(T_s - T_{amb})}{q_0} \quad \textbf{(3.24)}$$

After that, in the case of 1st order network, R_{cond} is the single value to be estimated with the least square method. In the case of 2nd order instead, there are 4 parameters of the equivalent circuit to estimate, R_{cond1}, R_{cond2}, C_{th1}, and C_{th2}. With this estimation of parameters, 1st order network parameters represent the physical properties of the li-ion cell, since 2nd order network just represents the thermal behaviour of the li-ion cell. TABLE 3.5 and TABLE 3.6 show the values of the parameters used in these models to reach the figures presented during the validation process.

TABLE 3.5 PARAMETERS OF THE 1ST ORDER *CAUER MODEL*.

Parameter	*Value*
C_{th}	*254.93 [J/ºC]*
R_{cond}	*2.63 [ºC/W]*
R_{conv}	*3.75 [ºC/W]*

TABLE 3.6 PARAMETERS OF THE 2ND ORDER *CAUER MODEL*.

Parameter	*Value*
C_{th1}	*298.22 [J/ºC]*
C_{th2}	*70.79 [J/ºC]*
R_{cond1}	*0.10 [ºC/W]*
R_{cond2}	*0.58 [ºC/W]*
R_{conv}	*3.75 [ºC/W]*

3.6 3D numerical model

Numerical temperature distribution models are commonly used in the field of batteries, however, other physical processes are governed by differential equations; chemical, electrical, mechanical or thermal processes can be modelled with these simulation tools. Complex differential equation problems can be solved with different numerical software but sometimes the result needed is not the evaluation of the equation in one point; in some cases the result has to be achieved for many points obtaining a map of the result; these kind of model can be very complex when the amount of points to evaluate is so high as in the case of temperature distributions. With this purpose, finite element simulation tools are the most used ones.

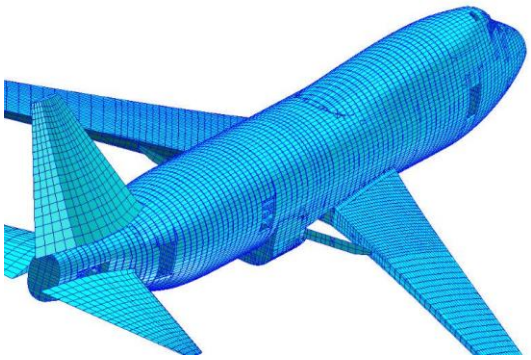

Figure 3.22: Example of a finite element application.

A finite element analysis consists of discretizing in nodes a large domain and solving the adequate differential equation in each node to achieve the result needed by the user. Ideally, this domain can be infinite because nodes can be as small as the user want, but in practice it is impossible to solve an infinite system and the number of nodes has to be limited. On the other hand, the number of nodes of the model can vary depending on the domain and size of the nodes. The smaller the nodes are, the better the accuracy is. So, finite element analysis consists of converting an infinite system to a finite one. (Figure 3.22)

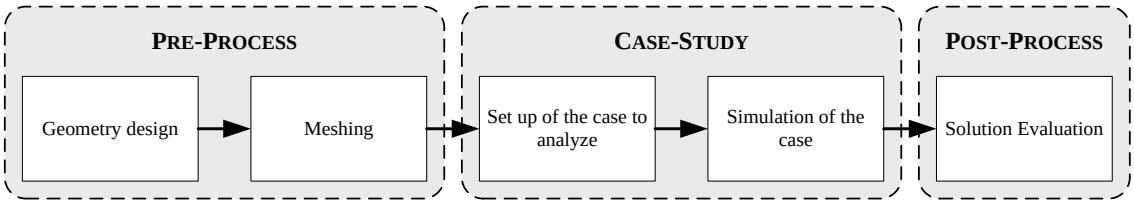

Figure 3.23: General steps followed during a finite element analysis.

Figure 3.23 shows a general procedure of finite element simulations. There are three main parts in this kind of simulations: pre-processing, case-study and post-processing. The unavailable information around the construction and materials of the cell under test make difficult to model the different layers within the cell to have an accurate temperature distribution in a single cell level. Besides, the final target of this work is to

be able to model large battery modules and modelling the layers of all the batteries of a battery pack would be very time consuming [43].

Another important issue was the internal heat generation of the cell; in li-ion cells heat generation rate is spatially dependent, however, in this work the cell is considered a single body and an average value of the generated heat is calculated for the whole battery and applied to the single body of the model. Following, the assumptions made in the single cell model are presented:

- Cell is considered a single body with user defined specific heat (J/kg^{o}C) and isotropic thermal conductivity (W/^{o}C m).
- Heat generation rate (W/m3) of the cell is considered uniform for the whole body.

The specific heat and thermal conductivity are obtained from the R_{cond} and C_{th} parameters of the *1st order Cauer model* in 3.5.1. In the single cell level, natural convection simulations have only been conducted; in order to simulate the natural convection a second fluid body is required in the model to calculate the energy exchange between the solid and the fluid. The aim of these simulations is to ensure that the assumptions made before are adequate to simulate battery modules and battery packs.

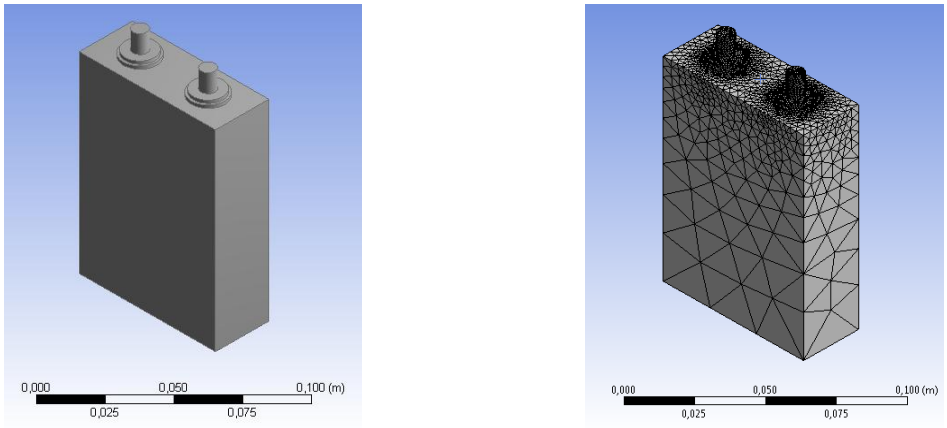

a) **b)**

Figure 3.24: Geometry and meshing of the single cell model.

During the pre-processing, the geometry and meshing of the model have to be defined (Figure 3.24). According to the geometry, it is important to build the model as simple as possible and avoid details in the model that will not influence the final solution; the reason is that the meshing process is simplified if the level of detail is not so high and the number of nodes of the mesh will decrease. In the cell shown power connection terminals can be avoided because the energy exchange with the fluid will be almost the same with or without these terminals; however, the meshing process is simpler since a coarse mesh is enough. Besides, it is easier to obtain good mesh qualities when the geometry is simple and with less mesh nodes.

Once the geometry (solid and fluid) has been meshed, next step is to set up the case study; in this research work *transient simulations* have been conducted to simulate the evolution of the surface temperature of the cell when a *internal heat generation* power

profile is applied. This power profile has been included into the model with a *user defined function* written in *c programming language*. Following, a summary of the parameters defined for a convection simulation is presented:

- Enable gravity effect.
- Enable the energy equation and define the turbulence model.
- Define air material for the fluid and a user defined material for the cell with thermal properties obtained from *1st order Cauer model*.
- Apply the variable power profile to the cell.
- Define pressure boundary conditions to the fluid volume outside faces.
- Change solver settings to the suitable ones for this kind of simulations.
- Initialize the simulations.

Figure 3.25 shows the meshing of the complete geometry for the single cell simulation. The below face of the fluid volume is a *pressure inlet* and the above face is a *pressure outlet.* Atmospheric pressure with ambient temperature is defined for these two *boundary conditions* in the model. The temperature of the cell changes heating the air surrounding it and provoking air circulation from the inlet to the outlet due to convection.

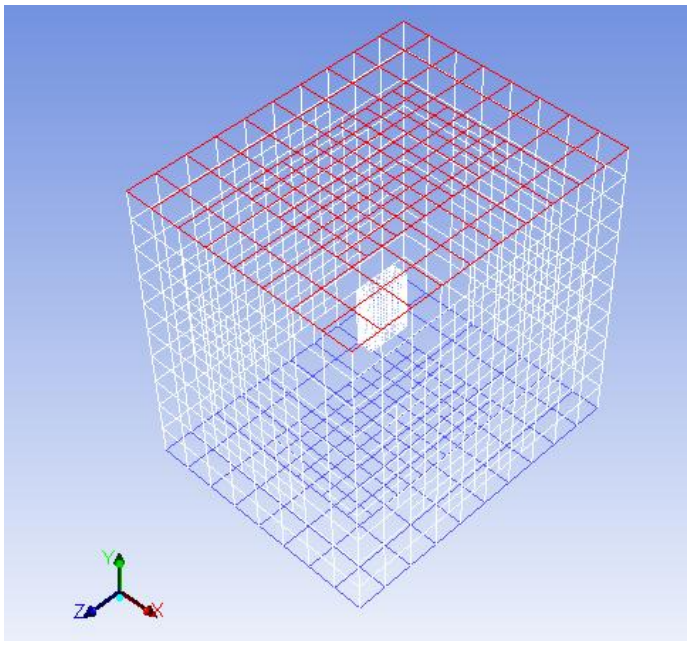

Figure 3.25: Single cell level mesh before solving the case.

According to the solving process, a *fixed time step* is defined while the cell was generating heat to reach a better accuracy. However bigger time steps are used with constant heat generations of the cell.

3.7 Validation of the developed thermal models

The validation of the methodology consists of comparing experimental results obtained during different charge and discharge cycles with simulation results obtained from both behavioural and numerical models. Firstly, each model results are presented and after that a comparison between the two models is shown to obtain the final conclusions. The li-ion cell used for the validation is a prismatic 6.5 Ah $LiFePO_4$ cell.

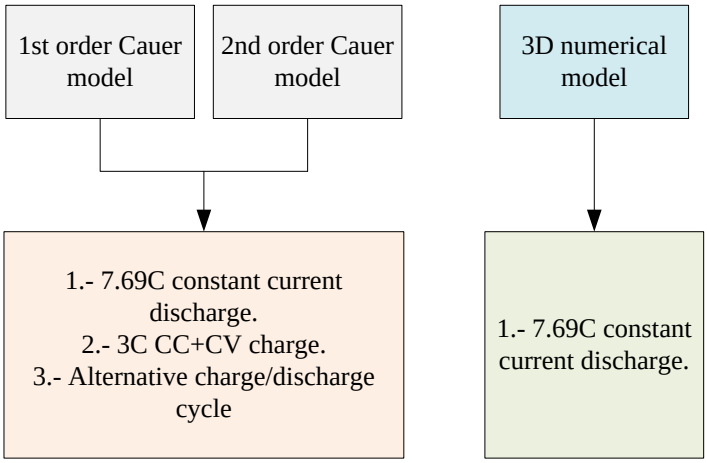

Figure 3.26: Summary of the results presented in this section.

3.7.1 Behavioural model

Figure 3.27 and Figure 3.28 show a 7.69C complete discharge of the Lishen cell with an ambient temperature of 25 ºC. The maximum error committed in this simulation is around 0.7ºC. The main difference between both models is that 1st order model reacts faster when the cell starts to generate power losses and when this losses are cut off at the end of discharge; 2nd order model instead has a slower reaction and a closer behaviour if it is compared with the real cell thermal response. However, it is considered that the 1st order model is accurate enough for the current simulations.

Figure 3.29 and Figure 3.30 show a 3C charge of the Lishen cell with an ambient temperature of 25 ºC; when the end of charge process is reached an error of 0.7ºC is reached.

Finally, Figure 3.31 and Figure 3.32 show a charge discharge cycle applied to the cell. The discharge current has been 50A and the charge current has been 30A. After each charge or discharge a rest period of 20 seconds was introduced. An error of 0.9ºC has been committed during the whole simulation in this case. The proposed internal heat generation model is less accurate during transients of the cell and can be one of the reasons why the error committed during the charge and discharge alternative cycle is higher than in the case of constant charge and discharge cycles. Finally, Figure 3.33 shows a comparison between both models to check the aforementioned differences between them.

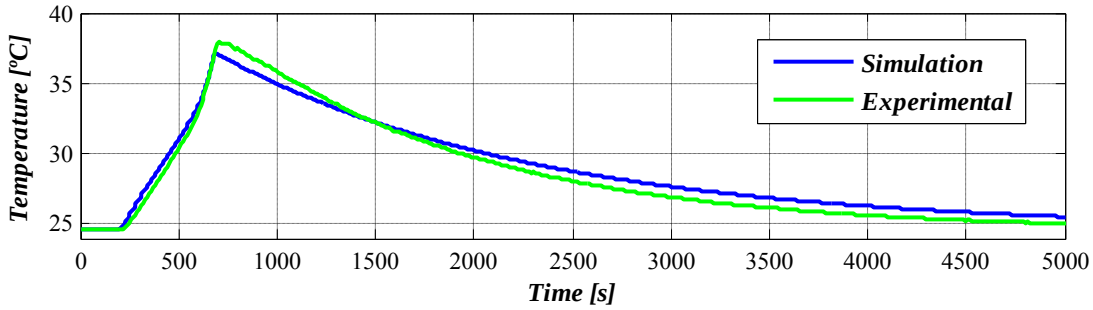

a)

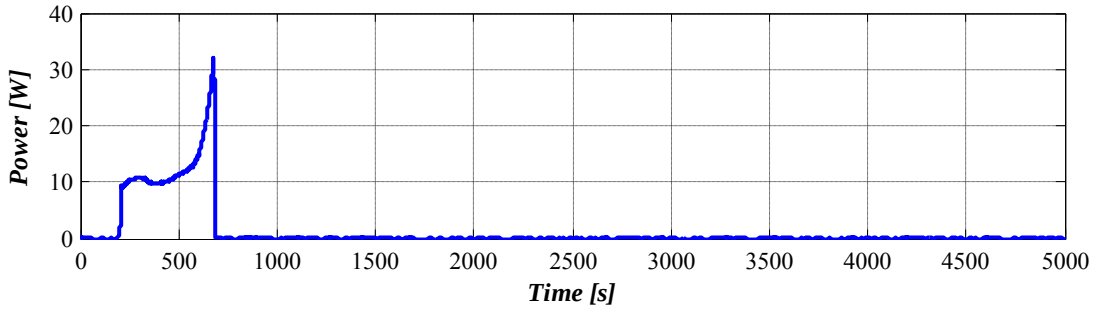

b)

Figure 3.27: 7.69C rate complete discharge results for the 1st order *Cauer model*; a) Surface temperature; b) Internal heat generation.

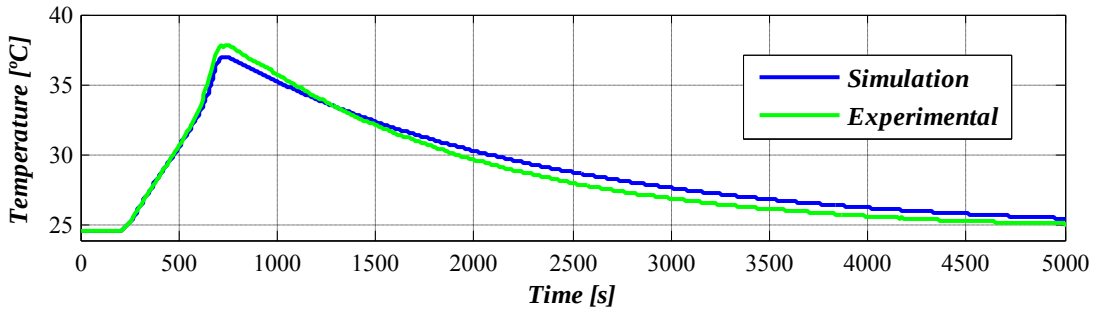

a)

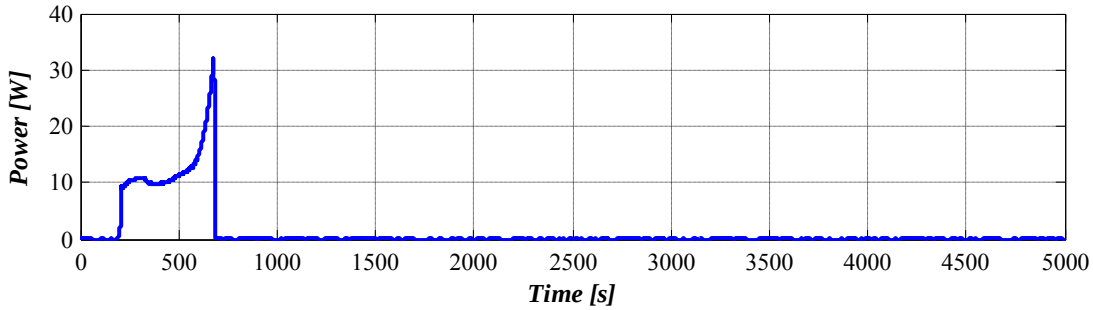

b)

Figure 3.28: 7.69C rate complete discharge results for the 2nd order *Cauer model*; a) Surface temperature; b) Internal heat generation.

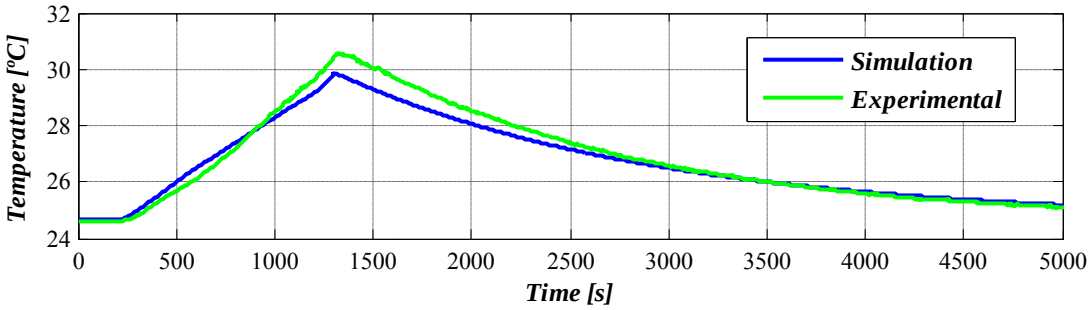

a)

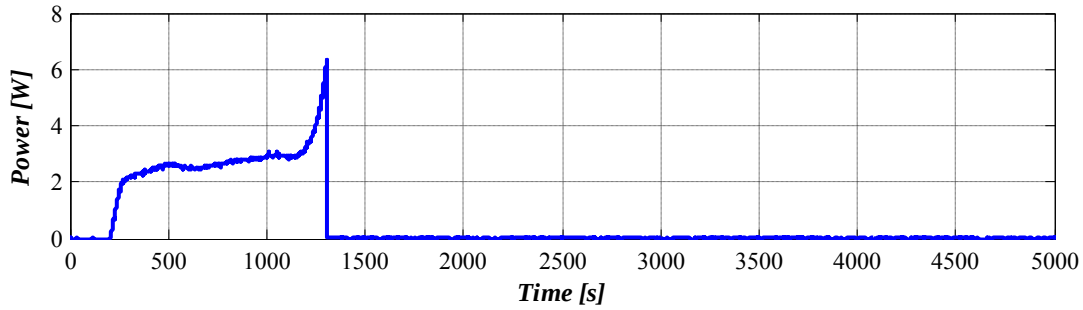

b)

Figure 3.29: 3C rate complete *CC+CV* charge results for the 1st order *Cauer model*; a) Surface temperature; b) Internal heat generation.

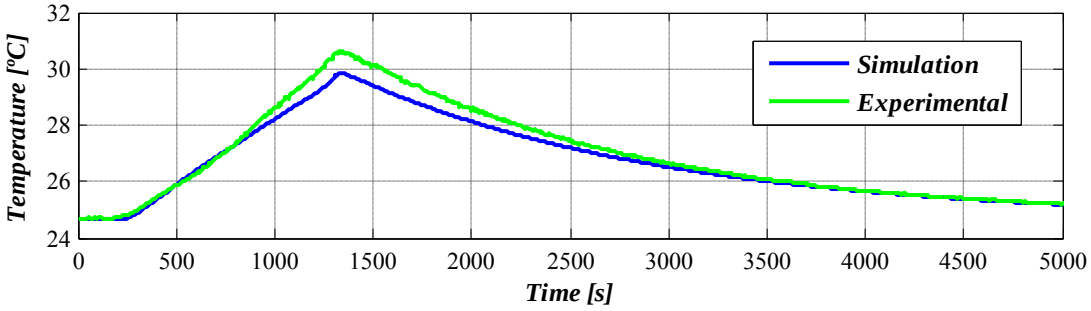

a)

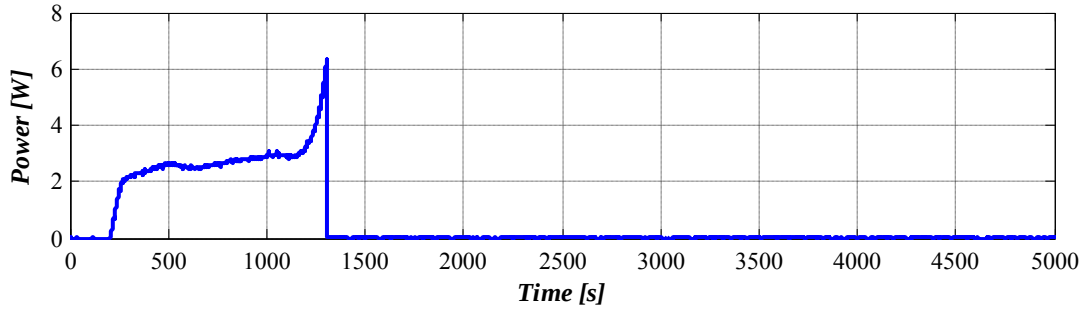

b)

Figure 3.30: 3C rate complete *CC+CV* charge results for the 2nd order *Cauer model*; a) Surface temperature; b) Internal heat generation.

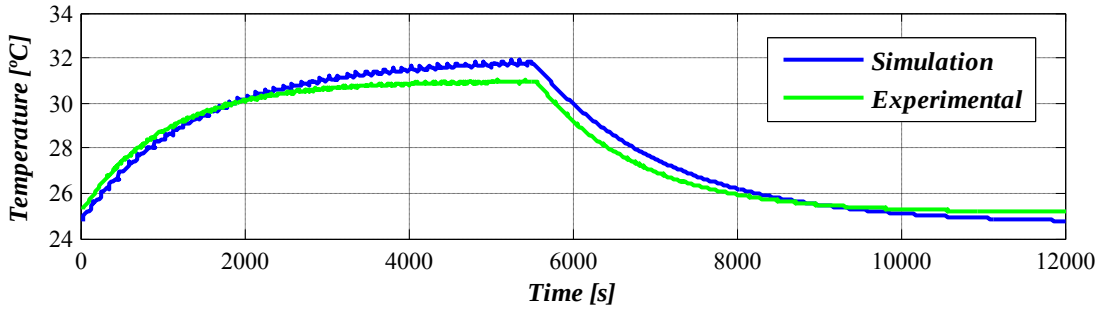

a)

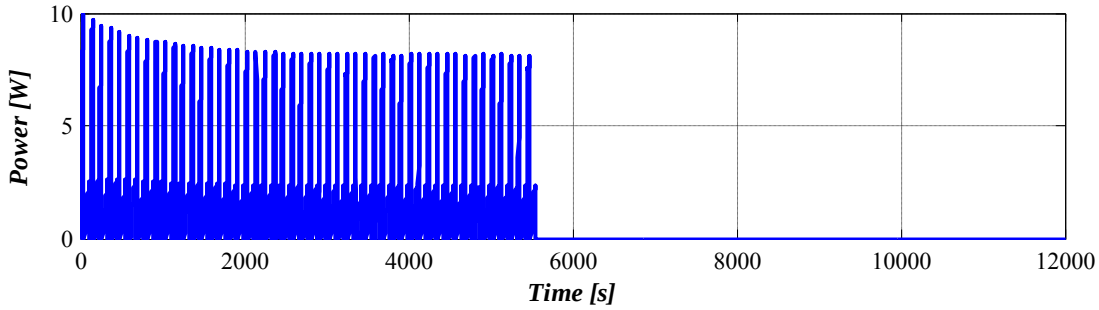

b)

Figure 3.31: Variable charge and discharge cycle for the 1st order *Cauer model*; a) Surface temperature; b) Internal heat generation.

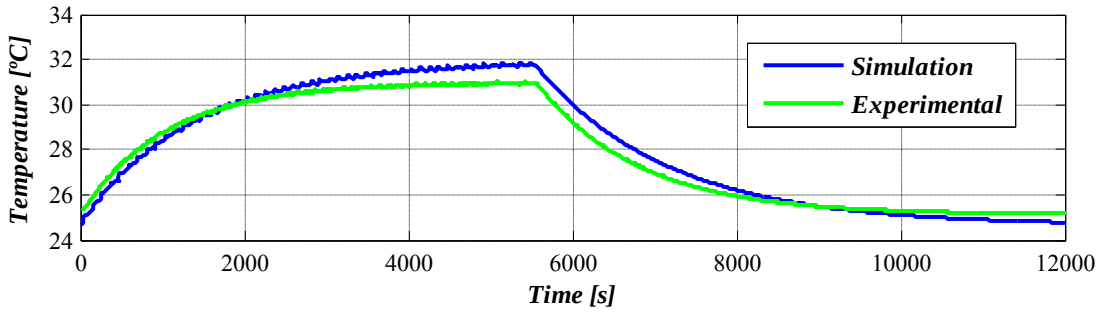

a)

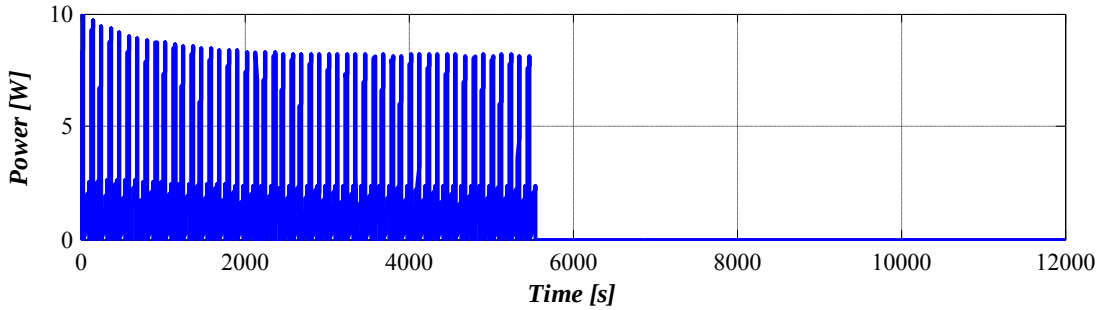

b)

Figure 3.32: Variable charge and discharge cycle for the 2nd order *Cauer model*; a) Surface temperature; b) Internal heat generation.

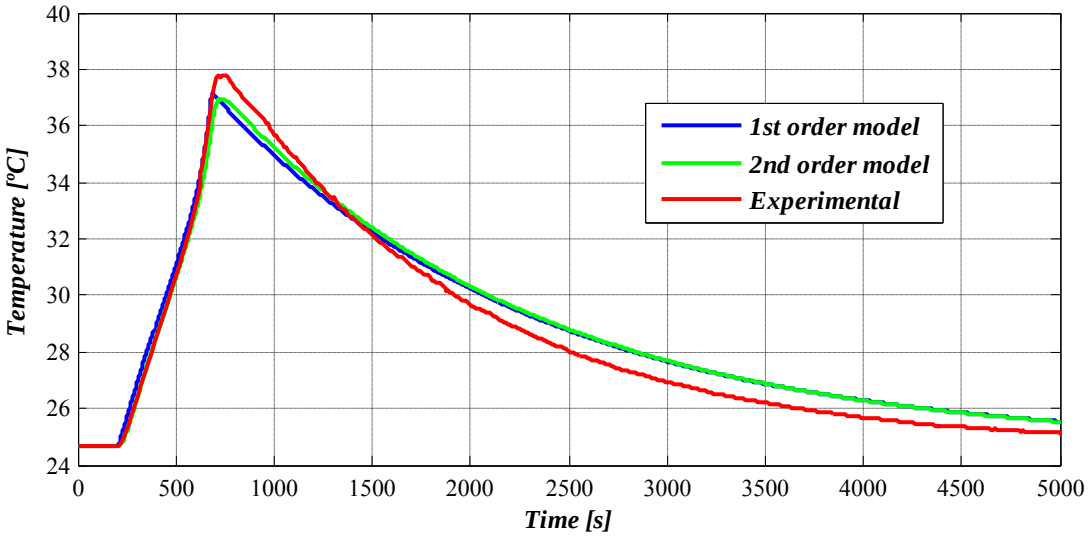

Figure 3.33: 7.69C rate complete discharge results; comparison between the experimental results and the behavioural models.

3.7.2 3D numerical model

Following, results obtained with 3D numerical model will be presented; Figure 3.34 shows a comparison between experimental 7.69C complete discharge results with the average temperature obtained from the 3D numerical model for this discharge rate.

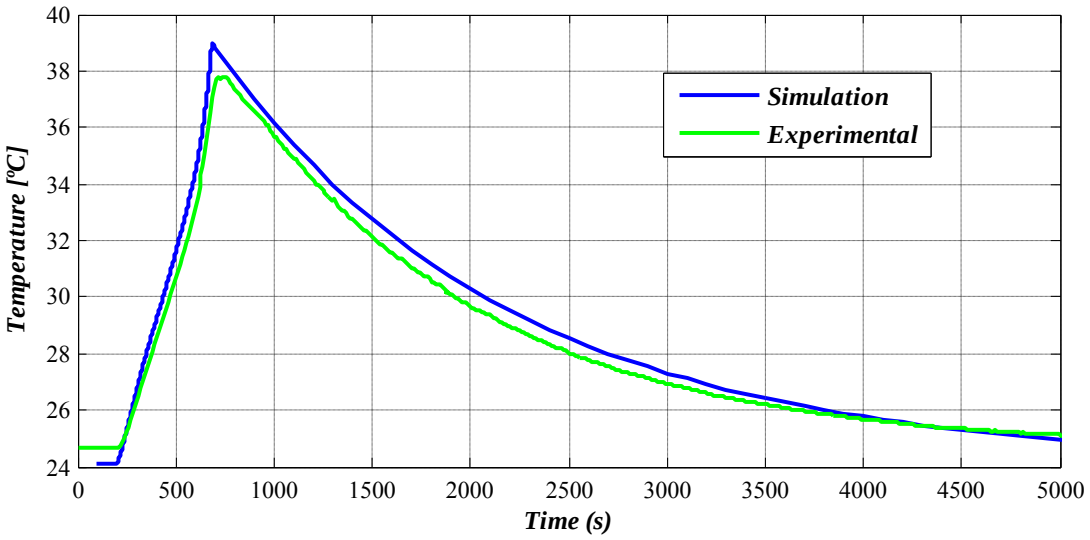

Figure 3.34: Comparison between *numerical model* and experimental results for a 7.69C discharge.

Defining the cell as a single body with average thermal properties has the consequence of reaching a 1st order model; this behaviour is similar to the behavioural *1st order Cauer network* since the reaction of the surface temperature of the model is instantaneous when the internal heat generation begins and when it is finished. Figure 3.35 shows a comparison between the two models and the experimental test results. Reaching high accuracies for this numerical model is difficult because of the amount of

estimated parameters in it. The *internal heat generation* is approximated with equation (3.6); average thermal conductivity and heat capacity values are defined for a 3D model; the whole cell is considered a single body with these thermal properties and with a uniform heat generation within it.

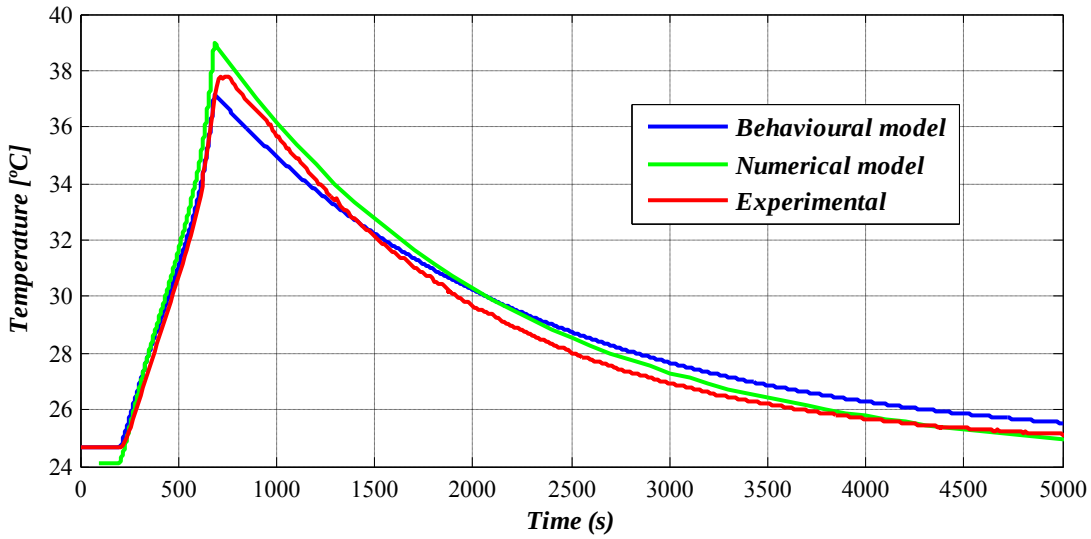

Figure 3.35: Comparison between *1st order Cauer model, numerical model* and the experimental results for a 7.69C discharge.

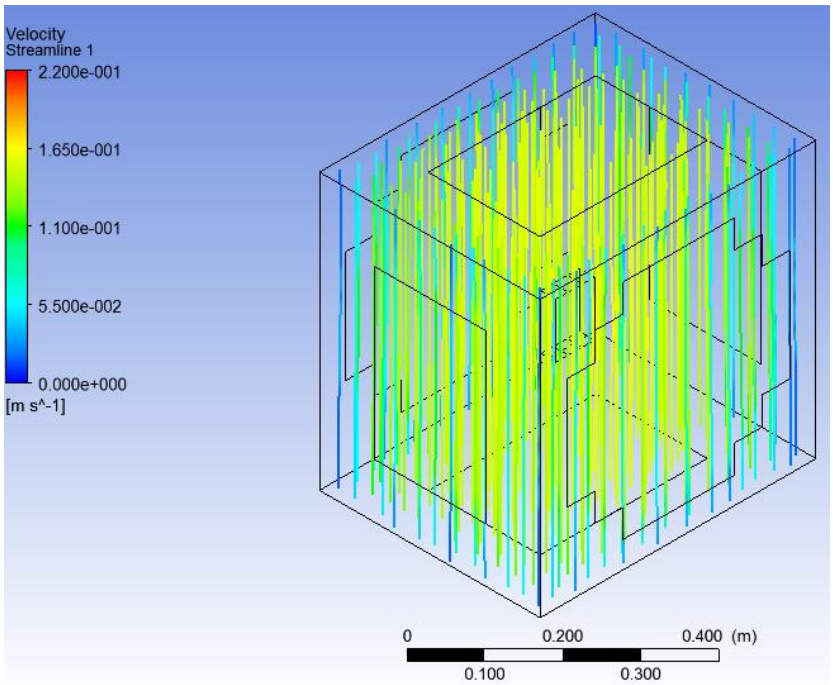

Figure 3.36: Velocity streamlines of the air flowing from the inlet to the outlet due to convection.

Figure 3.36 shows the effect of convection analyzed during the *post-processing*; in this case, air is flowing at a mean velocity of 0.165 m/s close to the cell and at a velocity of 0.055 m/s close to the walls limiting the model because these boundaries are at ambient constant temperature. The air flux is straight because the walls are neither an inlet nor an outlet, so they do not affect the evolution of the flux.

Figure 3.37 shows the temperature contour plot of the model close to the end of discharge time. The objective is to see the temperature gradients provoked due to the heating of the battery. The cell reaches a temperature between 314 K and 312 K (41ºC and 39ºC) at this step time; this figure also shows the temperature gradients near the battery.

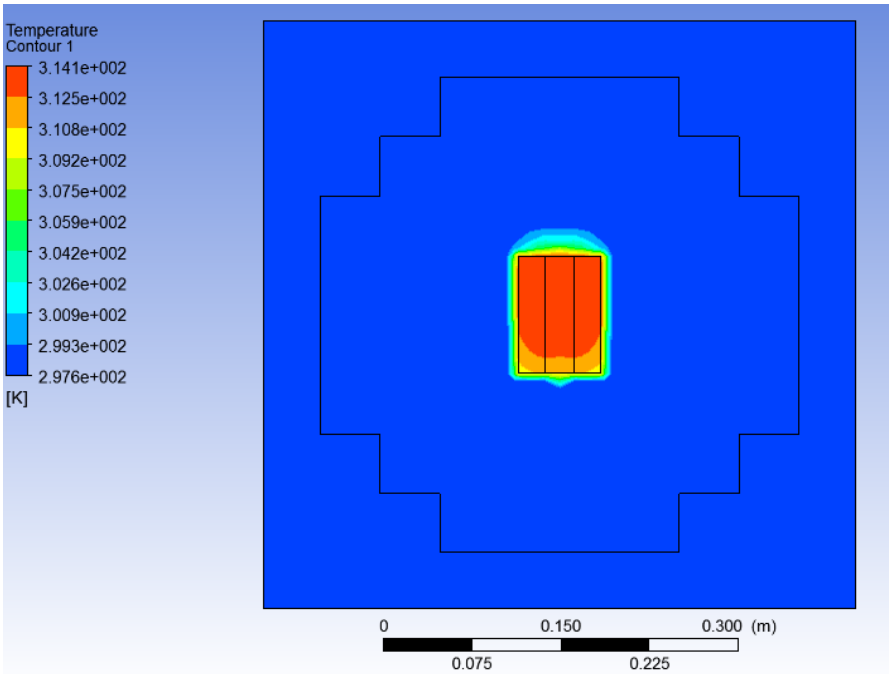

Figure 3.37: Temperature contour plot at the end of discharge time.

The model proposed in this work permits predicting an average temperature of the surface of the cell. However, no temperature distribution is obtained with this model since heat generation is considered uniform for the entire cell and thermal properties are average and isotropic also. As mentioned before, information about the materials within the cell and dimensions of the layers are required to calculate temperature distributions.

On the other hand, the methodology presented in this work does not require a fine mesh and thus, the time consumed during the solving process is less than the time consumed by a simulation with each single layer in a li-ion cell.

3.8 Conclusions of this chapter

This paper presents a methodology based on experimental tests to calculate the parameters of an equivalent thermal model for lithium ion cells. These parameters are used to build up two *Cauer* behavioural models and a 3D numerical one.

According to the modelling of the internal heat generation of a li-ion cell, it is concluded that equation (3.6) and the assumptions made are adequate to achieve a good approximation of this parameter. The validation of the equation has been done in an indirect way, measuring temperatures on the surface of the cell and comparing them with the ones achieved from the models, in which the heat generation is calculated. However, this equation is less accurate with alternative charge and discharge cycle because during transients a percentage of the output current is not generating losses inside the cell but this equation does not take it into account. Besides when complete discharges of the cell are simulated it is important to have a good estimation of the *SOC*; small errors in this estimation can lead to big errors of the internal heat generation due to the fast increase of the internal resistance when low *SOC* values are reached. Special heat generation measurement devices as calorimeters can quantify the percentage of error committed by the internal heat generation model and can help to improve it.

Regarding the thermal characterization process the accuracy of the measurements during the experimental tests is the most important aspect to improve; during the heat capacity test, the insulation of the cell has been validated due to the linear charge of the equivalent thermal capacitor of the model. However, during this test and power pulse test the internal heat generation power pulse is calculated before the test taking into account the *EIS* results; a online measurement of the internal resistor R_0 during both tests can improve the accuracy of the parameters calculated during these experimental tests, C_{th}, R_{cond} and R_{conv}. Special calorimetric equipment can help when defining all these parameters.

The overall methodology proposed during this chapter is validated with the results presented for both models. *Cauer* behavioural models show an error of less than 1ºC for the results shown during the validation. 3D numerical models show bigger errors depending on the current profile applied, reaching 1.8ºC of temperature error. However, the methodology proposed is considered adequate since a complex electrochemical process has been modelled making different assumptions with good accuracy.

The main contribution of this chapter is to define a methodology to thermally characterize and model a li-ion cell without using specific expensive equipment for thermal purposes. The methodology includes all the steps required to build up a thermal model for a li-ion cell and presents results for different current profiles to validate it.

However, the main objective of this work is to enlarge the lifespan of battery modules for power applications; thus, the following chapters are related to modules instead of talking about single cells, concretely next chapter analyzes the problems of using li-ion battery modules in power applications..

Chapter 4. THERMAL EFFECTS OF LITHIUM ION BATTERY MODULES IN POWER APPLICATIONS

The following chapter analyzes the effects of high current demands in the thermal behaviour of li-ion battery modules. Firstly an introduction to this topic and the state of the art in terms of failure modes, calendar life and cycle life will be presented; after that the thermal behaviour of a battery module under a power application current demand will be shown to prove that temperature distribution and maximum temperature of the battery module are affected severely. After analyzing these results several conclusions about this topic will be presented to conclude the chapter.

4.1 Introduction

Nowadays li-ion cells nominal voltage is around 3.2V and 3.8V for most of the available technologies; in terms of current capability, this technology is promising due to the power cells, with hundreds of amperes available depending on the size of the li-ion cell. However, increasing the delivered current to reach higher powers has different disadvantages; the most important one is the increase of Joule effect power losses and the size of the cables to carry this high current. Another option is to increase the voltage of the energy storage system serializing li-ion cells building up battery modules and increasing the current of the energy storage system parallelizing li-ion battery modules. Several configurations can be defined to reach the power required by the application.

Nevertheless, increasing the available power of the energy storage system presents several problems due to the serialization of cells and due to the increase of the delivered current; when li-ion cells are serialized there are usually voltage unbalancing problems due to differences between cells within the same module and voltage balancing systems are required to mitigate this problem. On the other hand, when high currents are delivered by the battery module the internal heat generation of the module is higher leading to important problems with temperature in the energy storage system.

Temperature is one of the key factors when working with lithium ion battery modules due to its influence in safety, performance and lifespan concerns in these devices; hence, it is compulsory to thermally manage the energy storage systems. Maximum temperature of the battery module is an important factor to control due to its influence in safety concerns for the user of the energy storage system. The other important factor to control is temperature distribution because of its influence on the aging process of the battery module. Thus, li-ion batteries must work in a certain temperature range to avoid security problems and to slow down the aging process of these devices. Commonly, the optimum temperature range is said to be from 20ºC to 40ºC [44].

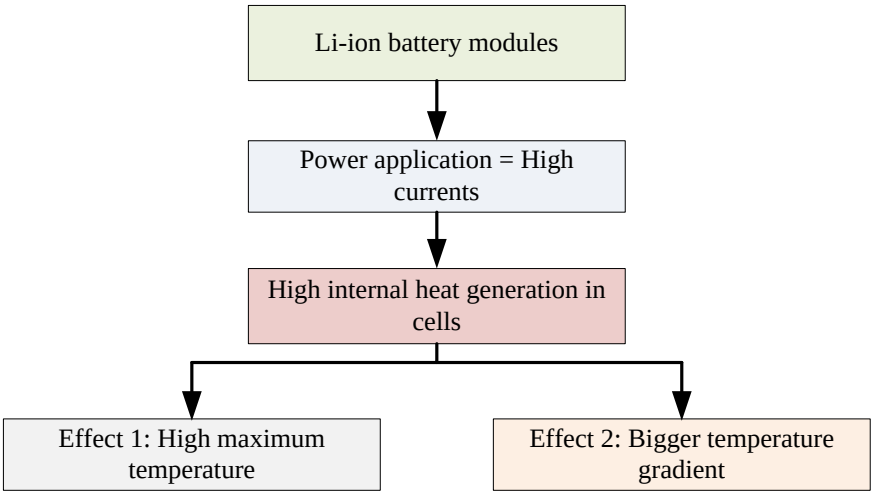

Figure 4.1: Overview of the effects of using li-ion cells for power applications.

4.2 State of the art

This state of the art will be focused in the aforementioned temperature related problems; according to security, there are problems due to very low temperatures or due to very high temperatures, when the phenomenon called thermal runaway can be triggered. On the other hand, aging problems are also high temperature dependent and they can affect the calendar and cycle life of the li-ion cell.

4.2.1 Failure modes in li-ion batteries due to temperature

Working at low temperatures can be a hazard for the integrity of the li-ion cell; there will be a reduction in current carrying capacity both in charge and discharge. This operating temperature makes the cell reduce its reaction rate capacity and consequently, makes more difficult the insertion of the lithium ions in the intercalation layer as in overvoltage operation. The lithium platting effect appears again and cell capacity is reduced.

Operating at high temperatures makes possible to work with higher power out of the cell because of the increase in reaction rate. However, a progressive degradation of the cell can reduce its life significantly. Besides, the higher the current in the cell is, the higher the power losses by Joule effect are. If temperature is not under control the temperature will increase and the thermal runaway effect can be triggered; there are several stages before thermal runaway while the operating temperature is rising. Following these stages are going to be explained:

- Breakdown of *SEI* layer. The principle causes to reach this stage are a physical penetration of the cell, or overheat provoked by a current raise or an overcharge. This situation occurs when the temperature rises beyond 80ºC into the cell. The consequence of this breakdown is another raise in temperature because there is a strong reaction between the anode and the electrolyte in the breakdown *SEI* layer area.
- Emission of gases. Heat generated in the anode causes the breakdown of the organic solvents of the electrolyte (Ethane, Methane...) making the pressure to increase. Despite of reaching enough temperature to these gases to take fire, until reaching 130ºC there is no oxygen to react with. However batteries sometimes have a safety vent to release the gases in a controlled way. When gases are released out and take contact with air, they can burn.
- At around 120º the polymer separator melts allowing the short circuits between electrodes.
- The heat accumulated inside the battery provokes the breakdown of the metal oxide cathode. Oxygen is now released and above mentioned gases react with the oxygen and burn. The breakdown of the cathode is highly exothermic, so the temperature continues increasing. The complete breakdown of the cathode is produced at more than 200ºC. Pressure and temperature continue rising until the complete destruction of the cell.

Ren et al. in [45] study the thermal runaway risk in commercial pouch cells using a pinch-torsion test. The pinch-torsion test is an alternative for the pinch test because a torsional component is included; it is demonstrated that the torsional component superimposed on compression loading can reduce the axial load required to induce internal short circuits with smaller short spot size. They conclude that with their method it is possible to evaluate the thermal stability of commercial cells. Ramadass et al. in [46] conduct controlled internal short circuit tests with their own method to evaluate different kind of short circuits within the li-ion cells. These tests were done for several *SOC*s and for several nail penetration speeds. The results showed higher thermal runaway risk when the *SOC* of the cell under test was higher.

4.2.2 Aging due to temperature in li-ion batteries

Aging is the most critical problem for battery manufacturers when designing an energy storage system based on li-ion batteries for a concrete application. Nowadays the price of these devices is high and it is difficult to design competitive energy storage systems for power applications if the cycle life of the system is not long enough. Hence, it is important to study the aging mechanisms in these devices and enlarge the lifespan of the battery system as much as possible. This state of the art is focused on aging mechanisms due to temperature effects although there are several factors that affect the life of the cell as *DOD* or current rate. There are several works on the estimation of the ageing process of li-ion cells; Prasad et al. in [47] develop an electrochemical model that depends on two key aging parameters, cell resistance and the solid phase diffusion time of lithium species in the positive electrode. Paul et al. in [48] research the heterogeneous aging processes of cells within battery systems due to different working conditions and tolerances during the manufacturing process. They present a method to estimate the battery life time taking into account cell to cell variation.

4.2.2.1 Calendar life

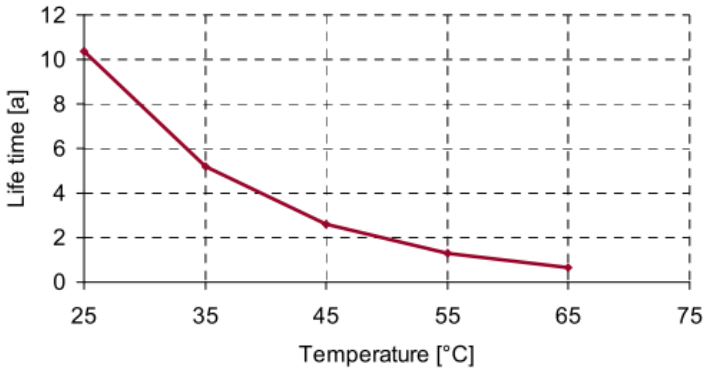

Figure 4.2: Li-ion cell calendar life depending on its storage temperature [49]**.**

The calendar life is defined as the elapsed time before the cell does not reach the requirements of the application weather it is in active or inactive use. It is a critical parameter since some applications are requiring large calendar life for the energy storage systems; for instance, in electric vehicle application the requirement is more

than 10 years, and depending on some parameters it is not possible to reach this specification.

Calendar life is directly affected by temperature as it can be seen in Figure 4.2. At 25ºC, the concrete cell of this study will last more than ten years until the cell is unusable. However, if the cell is storing energy at a higher temperature during its life, for instance 35ºC, it is possible to reduce its calendar life to the 50% for this concrete li-ion cell. The calendar life is not only affected by temperature although in this work is the main parameter of interest; high *SOC* values affect the calendar life of li-ion cells.

Several authors conclude that there is a strong influence of temperature in the calendar life of li-ion cells. Zhang et al. in [50] researched the calendar life of li-ion pouch cells and presented several results of the capacity loss of the cell due to high temperatures. Figure 4.3 shows one of these results; the cell storing the energy at 45ºC lost its capacity faster than the cells storing the energy at lower temperatures.

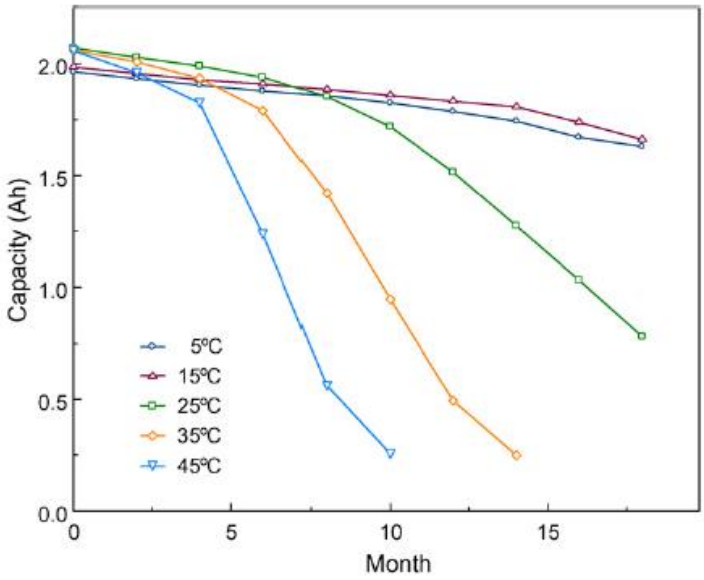

Figure 4.3: Capacity fade of pouch cells for different temperatures. [50]

Eddadech et al. in [51] presented a method for calendar ageing quantification of power batteries taking into account the *SOC* and temperature effects. They concluded that cells storing energy at higher temperatures increased their internal resistance more than cells storing the energy at lower temperatures. Käbitz et al. in [52] obtained experimental results for the calendar life of li-ion pouch cells for different temperatures. Their results showed a strong dependency of capacity loss with temperature; at 40ºC the cell lost a 15% of its nominal capacity in 100 days since at 60ºC the capacity fade for the same conditions was 45%. Other authors also conducted several experimental tests and got similar results according to calendar life [53], [54].

4.2.2.2 Cycle life

Cycle life instead is the number of complete charge and discharge cycles that can be performed with a cell before reaching the 80% of its rated capacity. Li-ion cells cycle

life is also directly affected by their working temperature; depending on this temperature their aging process will be different and their available capacity and power capability will decrease depending on it. Figure 4.4 shows the available number of cycles of a li-ion cell depending on its working temperature; the optimum working temperature for this cell is around 23ºC although each li-ion cell will have its own optimum temperature.

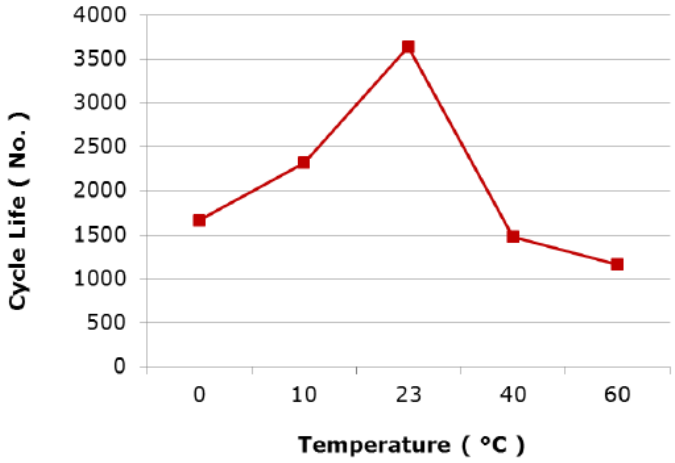

Figure 4.4: Li-ion cell cycle life depending on its working temperature [55]**.**

Wang et al. in [1] studied the influence of some parameters in the cycle life for $LiFePO_4$ cells; they concluded that temperature is one of the most relevant factors in the reduction of the cycle life in li-ion cells, although other factors like depth of discharge and current rate are also important. They also developed a model to predict the capacity loss in these cells; a comparison between the results obtained from the model and experimental results is presented in Figure 4.5. Results show the aforementioned temperature dependency; measured cells at 60ºC loose more capacity than the ones cycled at 15ºC.

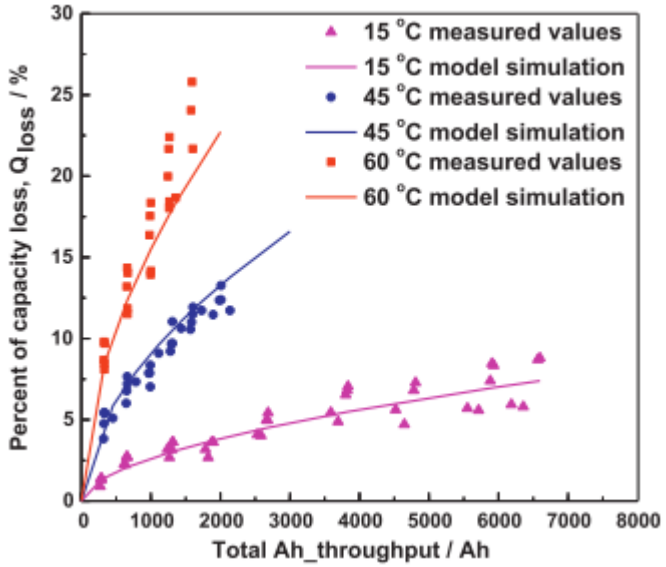

Figure 4.5: Comparison between simulated and experimental results of capacity loss at different temperatures [1]**.**

Amine et al. in [56] also studied the same temperature related phenomena. In this concrete research the tested temperatures are room temperature, 37ºC and 55ºC.

Käbitz et al. in [52] concluded that there is a strong influence of *DOD* in the cycle life of li-ion cells but they also include temperature as one of the reasons for this degradation. Other studies like [53], [54] and [57] studied the phenomena of temperature and cycle life during their researches with similar results.

4.2.3 Conclusions of the state of the art

From this state of the art it is concluded that it is compulsory to manage temperature in li-ion battery modules for power applications. On one hand there is a security problem when very high temperatures within the cell (over 80ºC) are reached; in this case it is possible to trigger a thermal runaway in which it is impossible to control the battery and it can be dangerous for the user because it can explode or even burn. Hence, it is important to limit the peak temperature adding cooling systems to the battery pack and cutting the current if necessary with the battery management system. Besides, very low temperatures (below -10ºC) can damage irreversibly the battery because of the lithium platting effect. Thus, it is important to add any heating system to the battery to avoid cycling at low temperatures or limit the power with the *BMS* system.

On the other hand, even if it is not a security problem, ageing is probably one of the most important challenges talking about li-ion batteries. Both calendar and cycle life are directly affected by storing temperature and cycling temperature respectively as it can be seen in bibliography. It is important to keep all the cells of the battery module or pack very close to the optimum temperature when storing energy and when cycling to be able to enlarge their lifespan; temperature control has to be accurate, because a variation of 10ºC in temperature has a huge influence in the calendar life and cycle life of the cell. Important investments have to be done to acquire this kind of systems nowadays and the reduction of the available capacity and the increment of the internal resistance due to both ageing effects can make the battery unable to reach the energy and power requirements of the application.

4.3 Thermal behaviour of a real module under power application current demand

In this section of the work experimental results of a li-ion battery module delivering energy for a power application will be shown; in these experimental results the thermal behaviour of the battery module will be analyzed and temperature distribution and maximum temperature will be evaluated.

There are several aspects that affect the temperature behaviour in li-ion battery modules; the mechanical assembly, the layout of the module, the thermal interface material if used or the thermal management system are probably the most important ones. The results presented below are results for different modules without thermal management system. The objective is to prove that it is important to work on the mechanical assembly, layout and cooling strategy because otherwise, temperature distribution and maximum temperature will have bad contributions in the performance and lifespan of the energy storage system. Figure 4.6 shows an 8 cell battery module composed by 8Ah cylindrical cells in series (8S1P configuration); in this module, cells are set up between some holders and due to this reason and due to the shape of the cells it is impossible to avoid air gaps between cells of the cylindrical module.

Figure 4.6: 8 cylindrical cell battery module.

Figure 4.7 shows the surface temperatures measured in every cell in the cylindrical module; at this moment it is not important to know which cell reaches the highest temperature, it is important to focus on the maximum temperature gradient across the module and on the maximum temperature reached. In this case, working at an ambient temperature of 25ºC the maximum temperature reached is more than 44ºC and the maximum temperature gradient at the end of discharge instant is bigger than 6ºC. As mentioned before 44ºC is normally a high working temperature for li-ion technology that can contribute into the acceleration of the ageing process in the cells within the module. Besides 6ºC of temperature gradient will lead to uneven aging processes for the different cells provoking a reduction in the performance of the battery module. Moreover, these results have been achieved for a 2C complete discharge process (constant 16A), and this current is not that high if this module is going to be used for power applications. Consequently, this module will need to be thermally managed if it is going to be used for power applications and probably under higher ambient temperatures.

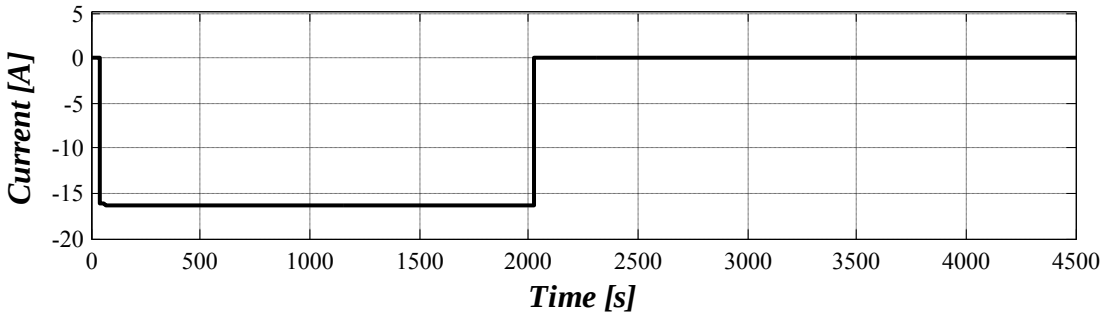

a)

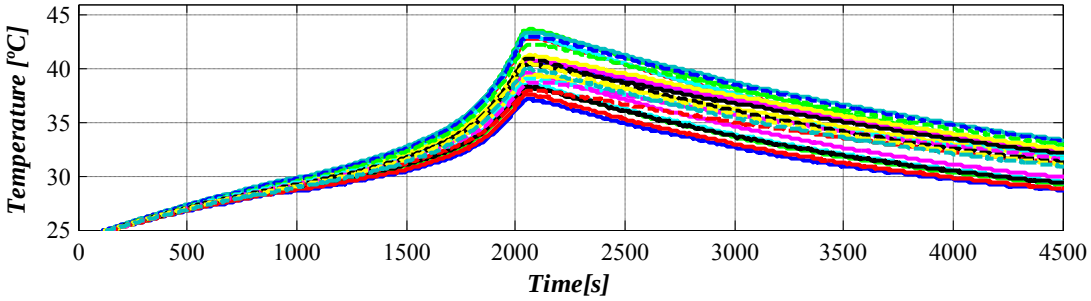

b)

Figure 4.7: a) Applied 2C discharge current profile; b) Surface temperature results for the cylindrical battery module.

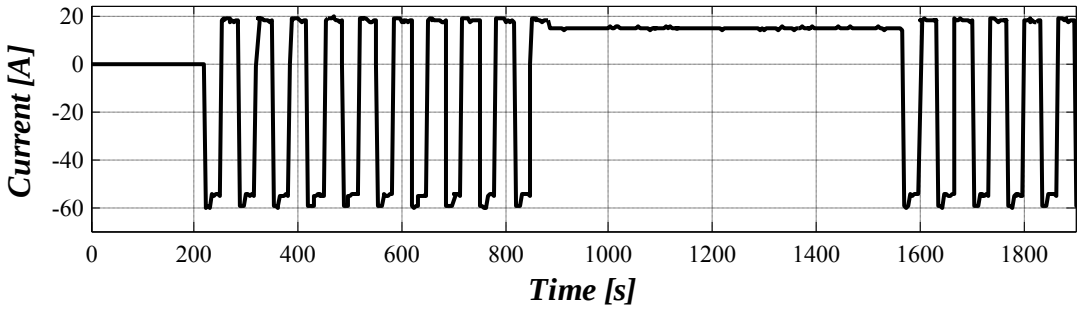

a)

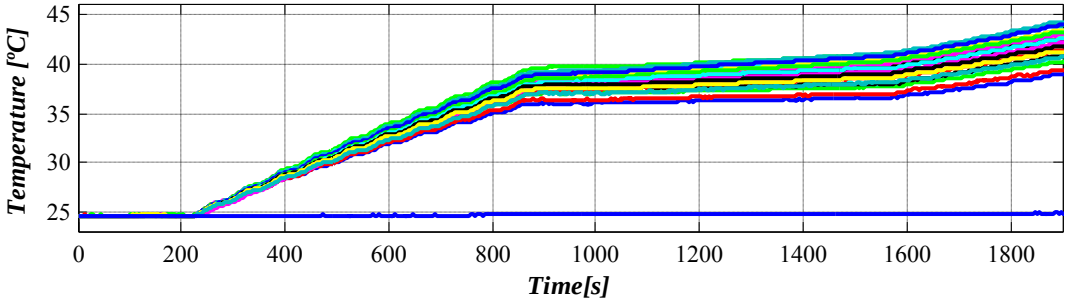

b)

Figure 4.8: Applied charge/discharge current profile; b) Surface temperature results for the cylindrical battery module.

The same effect can be seen in this module when an alternative charge and discharge power cycle is applied; Figure 4.8 shows an alternative charge and discharge power cycle applied to this module with peak discharge currents of 60A and peak charge currents of 20A. During these experimental tests a temperature alarm was defined to avoid security problems in 45ºC and the module reached this value before reaching 2000 seconds. Furthermore, the temperature gradient at the end of the test was almost 6ºC, a value that is considered too high in many other works for small modules. Depending on the module, results can be different for the same current profiles. Hence, it is important to evaluate the thermal behaviour of any battery module for a concrete application and for the worst ambient conditions to ensure that it is going to reach the requirements of the application in any case.

The uneven temperature distribution is provoked by differences during the manufacturing of the cells but also due to the selected cell, mechanical assembly and layout of the battery module. In spite of using cells from the same type and manufacturer for a battery module each cell has its own characteristics (for instance internal impedance and maximum capacity), thus, their thermal behaviour is not the same despite the same current is flowing through them in a module. These small differences in capacity and impedance for different *SOC* values lead to different heat generation rates in each cell, and consequently different working temperatures; this effect is better seen when deep discharges are reached because of the faster increase of the internal impedance when these *SOC* ranges are reached. Uneven temperature distributions for li-ion battery modules lead to different ageing processes for them and consequently the performance of the module can be reduced considerably.

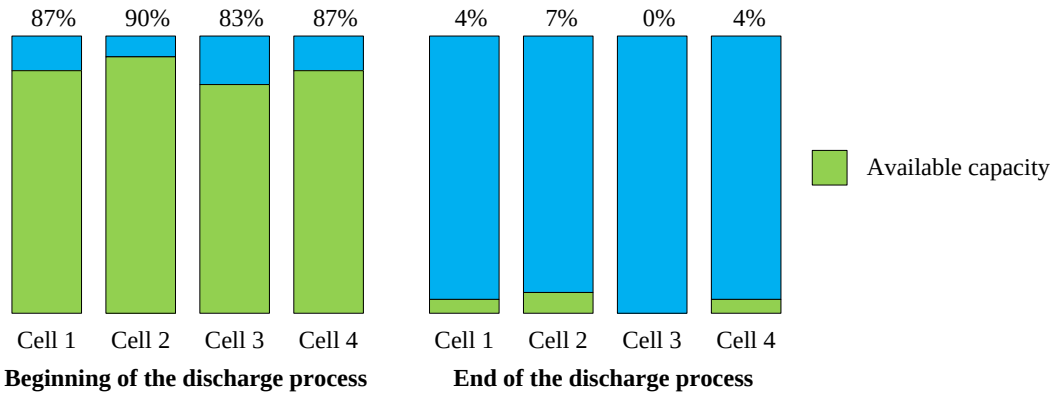

Figure 4.9: Consequences of non uniform aging processes for cells connected in series.

In modules with cells connected in series the available capacity is limited by the cell with less capacity or the most aged one; this cell will be the first one reaching the end of discharge voltage and the *BMS* will finish the discharging process. In this case all the cells in the module are not completely discharged and all the available energy is not used for the application (Figure 4.9). For these cases balancing systems are used to avoid these differences and discharge all the available energy exchanging energy between cells; however this aging mismatch can be mitigated with a better thermal management.

4.4 Conclusions

First conclusion is that it is important to limit the peak temperature of the li-ion battery module in order to ensure a safe operation of the energy storage system. Secondly, temperature affects the calendar and cycle life of li-ion cells and it is important to keep it within a safe range and as close as possible to the optimum working temperature to enlarge the lifespan of the battery module.

The third conclusion is that depending on the cell format and the mechanical assembly, a battery module without *BTMS* can reach undesirable maximum temperatures and big temperature gradients across the module as in the previously shown battery module.

The last conclusion of this chapter is that the maximum temperature gradient of the battery module has to be reduced as much as possible to avoid uneven ageing processes for the different cells conforming the module. With this strategy the available energy will be better utilized.

With this scenario there are four possible thermal behaviours according to maximum temperature of the module and maximum temperature gradient:

- High (Max T) and big (ΔT): Means that all the cells in the module will be aged rapidly and moreover, their ageing process will be different with some of them with a more accelerated ageing process.
- High (Max T) and small (ΔT): Means that all cells in the module will be aged rapidly but all the ageing processes are similar, easier to determine by state of health models and taking advantage of all the available energy.
- Low (Max T) and big (ΔT): Means that all the cells are surrounding their optimum working temperature but the temperature gradient provokes uneven ageing processes and consequently reduces the advantages of the module in terms of energy.
- Low (Max T) and small (ΔT): It is the ideal behaviour, all the cells working at their optimum temperature with no differences in their ageing processes.

The optimum scenario is the last one and the target of the thermal management system in this work is going to be close to it.

The following chapter analyzes the strategies utilized nowadays to improve the temperature distribution in battery modules and proposes the strategies used in this work for this purpose.

Chapter 5. MINIMIZATION OF THE TEMPERATURE GRADIENT IN LI-ION BATTERY MODULES

The following chapter deals with the temperature gradients in li-ion battery modules and the strategies to minimize them; after a brief introduction talking about the maximum temperature gradients permitted by other authors in their designs, the state of the art according to different temperature gradient minimization strategies will be presented. After that, the solutions adopted to minimize the temperature gradient in three different battery modules will be presented. Depending on the format of the cell selected to build up the battery module the strategy is different in terms of mechanical design, thermal interfaces between cells and the solutions to improve the temperature gradient. After analyzing these strategies, results for the three modules under different working conditions will be shown. Finally, the conclusions obtained from this chapter will be explained to conclude with this topic.

5.1 Introduction

The strategy followed in this work to optimize the thermal behaviour of battery modules for power applications is shown in Figure 5.1. During the current chapter the *STEP1* of the methodology is developed, the step related to the minimization of the temperature gradient of the battery module. Next chapter, Chapter 6 deals with the design of the cooling system of the *BTMS*. It is considered an important issue to minimize the temperature gradient first; if temperature gradient is reduced until an acceptable value, the cooling system will only have to take care of reducing the average temperature of the module until a desired value. Otherwise, the designed cooling system will take care of reducing the average temperature and reducing the maximum temperature gradient of the module. The main advantages of this strategy are:

- Simple control in the cooling system.
- Less actuators in the cooling system.
- Under low power requirements the cooling system is not working because the temperature gradients are minimized without its contribution.
- The power requirement of the cooling system only depends on the maximum power losses generated under the current profile of the application.

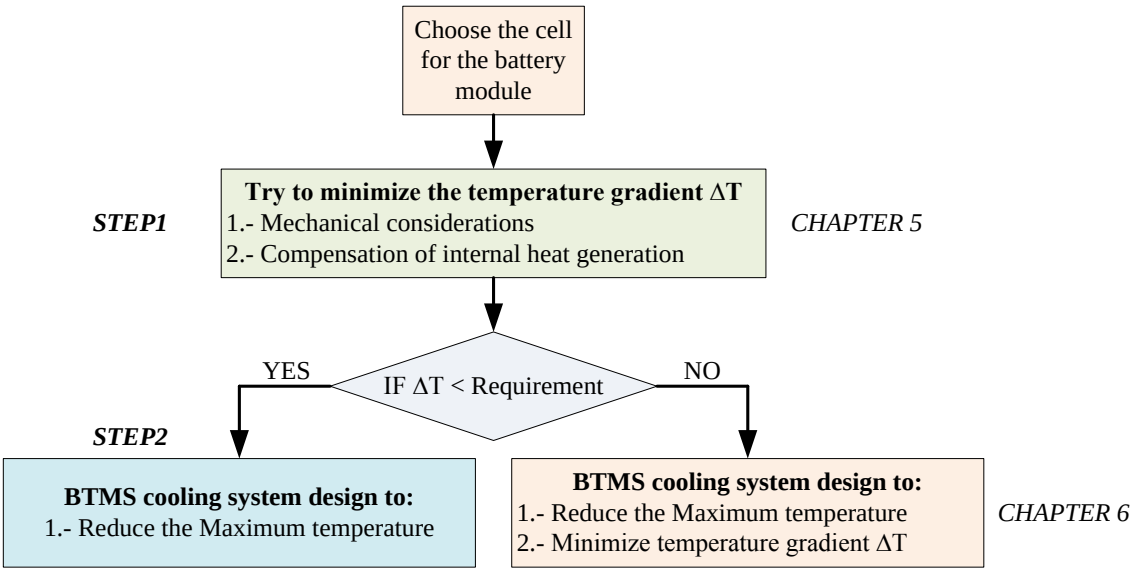

Figure 5.1: Overview of the methodology followed in this work to thermally manage li-ion battery modules.

According to the maximum temperature gradients permitted in battery modules Pesaran et al. in [4] give some recommendations depending on the size of the battery module or pack:

- Small modules: 2-3ºC
- Large modules: 6-7ºC
- Small packs: 2-3ºC
- Large packs: 7-8ºC

Besides, they define the temperature range of a li-ion battery module or pack between 20ºC and 40ºC, so 40ºC is used in their work as the maximum temperature for the cell. There are several factors that influence the thermal behaviour of a li-ion battery module; some of them are uncontrollable, like the energy and power required by the application, the environmental factors, or the available space for the energy storage system. However, there are other factors influencing the thermal behaviour of battery modules that can be modified to get better results reaching the requirements of the application. The format of the cell selected for the energy storage system, the mechanical layout or the thermal management system chosen can influence the thermal behaviour and can be changed during the design of the battery module or pack.

As mentioned before, the objective of this chapter is to propose different solutions to minimize the maximum temperature gradient of li-ion battery modules before designing the cooling system associated to the *BTMS*. Depending on the cell of the module different mechanical considerations will be taken into account first to reach the objective. If it is not possible to reduce the gradient mechanically, the solution of compensating the internal heat generation of the cells within the module will be proposed. It is possible that the maximum temperature gradient of any module is not reduced under the desired value with these considerations; in that case, the cooling system designed in Chapter 6 will have to take care of it.

5.2 State of the art

The state of the art of the chapter is about the strategies utilized nowadays to solve the problem with the temperature gradient in li-ion battery modules and packs. One of the possible solutions to improve this problem is to change the layout of the cells within the module; aspects like the space between cells from the same module or between different modules of a battery pack are analyzed. Other battery module manufacturers improve their temperature distribution taking advantage of intelligent materials; these materials are able to change their thermal conductivity depending on the temperature of the battery in contact with them. Another option is to enhance the heat transfer coefficient of the battery module through a cooling system; the most used solutions for cooling systems in batteries are forced air cooling, liquid cooling, using phase change materials or thermo electrical actuators. In most of the cases a combination of the solutions proposed is utilized to reach the desired temperature distribution.

5.2.1 Layout of the battery module

The layout of the cells within a battery module is one of the most important issues when assembling these devices due to its influence in the temperature distribution and maximum temperature of the energy storage system. Thus, it is important to analyze the different possibilities available depending on the format of the cell utilized for each module. Cylindrical cells are commonly mounted between holders to implement battery modules as in Figure 5.2 a; the shape of the cell and the holders lead to a small gap between the cells of the module. These gaps are commonly used to implement the air forced or liquid thermal management system depending on the size of the gap.

Prismatic and pouch cells instead permit to implement more compact modules assembling the cells without air gaps between them as in Figure 5.2 b; however, prismatic and pouch cells can be mounted within a module with gaps between them to improve the heat transfer of the cells to the ambient or to include any kind of thermal management system in the layout of the module.

a) **b)**

Figure 5.2: a) A123 cylindrical battery module; b) A123 pouch battery module.

Battery modules without air gaps between cells usually need thermal interface materials between cells to improve the heat transfer between them; these *TIM* materials avoid air bubbles between cells due to irregularities on their surfaces, Figure 5.3.

Figure 5.3: Prismatic cells battery module with a thermal interface material between cells.

There are several studies researching the topic of the air gaps between cells; Fan et al. in [58] use a *CFD* simulation tool to get results about different air gap lengths in a li-ion pouch battery module. These gaps between cells are utilized to force air with a fan and the target of the research is to evaluate the influence of these gaps in the cooling system.

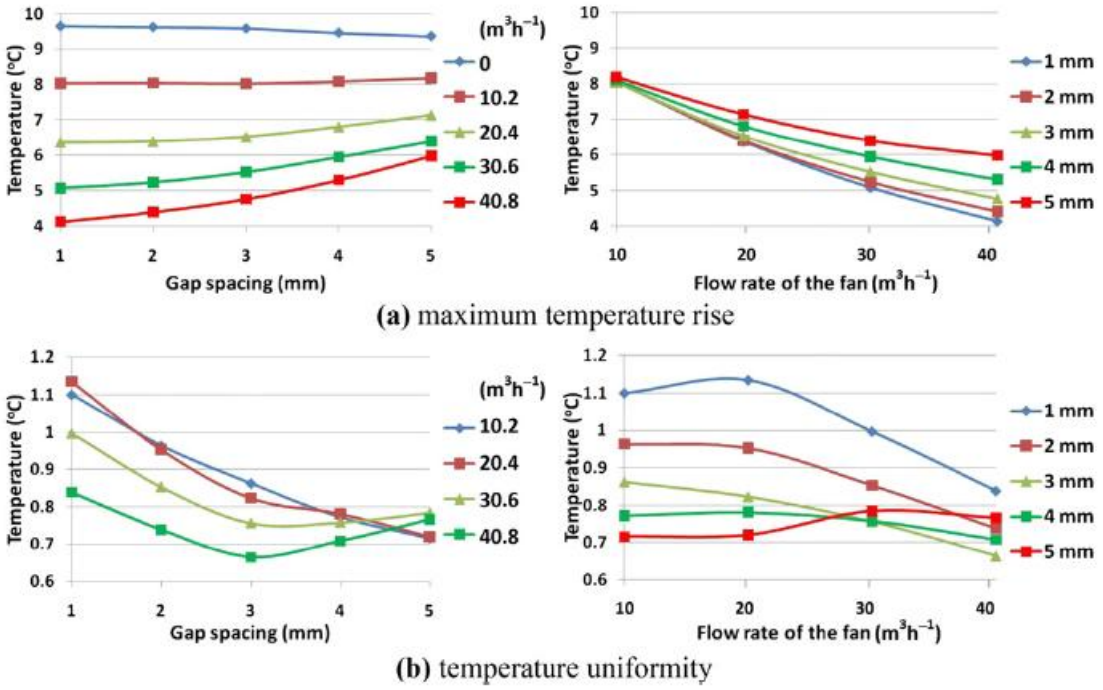

Figure 5.4: Summary of the results obtained by Fan et al. in terms of maximum temperature rise and temperature uniformity for a li-ion battery module cooled by forced air. [58]

They evaluate different gaps and air velocities to get their conclusions, Figure 5.4; according to maximum temperature rise, if the air flow rate is increased, with the same gap spacing, the maximum temperature rise is reduced. However, as the gap spacing is increased with the same air flow rate, the maximum temperature rise is increased. This effect is due to the higher velocities obtained in the gaps between cells with smaller

gaps. However the static pressure is increased in these cases and the fan used will need more power to reach the same velocities. According to the temperature uniformity, higher air flow rates improve this uniformity, but as the gap spacing is increased this improvement gets worse. The conclusion is that with big gap spacings (5mm in this case), increasing the air flow rate can damage the temperature distribution of the module.

Fathabadi in [59] researched the effect of the spacing between modules within a battery pack to implement a cooling system. Concretely he researched the thermal behaviour of a battery pack with cooling channels between modules and with air forced cooling. Their results show very uniform temperature distributions between modules; however, this thermal analysis is done using the partial equations which describe temperature distribution in the battery pack together with the related boundary conditions. It can be interesting to validate these results with experimentally obtained data.

5.2.2 Intelligent materials

There is another solution presented by Neumeister in [44] to improve the temperature distribution in li-ion battery modules; he presented an intelligent thermal interface material to improve the distribution of the module. In this work a liquid cooling strategy is implemented to improve the thermal behaviour of a li-ion module. The liquid cooling media is placed at the bottom of the cells as in Figure 5.5; while the liquid is extracting heat from the first cells of the module, this liquid is increasing its temperature and provokes uneven temperature distributions in the battery module. Hence, at the standard solution high liquid velocities are required in the cooling system to guarantee a small temperature gradient of the liquid. The consequence is a bigger pump with higher power consumptions.

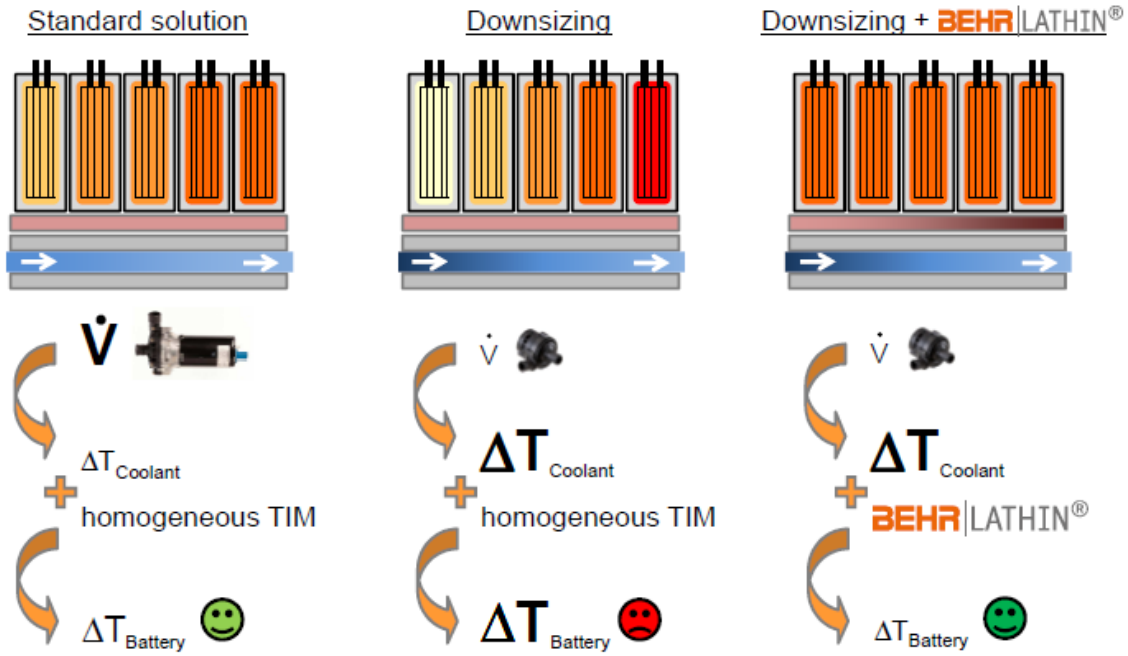

Figure 5.5: Behr company intelligent material purpose overall scheme. [44]

In order to reduce the power consumption the pump is reduced during the downsizing solution. The consequence is a bigger temperature gradient of the liquid flowing through the battery module and bigger temperature gradients in the battery module. The solution acquired to avoid this effect is to include an intelligent material in the interface between the battery module and the cooling media. This intelligent material is able to compensate the temperature gradient of the coolant by increasing or reducing its thermal conductivity in each zone.

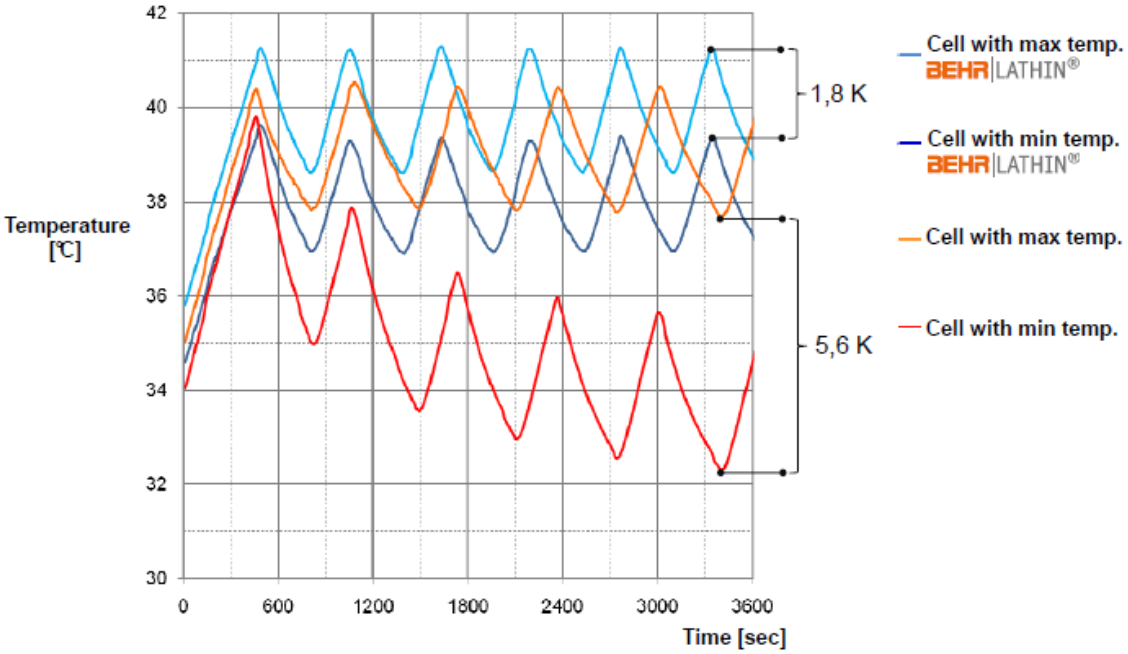

Figure 5.6: Results obtained in [44] **with and without the intelligent material.**

Results with the downsizing solution and with the downsizing plus intelligent material are presented in Figure 5.6; without the intelligent material the maximum temperature difference between cells is 5.6ºC. Including this intelligent material this result is improved until 1.8ºC, although the maximum temperature of the module is higher. Hence, the main problem of the standard solution, the high power consumption of the pump is solved including this material in the interface between cells and cooling media.

5.2.3 Thermal management systems

The third solution to improve temperature distributions in li-ion battery modules is directly related to the thermal management system associated to the battery modules for a power application. The solution is to increase the heat transfer of the cells to the ambient or to the cooling media with forced cooling. If this convective heat transfer is increased the temperature gradient will be reduced. In this section of the state of the art different cooling strategies used in li-ion batteries will be analyzed and different works of other authors will be included. The most common solutions are forced air cooling and liquid cooling. However, solutions based on *PCM* materials, thermo-electrical cells or heat pipes are becoming more important in the field of batteries nowadays.

5.2.3.1 Forced air cooling

Cooling a battery module or pack with forced air consists of blowing air at the ambient temperature directly to the battery pack to increase its convective heat transfer coefficient in order to evacuate more heat than without ambient air. There can be one or more blowers divided along the battery pack and different layouts for them with this technique. The advantage of air cooling is the simplicity against other techniques like liquid cooling. However, other techniques allow higher heat transfer coefficients, an important issue in high power applications.

Two different blowing strategies are commonly used with forced air cooling, Figure 5.7; the advantages of parallel cooling are better temperature distribution and better heat transfer to the ambient. However, depending on the size of the module or pack, the number of blowers required increases. In a serial configuration, the number of blowers is normally reduced; however, the air introduced in the module is heated throughout the module and provokes uneven temperature distributions.

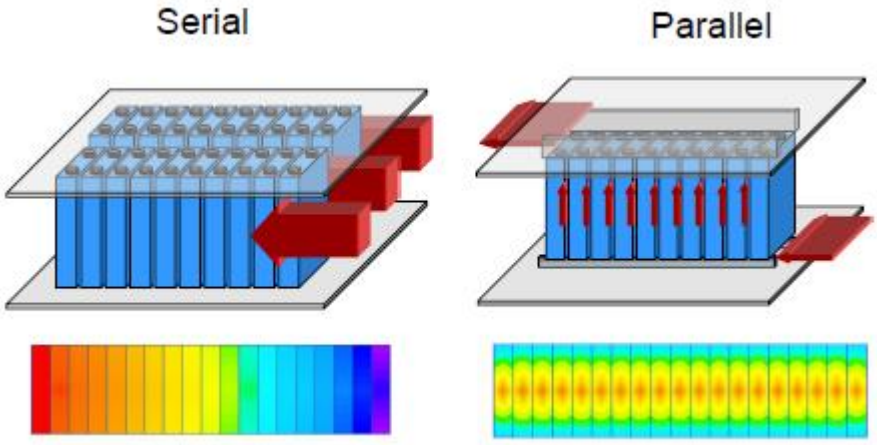

Figure 5.7: Serial and parallel air force cooling set ups. [55]

There are several works researching forced air cooling systems in li-ion batteries; Park in [60] presents different cooling strategies for a li-ion battery pack changing the heights of the manifolds used for the ventilation, changing the direction of the flow and including a pressure relief ventilation in one of the manifolds, Figure 5.8.

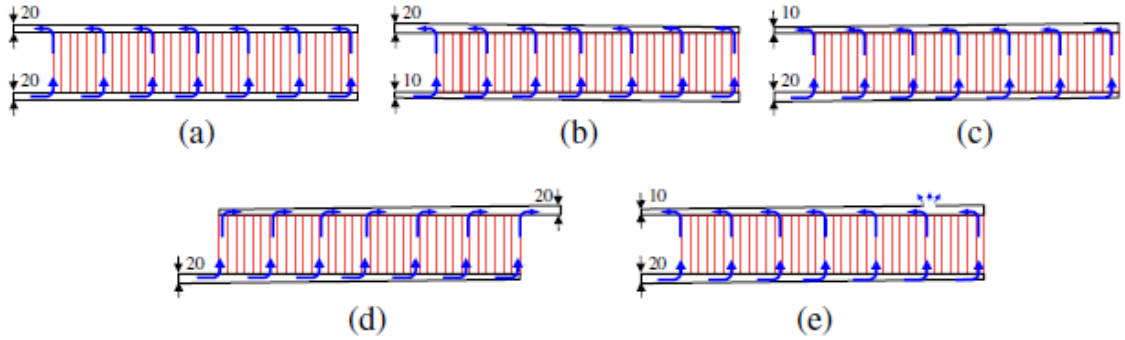

Figure 5.8: Different air forced cooling strategies changing the height of the manifolds, the direction of the flow and including a pressure relief ventilation [60]**.**

Depending on the air forced cooling strategy utilized, temperature distribution and maximum temperature results are completely different. The results presented in Figure 5.9 are simulation results obtained from a three dimensional thermal model presented in the same work. Results show different temperature distributions depending on the cooling strategy used. In this case best temperature distributions are achieved with *type IV* and *type V* strategies with 22ºC and 18.2ºC temperature gradients for the battery pack under test.

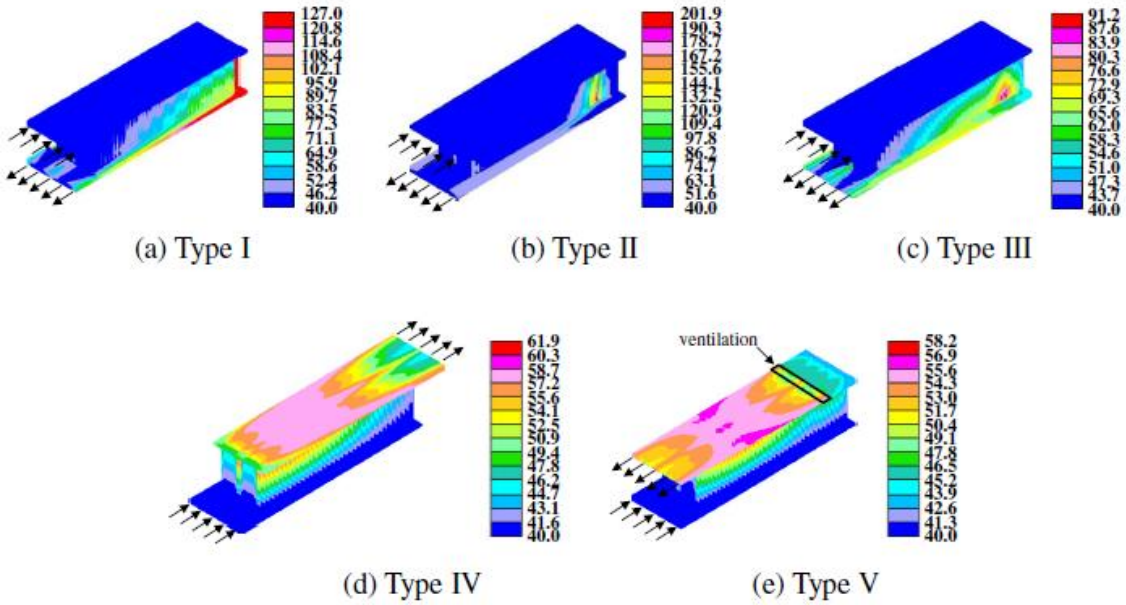

Figure 5.9: Temperature distribution for the different cooling strategies presented in [60]**.**

Xun et al. in [61] analyze the effect of the dimensions of cooling channels between cylindrical cells of a battery pack for different air flow rates. An analytical model is compared with a numerical model and several results are presented in this work. Although the battery pack simulated is big, the simulation domain is reduced because of the symmetry of the module to reach the final results faster.

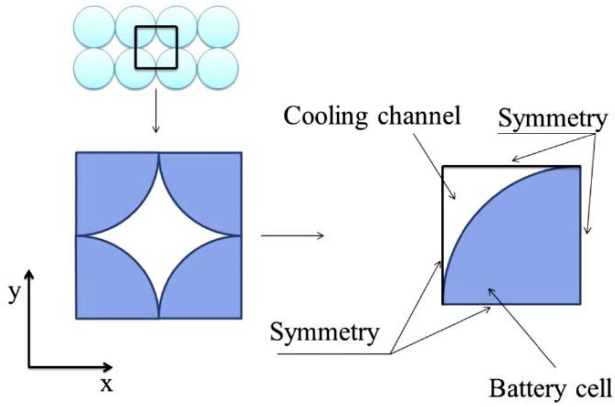

Figure 5.10: Set up of the analyzed domain both for analytical and numerical model [61]**.**

Two parameters are defined in this work to evaluate the cooling system, the compactness and the cooling energy efficiency. Their results show that increasing the

cooling channel improves the cooling energy efficiency but results in more unevenly distributed temperature.

Li et al. in [62] presented a two dimensional model solved by a *CFD* simulation tool; they simulated a cylindrical li-ion battery module with air forced cooling system and the simulation results were validated with experimental results. Figure 5.11 shows the experimental set up to obtain the experimental results; in this work a serial flow strategy is selected for the air flow cooling system. The objective of this work is to evaluate the influence of the cooling system in the temperature distribution of the module.

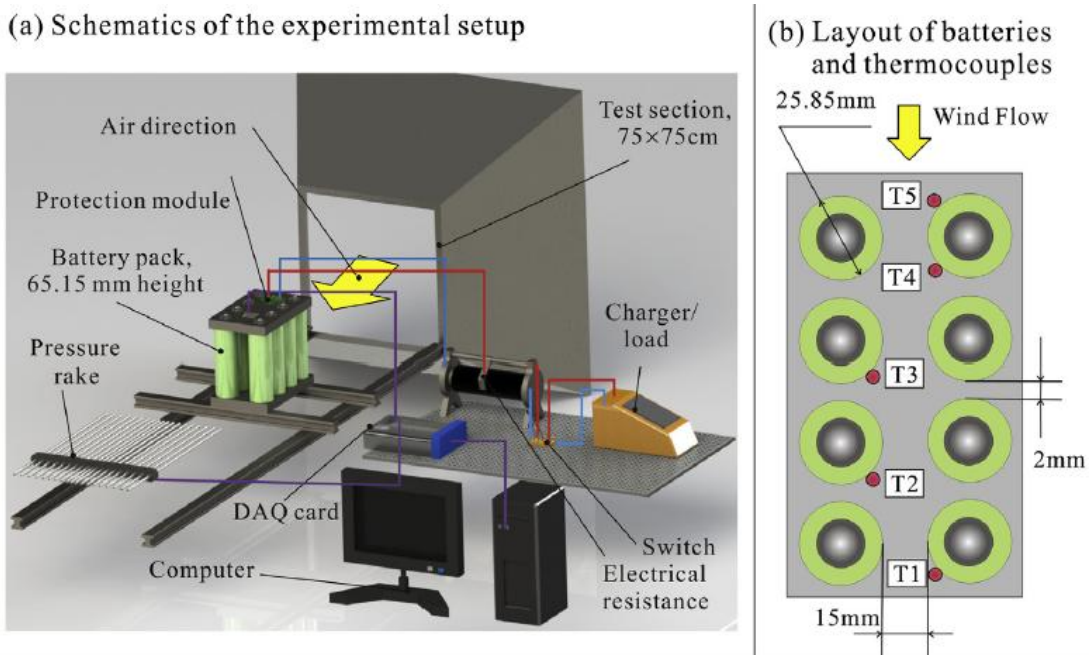

Figure 5.11: Description of the experimental set up to achieve the experimental results [62].

Results for different flow rates were simulated and experimentally obtained to validate the numerical model. Figure 5.12 a shows a comparison between experimental and simulation results for different air flow rates to validate the 2D model; results show good agreement between both results. Figure 5.12 b shows a simulation result for different air flow rates to evaluate temperature distribution in larger battery modules.

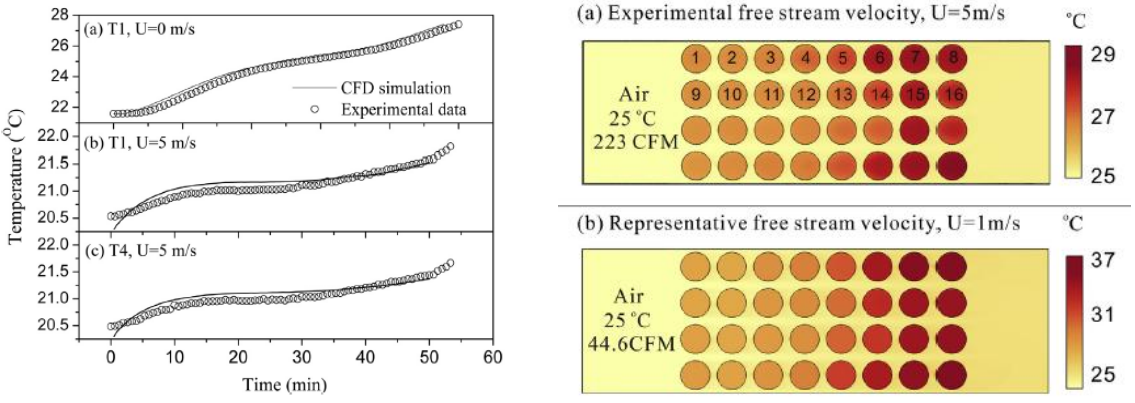

a) **b)**

Figure 5.12: a) Comparison between experimental and simulation results for different flow rates; b) Simulation of larger battery modules to evaluate temperature distribution for different flow rates.

Results show that if the air flow rate is not high enough the temperature distribution is not uniform; in the case of 1m/s the temperature gradient within the module is close to 4ºC; however, when the flow rate is increased to 5m/s, this gradient is reduced until 0.6ºC, a good result taking into account the dimensions of the module evaluated.

Giuliano et al. in [63] developed an air cooled thermal management system for high capacity lithium titanate batteries; the key component of the thermal management system is a heat exchanger based on open cell aluminium foam to increase the effective heat transfer coefficient. Heat exchanger plates are inserted between the cells of the module and are ventilated with fresh air. Thermochromic liquid crystal (*TLC*) strips are included in the front cell to measure its surface temperature during the experimental tests. Heat is evacuated through the bottom of the cells with the heat exchanger. (Figure 5.13)

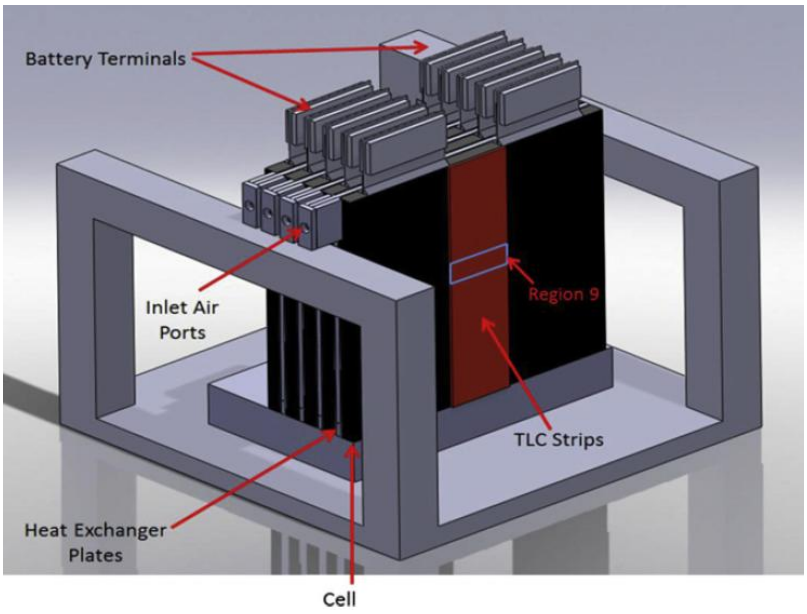

Figure 5.13: Solid model of the experimental set up in this work [63]**.**

Experimental results show that the temperature rise of the battery is restricted to 10ºC above ambient temperature even under 200A charge and discharge cycles. Figure 5.14 is showing some results for this case; Temperature at region 9 rises from 25ºC to 35ºC during the experimental test. The authors mention the little fluctuations of the temperature because cells are working at high values of their *SOC*. the inlet air is always at the same temperature but the outlet air is heated until the same temperature as the cell.

The authors conclude that the system can benefit from further improvements like a thermostatic control to regulate the air flow based on battery current demand and ambient temperature. Varying the air flow rate as required would improve the efficiency of the overall system, an important issue if an electro mobility application is considered. They also conclude that the ambient temperatures are low and the effect of the natural convection benefits their results. The future work is to test this system in real electric vehicle application to check the temperature rise with real conditions.

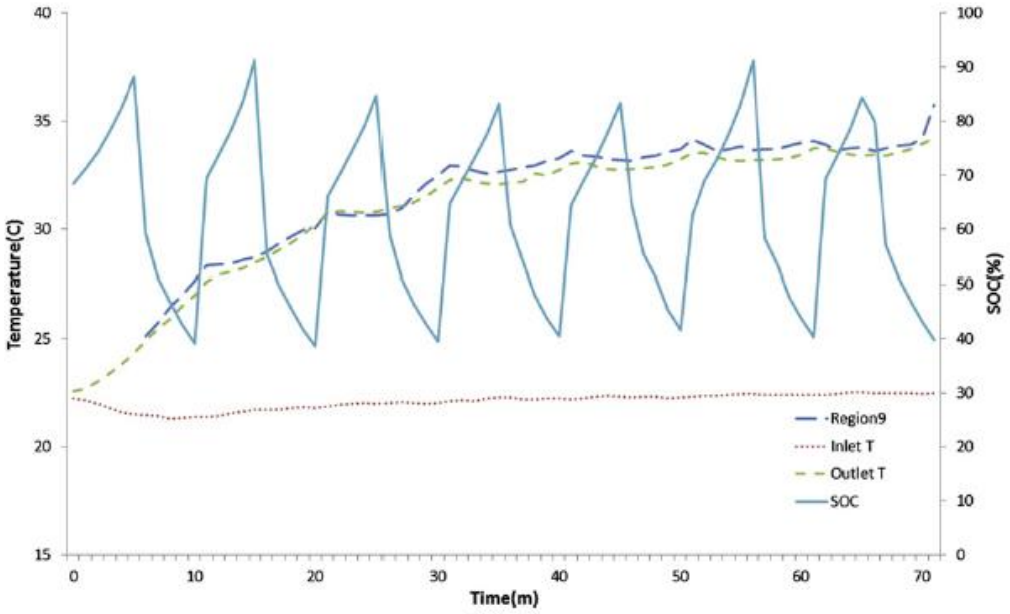

Figure 5.14: Results for a 200A charge and discharge cycle measuring the inlet and outlet air, temperature at region 9 and the SOC fluctuation [63]**.**

Park et al. in [64] analyzed the battery cell arrangement and heat transfer fluid effects on the parasitic power consumption and the cell temperature distribution in a hybrid electric vehicle. In this work a simulation model is compared with experimental results to validate it. Besides, different cell arrangements are tested to evaluate the efficiency of the overall system within the hybrid electric vehicle.

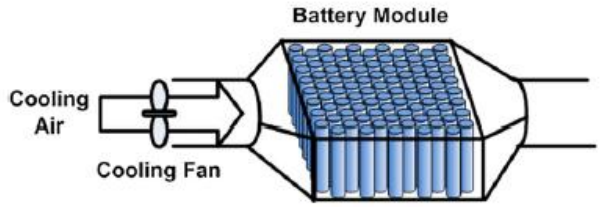

Figure 5.15: Set up of an air cooled battery pack [64]**.**

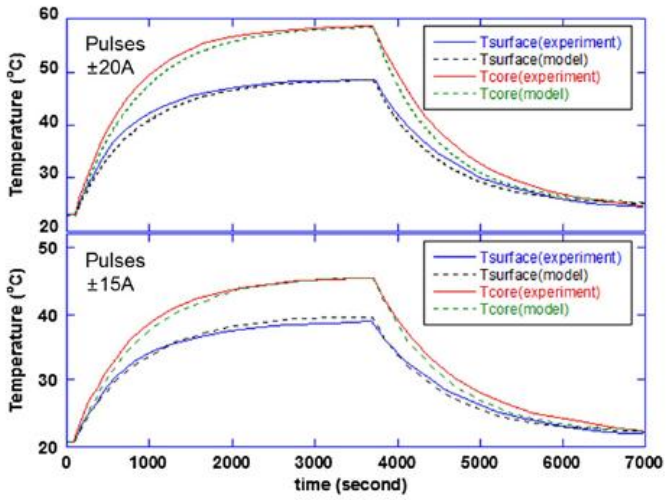

Figure 5.16: Validation of the model during current pulse experimental tests [64]**.**

Results show good agreement between the model and the experimental results according to Figure 5.16. After validating the model, it is used to achieve the aspect ratio with the best efficiency for the battery pack under test. Besides, several conclusions are obtained from this study; a wide battery is beneficial to minimize the cell to cell temperature variation but it requires more cooling air flow rate resulting in high power consumptions.

There are many other works researching the same field, air forced cooling with battery systems, validation of models or different cooling strategies [65]–[69].

5.2.3.2 Liquid cooling

Liquid cooling is another common cooling strategy in li-ion battery applications. The main advantage is the high heat transfer rate achievable with this cooling strategy. There are two different liquid cooling techniques: direct cooling or indirect cooling. Direct contact liquid cooling is the same technique as the one used with transformers; the device is submerged in the dielectric fluid and heat is evacuated to the mineral oil. The liquid used for a direct contact liquid cooling is commonly mineral oil to guarantee the electrical insulation of the battery pack.

When indirect liquid cooling is used, liquid can be dielectric or not, so water/glycol can be used because it is not in direct contact with the device. There are different techniques to insulate the liquid from the battery pack:

- Tubes around each module or around the pack.
- With a jacket around the module or pack.
- Cooling plates.

Pesaran et al. in [70] made a comparison between forced air and direct contact liquid cooling with mineral oil. With a reference of 50 g/s air mass through rate, which at atmospheric conditions (25ºC) has a volumetric flow rate of 43 L/s, the average heat transfer rate is 25 W/m^{2}K. An equal mass of mineral oil was equivalent to 0.057L/s in volumetric flow rate, resulting in an average heat transfer of 57 W/m^{2}K (2.3 times higher than air).

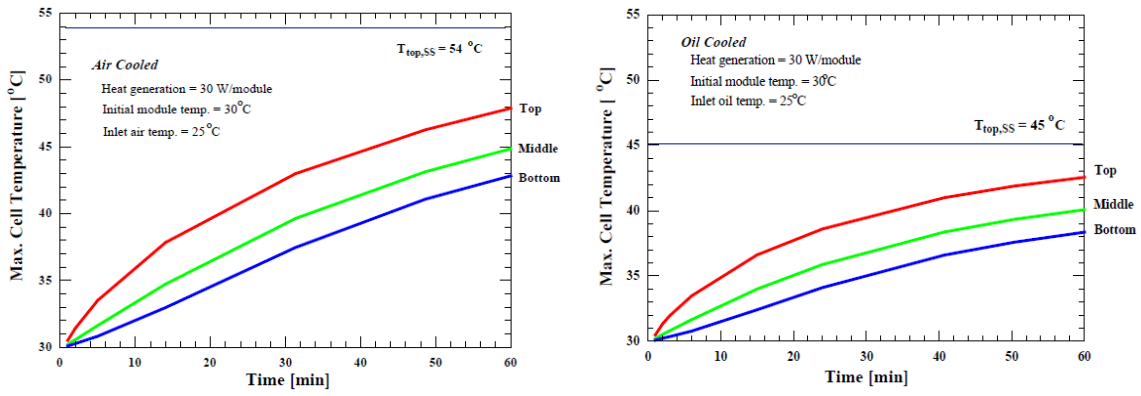

a) **b)**

Figure 5.17: a) Air cooled battery module transient and steady state thermal behaviour; b) Oil cooled battery module transient and steady state thermal behaviour [70].

Results show an important improvement in the heat transfer coefficient with liquid cooling since the steady state temperature is reduced from 54ºC with air cooling to 45ºC with liquid cooling.

Jarret et al. in [71] research the influence of operating conditions on the optimum design of electric vehicle battery cooling plates; a CFD simulation tool is used to parameterize a model and evaluate different cooling plates and the temperature distribution of the coolant flowing. The target is to reach a uniform temperature distribution of the coolant achieving the optimum parameters of the cooling plate.

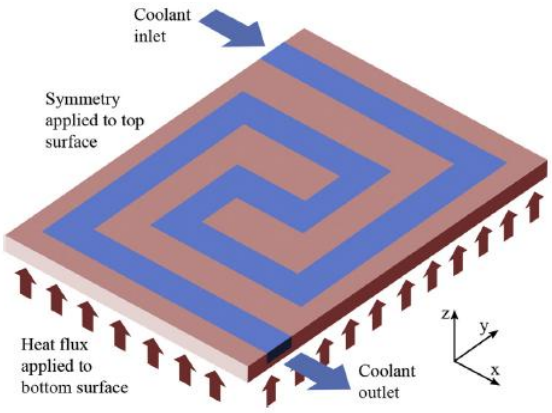

Figure 5.18: Cooling plate *CFD* analysis in [71]**.**

Behr Company analyzed different configurations with fluid ducts, cooling plates, and also, fluid ducting plates in [72]. Following a brief explanation is presented to understand these concepts. They presented the following schematic of a cell, where different potential cooling contact points and heat flows are presented. Housing and electrode connection points are pointed out as the places to do the cooling contact points, Figure 5.19.

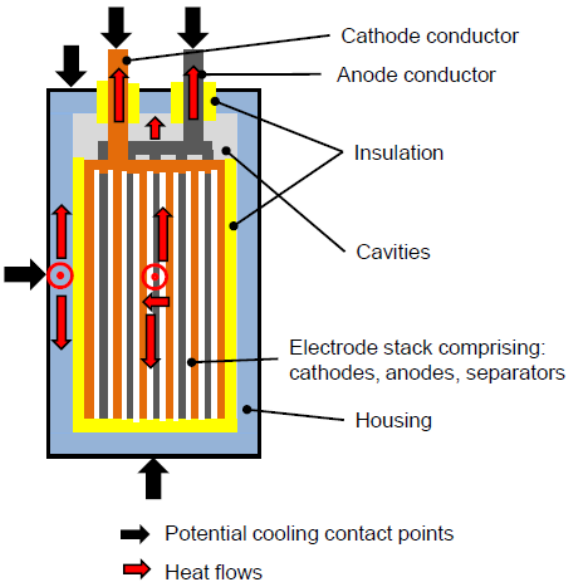

Figure 5.19: Behr group schematic of a cell [72]**.**

With this schematic of a cell, several liquid cooling strategies are analyzed in Figure 5.20. The first option is the base or head cooling. It consists of evacuating heat with a fluid duct in the base or head of the cell. Second one evacuates heat by a cooling plate placed in contact with a cell and the cooling plate drives heat to the fluid duct as in the previous option. The fluid-ducting cooling plate option evacuates heat by means of a cooling plate, as in the previous option, but instead of driving heat to a duct placed in the base, it is a fluid cooling plate. Last option, conductor cooling, consists of cooling directly the electrode connection points instead of the base or sides of the battery.

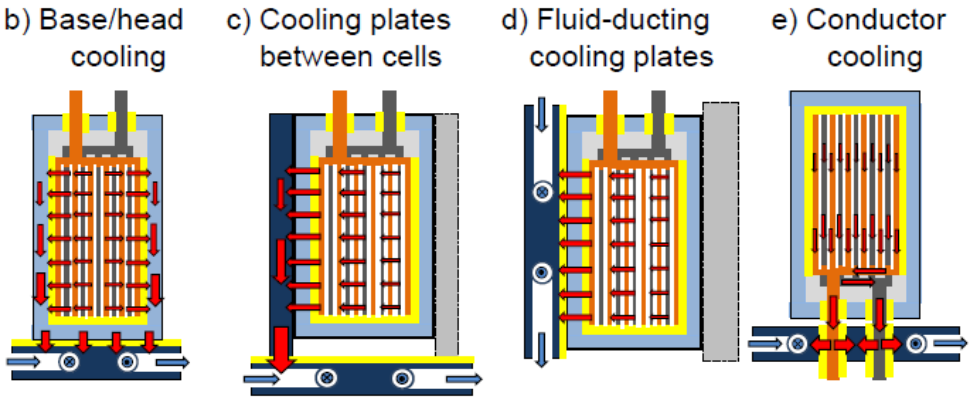

Figure 5.20: Behr group, different cooling strategies [72].

TABLE 5.1 sums the information given by Behr related to the advantages and disadvantages of the cooling methods. They evaluated the cooling methods in terms of cell assembly in a battery, cooling effectiveness and the package space required in battery.

TABLE 5.1 SUMMARY OF THE ADVANTAGES AND DISADVANTAGES OF EACH COOLING STRATEGY.

Cooling method	Base/Head cooling	Cooling plates between cells	Fluid-ducting cooling plates	Conductor cooling
Cell assembly in battery	+	0	-	+
Cooling effectiveness	+	+	++	+
Package space required in battery	++	+	-	++

The fluid ducting cooling plate method (option d in Figure 5.20) is presented as the most effective strategy; however, they mark it with a negative point in both assembly and package space required. The highest mark in package space required is for base/head cooling (option b) and conductor cooling (option e), because in the other ones ducts or cooling plates are placed between modules. They also present the same mark in effectiveness and assembly of cells in a battery. Lastly, the option cooling plates between cells present a “0” mark in assembly of cells in battery because despite of not being a positive point for this method, it is not critical. It is a good option in terms of effectiveness and package space required.

5.2.3.3 Solutions based on PCM

Phase change materials (*PCM*) are increasing their interest for battery applications; these materials are able to absorb energy from battery modules or packs when changing their phase. If the cells within the module reach high temperatures, *PCM* will absorb energy limiting temperature rise. Commonly, solid heatsinks are implemented with these materials and the cells are inserted in these heatsinks. Figure 5.21 shows different heatsink structures obtained from the study of Ling et al. [73]. This work is a review on thermal management systems using phase change materials for electronic components, Li-ion batteries and photovoltaic modules.

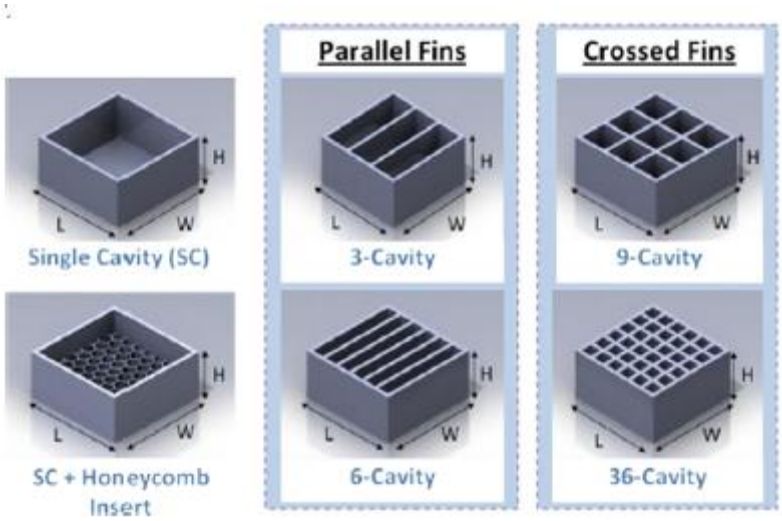

Figure 5.21: Different *PCM* heatsink structures for cooling battery systems [73]**.**

Kizilel et al. in [74] used a *PCM* matrix to build a battery module (Figure 5.22). The pack of the experimental study consists of 67 modules, each containing 20 commercially available 1.5Ah Type 18650 high power cells. Each module consists of five strings of four cells in series with the five strings in parallel. The nominal voltage and capacity of each module is 14.4 V and 7.5 Ah.

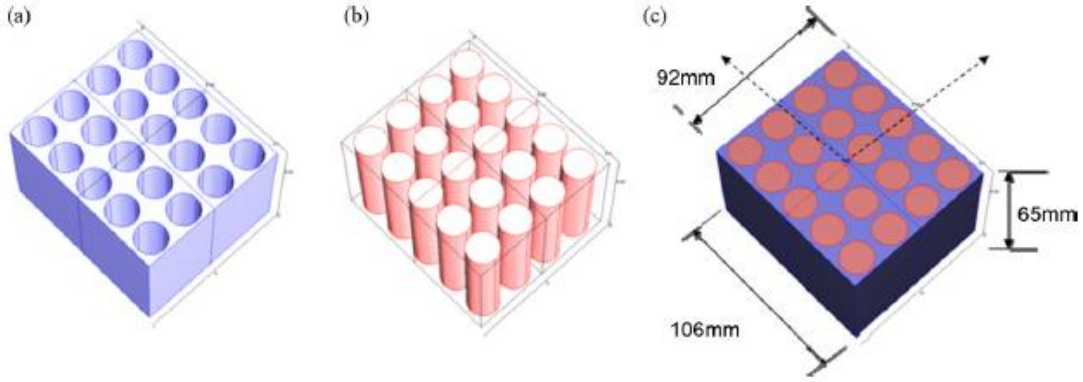

Figure 5.22: Schematic representation of 5S4P module configuration: (a) PCM filled closed box, (b) Li-ion cells and (c) battery module [74]**.**

This pack was designed for a Ford Escape Hybrid in order to replace the NiMH current pack. Results showed a more efficient behaviour of *PCM* versus forced air in terms of lower maximum temperature in the pack; besides, temperature gradient was smalled as shown in Figure 5.23. The effectiveness of the *PCM* against thermal runaway was also evaluated in this work with good results. Temperature distribution was much more uniform than with forced air even under extreme conditions.

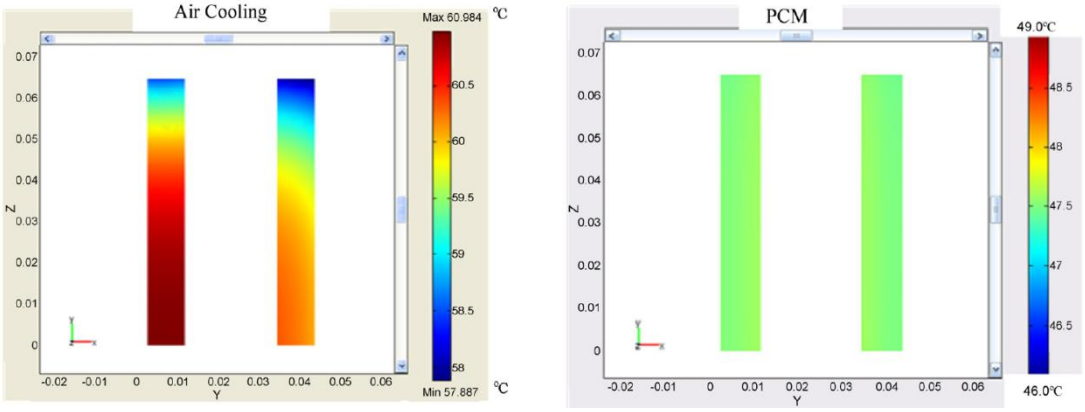

a) **b)**

Figure 5.23: Temperature profiles in two adjacent cells with Tamb =40◦C, discharge rate = 6.67 C, 50 A/module. a) Air forced cooling; b) PCM [74]**.**

Tamburrino et al. in [75] used a *PCM* for li-ion batteries for electric car and scooter applications. In this work when *PCM* reaches 55ºC, it melts and absorbs the heat in the module to avoid a sharp rise in the module. The module used was similar to the one used by Kizilel et al. in [74]. In this case 2.4Ah cells were used to assemble a 7S2P module configuration. According to the experimental set up of the work, 2 thermocouples, one at the corner and another one at the centre of the module measured 2 different points of the battery. The module was tested at 4.8A, 8A and 10A.

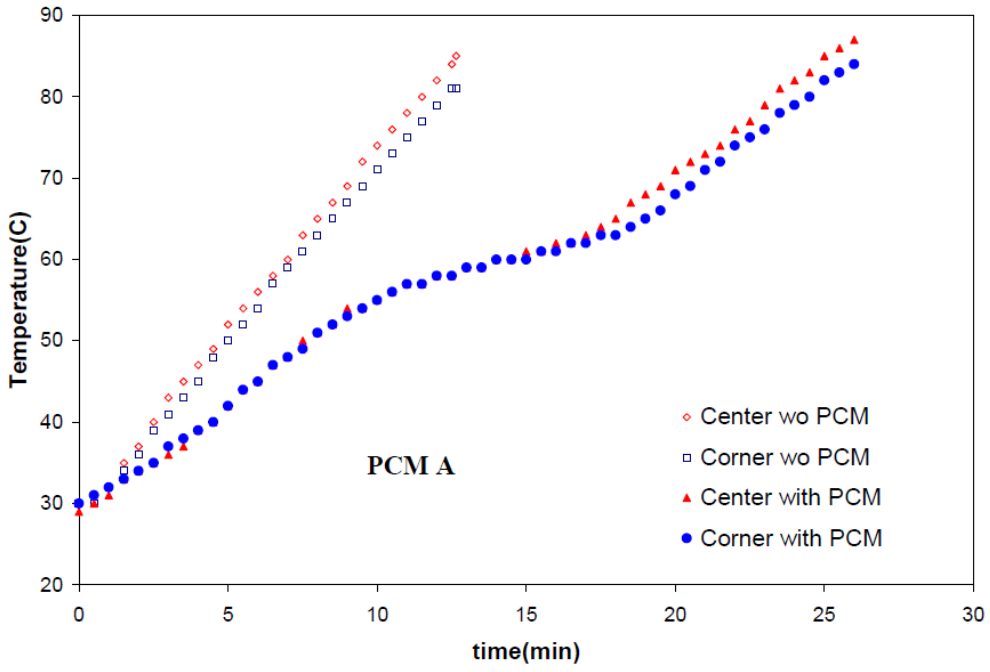

Figure 5.24: Temperature behaviour of the module with and without PCM [75]**.**

When temperature reaches 55ºC PCM melts and removes heat from the battery module. This way the rise of temperature is put back in time. Temperature distribution during this experimental work was uniform, 2-3ºC between centre and corner of the matrix.

Sabbah et al. in [76] presented a comparison between active air cooling strategy versus a passive phase change material one. It was mentioned a desired working range from 20-50ºC. A module based on 18650 high power cells (1.5Ah) was used for the experimental work. Discharges at 3A and 10A were done at two different ambient temperatures, 25ºC and 45ºC. At high rates, air cooling was not able to reduce temperature of the cell, therefore provoking unbalances along module.

Other authors also research the same effects of *PCM* materials in the cooling of li-ion battery modules in the following works [77], [78].

5.2.3.4 Peltier effect heat pumps

Alaoui et al. in [79] use Peltier effect heat pumps to design the *BTMS* of a battery pack for an electric vehicle application. Figure 5.25 the basic thermal unit setup of the Peltier module. These modules can be used to heat and cool the energy storage system depending on the current direction. The lifetime of these devices is long, the maintenance costs are very small and the system is environmentally friendly.

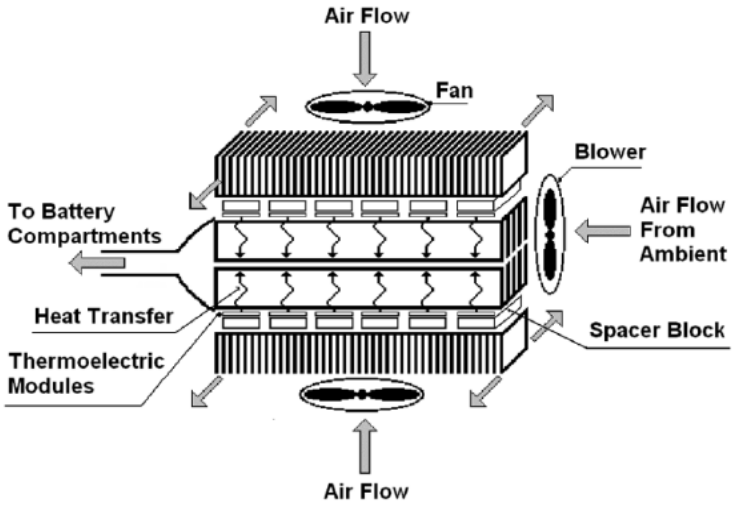

Figure 5.25: Basic thermal unit setup [79].

Figure 5.26 shows the temperature results during the heating and cooling experimental tests; *Temp@A* is the temperature measured at the frontal battery box and near the Peltier module and *Temp@B* is the temperature measured at the rear battery compartment, far from the Peltier module. During the heating test 1.5Ah were utilized to warm up the battery from 17.5ºC until 29ºC. Meanwhile, during the cooling test 2.6Ah were utilized to cool down the battery from 17ºC to 13ºC.

TABLE 5.2 and TABLE 5.3 show the results for different current values applied to the Peltier module. Third column is the coefficient of performance (*COP*), and is an efficiency ratio of the cooling/heating effect produced divided by the input energy. Last

column value in both tables is the maximum coefficient of performance that any refrigeration and heat pump cycles can have while operating.

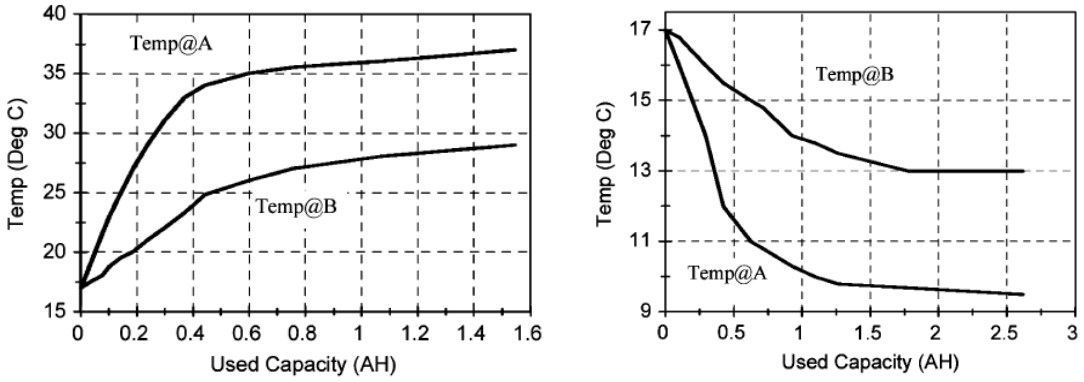

Figure 5.26: a) Heating test results; b) Cooling test results [79]**.**

According to the *COP* value obtained during cooling tests, the efficiency of the Peltier module when cooling is almost the same for the current range applied in this work with an average value of 0.23. However, with these devices, lower temperatures than 10ºC are hardly reached.

TABLE 5.2 COOLING PERFORMANCE RESULTS

Input Current (A)	Maximum Temperature (ºC)	C.O.P	βmax
5	11	0.21	1.27
7	10	0.22	1.43
10	9.5	0.25	1.83

However, during the heating tests bad efficiencies are obtained when low currents are used to heat the battery module because high values of *COP* are obtained for 4A and 7A. However, with 10A this value is reduced until 0.3, an acceptable value. Comparing both tables, the conclusion is that cooling performance is more efficient than heating performance.

TABLE 5.3 HEATING PERFORMANCE RESULTS

Input Current (A)	Maximum Temperature (ºC)	C.O.P	γmax
4	37	1.036	1.85
7	44	0.6	1.63
10	52	0.3	1.48

The same author in [80] implements a BTMS for a 60Ah battery pack for electric vehicles to limit the temperature rise of the battery pack under a 3C current demand. The battery pack without BTMS is heated until 58ºC; this value is reduced to 47ºC with the BTMS based on Peltier modules. However, the author mentions that the weight of the overall system is increased a 64.4% and its volume is increased a 152.88% due to the heatsinks included. Special effort must be done in this sense to improve heatsinks for this application.

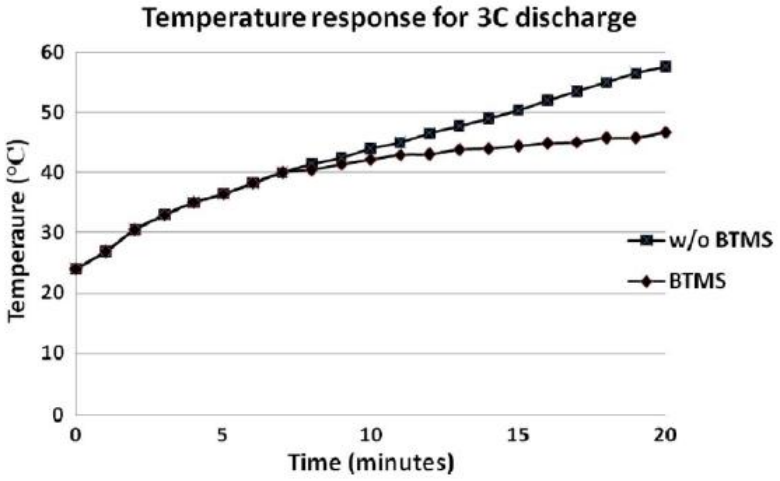

Figure 5.27: Temperature response for a 3C constant current discharge test [80]**.**

5.2.3.5 Heat pipes

Some authors are researching the efficiency of including heat pipes into the cooling systems for lithium ion batteries [81], [82]. Tran et al. in [81] compare a cooling system based on a heatsink with the same cooling system but including a heat pipe to enhance its behaviour. They want to include this new cooling system to cool down a cylindrical module for HEV application.

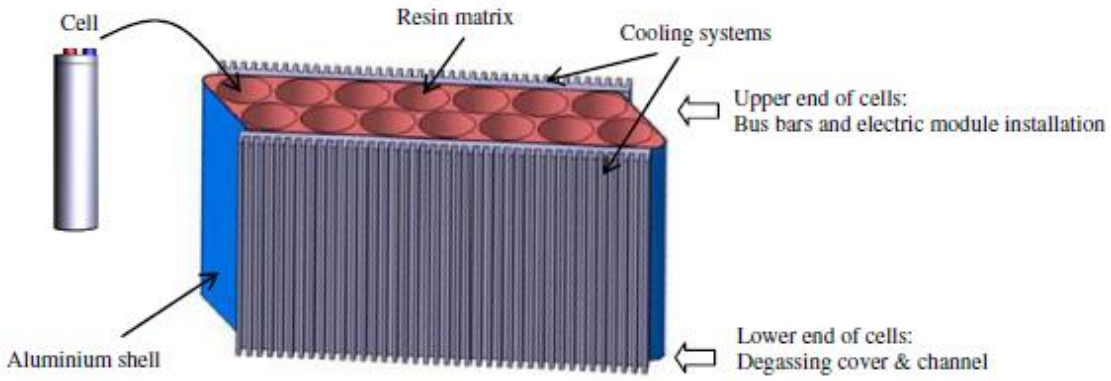

Figure 5.28: Cylindrical cell module for *HEV* application [81]**.**

After applying a power profile to the battery module the average power generated by the module was calculated to be over 100W but with peaks reaching values over 1100W. Instead of using directly the battery module to test the cooling system, a flat heater was used to reproduce the average heat flux and an induction heating machine was employed to generate the transient heat flux. Figure 5.29 shows the schematic of the heat pipe utilized during the experimental tests in this work. Figure 5.30 shows the schematic of the cooling systems tested under induction heating coil.

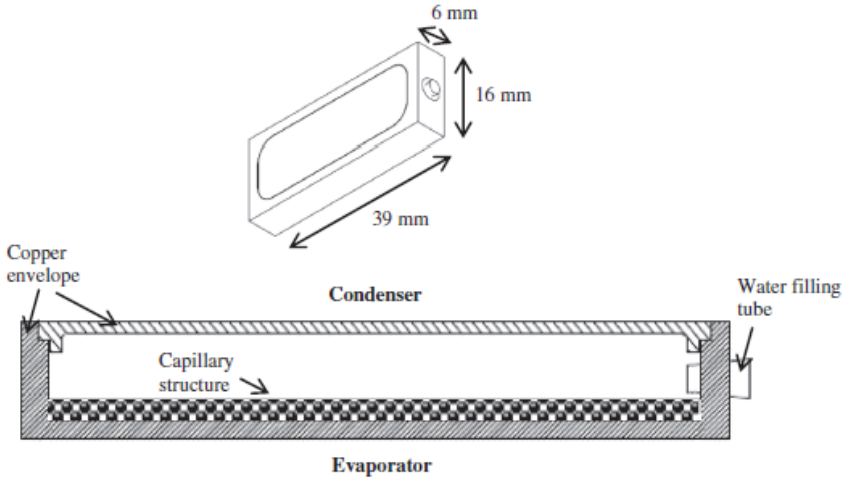

Figure 5.29: Schematic of the experimental heat pipe utilized [81].

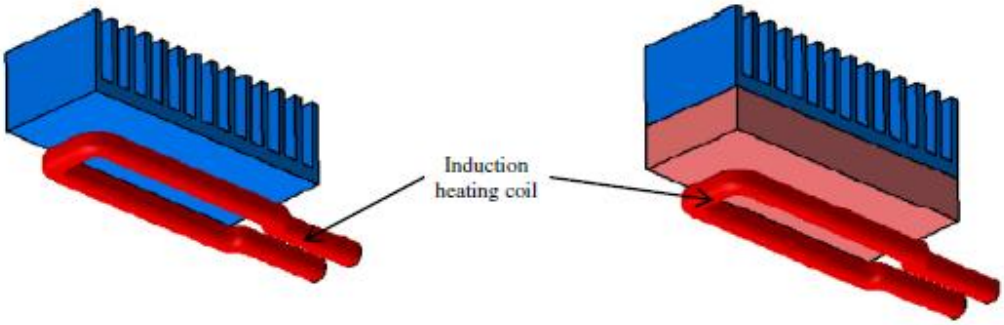

Figure 5.30:Schematic of the cooling systems under induction heating coil. [81]

Figure 5.31 shows the results obtained from the experimental tests for different cooling conditions; under natural convection and 0.2m/s forced convection heat pipe reduces the maximum temperature of the module, however when this flow is increased, it has no influence on its behaviour as it can be seen for the cases with a flow higher to 0.2m/s.

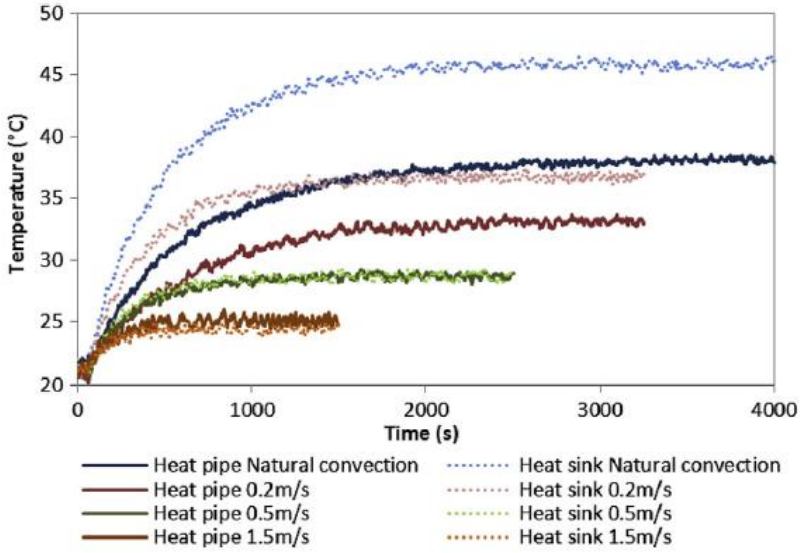

Figure 5.31: Comparison between heatsink and heatsink plus heat pipe under different cooling conditions [81].

5.2.4 Conclusions of the state of the art

According to the bibliography analyzed the most used thermal management systems are based on forced air cooling, liquid cooling and phase change materials. Thermo electrical modules based on Peltier effect heat pumps and heat pipes are less used for this kind of application so are discarded in this work. Cooling systems based on *PCM* materials are efficient depending on the amount of heat to evacuate from the battery module or pack because they are not able to absorb infinite energy. In this sense, it is considered that active cooling systems, liquid and forced air cooling are more adequate for power applications. Figure 5.32 presents the advantages and disadvantages of these cooling strategies; forced air cooling is cheaper and does not need maintenance. Besides it requires less components, it is lighter and it is easier to assemble. Liquid cooling instead reaches higher heat transfer coefficients and better temperature distributions in packs. Moreover, the volume utilized by the cooling system is less in this case without taking into account the heat exchanger, it makes less noise around the battery pack and it can be integrated with a heater or a chiller.

	Air	Liquid
Heat transfer	-	+
Temperature distribution in pack	-	+
Costs	+	-
Maintenance	+	-
Volume	-	+
Weight	+	-
Noise	-	+
Integration with heater and chiller	-	+
Modularity / Flexibility	-	+
Components	• Fan • Flow guiding parts • Filter	• Pump • Flow guiding parts • Compensating reservoir • Heat exchanger • Fan

Figure 5.32: Advantages and disadvantages of forced air cooling vs. liquid cooling [55]**.**

In this work forced air cooling systems will be used to design the cooling systems for the battery modules. The main reason is the simplicity of the system against the liquid cooling. The main challenge is to be able to reach very good temperature distributions and to limit the peak temperature of the modules. Furthermore, the cost is considered an important advantage in these systems and the volume and noise are not considered important disadvantages since the aim of the work is not a product. In this work single battery modules are going to be designed so the modularity is not considered an important drawback.

During this chapter, three different li-ion battery formats will be analyzed; depending on the format of the cell the minimization of the temperature gradient will be done by improvements of the layout of the module, compensation of the internal heat generation of the cells within the module or improving the heat transfer coefficient with a forced air cooling system.

5.3 Prismatic cells module

During the following section an 8 cell prismatic battery module is going to be thermally analyzed; the objective is to minimize its temperature gradient before designing a cooling system in Chapter 6. The main unit in this module is a 6.5Ah Lishen $LiFePO_4$ prismatic power cell. TABLE 5.4 shows its main characteristics; its high discharge current makes it suitable for power applications.

TABLE 5.4 PRISMATIC CELL MAIN CHARACTERISTICS

Feature	Specification
Nominal capacity	6.5Ah
Charging end voltage	3.65V
Average working voltage	3.2V
AC impedance	1.5mΩ
Standard charge method	CC/CV
Current	0.5C
Voltage	3.65
End current	350mA
Maximum charge current	5C (Continuous) 10C (10seconds)
Maximum discharge current	25C (Continuous) 30C (10seconds)
Discharge end voltage	2V
Maximum operating temperature range	
Charge	0ºC-45ºC
Discharge	-20ºC-60ºC

Figure 5.33 shows the 6.5Ah Lishen prismatic power cell; the weight of the cell is 392 grams and its dimensions are 112x27x70 millimetres. The prismatic format of the cell permits a more compact battery module depending on the air gap between cells. The size of the module is considered a key factor in electro mobility since the available space in this kind of application is very limited. Hence, increasing the volumetric energy density is crucial to improve the quality of the battery module for these applications. Following, the thermal behaviour of an 8 cell battery module is analyzed depending on the air gap between cells; the target is to select the most suitable gap to reach a trade off between thermal behaviour and volumetric energy density.

Figure 5.33: 6.5Ah Lishen prismatic power cell.

5.3.1 Analysis of the air gap between cells in battery modules

The objective of this analysis is to test the effect of the air gap between cells in the temperature distribution of an 8 cell prismatic battery module. In order to reach this target, the same module will be tested under certain current profiles with an air gap of 5mm, another one of 1.5mm and without air gap including a thermal interface material (*TIM*). These modules will be tested under two different current profiles: a 60A constant current discharge from 100% *SOC* to 0% *SOC*, and an alternative charge/discharge cycle shown in Figure 5.36. Temperature distribution results are obtained from these experimental tests. Sixteen thermocouples are located in different points of the li-ion module, two per cell; Figure 5.34 shows these locations in the prismatic module.

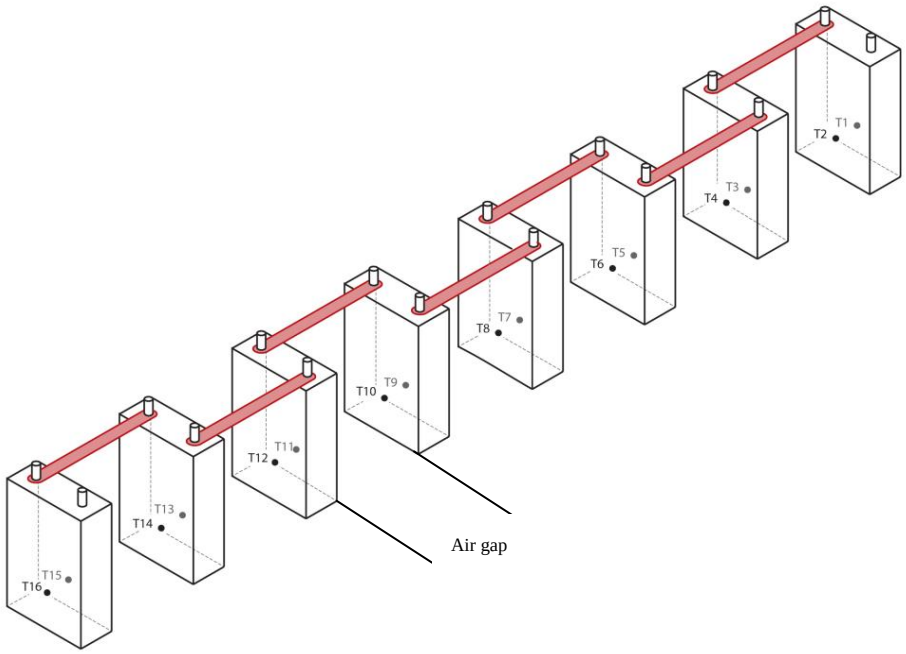

Figure 5.34: Location of the thermocouples measuring the prismatic module.

Figure 5.35 a shows the results for an air gap of 5mm during the 60A constant current discharge, it shows the temperature distribution during the whole test. Figure 5.35 b shows the distribution for the end of discharge instant for the three air gaps during this test. In this concrete instant, the maximum temperature gradient is 2.8ºC and the maximum temperature reached is about 40ºC for 5mm air gap; as the air gap is reduced the temperature gradient of the module is reduced as well; for the case of 1.5mm air gap the maximum temperature gradient during a 60A constant current discharge is reduced until 2.4ºC. However, the maximum temperature reached is similar, 40.8ºC. The main drawback of this layout is the increment of the static pressure if a forced air cooling system is included. In this case, for the same air velocity, higher static pressures have to be overtaken due to the reduction of the air channels; for the case without air gaps between cells, the maximum temperature gradient of the module is reduced comparing it with the previous two layouts. This gradient is 1.8ºC at the end of discharge instant because thermocouples *T1* and *T16* have a lower temperature since they are directly in contact with the ambient, otherwise it would be even smaller. Heat is also accumulated in the centre of the module. In this case there is no option to include directly a forced air cooling system because of the absence of cooling channels.

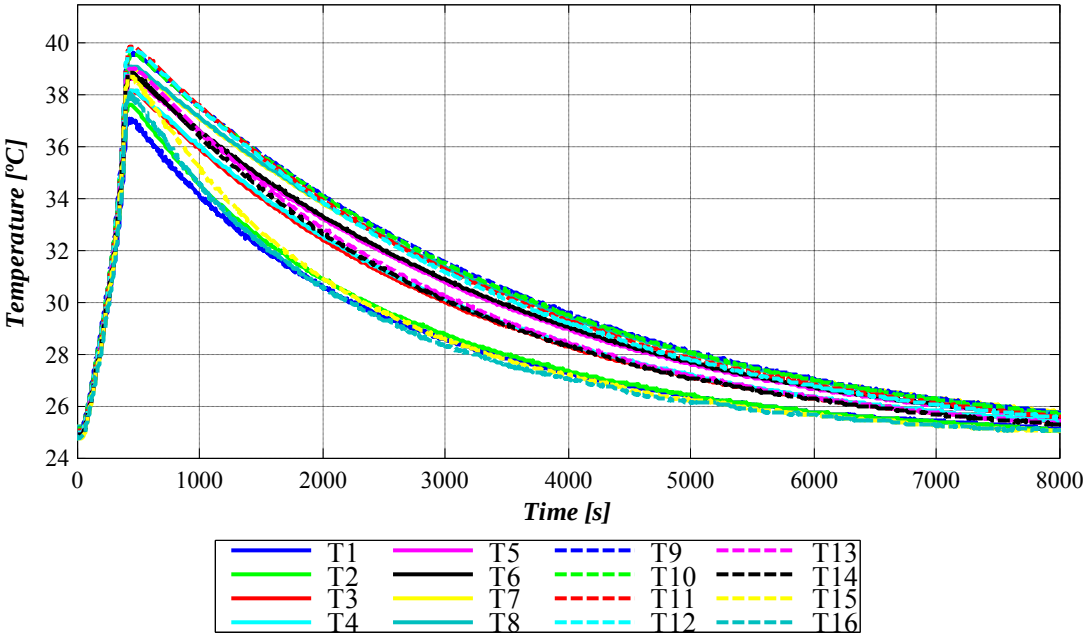

a)

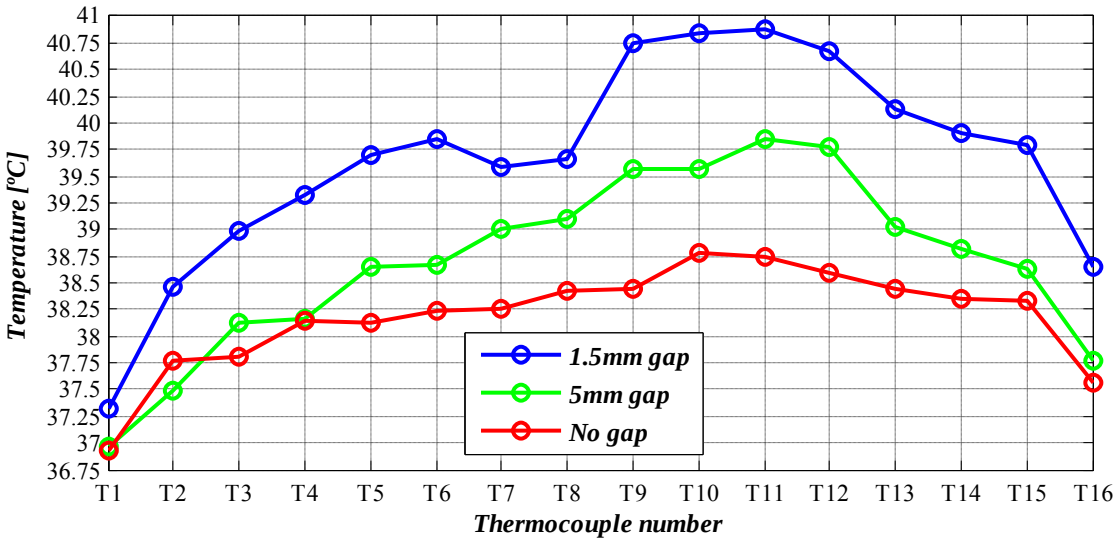

b)

Figure 5.35: 60A complete discharge results for the prismatic module; a) Surface temperatures during the test for a 5mm air gap module; b) Temperature distribution at the end of discharge moment for the three modules.

Following results for the alternative charge/discharge cycle are presented; Figure 5.36 shows the current applied to the cell during the alternative charge and discharge cycle. A peak current of 60A during discharge and a peak current of 15A during charge are applied. Figure 5.37 a shows the results for the module without air gap during the whole test; Figure 5.37 b instead shows a comparison between the three air gaps for this kind of test at the instant before cutting the current. The module without air gap reaches a maximum temperature of 40ºC with a maximum temperature gradient of 3ºC; 39.9ºC of maximum temperature and a gradient of 5.3ºC are measured for the module with 5mm

air gap. Finally with an air gap of 1.5mm, the maximum temperature reached by the module is 38.25ºC with a maximum temperature gradient of 4ºC.

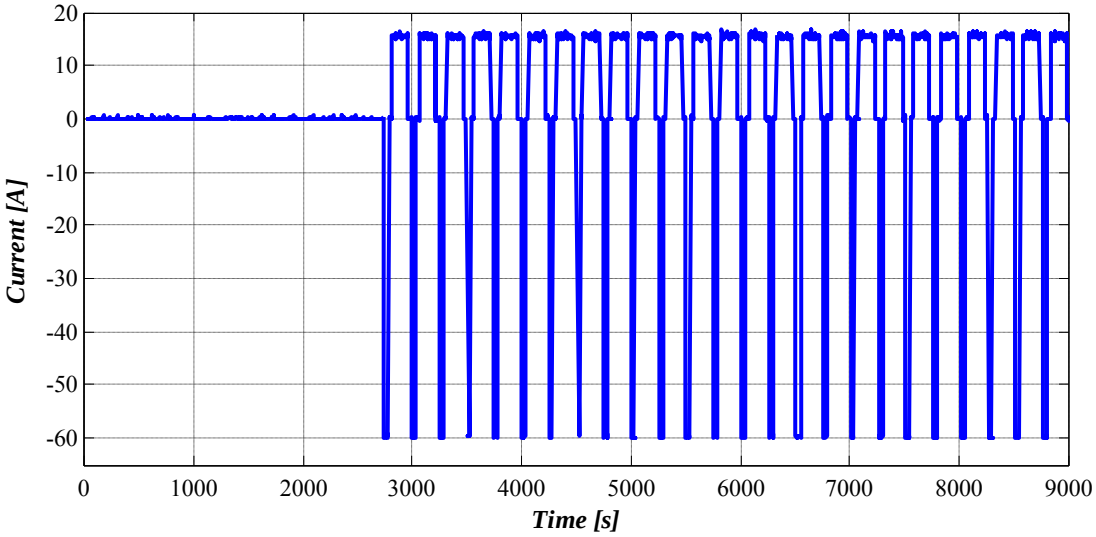

Figure 5.36: Applied alternative charge/discharge cycle.

One of the main targets of the methodology presented in this work is to reduce the maximum temperature gradient before designing the battery thermal management system taking advantage of alternative strategies. Hence, for this concrete module, a layout without air gaps was considered according to the results presented before to reach this objective. A thermal interface material is used to avoid air bubbles between cells due to irregularities on the surfaces of the cells. This material has a thermal conductivity of 2.5 W/mK and improves the energy transfer between cells to reduce the temperature mismatch.

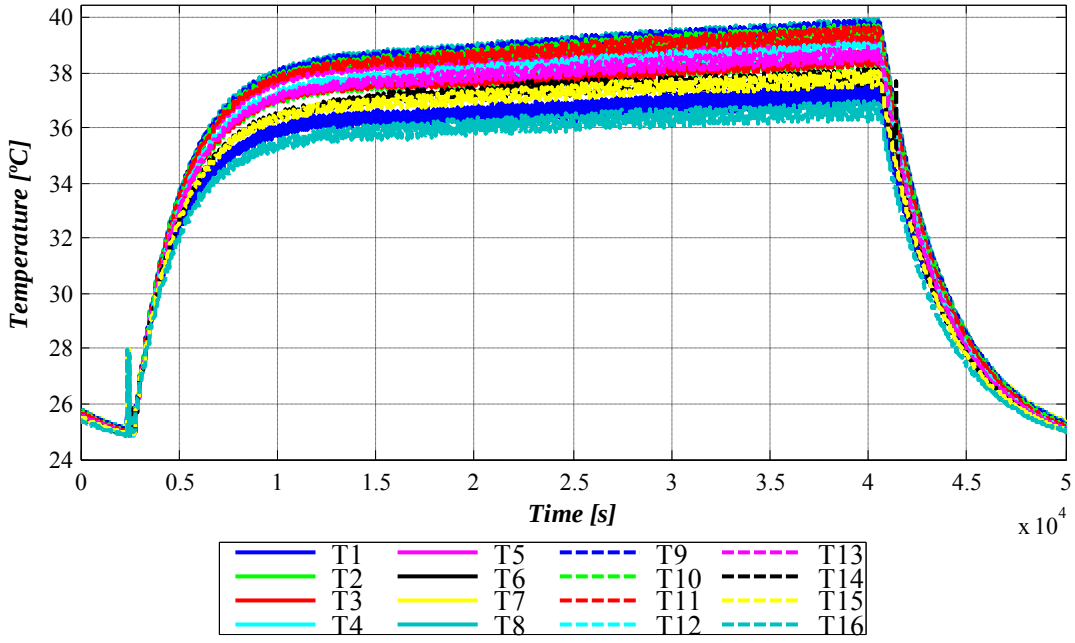

a)

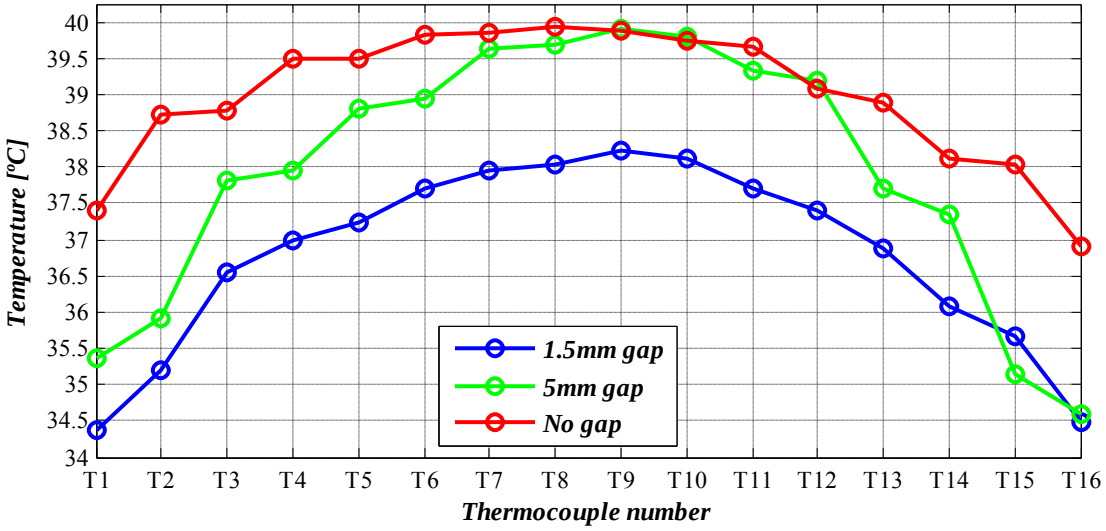

b)

Figure 5.37: Alternative charge and discharge cycle results for the prismatic module; a) Surface temperatures during the test for the module without air gap; b) Temperature distribution for the three modules at the instant before cutting the application current.

All these results are summarized in TABLE 5.5 to show the improvement in the thermal behaviour when the air gaps are removed for this concrete battery module. However, it is not possible to reduce the air gap for any battery module due to mechanical restrictions of the thermal management system or even because of the shape and size of the cells used to assemble the module.

TABLE 5.5 SUMMARY OF THE RESULTS PRESENTED

Air gap	60 A complete discharge test		Variable charge/discharge test	
	ΔT_{max} [ºC]	T_{max} [ºC]	ΔT_{max} [ºC]	T_{max} [ºC]
1.5mm	2.4	40.8	4	38.25
5mm	2.8	39.8	5.3	39.9
No gap	1.8	38.75	3	40

5.3.2 Convective heat transfer coefficient compensation

Another improvement in the layout of the prismatic module is to reduce the convective heat transfer coefficient of the first and last cells of the module. These cells have a bigger surface in touch with the ambient and the heat flux transferred by convection is higher than in the other cells. The effect of this mismatch in the heat transfer coefficients can be clearly seen in the results presented previously in 5.3.1; *T1* and *T16* always measure lower temperatures than the other thermocouples increasing the value of the maximum temperature gradient of the module.

The proposed solution is to thermally insulate the surfaces where these thermocouples are located to improve the temperature distribution. If these surfaces are thermally insulated, all the cells have the same convective heat transfer coefficient and the maximum temperature gradient will be reduced.

Figure 5.38: Lishen module layout with *TIM* between cells and thermal insulator materials to match convective heat transfer coefficients.

Figure 5.38 shows the final assembly of the module. Figure 5.39 shows a comparison between the same module with and without the thermal insulation materials to compensate the convective heat transfer coefficient. When this material is included into the module temperatures *T1* and *T16* increase their value for the same current profile demand and the maximum temperature gradient is reduced improving the overall thermal behaviour of the module.

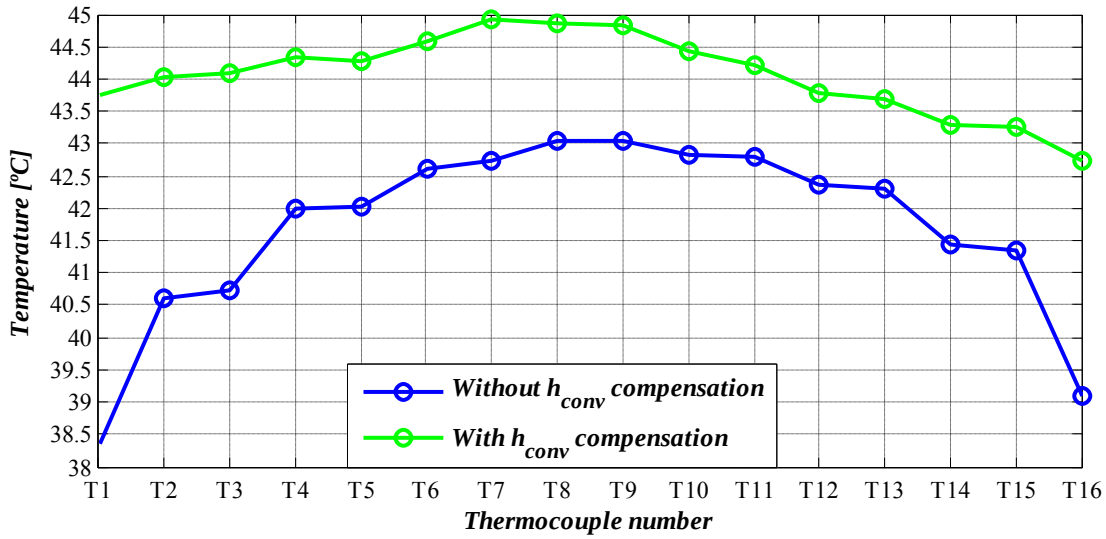

Figure 5.39: Comparison of temperature distributions for the module without air gaps and the alternative charge/discharge cycle without and with convective heat transfer coefficient compensation.

Without the compensation of the heat transfer coefficient the maximum temperature gradient for a concrete instant is 4.75ºC, and with this compensation this value is reduced to 2.25ºC. The reduction of the overall module surface in contact with air leads to a higher maximum temperature of the module from 43ºC to almost 45ºC. However, it is considered that this increase can be compensated with a suitable cooling system without an important increase of its power consumption.

5.4 Cylindrical cells module

Following, a proposal to reduce the maximum temperature gradient in a li-ion cylindrical battery module is going to be presented. The cylindrical cell utilized in this work is an 8Ah LiFebatt $LiFePO_4$ power cell and its main characteristics are summarized in TABLE 5.6. The high discharge current capability of 25C makes it suitable for power applications as in the case of the prismatic cell.

TABLE 5.6 CYLINDRICAL CELL MAIN CHARACTERISTICS

Feature	Specification
Nominal capacity	8Ah
Charging end voltage	3.65V
Average working voltage	3.3V
AC impedance	2mΩ
Standard charge method	CC/CV
Current	0.5C
Voltage	3.65
End current	400mA
Maximum charge current	4C (Continuous)
Maximum discharge current	25C (Continuous)
Discharge end voltage	2V
Maximum operating temperature range	
Charge	0ºC-45ºC
Discharge	-20ºC-60ºC

Figure 5.40 is showing the cylindrical cell utilized in this work; the weight of this cell is 290 gr. and the dimensions of the cell are 38mm diameter and 123mm height. Cylindrical cells are usually mounted between some specific holders depending on their size. In this case the layout of the module is limited to an assembly with these holders although it is possible to design your own structure. When the 8 cell module is assembled with the holders some air gaps of 1mm between cells are impossible to avoid; these air flow channels give the possibility to implement a cooling system directly blowing the cells of the module.

Figure 5.40: LiFebatt cylindrical power cell.

Depending on the layout of the module, temperature distribution is less influenced by the layout and more influenced by the mismatch between the internal heat generations of the cells of the module. In the prismatic module without air gaps presented before, heat is usually accumulated in the middle of the module, so the distribution is mainly affected by the layout (Figure 5.41 a). However, in the cylindrical module analyzed in this paragraph, temperature distribution is mainly affected by the internal heat generation mismatch (Figure 5.41 b).

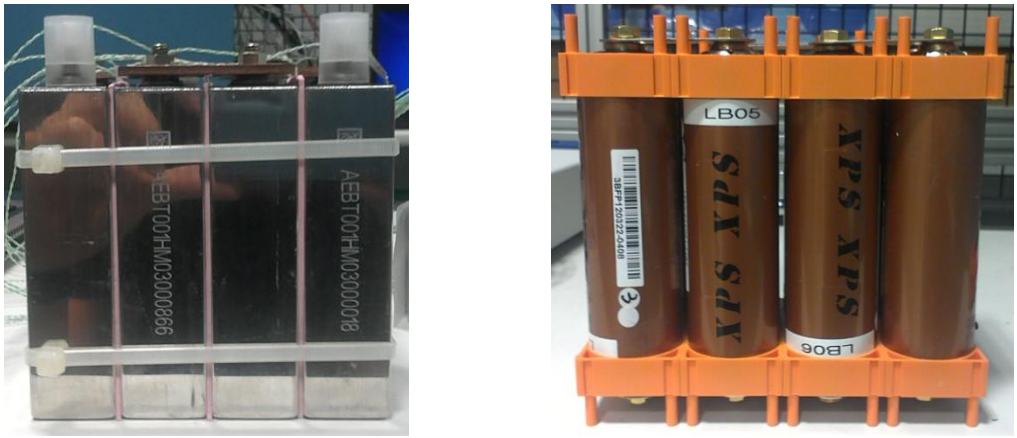

a) **b)**

Figure 5.41: Examples of different modules; a) Prismatic mini-module; b) Cylindrical module.

There are two main reasons to have internal heat generation mismatches between cells: first one is differences between parameters of the cells like internal impedance, nominal capacity or state of charge; second one is the mismatch between aging processes of the cells. This second effect will be reduced if the maximum temperature gradient is minimized. The small differences in capacity and impedance for different state of charges (*SOC*) lead to different heat generation rates in each cell; this effect is better seen when deep discharges are reached because of the faster increase of the internal impedance when these *SOC* ranges are reached. Hence, the results for this module will be for 1C and 2C constant current discharges. Before each discharge the module is charged with a C/20 current until all the cells of the module reach 3.65V taking advantage of a passive voltage balancing system to equalize the voltages. Thus, all the cells are considered to be charged to the 100% of their *SOC*. The locations of thermocouples to measure temperatures along the module are shown in Figure 5.42.

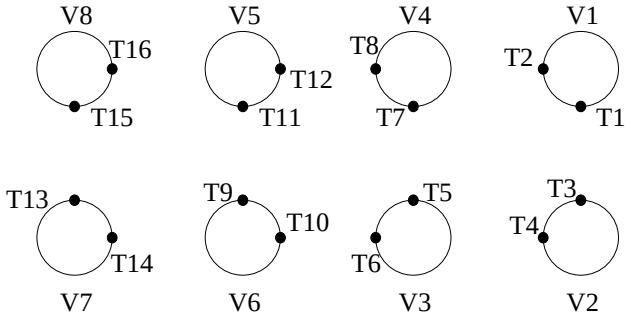

Figure 5.42: Location of the thermocouples in the cylindrical battery module.

Figure 5.43 shows a 1C constant current discharge for the cylindrical module; in this figure the dependency of the temperature distribution on the internal heat generation

mismatch can be analyzed. There is a correlation between temperature and voltage distributions; highest temperatures during the tests are measuring cells with lower voltages. In Figure 5.43 a, thermocouples *T7* and *T8* are the highest ones, and *T9* and *T10* are following them. These thermocouples correspond to *V4* and *V6* respectively, the lowest values according to voltage distribution results.

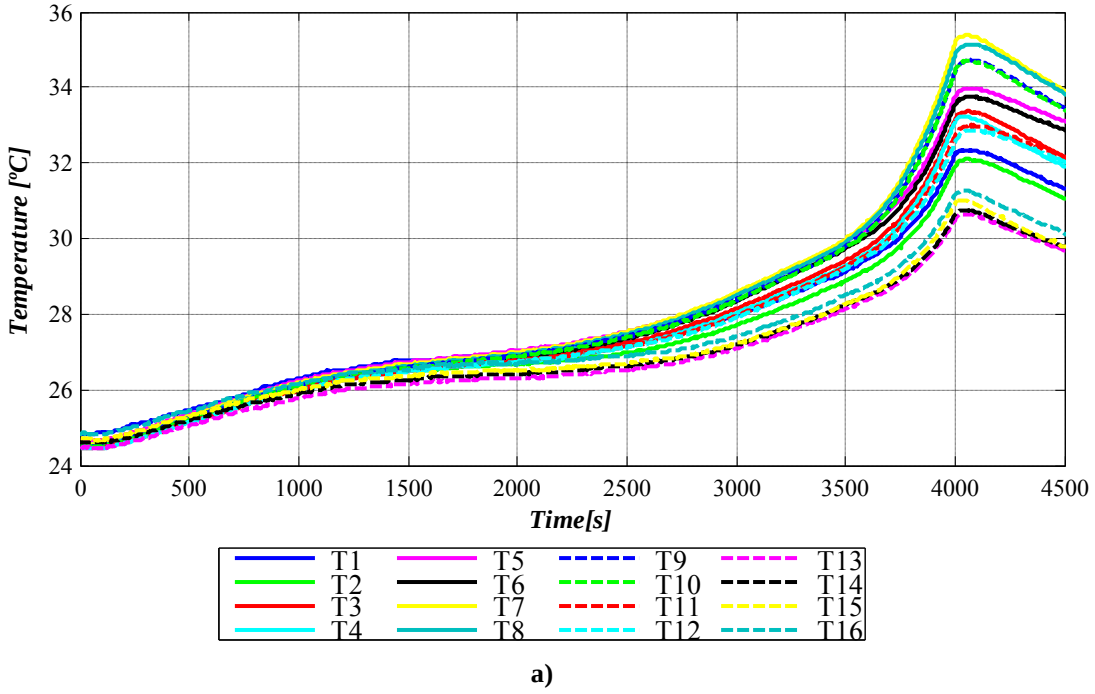

a)

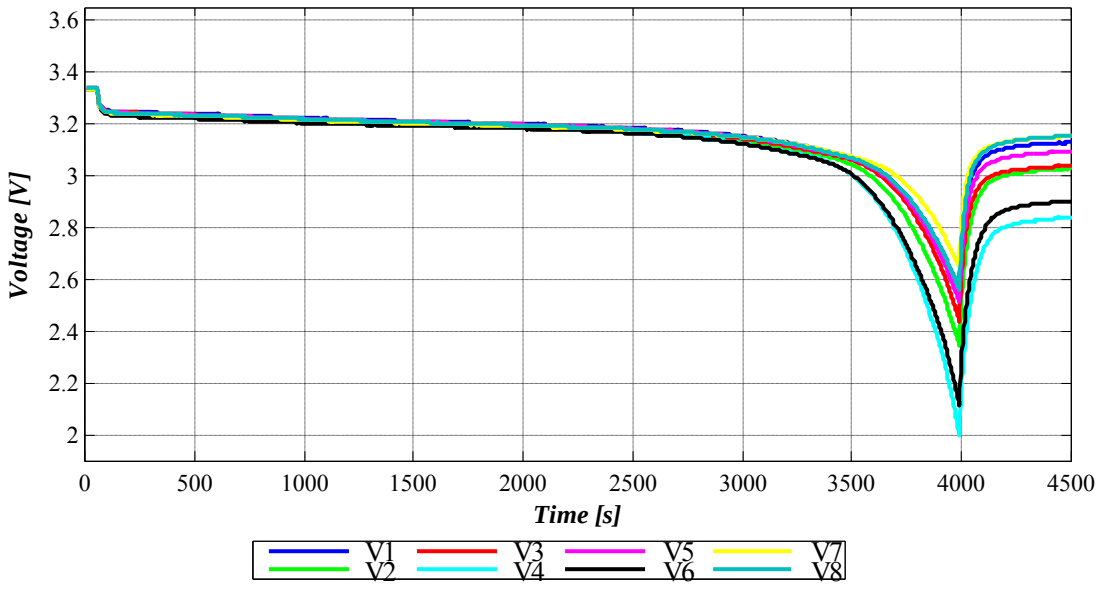

b)

Figure 5.43: Constant current 1C discharge test for the cylindrical battery module; a) Temperature distribution; b) Voltage distribution.

On the other hand, *T13* and *T14* measure the lowest temperature values during the test and *V7* is the voltage with the highest value in the voltage distribution figure. Cells with lower voltage values reach lower values of SOC and consequently higher internal impedances values. These higher internal impedances provoke temperature mismatch in

the battery module. Besides, the maximum temperature gradient obtained is 4.8ºC, and it is compulsory to reduce this value as much as possible.

The main target of the following experimental tests is to propose a solution to improve the internal heat generation mismatch for a cylindrical battery module. In order to reach this target, different voltage balancing systems will be analyzed under 1C and 2C discharge rates in the aforementioned module; these experimental tests are summarized in TABLE 5.7. Three different voltage balancing systems will be analyzed; low current passive balancing, high current passive balancing, and an active inductive voltage balancing. Voltage balancing systems are always included into the design of a battery module or pack; the proposal is to minimize the mismatch between the *SOC* values of the cells within the module taking advantage of the voltage balancing systems and as a consequence reduce the mismatch between internal impedances of the cells within the module. Reducing this mismatch will lead to the minimization of the temperature gradient of the battery module due to a compensation of the internal heat generation of the cells.

TABLE 5.7 SUMMARY OF THE EXPERIMENTAL RESULTS CONDUCTED

	Rate	
Without balancing	1C	2C
Low current passive balancing	1C	2C
High current passive balancing	1C	2C
Active balancing	1C	2C

In these experimental tests the evaluated variables are the temperature distribution of the module and the energy delivered by the module because including the balancing system can lead to a loss of available energy.

5.4.1 Analysis of the different voltage balancing systems utilized

The strategy used with all the voltage balancing systems follows equation (5.1).A threshold value is defined to fix the value when the voltage balancing is going to start working. V_{lim} is the voltage limit, V_{low} is the lowest voltage of one of the cells of the module and $V_{threshold}$ is a user defined value, 5 mV during these experimental tests.

$$V_{lim} = V_{low} + V_{threshold} \quad \textbf{(5.1)}$$

5.4.1.1 Passive voltage balancing 1 (PB1)

The passive voltage balancing system consists of an electronic switch and a 12 ohm resistor in parallel with each cell working independently.

$$I_{bal} = \frac{V}{R_{bal}} \quad \textbf{(5.2)}$$

When one of the voltages in the module is higher than the lowest one, the electronic switch is closed and the current I_{Bal} is discharged during a fixed period to do the balancing. The value of this current depends on the actual voltage of the cell and the fixed value of the resistor, (5.2).

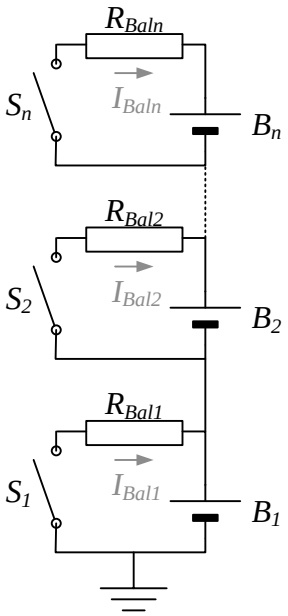

Figure 5.44: Passive voltage balancing system schematic.

5.4.1.2 Passive voltage balancing 2 (PB2)

The second balancing system is equal to the previous one but with a lower fixed resistor value to increment the value of the balancing current I_{Bal}. In this case, the value of the resistor is 3.8 ohm.

5.4.1.3 Active voltage balancing (AB)

The active balancing system consists of a Sepic based multistacked converter [83]. When the switch *S1* is on the inductors are charged from all the cells and when the switch *S1* is off the energy is released. In the single switch balancing system the energy is released to the lowest voltage cell. This natural behaviour of the converter permits to balance the voltages with a fixed duty cycle of the switch *S1* with an open loop control. The active voltage balancing topology used can be seen in Figure 5.45.

5.4.2 Results and discussion

Results show better temperature distributions when the voltages of the cells within the module are more balanced for passive balancing systems. When active voltage balancing systems are used temperature distribution is improved because of the compensation of the power losses although voltage mismatch is similar to the case without voltage balancing.

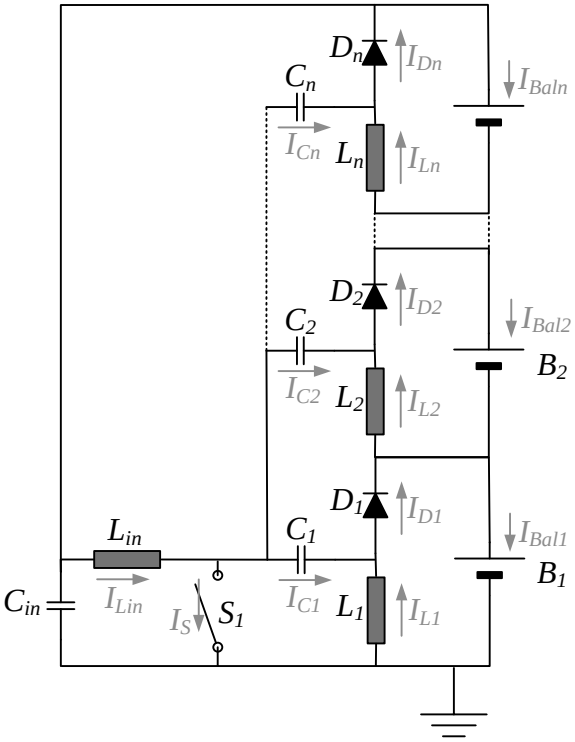

Figure 5.45: Active balancing system schematic.

5.4.2.1 Passive voltage balancing results analysis

PB1 and *PB2* voltage balancing systems improve the voltage distribution when the end of discharge is reached; as a consequence, temperature distribution is also improved. For 1C discharge rate, the $(\Delta V)_{max}$ without voltage balancing is 0.64 V; *PB1* reduces this value to 0.414 V and with *PB2*, this value is reduced until 0.21 V. According to temperature distribution, when no voltage balancing system is used $(\Delta T)_{max}$ is about 4.75 ºC; for *PB1* this value is reduced to 3.22 ºC and with *PB2* the maximum improvement is obtained with 2.17 ºC. Figure 5.46 shows the results for 1C rate and *PB2* voltage balancing. *PB2* gets better results since it has higher current capability, but also higher power losses.

For 2C rate, results are similar since *PB2* is the system with better results; however, as the current rate is increased, the effect of *PB1* and *PB2* in the temperature distribution is less important. Besides, with this rate the end of discharge is reached faster and the balancing system works during a shorter period of time. Without voltage balancing the $(\Delta V)_{max}$ is 0.462 V and the $(\Delta T)_{max}$ is 5.1 ºC; *PB1* obtains intermediate results although it also improves the temperature distribution of the module, with a $(\Delta V)_{max}$ of 0.33 V and a $(\Delta T)_{max}$ of 4.31 ºC. With *PB2* these values are reduced to 0.114 V and 2.78 ºC respectively.

However, passive balancing systems reduce the battery module available energy to balance the voltage; this is the main drawback of this kind of balancing systems. In order to measure the impact of this problem, the evaluated parameter is the energy delivered by the module during each discharge (*E*).

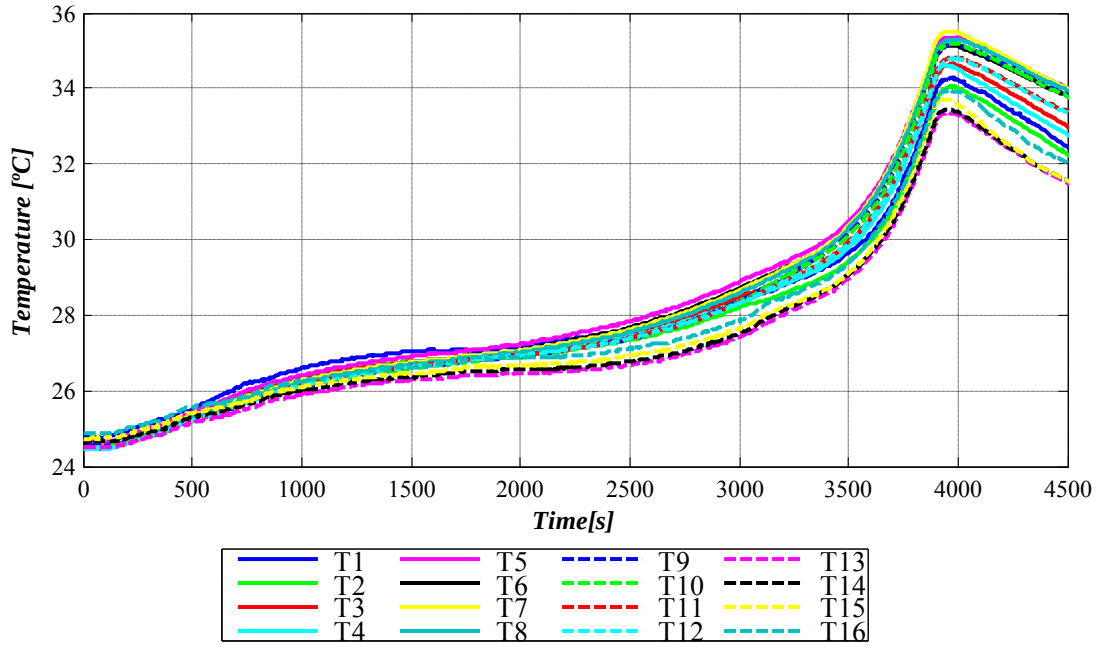

a)

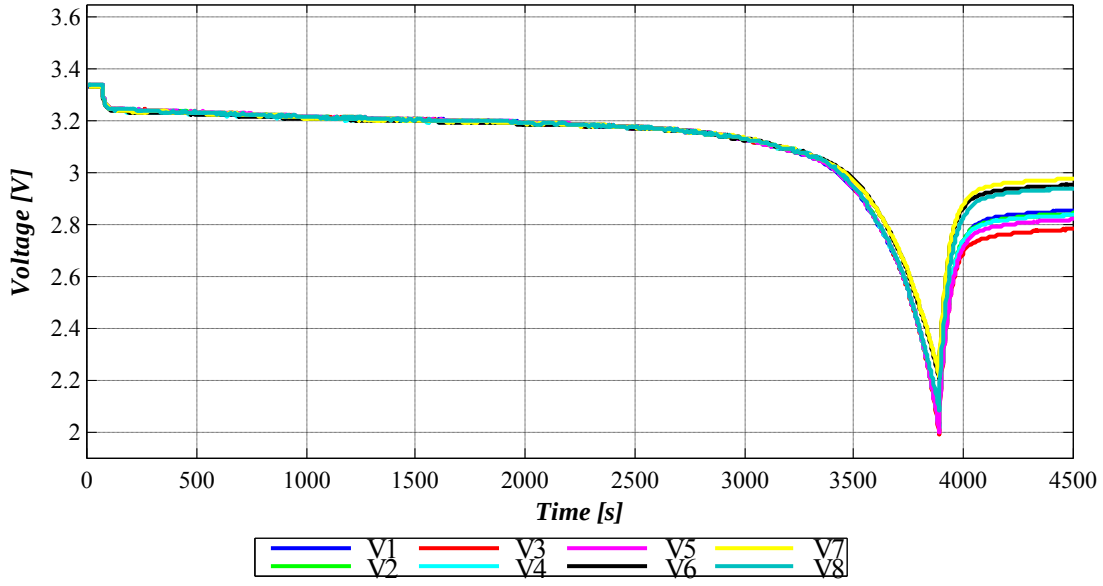

b)

Figure 5.46: Results for passive balancing 2 (*PB2*) during a 1C complete discharge; a) Temperature distribution; b) Voltage distribution.

In the case without voltage balancing system, the energy delivered by the module (*E*) for 1C discharge rate is 8.88 Ah; for *PB1* this energy is reduced to 8.664 Ah, and for *PB2*, *E* is reduced until 8.447 Ah due to its higher current capability. For 2C rates, without voltage balancing the energy delivered is 9 Ah; for *PB1* this value is again reduced to 8.797 Ah, and for *PB2* is again reduced until 8.694 Ah. In applications without grid connection where the available energy is the most important parameter for the user, this loss of energy can be important. The increase of the energy delivered from 1C rate to 2C rate is considered to be an effect of the improvement of the efficiency due to the higher working temperature for the 2C rate scenario.

5.4.2.2 Active voltage balancing results analysis

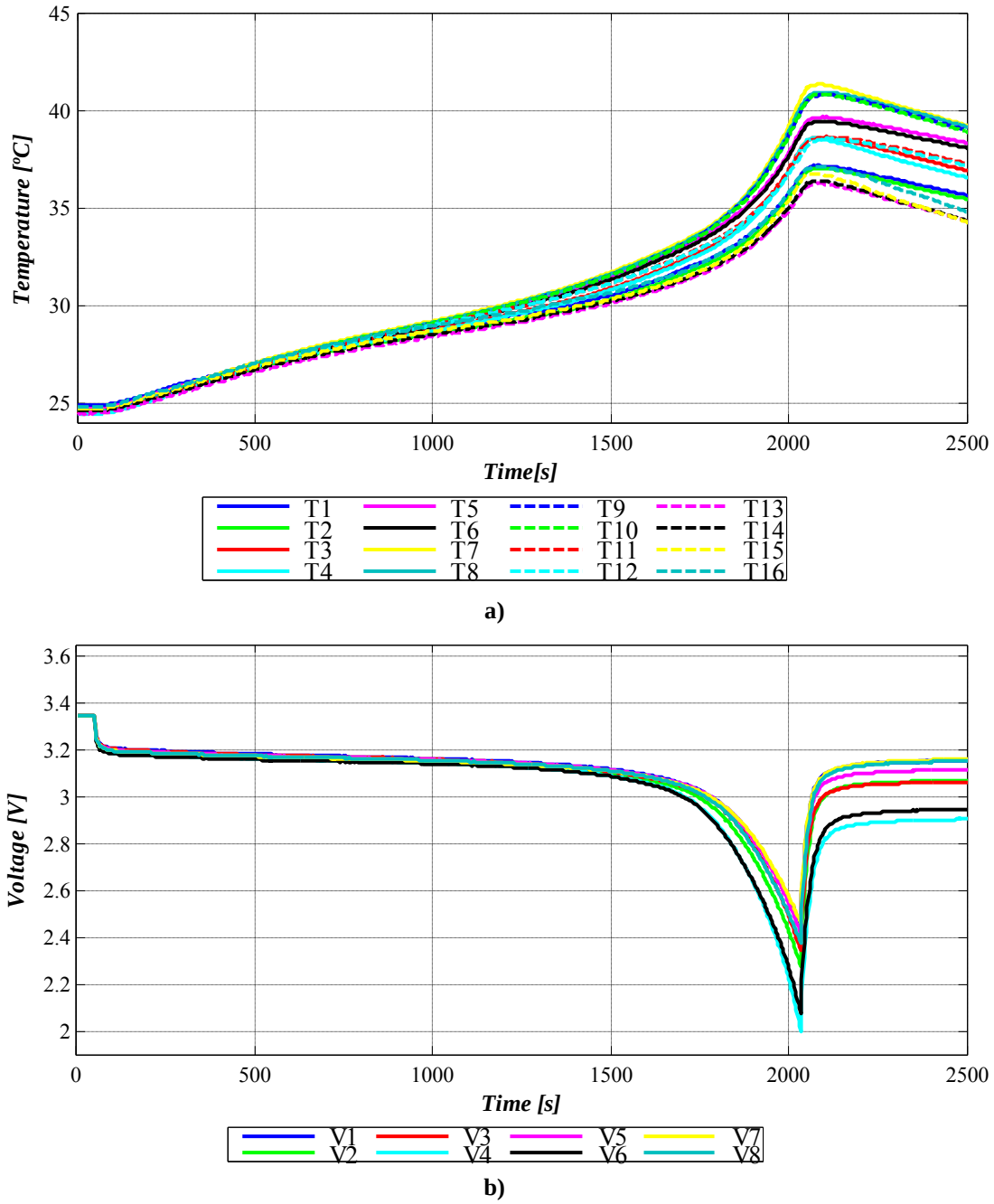

Figure 5.47: Results for a 2C discharge rate without voltage balancing; a) Temperature distribution; b) Voltage distribution.

In order to improve this parameter the active voltage balancing is proposed; in this voltage balancing system the energy is transferred from the cell with more remaining energy to the weakest cell to balance its voltage. Obviously, there are power losses for this system, but if the current managed is high enough, the discharge process will be longer, improving the amount of energy delivered by the battery module.

Figure 5.48 shows the results of voltage and temperature distribution with 2C discharge rate and with *AB* system. For this voltage balancing system, in the scenario of 1C discharge rate, $(\Delta V)_{max}$ is 0.6 V and the $(\Delta T)_{max}$ is about 3.2 ºC. However, the energy delivered by the module is higher than in the other cases, 9.06 Ah, concretely. For the 2C discharge rate, the $(\Delta V)_{max}$ is 0.58 V and the $(\Delta T)_{max}$ is about 3ºC. In this case, there is no improvement in the energy delivered comparing it with the case without balancing.

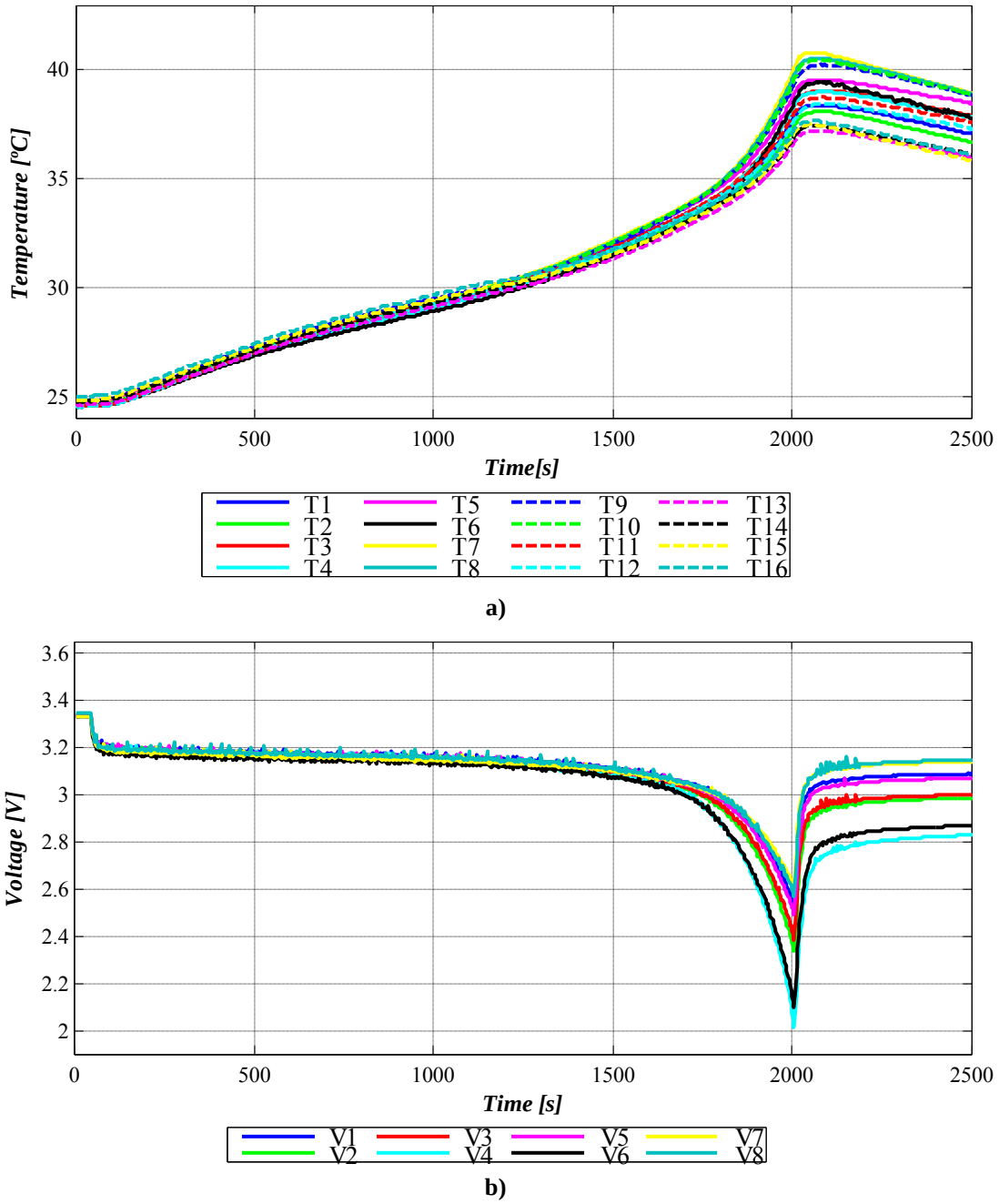

Figure 5.48: Results for active balancing (*AB*) during a 2C complete discharge; a) Temperature distribution; b) Voltage distribution.

In this balancing system the balancing current depends on the voltage differences between cells and the inductors; at the beginning of the discharge the differences are

quite low and also the energy transferred between cells. When low *SOC* values are being reached, the voltage differences are higher and the balancing currents increases; however, for 2C discharge rate the end of discharge is reached in a short period of time, thus, the *AB* is not able to improve the delivered energy for this rate.

5.4.2.3 Comparison between passive and active balancing

TABLE 5.8 shows the results obtained for the experimental tests presented in this section; results show a reduction of the temperature gradient when voltage balancing systems are included for both discharge rates. For 1C rate the maximum reduction reached is around 54% and is obtained with *PB2*. However, this voltage balancing reduces the module available energy in a 4.87%. With the *AB*, the temperature gradient is improved in a 33% but the available energy is improved in a 2%. Similar results are obtained for a 2C discharge rate. *PB2* improves the temperature gradient of the module in a 45.5% but reduces the available energy a 3.4%. *AB* instead, reduces the temperature gradient a 41%, but is able to keep the same available energy as in the case without voltage balancing.

TABLE 5.8: SUMMARY OF THE RESULTS.

Balancing system	1C complete discharge			2C complete discharge		
	ΔT_{max} [ºC]	T_{max} [ºC]	E [Ah]	ΔT_{max} [ºC]	T_{max} [ºC]	E [Ah]
No Balancing	4.75	35.2	8.88	5.1	41.3	9
PB1	3.22	35.3	8.664	4.31	41.6	8.797
PB2	2.17	35.5	8.447	2.78	42	8.694
AB	3.2	35.4	9.06	3	40.8	8.99

Both passive and active balancing systems try to reduce the differences between internal heat generations between cells. Passive balancing systems discharge energy from the cells with higher *SOC* trying to bring these cells to the *SOC* of the weakest cell. The consequence is that the internal heat generation of all the cells is more uniform but also higher because the *SOC* is lower and the internal resistance of all the cells increases.

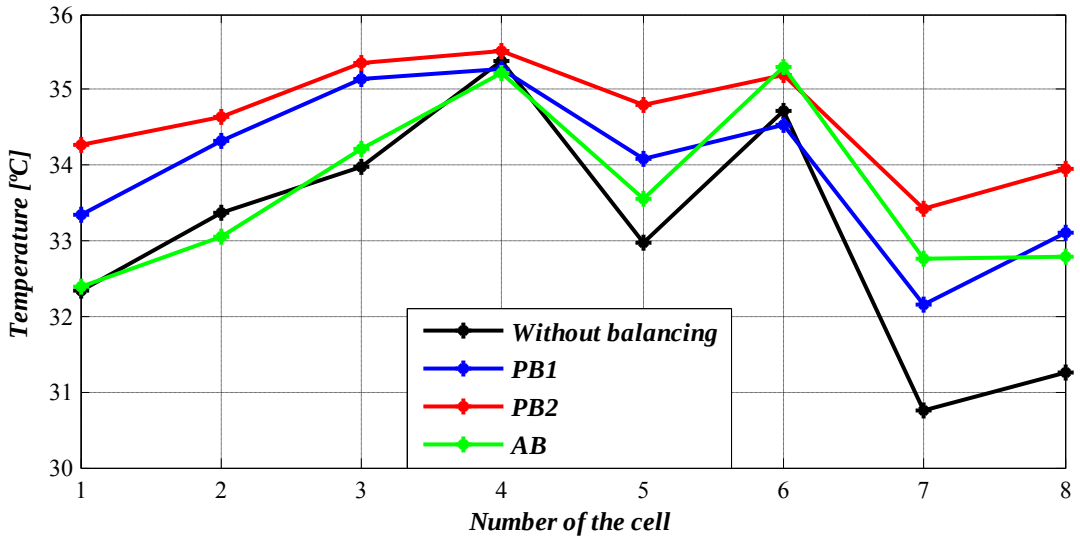

a)

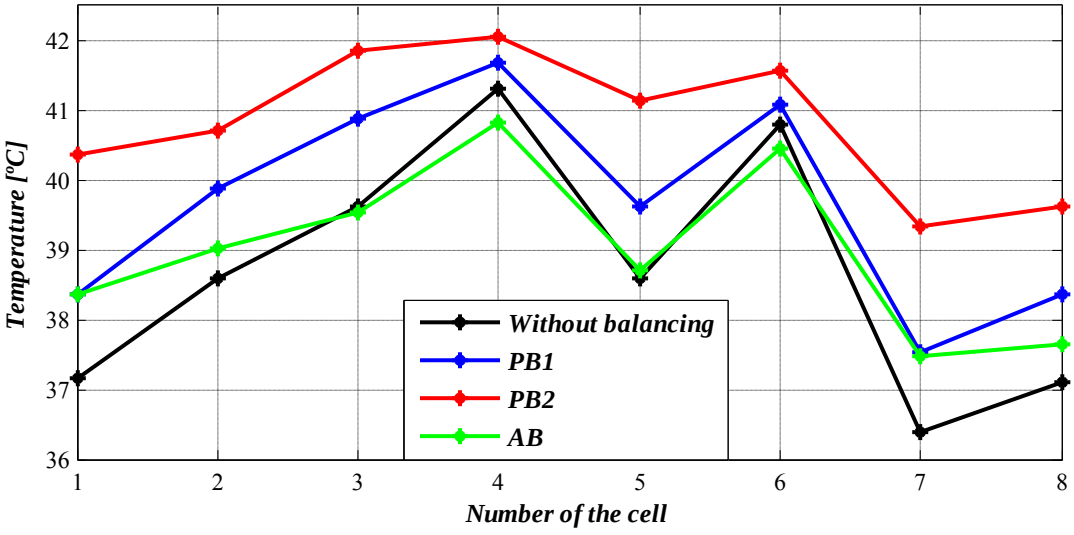

b)

Figure 5.49: Temperature distribution for the end of discharge moment with different voltage balancing; a) 1C current rate; b) 2C current rate.

Figure 5.50 a shows a practical example of passive balancing system used in this work; the upper cell is the most charged one so its balancing current is the highest one, 1A in the example. This cell has to deliver the current demanded by the application 16A and the current demanded by the voltage balancing system, 1A. Another cell can be at a lower *SOC*, thus, with a lower terminal voltage, and its balancing current will be lower. The down cell in Figure 5.50 a is the cell with the lowest *SOC* and its balancing current is 0A. If the power losses of each cell are approximated by (5.3), the consequences are higher internal heat generation in upper cell, hence, surface temperature increase, and a greater reduction of the *SOC*, leading to an increase of its internal impedance.

Active balancing systems try to increase the *SOC* of the weakest cell transmitting energy from the cells with higher *SOC*. Figure 5.50 b shows a practical example of this balancing system. Imagine a 16A constant current discharge application; the upper cell, the most charged one, has to deliver 17A because the balancing system is demanding 1A. Another cell is less charged and only delivers 16.5A; the improvement of the active voltage balancing is that return this energy to the weakest cell. The consequence is that the weakest cell delivers only 14.5A, reducing its internal heat generation even if its internal impedance is higher due to the lowest *SOC*. Besides the upper cell generates more losses and increases its surface temperature, reducing the maximum temperature gradient.

$$Q = R_{int}\,(I_{cell})^2 \tag{5.3}$$

The difference between these strategies is clearly seen in Figure 5.49 b. With *PB2* the power losses of the battery module are increased and a higher maximum temperature is reached. However the temperature distribution is more uniform because the internal heat generation mismatch is compensated. *AB* instead reduces the heat generated by the weakest cell and increases the other heat generations. Thus, the maximum temperature of the module is reduced and also the temperature distribution. Closer results to *PB2* can be reached with *AB* if the inductors of the system are bigger to store more energy with

lower voltage differences. Besides, the available energy with *AB* is similar to the case without balancing but *PB* reduces the available energy significantly.

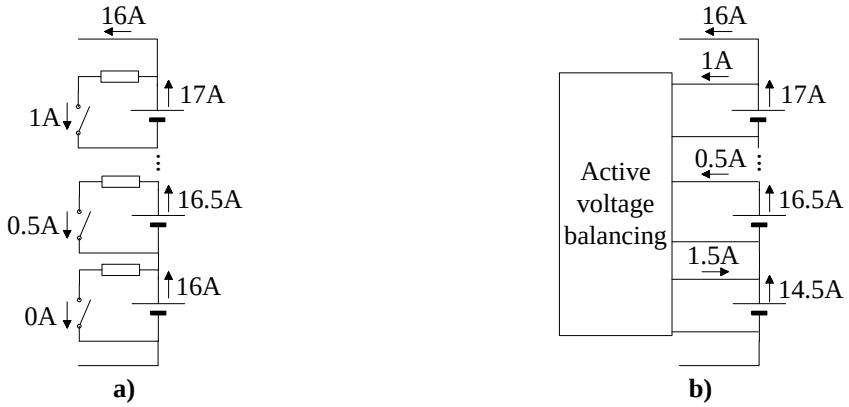

Figure 5.50: Practical examples of the voltage balancing circuits; a) Passive voltage balancing; b) Active voltage balancing.

5.5 Pouch cells module

The pouch cell utilized is a 7Ah EIG $LiFePO_4$ power cell; as in the previous cases, it has a high discharge current capability to ensure its use in power applications. Its main characteristics are summarized in TABLE 5.9.

TABLE 5.9 POUCH CELL MAIN CHARACTERISTICS

Feature	Specification
Nominal capacity	7Ah
Charging end voltage	3.65V
Average working voltage	3.2V
AC impedance	<3mΩ
Standard charge method	CC/CV
Current	0.5C
Voltage	3.65
End current	350mA
Maximum charge current	4C (Continuous)
Maximum discharge current	15C (Continuous) and 20C (t<30 seconds)
Discharge end voltage	2V
Maximum operating temperature range	
Charge	0ºC-40ºC
Discharge	-30ºC-55ºC

This cell format is considered promising due to its high specific power, and it is considered the best one for electro mobility because very compact battery modules and packs can be designed. The dimensions of this cell are 222 x 129 x 4.5mm (Figure 5.51), and its weight is 245 gr.

Figure 5.51: EIG pouch power cell.

The strategy followed with this module to reduce the maximum temperature gradient is the same as in the case of prismatic module due to their similar characteristics. However, pouch cells have a non rigid case, and it is more difficult to assemble a rigid battery module without adding more parts to the assembly. Besides, the terminals of these kind of cells are tabs and it is more difficult to interconnect cells with these connectors. Following some figures regarding to the assembly process will be shown.

5.5.1 Pouch module assembly process

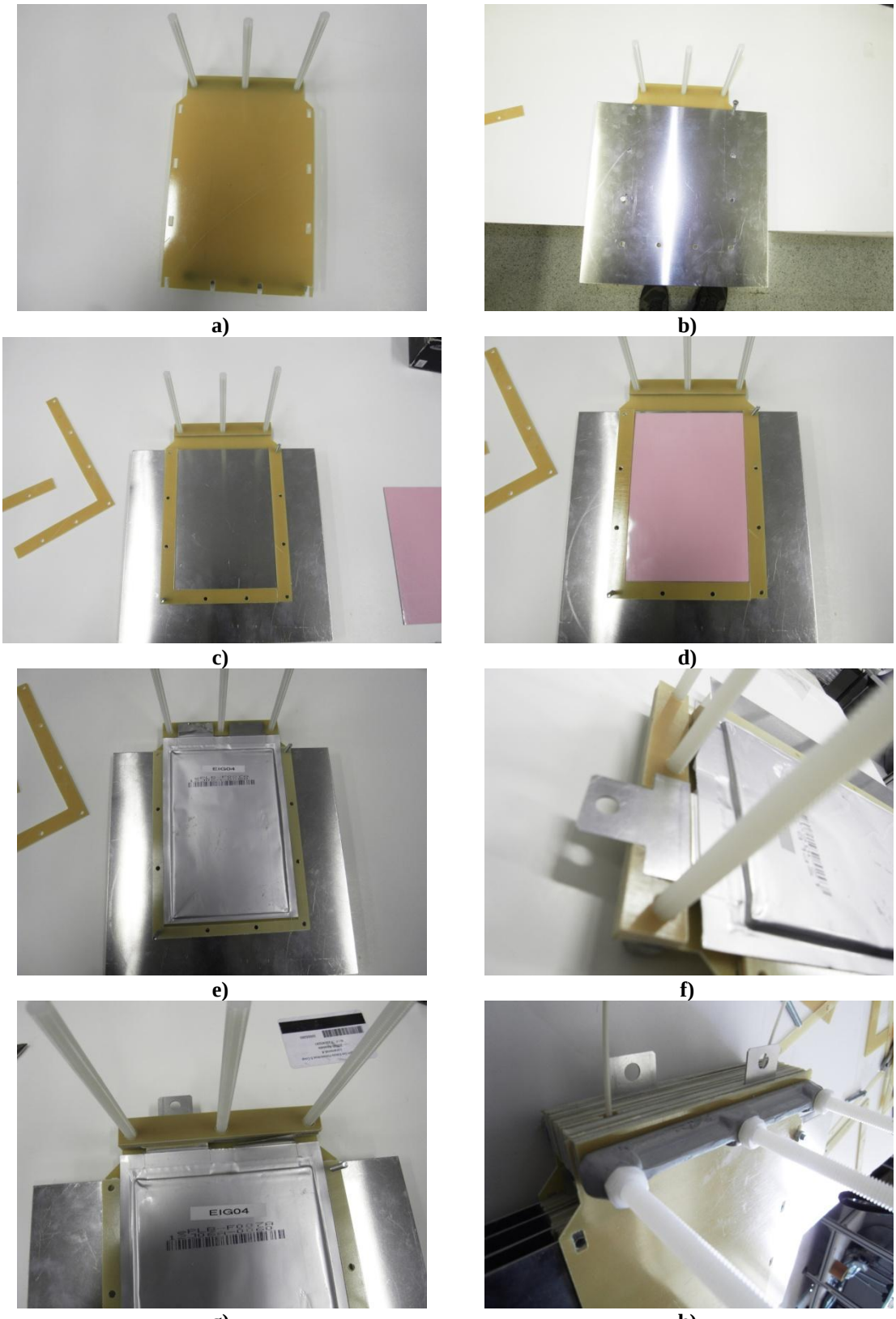

Figure 5.52: Pouch module assembly process; a) Cover layer; b) Heatsink; c) Cell holder; d) *TIM*; e) Including pouch cell; f) Power terminal; g) Layered terminal structure; h) Overall structure.

Figure 5.52 shows the process followed to assemble a li-ion pouch cell module; the parts included in this assembly are: a cover layer, heatsinks at both sides of cells, thermal interface materials (*TIM*) and a layered cell holder structure. Each cell is inserted into a layered structure with two TIM layers covering the cell. Over the *TIM* layers heatsink layers are included to extract heat from the surface of the cell. Aluminium terminals are included in the design to connect the positive and negative battery module terminals (Figure 5.52 f).

In order to sense each cell voltage more parts are included into the design process; Figure 5.53 a shows the sensing layer and the connection cable. The tab of the cell to be sensed has to be in contact with this layer to sense the voltage. Then, this layer is covered with a non conductive one and is pressed to get a good electric contact.

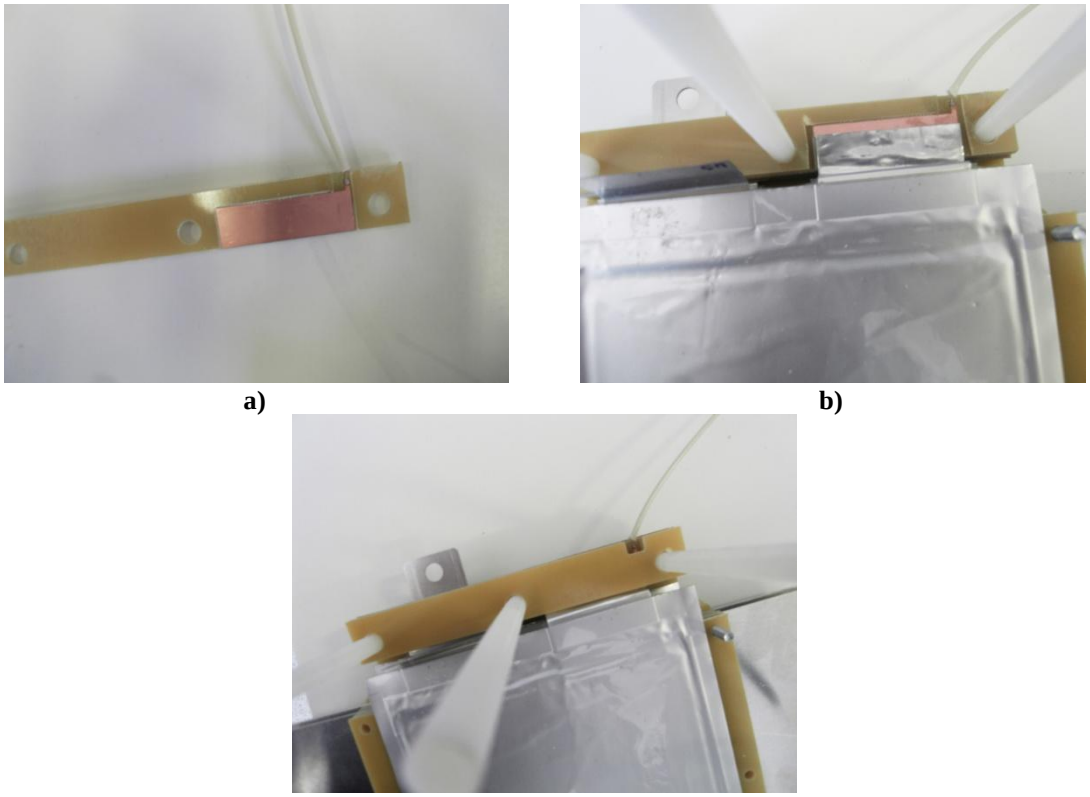

a) **b)**

c)

Figure 5.53: Cell voltage sensing assembly.

Figure 5.54 shows the final assembly of the pouch battery module; the objective of this battery module assembly process is to analyze the advantages and disadvantages detected during the process. The main disadvantages are the impossibility to design a rigid battery module without including more parts and the interconnection of cells. Bad interconnection of cells can lead to high contact resistances in these points and hence, higher heat losses near terminals. Ultrasonic welding is usually utilized when working with this cell format to avoid this problem. Besides, the non rigid case makes difficult to ensure good thermal contacts between cells because it is not possible to press the module to eliminate air bubbles between them. In this case the advantage of these cells is not clearly seen because it is not an industrial assembly. The available space required by the module is big comparing it with the previous modules.

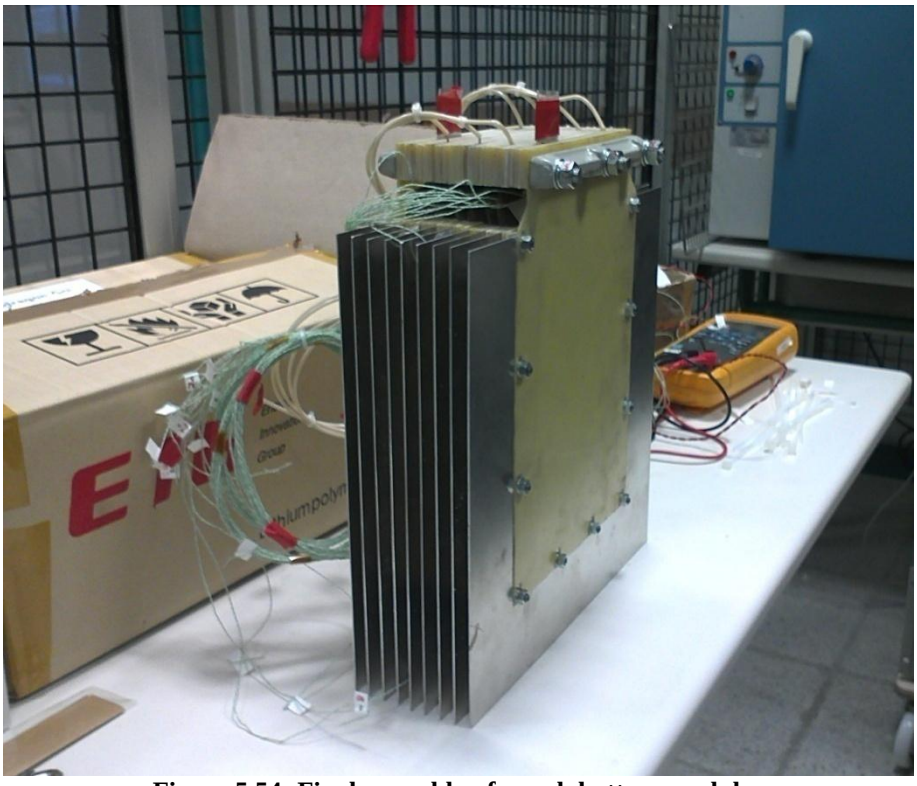

Figure 5.54: Final assembly of pouch battery module.

In order to choose the size of the heatsink layers the correlations given by Ellison et al. in [84] for natural convection have been followed; the heat transfer of the heatsink plates for a heatsink temperature of 35ºC and an ambient temperature of 25ºC is calculated following. Equation (5.4) represents the convective heat transfer coefficient of a vertically oriented flat plate under natural convection flow regime; h_{conv} is the convective heat transfer coefficient [W/in ºC], C and n are constant correlation values given in [84], k_{air} is the thermal conductivity of the air [W/in K], γ/β is a function related to the *Rayleigh number* calculated in [84] for different heatsink temperatures [1/in^3] and β is the thermal expansion coefficient and its calculation is based on the ideal gas law [1/K]. ΔT is the difference between the heatsink and ambient temperatures (T_h and T_a) [ºC] and H is the height of the vertical plate [in].

$$h_{conv} = C k_{air} \left(\frac{\gamma}{\beta}\right)^n \beta^n \left(\frac{\Delta T}{H}\right)^n \quad \textbf{(5.4)}$$

For this analysis the surface in contact with air has to be taken into account. Figure 5.55 shows the different zones of the heatsink in contact with air. *H1* is defined as the height of 1 and 3 zones and its value is 270 mm and *H2* is the height of zone 2 and its value is 50 mm. As the heights are different the heat transfer coefficient will be different also. The value of constant C is 0.59 for natural convection, k_{air} and γ/β are calculated for the mean film temperature (30ºC) and follow equations (5.5) and (5.6), β is 0.00335 for an ambient temperature of 25ºC, and n is 0.25 according to the correlations obtained from [84]. The value used for ΔT in this calculation is 10ºC.

$$k_{air} = 6.0583x10^{-4} + 1.6906x10^{-6}\left(\frac{\Delta T}{2} + T_a\right) \quad \textbf{(5.5)}$$

$$\frac{\gamma}{\beta} = 5.460x10^{5} e^{-9.2817\,x10^{-3}\left(\frac{\Delta T}{2}+T_a\right)} \quad \textbf{(5.6)}$$

The convective heat transfer coefficients obtained from these calculations are 0.0028 for height *H1* and 0.0042 for height *H2* [W/in^2 ºC]. The surfaces in contact with air for both convective heat transfer coefficients and 1 heatsink plate are then calculated with equations (5.7) and (5.8). The calculated values are given in inches to do the calculation; *A1* is 83.76 [in^2] and *A2* is 20.17 [in^2].

$$A_1 = 4 \cdot H1 \cdot W1 \quad \textbf{(5.7)}$$

$$A_2 = 2 \cdot H2 \cdot W2 \quad \textbf{(5.8)}$$

The calculated surfaces and convective heat transfer coefficients are used in equation (5.9) to calculate the amount of energy evacuated by convection for each zone of the heatsink for a ΔT of 10ºC.

$$Q_{convection} = A\, h_{conv}\, (\Delta T) \quad \textbf{(5.9)}$$

Finally, the overall $Q_{convection}$ of one heatsink plate is calculated to be 2.66 W for an ambient temperature of 25ºC and a heatsink temperature of 35ºC. The pouch module contains 9 heatsink plates, so the total heat evacuated by natural convection with the selected plate dimensions is 24 W.

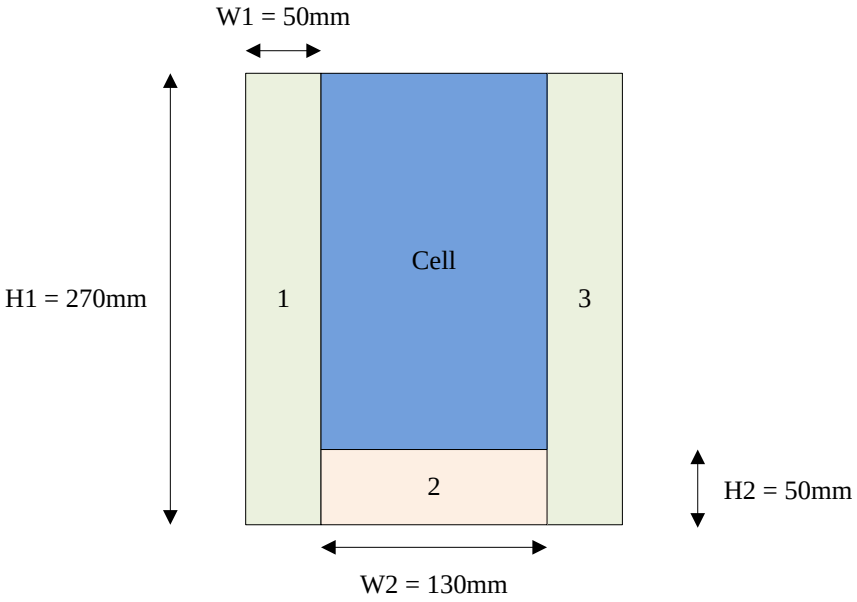

Figure 5.55: Schematic of one side of the heatsink plate used in the pouch module.

In order to validate this calculation an alternative charge and discharge cycle has been applied experimentally to the pouch module. A mean value of the internal heat generation of each cell is calculated after applying this current profile; this mean value

is around 2.5 W for each cell, so the internal heat generation of the module is around 20W. Figure 5.56 shows the temperature distribution of the pouch module after applying the alternative charge and discharge cycle previously mentioned. The temperature difference required between the ambient and the heatsink temperature to evacuate 20W is 8.65 ºC (33.65ºC on the surface of the heatsink) according to the calculations done in this work. However, the temperatures of the module are higher for this experimental test, around 37ºC. Temperatures of the heatsink plates are not measured but the thermal resistance between the cell and the heatsink can lead to a temperature drop between the cells and the heatsink plates so the calculation is considered accurate enough for the design.

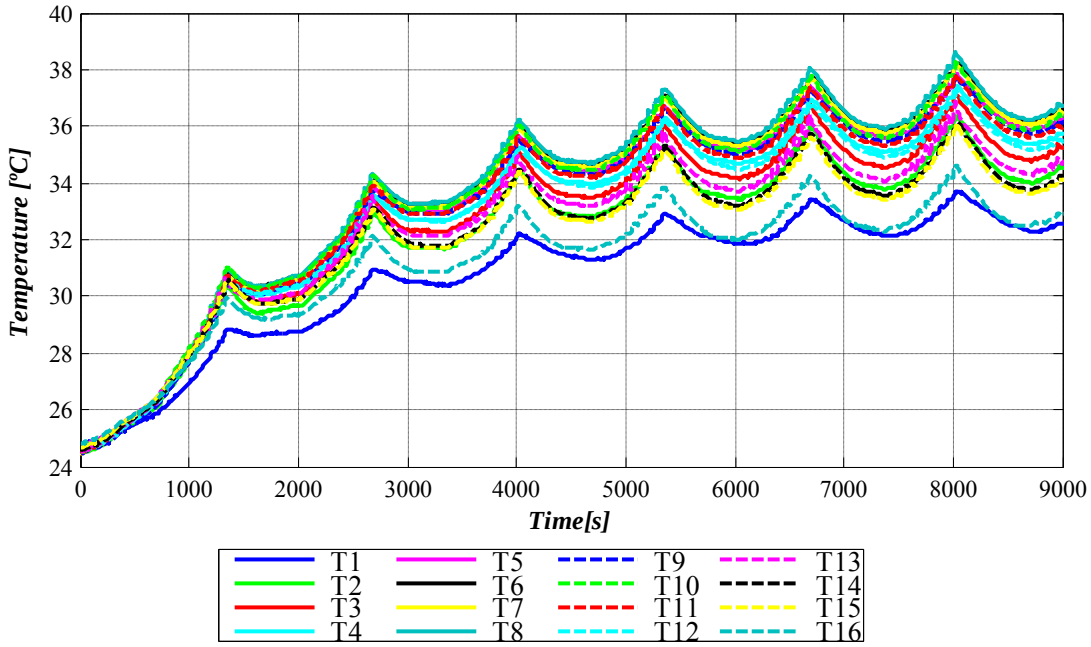

Figure 5.56: Results for an alternative charge and discharge cycle applied to the pouch module with an ambient temperature of 25ºC.

Increasing the surface of the heatsink plates can improve the overall thermal behaviour of the pouch module. However, the size of the module is an important issue in this work and the obtained heat evacuation capability is considered to be enough for the elevator application current profile.

5.6 Conclusions

Following, the conclusions of the chapter are presented divided into three groups: prismatic module conclusions, cylindrical module conclusions and pouch cell conclusions.

5.6.1 Prismatic module conclusions

Conclusions about the air gap between cells are obtained from the analysis with the prismatic module. Bigger air gaps increase the maximum temperature gradient of the prismatic module; however, bigger air gaps are suitable to include a forced air cooling system blowing directly to the cells since the static pressure of the system is reduced leading to lower power consumptions of the *BTMS*. When the air gaps are reduced, the static pressure that the cooling system has to overcome is bigger and also its power consumption. In the case of avoiding air gaps the maximum temperature gradient is reduced but the forced air cooling will not blow directly the cells because of the absence of cooling channels.

Concretely, the results presented in this chapter regarding temperature gradients are the following ones: during the constant current discharge the maximum temperature gradient for 5mm air gap module is 2.8ºC, 2.4ºC for 1.5mm air gap and 1.8ºC for the case without air gaps; with the alternative charge/discharge cycle 5.3ºC for 5mm air gap module, 4ºC for 1.5mm air gap and 3ºC for the case without air gap. The layout selected for this module is then non air gap layout with *TIM* material to reduce the temperature gradient.

Besides, a compensation of the convective heat transfer coefficient is done to the 1st and 8th cells permits reducing even more this gradient. *T1* and *T16* measure temperatures closer to the maximum temperature improving module average temperature distribution.

5.6.2 Cylindrical module conclusions

In the case of cylindrical module, a novel procedure to reduce temperature gradient is proposed taking advantage of voltage balancing systems. Voltage balancing systems are commonly used to avoid *SOC* mismatches between cells within the same module improving their voltage distribution. However, if higher balancing currents are reached for these systems, an important improvement in the temperature distribution can be also obtained in applications where the depth of discharge is high due to the internal heat generation compensation.

PB2 voltage balancing system improves the temperature distribution of a li-ion battery module in a 54% for a 1C rate of discharge since this parameter is improved from 4.75ºC to 2.17ºC. When the current rate is higher, 2C, the improvement is reduced to a 45% (from 5.1ºC to 2.78ºC) because the duration of the discharge is reduced. However,

if the balancing current is increased to reach better results with high current rates, the efficiency of the system is reduced. With 1C rate the energy delivered by the module with a *PB2* is reduced in a 5% if it is compared to the case without voltage balancing (from 8.88Ah to 8.45Ah); with 2C rate the available energy is also reduced in a 3.5% (from 9 to 8.7 Ah).

AB mitigates this problem or even improves the available energy for certain working conditions. With a 1C rate scenario the energy is improved in a 2% and when 2C discharge rate is applied the available energy is reduced in a 0.66%. However, the improvement in the temperature distribution is not as notable as with *PB2*. Whit 1C rate an improvement of a 33% is reached (4.75ºC to 3.2ºC); according to 2C rate of discharge the improvement is a 31% (5.1ºC to 3.51ºC).

Comparing both voltage balancing systems it is concluded that passive balancing reaches better temperature distributions but increases the maximum average temperature of the module and reduces the available energy significantly. The active balancing instead reduces the temperature distribution without increasing the average maximum temperature, and also delivers the same energy as the case without voltage balancing.

$LiFePO_4$ cells have a very flat voltage profile in a big range of their *SOC*, from 90% to 20%; hence, this strategy based on voltage differences between cells is hardly applicable if all the cells have similar *SOC*. That is the reason why all the results presented are during complete discharge processes, to reach low values of *SOC*. It should be pointed out that during the search in bibliography, similar proposals have not been found.

5.6.3 Pouch module conclusions

Pouch module conclusions are related to advantages and disadvantages of these cells to be assembled into a battery module. The main advantage of these cells is that more energy can be available in a smaller space, a very important issue in electro mobility applications. However, after the assembly process of this work, several drawbacks have been detected; the non rigid case of these cells forces to include additional parts to build up a rigid structure for the module unlike the cases with cylindrical and prismatic cells. Besides, it is not possible to press one cell against the other to erase air bubbles since the case is not rigid and cell can be damaged. Furthermore, the interconnection of the tabs can lead to high contact resistances leading to higher temperatures close to the power terminals. Special ultrasonic welding equipment can be required in these cases to mitigate this problem.

The sizes of the heatsink plates are selected calculating their convective heat transfer coefficients by correlations. Under thermal conditions of 35ºC on the surface of the plate 24 W can be ideally evacuated by the designed heatsink. However, this calculation does not take into account the thermal resistances between cells and heatsink plates, it is considered that the cells and the heatsinks are exposed to the same temperatures. As the module is not pressed to avoid air between cells and heatsinks a temperature drop is created between them; this temperature drop provokes higher working temperatures of the cells within the module to evacuate the same amount of heat by the heatsink plates.

Chapter 6. METHODOLOGY TO DESIGN FORCED AIR COOLING SYSTEMS FOR LI-ION BATTERY MODULES

The following chapter deals with the methodology to design forced air cooling systems for the previously presented battery modules; the introduction paragraph will lead to a brief state of the art regarding to an approach for designing thermal management systems for electric and hybrid vehicle battery packs. After that the requirements of the application analyzed in this work will be defined; maximum ambient temperature, application current profile, maximum temperature of the module and maximum temperature gradient permitted; then the thermal behaviour of the three modules without cooling system will be tested to check if they reach the requirements.

Afterwards, the *CFD* simulation tool utilized during this chapter to calculate the parameters of the cooling system will be presented. Following the steps followed to calculate the suitable forced air cooling system for each module will be explained. Finally the *CFD* simulation tool will be validated with experimental results and the chapter will be ended with several conclusions.

6.1 Introduction

After improving the layout of the battery module when possible to minimize the temperature gradient and proposing other strategies to reduce it, it is time to design the associated cooling system. Figure 6.1 is showing the steps followed to design the forced air cooling systems for the modules presented during the previous chapter. First the requirements of the application must be defined; the current profile for the application and the maximum ambient temperature are crucial because of their influence in the internal heat generation and initial temperature of the experimental tests. Besides, the maximum temperature allowed for the analyzed application and the maximum temperature gradient permitted has to be defined.

Afterwards, next step is to check if the available modules reach the requirements previously defined without using a cooling system. In this sense, the ambient conditions will be the worst ones and maximum temperature and maximum temperature gradient are the objectives.

Finally, if the cooling system is needed, last step is to design this cooling system; the location and cooling strategy has to be selected; then, the static pressure of the system for different flow rates and the minimum flow rate required are calculated; finally, the blower or blowers are selected and the cooling system is included into the design.

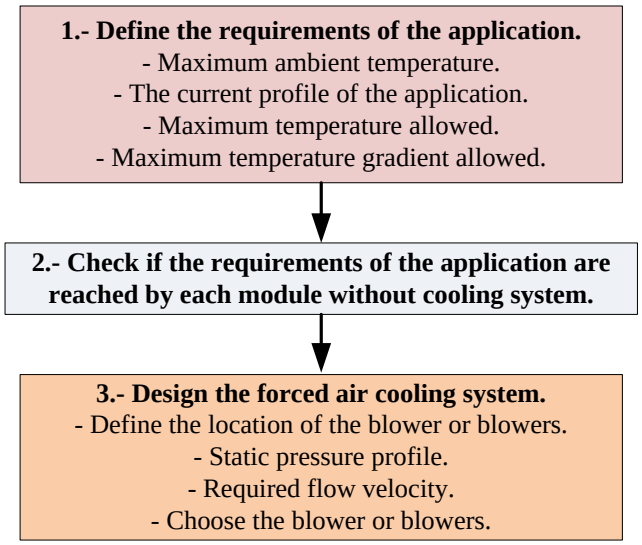

Figure 6.1: Overall structure followed to design the forced air cooling system.

In order to validate the previous design the complete module (Battery + *BTMS*) is tested under the worst ambient condition to verify if the maximum temperature and temperature gradient objectives are achieves after including the cooling system.

6.2 State of the art

The state of the art in this chapter is about a methodology to design *BTMS* systems for battery modules and packs. Pesaran et al. in [4] presented their approach to design a *BTMS* system for *EV* and *HEV* applications. They specify several steps to follow in order to reach the best performance of the pack after including the thermal management system. Following a summary of the steps pointed out in their work:

1. ***Define the BTMS objectives and constraints***: Identify specifications as average temperature of the pack, and ΔT in a module or in a pack. Besides, identify geometry, dimensions, number of modules, orientation and the layout depending on the application.
2. ***Obtain module heat generation and heat capacity***: Measure, estimate or calculate the internal heat generation for a single cell, a module or the whole pack under certain charge/discharge conditions and different temperatures. Measure, estimate or calculate the overall heat capacity of a module at various states of charge and temperatures.
3. ***Perform a first order BTMS evaluation (Preliminary selection)***: Evaluate the temperature of the pack with different heating/cooling systems. Air, liquid; different flow rates; direct or indirect; series or parallel...Make a selection of the proper *BTMS* with the results and evaluate if the temperature of the pack is kept within the specified range. In this step the thermal conductivities in the interfaces between the modules and the *BTMS* are needed.
4. ***Predict the battery module and pack behaviour***: Evaluate the non-uniformity of temperature in a single module and the non-uniformity along the whole pack for various conditions. Set parametric simulations change critical parameters to evaluate the best configuration possible. Select the best configuration for the *BTMS* and estimate the fans or pumps parasitic power requirements.
5. ***Design a preliminary BTMS***: Evaluate cost, maintenance, energy need, ease of operation...
6. ***Build and test the BTMS***: Build a battery pack with a *BTMS* and validate the previous work. If the result is not the desired one repeat steps 4 and 5.
7. ***Optimize the system***: Try to optimize the whole system as much as possible. This is a summary of the method presented in [25]. Some of the steps can be done again before building the *BTMS* in order to reach the best option for the concrete application. In this work the best average operating temperature for li-ion batteries is said to be 30ºC. Besides, they talk about a maximum ΔT of 2-6ºC for a single module, and a ΔT of 2-8ºC in the whole pack.

This chapter deals with the definition of another methodology to design BTMS systems; in this work only the cooling system will be analyzed and it will be a forced air cooling system. The air cooling will increase the heat transfer coefficient between cells and ambient to reduce the maximum temperature of the module and reduce the maximum temperature gradient of the module.

6.3 Definition of the final application requirements

Following, the requirements to be achieved by each module will be presented for the concrete application. It is an application for an elevator and the battery pack will contribute with the main grid supporting a percentage of the energy demanded by the elevator. Besides, the energy produced during the braking process will be delivered to the energy storage system increasing the efficiency of the overall system. Furthermore, when the main grid fails, the energy storage system is able to deliver the energy required to bring the elevator to a safe position until the problem is fixed.

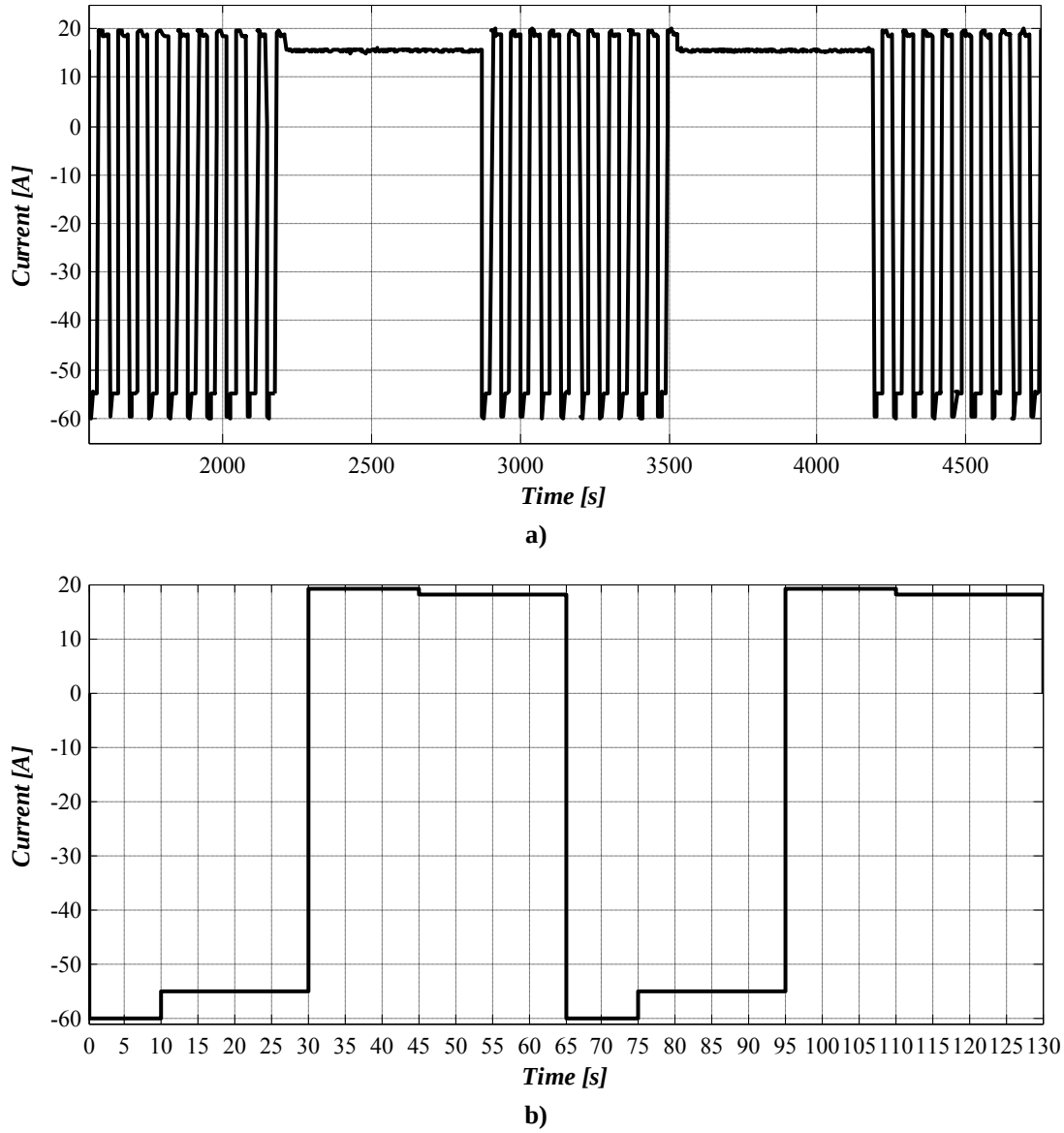

Figure 6.2: Final application current profile; a) 10 elevator cycles and the recharge process; b) Zoom of two elevator cycles.

Figure 6.2 shows the final application current profile during normal operation; this profile emulates 10 elevator cycles before recharging the battery module with a constant

current to bring the module to the initial *SOC*. After the discharging process, 10 elevator cycles are simulated again; this process can be repeated several times. During the discharge process, a peak current of 60A during 10 seconds is demanded by the application followed by a constant current discharge of 55A during 20 seconds. After that, a regeneration process is emulated with a charging peak current of 19A during 15 seconds followed by a constant current charge process of 18A during 20 seconds. The recharging process after 10 elevator cycles is done with 15A constant current charge until the module reaches the initial *SOC*.

This current profile will lead to an important amount of power losses within the module and the internal temperature of each cell will be increased. Besides, the absence of times without current between the discharge and charge processes makes this temperature increase to be more important. However, this current profile is considered because it is a demanding case.

The maximum ambient temperature is an important parameter to define the forced air cooling system. In this work a maximum ambient temperature of 35ºC is defined so the aforementioned current profile will be applied under this ambient condition to test the worst conditions. Apart from the ambient temperature, the maximum temperature permitted has to be defined; it is important to define this temperature to avoid accelerated aging of the cells within the module. In this work this value is 45ºC.

The 35ºC ambient temperature is probably a low value depending on the real location of the battery module and the 45ºC maximum temperature is not the optimum temperature value to minimize the aging processes for li-ion cells. However, in this work passive forced air cooling systems will be designed, hence, the ambient air will be directly blown instead of cooling it down before being blown as in active cooling. With this scenario the ambient temperature of 35ºC is considered high enough and the maximum temperature of 45ºC is considered a good target. According to maximum temperature gradient permitted for the battery modules, a value between 2-3ºC is considered a good target. in bibliography a value between 2-6ºC is accepted but in this work it is considered very important to reduce it taking into account the conclusions obtained during the state of the art in Chapter 4.

First step is to evaluate the thermal behaviour of the three modules under the current profile of the final application and under 25ºC and 35ºC ambient temperature to measure the increment of the temperatures of the modules. Figure 6.3 shows the evolution of the temperatures of the prismatic module under the final application current profile and an ambient temperature of 25ºC. The maximum temperature of 45ºC is reached during this experimental test and a maximum temperature gradient of 2.5ºC is measured when 45ºC are reached. If the ambient temperature is increased until 35ºC the maximum temperature of 45ºC will be reached in a few elevator cycles; the conclusion is that the prismatic module requires a cooling system to achieve the requirements of the application previously defined.

The cylindrical battery module is tested under the same conditions and the results show similar problems; the maximum permitted temperature of 45ºC is reached by this module after less than 20 elevator cycles. After first 10 elevator cycles, the maximum temperature of the module is almost 40ºC and after first recharging process this value is

increased to 42ºC. When the elevator cycles begin again the temperatures increase again until 45ºC and the experimental test is finished. Besides, the maximum temperature gradient is almost 6ºC at the end of the experimental test. A cooling system is required for this module to reach the requirements of the application. Special effort must be done to improve the temperature distribution and to be able to apply the application profile under 35ºC of ambient temperature.

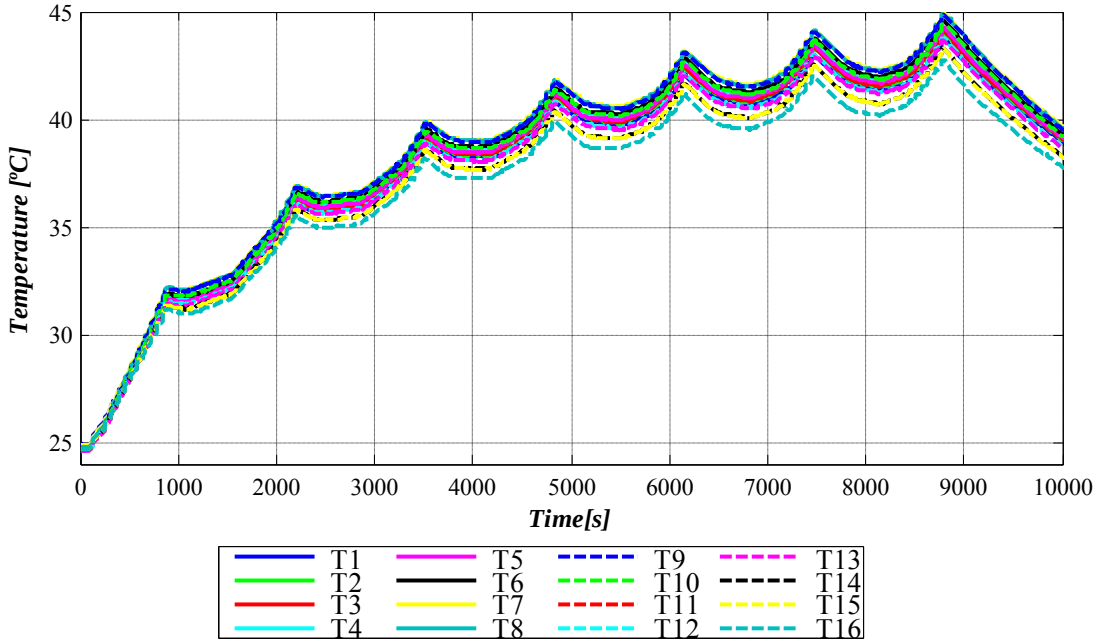

Figure 6.3: Evolution of the temperatures of the prismatic module without *BTMS* under application current profile and 25ºC ambient temperature.

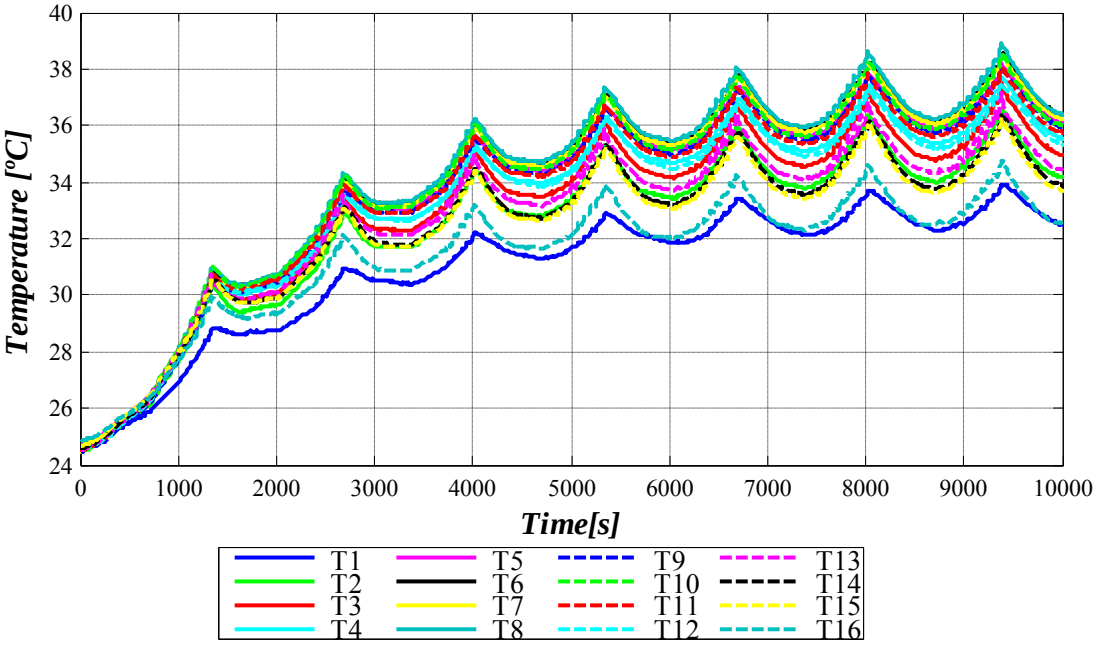

Figure 6.4: Evolution of the temperatures of the pouch module without *BTMS* under application current profile and 25ºC ambient temperature.

The pouch module has been tested under the same conditions (Figure 6.4); the maximum temperature reached by this module is 39.5ºC after more than 70 elevator cycles. This value is reduced comparing it with the other battery modules. However the maximum temperature gradient measured at the end of the experimental test is 5ºC. This module is tested under an ambient temperature of 35ºC without any cooling system and it can work for several elevator cycles until reaching the 45ºC alarm temperature. The conclusion is that a cooling system is required to reduce the temperature gradient of the module, and also to improve the heat transfer with the ambient to reach the requirements under35ºC of ambient temperature.

6.4 Battery module model proposal

A *CFD* simulation tool is utilized in this work to help into the design of the forced air cooling system of each battery module. A 3D model based on the model presented in 3.6 for a single cell is utilized in this chapter for battery modules. The assumptions made are the following ones:

- Each cell of the module is considered a single body. The different parts inside the cells are not modelled in the geometry.
- An average heat capacity is calculated experimentally following the heat capacity test in 3.4.2 for the prismatic, cylindrical and pouch cells. This average value will be the heat capacity of each cell within the module.
- An isotropic thermal conductivity is considered for each cell of each module. This value is obtained applying the methodology presented in 3.5.3 in each cell.
- The internal heat generation of each cell of the module is calculated from the model presented in 3.3 and it is considered uniform for the whole single cell.
- The output of the model will be an average value of the surface temperature of each cell within the module.

Figure 6.5 shows the overall scheme of the model utilized with the *CFD* simulation tool to help in the design of the cooling systems. The inputs of the model are the internal heat generation rate of each cell of the module ($q_1...q_8$ *[W]*), and a constant ambient temperature ($T_{ambient}$ *[ºC]*). Each cell is modelled as a single body with an average heat capacity (Cth_{avg} *[J/ºC]*) and an isotropic thermal conductivity (*k [W/mºC]*). The outputs of the model are average temperatures of different surfaces of the module; depending on the module there will be a different amount of output temperatures.

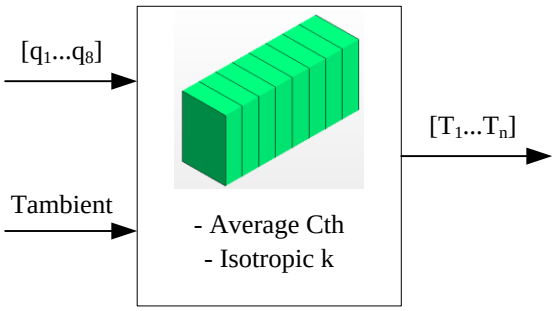

Figure 6.5: Overall scheme of the model used with module simulation.

With this model different simulations are conducted; steady state natural convection simulations, transient natural convection simulations, steady state forced air cooling simulations and transient forced air cooling simulations. Any power profile can be simulated with this simulation tool, but this work is focused on the final application current profile aforementioned and on the internal heat generation provoked by that current profile in each module.

6.4.1 3D model geometries

The geometries of the three modules are implemented into the *CFD* simulation tool taking into account the dimensions of each cell. The 3D model of the cells is simplified as much as possible because the spatial resolution across each cell is not important for this simulation tool. Figure 6.6 shows the geometries utilized in the simulation tool for the different modules; in the real prismatic module the thermal interface between cells is done with a *TIM*, and in this simulation tool a thermal resistance R_{TIM} is defined between cells to model this effect although *TIM* is not included into the model.

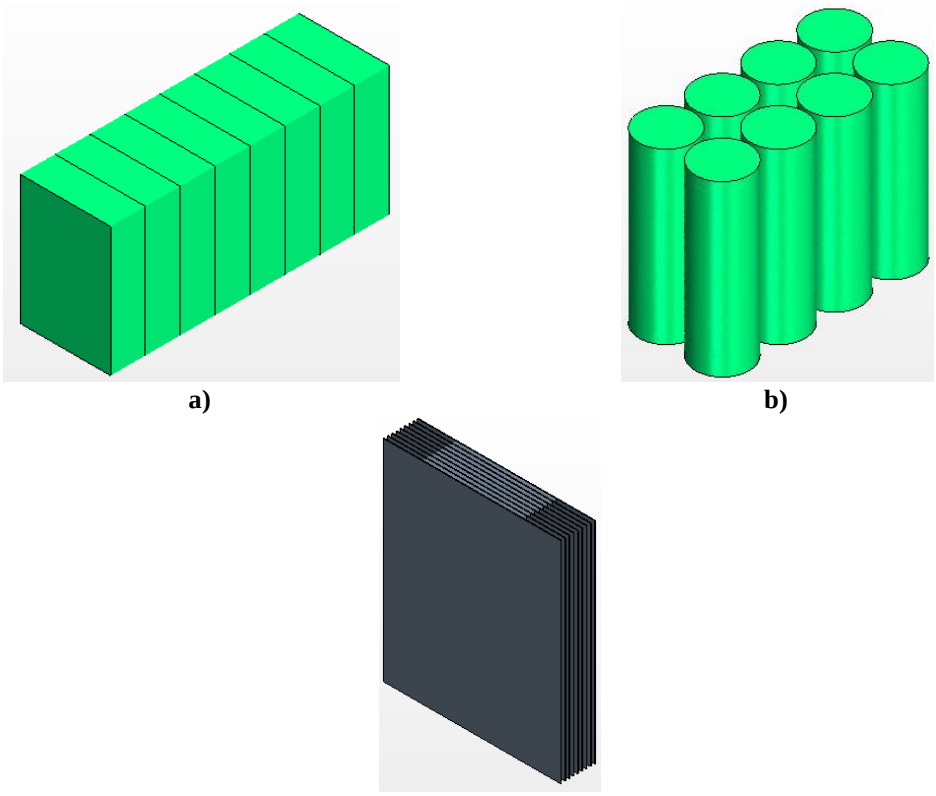

a) **b)** **c)**

Figure 6.6: Geometries of the battery modules without cooling systems; a) Prismatic module; b) Cylindrical module; c) Pouch module.

This R_{TIM} is calculated with (6.1) taking into account the thermal conductivity k_{TIM} of the material, 2.5 [W/mºC]; the thickness l_{TIM} of the layer included between cells 1.52 [mm] and the surface A_{TIM} of the layer (100 x 70 [mm^2]). The resulting thermal resistance value is 0.087 [ºC/W].

$$R_{TIM} = \frac{l_{TIM}}{k_{TIM} A_{TIM}} \quad \textbf{(6.1)}$$

In the cylindrical module geometry the air gaps between cells have been modelled; these air gaps have a thickness of 2 mm. According to the pouch module the aluminium heat sink plates and the cells have been included into the geometry; the *TIM* between the cell and the heat sink plate is not included but as in the prismatic module a thermal resistance is included. In this case the *TIM* surface is bigger and the thermal resistance value is reduced to 0.021 [ºC/W].

6.4.2 Internal heat generation profile

The current profile of the final application can be applied to the internal heat generation model presented in 3.3 to obtain an internal heat generation profile of each cell within the module. Depending on the module, these generations will be different due to the influence of their internal resistance, *OCV* and entropic heat coefficient into the calculation.

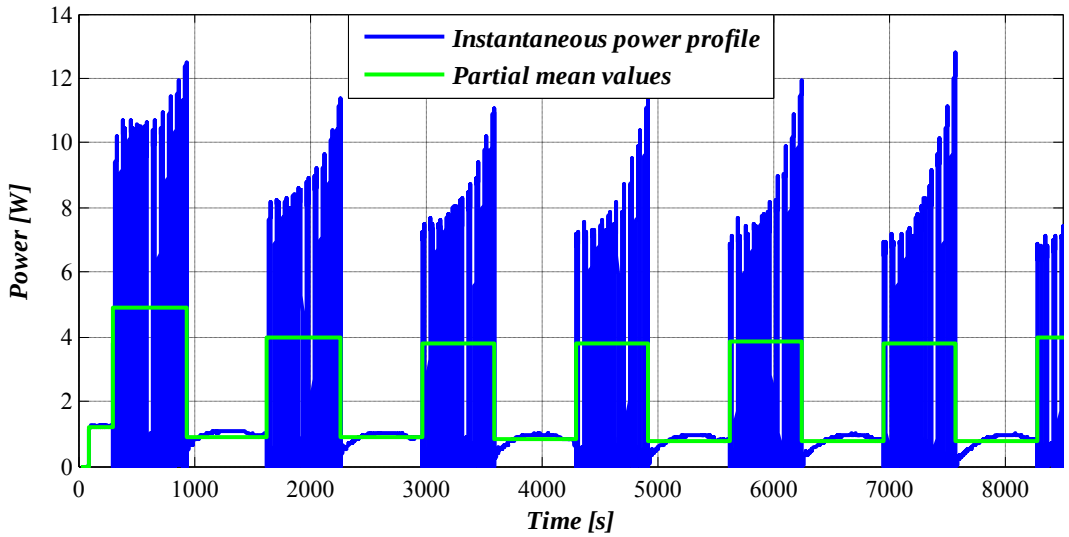

Figure 6.7: Internal heat generation of one prismatic cel during the final application current profile test; in blue, the instantaneous profile; in green, the partial mean values of this profile.

The dynamics of the internal heat generation profile during the elevator cycles requires a short time step for the 3D simulations when transients are simulated; 1 second time step or even a shorter one is required for this application. This dynamics is too fast during the elevator cycles comparing it with the dynamics of the temperature response of the cells within the module and it is filtered during the experimental tests. Besides, the overall experimental test can last more than 10000 seconds and each time step can last several minutes depending on the size of the 3D model. Thus, the transient simulation is very time consuming if the internal heat generation power profile is directly applied to the model.

Figure 6.7 shows in blue the instantaneous internal heat generation profile of one cell of the prismatic module when the final application current profile is applied. In green, it is shown a profile applying the mean values of the instantaneous profile. A mean value of the 10 elevator cycles and a mean value of the recharge process are applied to reduce the computational time of the simulations. With the partial mean values profile, transient simulations with big time steps can be conducted since the same internal heat generation values are applied for longer times.

6.4.3 Including the ambient temperature input into the simulations

The ambient temperature input is included into all the simulations in this work as a constant value; it is defined as the initial temperature of all the parts of the model, all the parts in the model are at this ambient temperature at the beginning of the simulation.

6.4.4 Natural convection simulation setup

When natural convection problems are simulated with this simulation tool several considerations have to be taken into account according to the physical properties of the air volume surrounding the battery module:

- Gravity effect must be enabled and its direction and magnitude have to be defined. In this work a gravity of -9.81 [m/s^2] in *y* axis has been defined.
- A laminar flow model has to be defined because the flow low velocity with natural convection.
- Although temperatures are not too high, a radiation model is included to take into account this effect because it can have influence in the final solution.

Figure 6.8 shows the geometry with the prismatic module and an air volume surrounding it; in order to simulate the natural convection *Air_top* and *Air_down* faces are defined as pressure outlets. In this faces the reference pressure is imposed simulating the free stream pressure. The gravity effect is defined as a negative value in the *y* axis and when the battery module is heated up an air flow is generated from *Air_down* towards *Air_top*, the natural convection air flow. All the faces of the air volume are set up to the ambient temperature and a temperature gradient will be established from the module until the outside of the delimited domain.

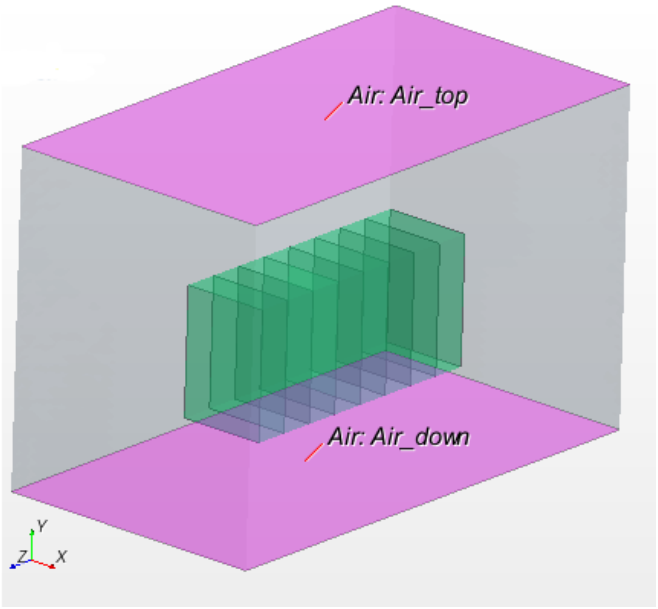

Figure 6.8: Setup of a natural convection simulation with the prismatic module.

6.4.5 Forced convection simulation setup

With forced convection problems instead another considerations have to be taken into account according to the physical properties of the air volume surrounding the battery module:

- Gravity effect is discarded if the forced air is directly blown into the battery module. If the cooling system cools down another component like a heat sink, both natural convection and forced convection problems are taken into account separately.
- A turbulent flow model has to be defined because there is a higher velocity of the flow with forced convection.
- A radiation model is also included to take into account this effect because it can have influence in the final solution.

Figure 6.9 shows the geometry with the cylindrical module and a forced air longitudinal cooling channel; in this case the *Air_in* is defined as a velocity inlet and the *Air_out* is defined as a pressure outlet. The velocity inlet is defined as constant for the whole surface and the reference pressure is imposed in the outlet to simulate the free stream pressure.

In these simulations the temperatures of the battery module are calculated; besides, depending on the velocity flow imposed to the inlet the static pressure in the inlet changes. If the velocity is increased, the blower located in the inlet will have to overcome higher pressures. It is possible to calculate the static pressure curve of the system by changing this velocity.

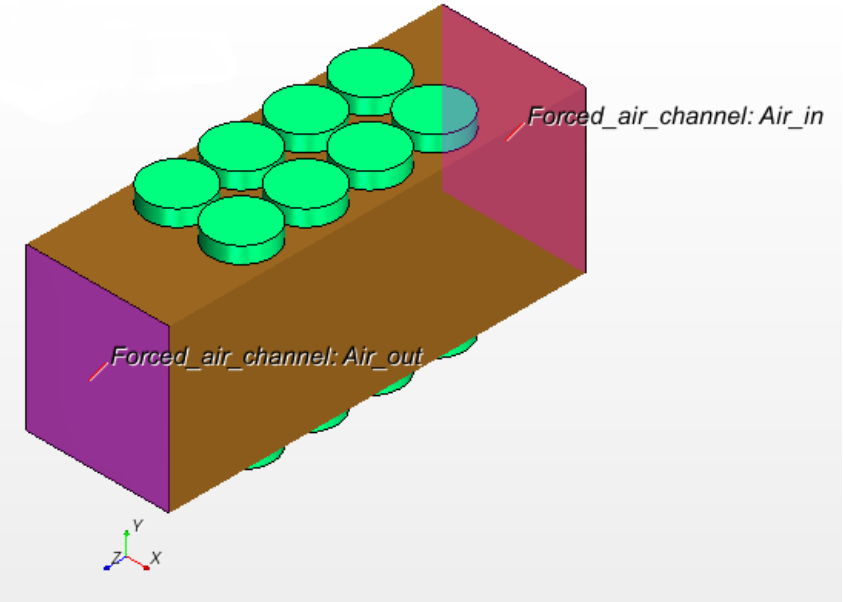

Figure 6.9: Setup of a forced convection simulation with the cylindrical module.

6.4.6 Simulation tool results

This simulation tool can calculate different results depending on the kind of the simulation. Four different simulations will be presented:

- Natural convection transient simulation.
- Natural convection steady state simulation.
- Forced convection transient simulation.
- Forced convection steady state simulation.

In all of these cases the most important result obtained is the temperature distribution of the battery module. It is not a distribution between different points of the same cell; it is a distribution between cells of the same module. 8 temperatures, one per cell, are obtained when the cylindrical module is simulated and 16 temperatures are obtained with the prismatic and pouch modules. These results are average values of the surfaces of the cells and not values of certain points of these surfaces.

In the case of natural convection simulations another results are obtained as well; the velocity of the air due to the natural convection effect or the temperature distribution into the air volume. In a forced convection simulation the static pressure in the flow channel inlet and the velocity profile through the flow channel are another results obtained.

When steady state simulations are conducted results are not calculated for different timestamps, these calculations are done for different simulation iterations; results are taken into account at the end of the simulation when the steady state is reached. The aim of transient simulations instead is to calculate the results for different timestamps to analyze the evolution of the calculated variables with time.

6.5 Calculation of the parameters of the cooling system

During the following section the forced air cooling system for each battery module is defined; the steps followed until the cooling system is defined and the blower or blowers are selected are:

1. Definition of the forced air cooling strategy; the location of the blowers, direct blowing to the cells or blowing through a heatsink.
2. Estimation of the static pressure change with the blower velocity; the static pressure of the system is calculated for different flow velocities in the location of the blowers.
3. Estimation of the minimum air volume required; the simulation tool is used to calculate the temperature distribution of the battery module at 35ºC of ambient temperature under final application current profile. The maximum temperature will be over 45ºC in the modules under test, and the minimum air volume required to reduce this maximum temperature under 45ºC is estimated.
4. The blower selected must be able to overcome the static pressure estimated for the minimum air volume required to reduce the maximum temperature below 45ºC.

6.5.1 Definition of the forced air cooling strategy

The strategy chosen for the cooling system of each module depends on the layout of the module analyzed. The prismatic cell under test has no gaps between cells so the solution of blowing air directly to the cells is not considered for this case. The solution selected is to mount the prismatic module above a heatsink and cool down this heatsink blowing air through it. Figure 6.10 presents the 3D model of the prismatic module and the heatsink together. The interface between each cell and the heatsink is done through a *TIM* again and in the simulation tool this interface is defined with the equivalent thermal resistance.

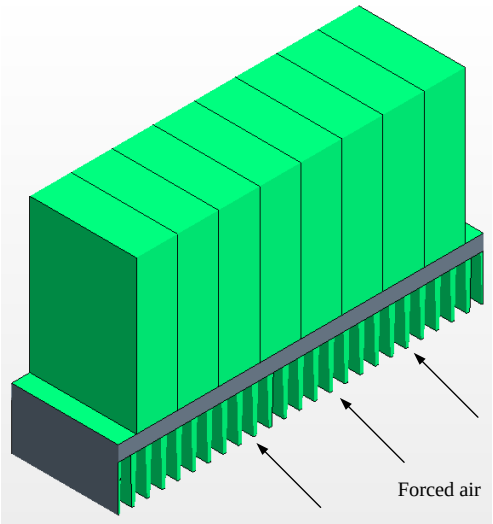

Figure 6.10: 3D geometry of the prismatic module above a heatsink.

According to the cylindrical module, the strategy adopted is to blow air directly into the cells of the module. Figure 6.11 shows the cylindrical module model with the forced air cooling used for the ventilation. In this case two possibilities will be studied: longitudinal ventilation and transversal ventilation. If the longitudinal ventilation is used the forced air cooling channel utilized is longer and the injected air can be heated up as the air passes the cooling channel, provoking an uneven temperature distribution in the battery module. Transversal ventilation can improve this distribution but the amount of air at which each cell is subjected will be less provoking a higher maximum temperature of the module. In this module the air gaps between cells are 1.5 mm gaps; these narrow air gaps will lead to an increment of the static pressure at the air inlet and the blower has to be able to overcome it.

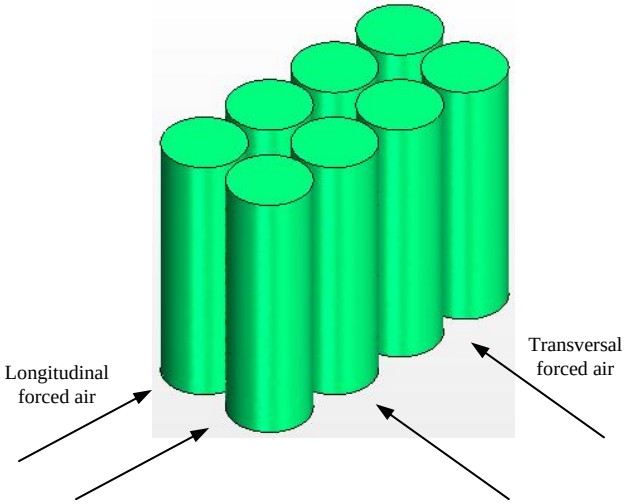

Figure 6.11: Cylindrical module 3D model with the forced air cooling channel.

The pouch module cooling strategy is to blow air through the forced air cooling channels shown in Figure 6.12; the heat accumulated inside the cells of the module is conducted to the heatsink plates, the heatsink plates are made of aluminium and this heat is rapidly spread in these layers. The strategy is to improve the convective heat transfer coefficient of these plates to improve the overall cooling system.

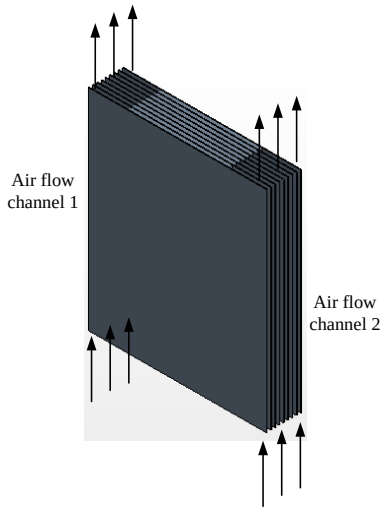

Figure 6.12: Pouch module geometry; a) Module with heatsink plates; b) Forced air cooling channels.

6.5.2 Estimation of the static pressure curve

The first parameter to estimate in order to choose a suitable fan for the forced air cooling system is the static pressure curve of the cooling system; a preliminary design is simulated with the *CFD* software and the static pressure is estimated for different fan velocities in a certain point near the blowers. The static pressure of the system is increased exponentially as the velocity of the fan raises. Depending on the static pressure, the fan will work with a certain velocity, the maximum velocity at which it is able to overcome the static pressure.

6.5.2.1 Prismatic module

The heatsink selected for the prismatic module is an extruded heatsink from Fischer Elektronik manufacturer. The dimensions of the heatsink are 230x70x40 mm; 230 mm is the width of the battery module and the *TIM*; the length of the heatsink is 70 mm because one cell width is also 70 mm. The height of the heatsink is 40 mm to avoid increasing the weight and size of the heatsink. This heatsink has been chosen due to its low thermal impedance under natural convection and forced convection. The manufacturer estimates a thermal resistance of 0.49 ºC/W for the heatsink with 70 mm length under natural convection. Under forced convection, with an air flow velocity of 2 m/s the thermal resistance of the heatsink can be reduced until 0.187 ºC/W or even more if the air flow is increased.

Under the final application current profile, the internal heat generation of the prismatic module is around 20 W, so the average temperature of the heatsink for an ambient temperature of 25ºC under natural convection is around 35ºC. If an ideal thermal contact is considered between cells and heatsink 35ºC is the temperature of the cells under the same conditions. With this rough estimation under natural convection it is considered a suitable heatsink for this module since with forced air cooling this behaviour will be much better.

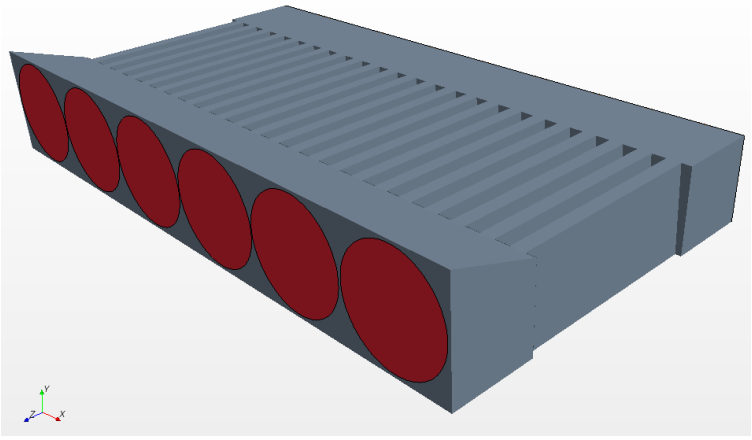

Figure 6.13: Model of the forced air cooling system for the prismatic module in *CFD*.

With this scenario, the design chosen is to place 6 square blowers of 40x40x28 mm blowing air through the heatsink. It is important to put a distance between the heatsink and the blowers to obtain a uniform air inlet to the heatsink. In this case a distance of 30

mm has been considered enough for this purpose. Figure 6.13 shows the model used for the estimation of the static pressure curve. As mentioned before an air velocity inlet is defined to simulate the blowers and a pressure outlet in the other side of the cooling channels to simulate the free stream pressure. The height of the cooling channels is 30 mm and the height of the blowers is 40 mm so the air is guided to the channels as shown in the figure.

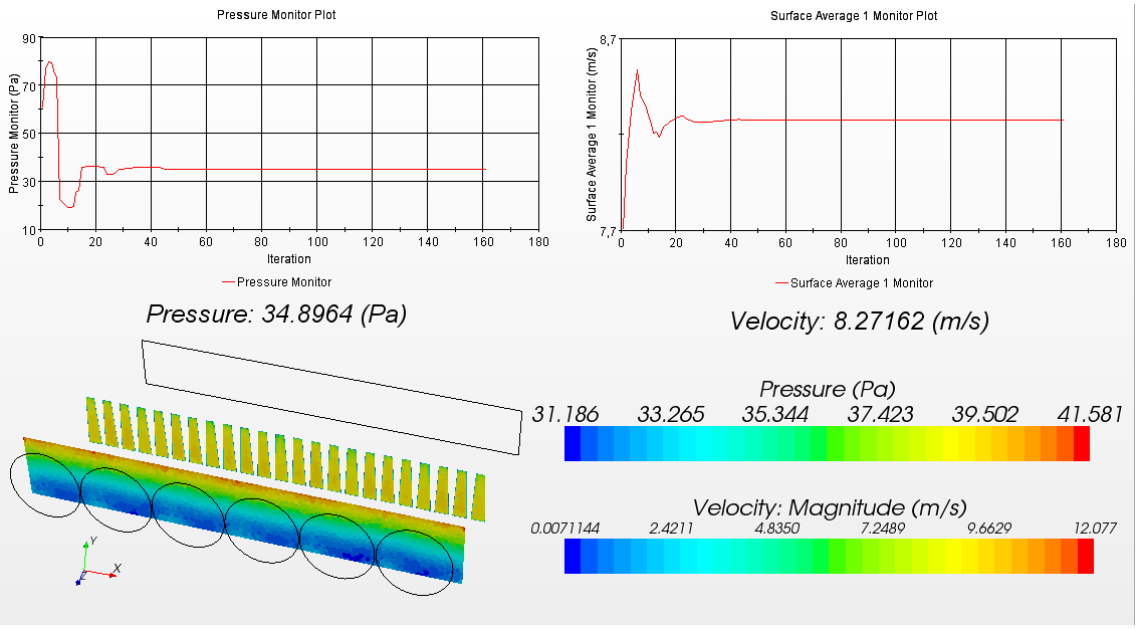

Figure 6.14: Results for an air velocity inlet of 5.5 m/s.

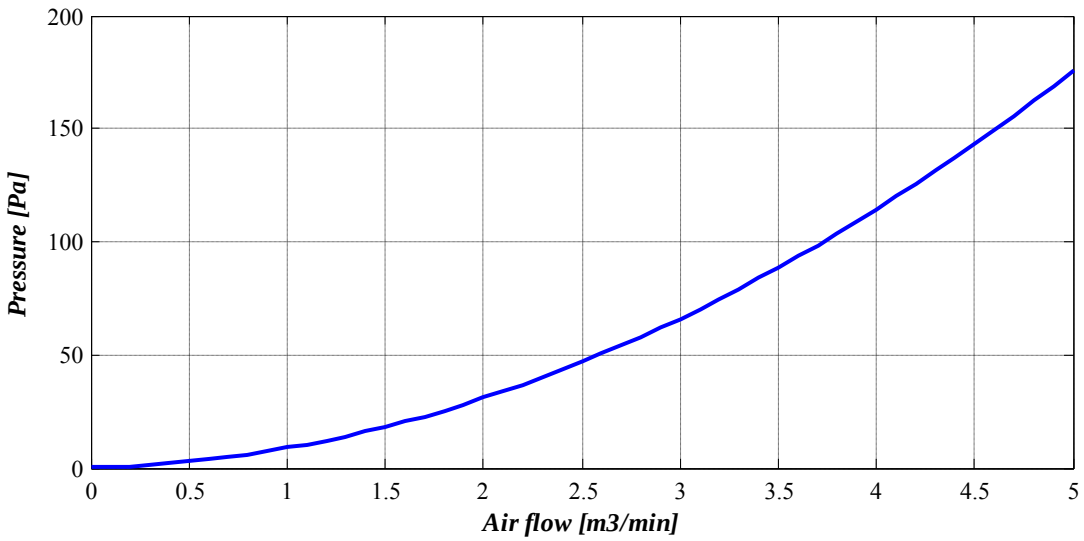

Figure 6.15: Static pressure curve for the prismatic module forced air cooling system under simulation.

Several results are obtained from this steady simulation with the *CFD* simulation tool; the average static pressure between the blowers and the heatsink is the target of the simulation. However, the air velocity in the cooling channels has been also estimated to help into the validation of the methodology. Figure 6.14 shows the results for the case of 8.27 m/s air velocity in the cooling channels; the static pressure calculated for this

case is 34.9 Pa. Besides, the pressure distribution for an imaginary plane close to the air inlet and the velocity distribution of the air channels can be also estimated.

Finally, Figure 6.15 shows the static pressure curve obtained for the prismatic module forced air cooling system designed by simulation. The static pressure increases exponentially with the mass flow inlet; with 2.4 m^3/min the static pressure of this system is around 43.35 Pa. When the mass flow inlet is increased until 3.7 m^3/min this value is increased until 100 Pa. The result for the static pressure under simulation will be validated later comparing these results with experimentally obtained results.

6.5.2.2 Cylindrical module

According to the cylindrical module, the cooling strategy is to blow air directly to the cells of the module. The static pressure curve of two different cooling strategies will be presented: longitudinal forced air cooling and transversal forced air cooling. Due to the dimensions of the cylindrical module the fan selected will be an 80x80 mm square fan.

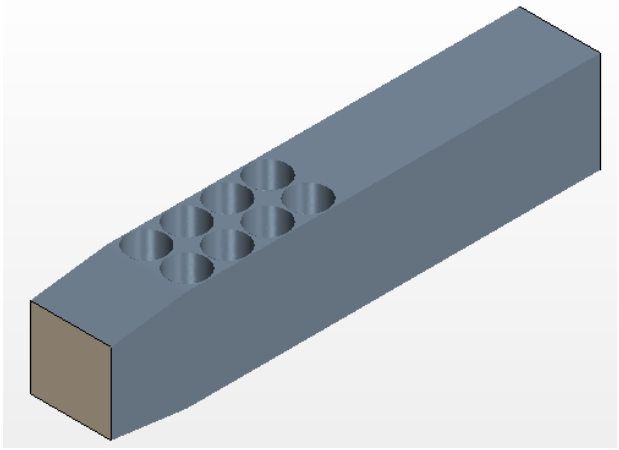

a)

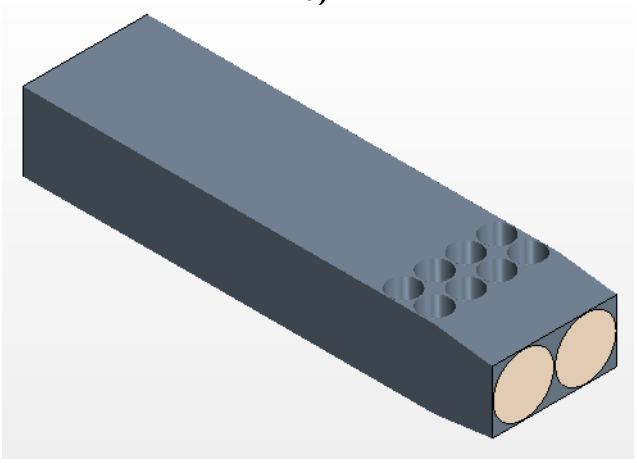

b)

Figure 6.16: Simulation models used to estimate the static pressure curve of the cylindrical module; a) longitudinal forced air cooling; b) transversal forced air cooling.

Figure 6.16 shows the simulation models used to estimate the static pressure curves for the longitudinal and transversal cooling strategies. In the longitudinal strategy only one

fan will be used to cool the battery module; in the transversal strategy two fans will be used for the same purpose. The static pressure of the longitudinal cooling will be higher than the transversal one for the same air flow due to the cooling channel length. Figure 6.17 shows the simulation results for both strategies under different air flows. The longitudinal forced air cooling strategy reaches high values of pressure with low air flows, 500 Pa with less than 0.5 m^3/min. Thus, the power consumption and size of the fan selected for this strategy will be higher. Besides, the cooling channel is larger and the temperature distribution will be less uniform. The main advantage is that it is enough with one fan to cool down the module.

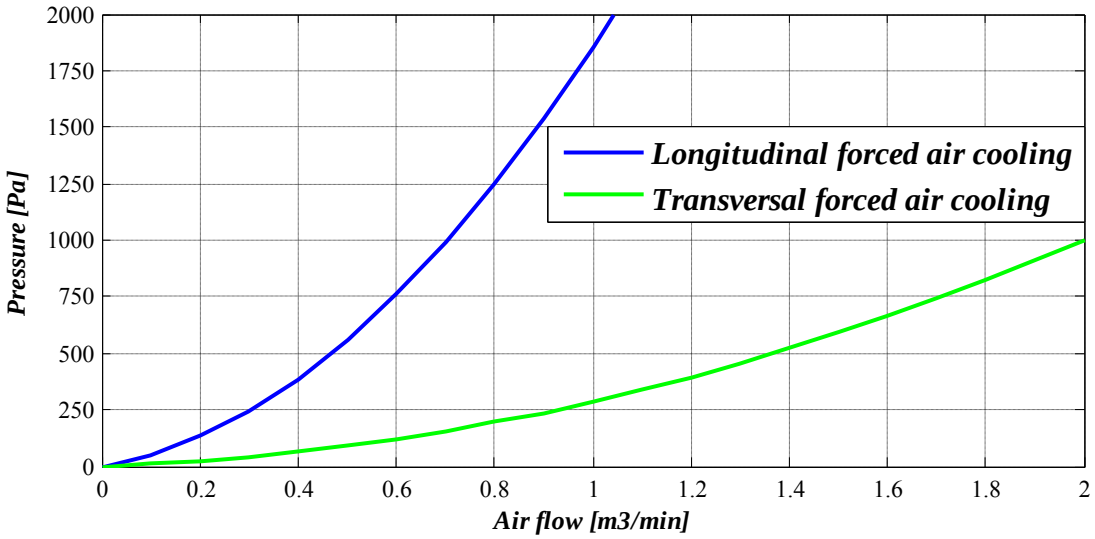

Figure 6.17: Static pressure curve for the cylindrical module forced air cooling strategies under simulation.

The fan selected for the transversal cooling strategy requires lower static pressure drops, thus, it will consume less power. Besides, the reduction of the cooling channel will improve the temperature distribution of the module.

6.5.2.3 Pouch module

The cooling strategy for the pouch module is to cool down the heatsink plates located between the pouch cells. In order to do it a final assembly with two fans will be developed. Figure 6.18 shows the simulation model used to obtain the static pressure curve for this cooling system.

Figure 6.19 shows the simulation results for the pouch module cooling system. According to the results the static pressure requirements are not demanding since 80 Pa are simulated with an air flow of 4 m^3/min. Different air flows have been simulated: with an air flow of 0.5 m^3/min the static pressure simulated is 2.42 Pa; if the air flow is increased until 1.5 m^3/min the static pressure is increased to 13.63 Pa; finally, when the air flow is set to 3 m^3/min, a static pressure of 47.5 Pa is simulated.

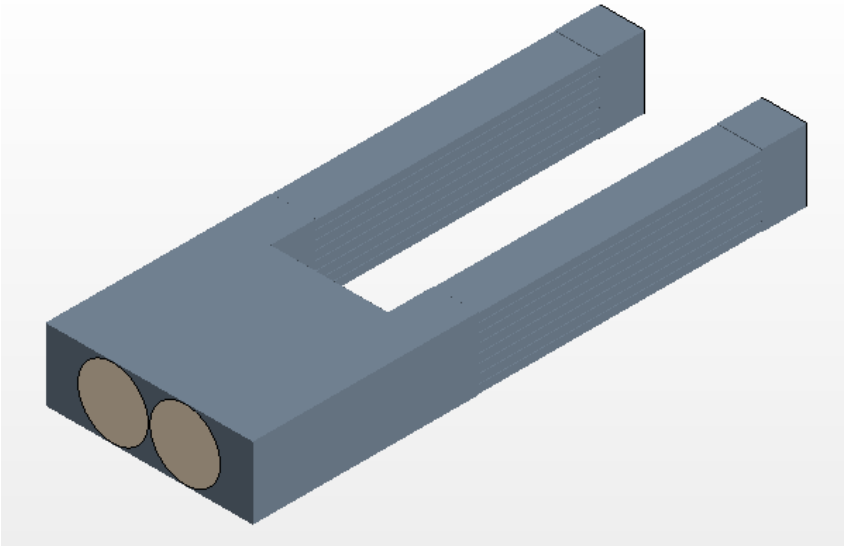

Figure 6.18: Simulation models used to estimate the static pressure curve of the pouch module.

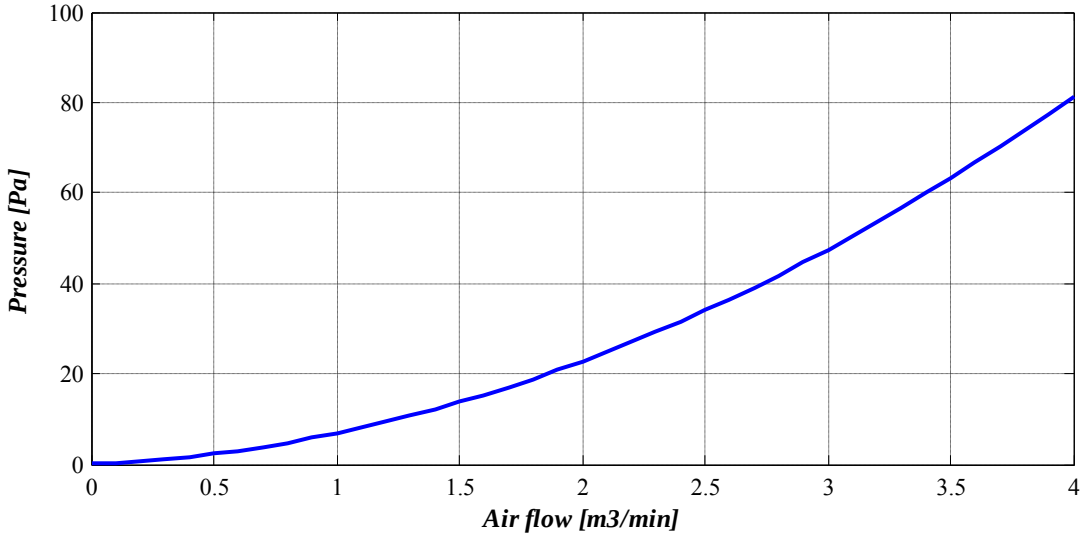

Figure 6.19: Static pressure curve for the pouch module forced air cooling system under simulation.

6.5.3 Estimation of the minimum air flow required

First step for the estimation of the minimum air flow required for the application is to analyze the accuracy of the simulation tool comparing the results obtained from a simulation with experimental results. The experimental test compared is the final application current profile at an ambient temperature of 25ºC for a natural convection case study. After ensuring that the model is accurate enough under natural convection case study this simulation tool is used to estimate the maximum temperature that the module can reach under the same current profile but at an ambient temperature of 35ºC.

The improvement of the efficiency of the li-ion cells under higher working temperatures is not taken into account for this case because the same power losses are applied in both simulations; however, the mean internal heat generation losses are reduced when the

working temperature rises. At the moment, experimental data is required to calculate the internal heat generation power profile and the modules are not tested under these conditions without cooling system because the working temperature rises too much, over 45ºC. In the future, this thermal simulation tool will be coupled with a li-ion cell electrical model to determine the internal heat generation of the cells without the need of experimental testing.

Finally, the designed forced air cooling system is included into the geometry model to evaluate its improvement on the maximum temperature and temperature distribution of the battery module. Different air flow inlets are simulated until the maximum temperature is reduced below 45ºC; that air flow $v_{fan(min)}$ is the minimum required by the module to work within the specified requirements at 35ºC of ambient temperature. Then the value of the static pressure $p_{fan(min)}$of the system with that air flow is obtained; with these two parameters the suitable fan can be selected. The requirement is that it has to be able to blow more than $v_{fan(min)}$ under $p_{fan(min)}$ static pressure.

6.5.3.1 Prismatic module

Figure 6.20 shows the results for the comparison between simulation and experimental testing of the prismatic module under the final application current profile and an ambient temperature of 25ºC under natural convection. Results show good accuracy in this simulation although it is a simplified model. The conclusion is that it is possible to estimate the steady state temperatures with the simulation tool although the transient behaviour is not accurately estimated. Temperatures are increased from 25ºC to 45ºC in this simulation; thus, if the ambient temperature is increased to 35ºC the simulation tool will estimate 55ºC of maximum temperature. As mentioned before the efficiency of the cells will be improved under this temperature and this effect is not taken into account.

After that, the designed forced air cooling system is included into the geometry model to simulate the same case study with the forced air cooling system. In this simulation different physical phenomena have to be simulated at the same time, thus, the simulation becomes slower. Actually natural convection of the cases of the cells to the ambient is simulated; besides, forced convection due to the cooling system is also simulated; finally, heat conduction between the different parts of the model is simulated. Applying the partial mean values profile reduces the time consumption of the simulation because this kind of simulation with different phenomena requires several minutes to calculate each time step.

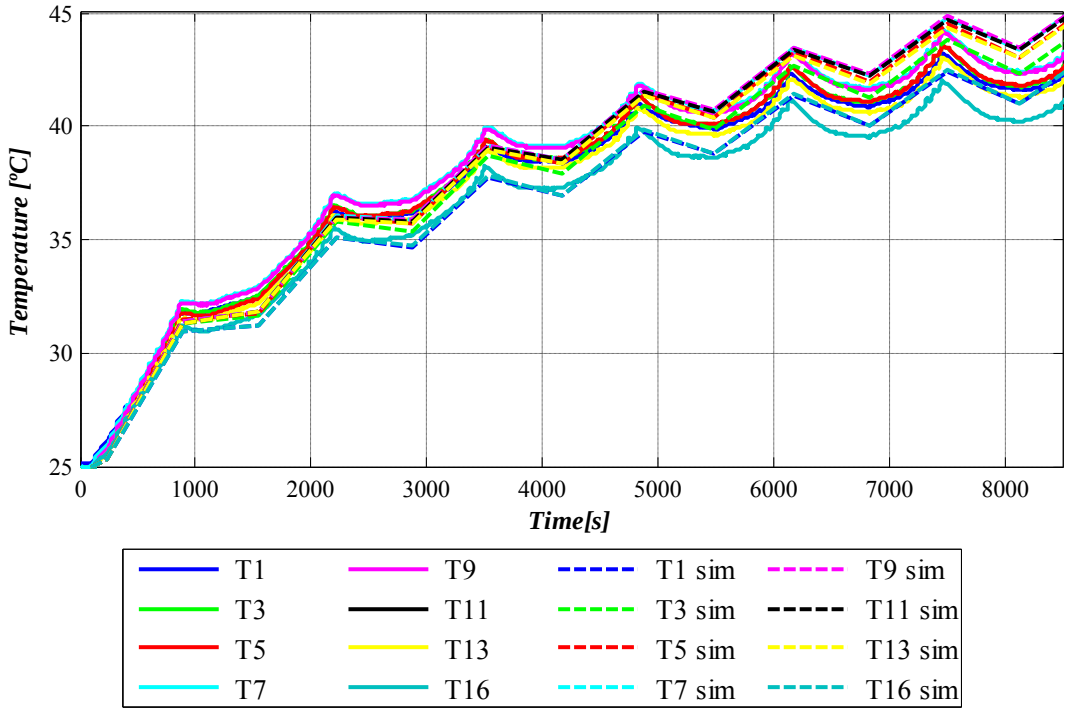

a)

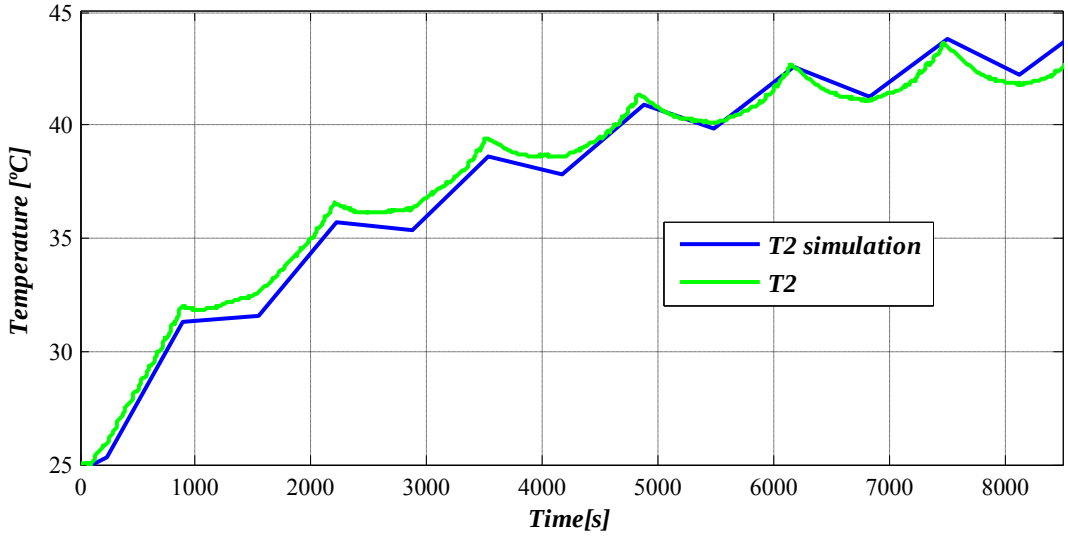

b)

Figure 6.20: Comparison between simulation and experimental results for the final application current profile test; a) One thermocouple per cell; b) Thermocouple T2.

Figure 6.21 a presents the final model utilized by the simulation tool to estimate the minimum air flow required to carry out with the requirements of the final application. After simulating different air flows at the inlet of the forced air cooling system, it is concluded that a volume of 1.2 m^3/min is required to avoid the maximum temperature of the module rise over 45ºC. Figure 6.21 b shows the results with this air flow at the inlet; the maximum temperature gradient estimated by the simulation tool for this case study is almost 1ºC. With this air volume the mean velocity into the air cooling channels is also estimated to be 4.4 m/s; looking at Figure 6.15, the static pressure of the

designed cooling system for this velocity is 10.4 Pa. Hence, the fan selected for the prismatic module cooling system needs the following specifications:

- $v_{fan(min)}$: 1.2 m^3/min
- $p_{fan(min)}$: 10.4 Pa

When the air volume is increased over 1.2 m^3/min results are similar to the ones obtained with 1.2 m^3/min. The conclusion obtained is that there is a bottleneck due to the low thermal conductivity of the li-ion cells. Heat is not transferred fast enough to the heatsink and even if the thermal behaviour of the cooling system is improved because of higher air volumes flowing, it is impossible to extract more heat from the battery module. This problem is directly related to the cooling strategy because if the air is directly blown to the cases of the cells the forced convection heat coefficient is improved and maximum temperatures and temperature distributions are improved since heat is not conducted to another body.

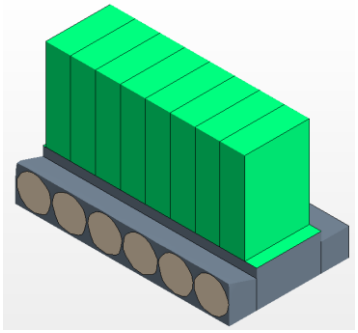

a)

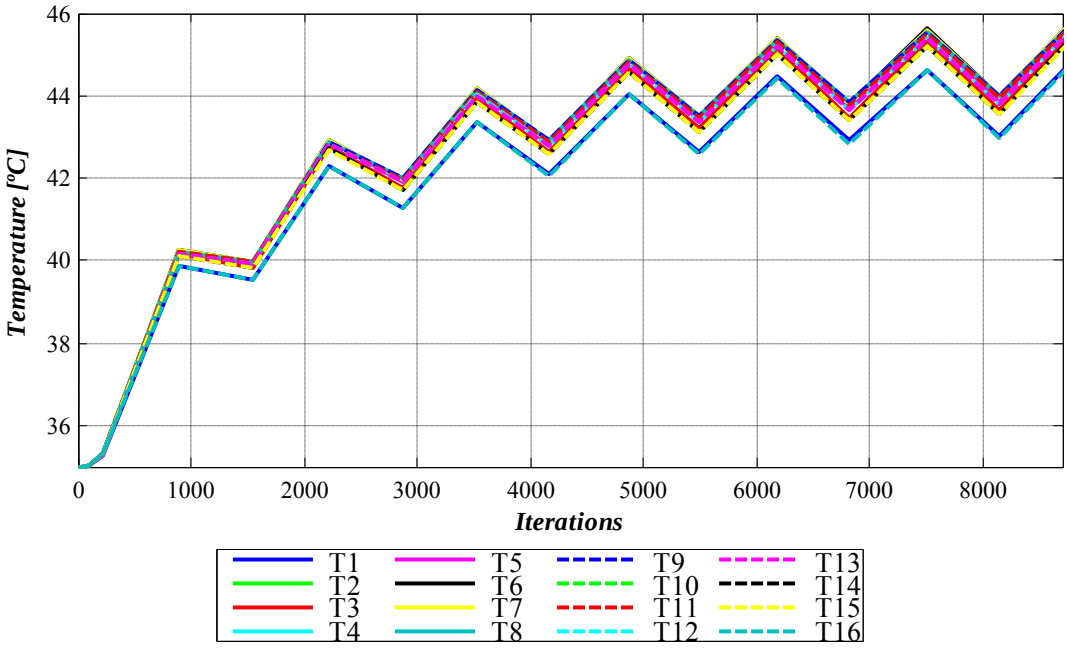

b)

Figure 6.21: Forced convection simulation results at 35ºC of ambient temperature for the prismatic module; a) Geometry model used to achieve the results; b) Transient simulation results for the prismatic module.

6.5.3.2 Cylindrical module

Figure 6.22 shows the comparison between simulation and experimental results for the cylindrical module under the final application current profile. This test is not finished experimentally because 45ºC are reached after 15 elevator cycles but the test is used to validate the simulation tool for the cylindrical module. As in the previous case, a cooling system is required to reduce the maximum temperature of the module below 45ºC because if the ambient temperature is increased to 35ºC this model will estimate a temperature over 60ºC for the cylindrical module without cooling system at the steady state.

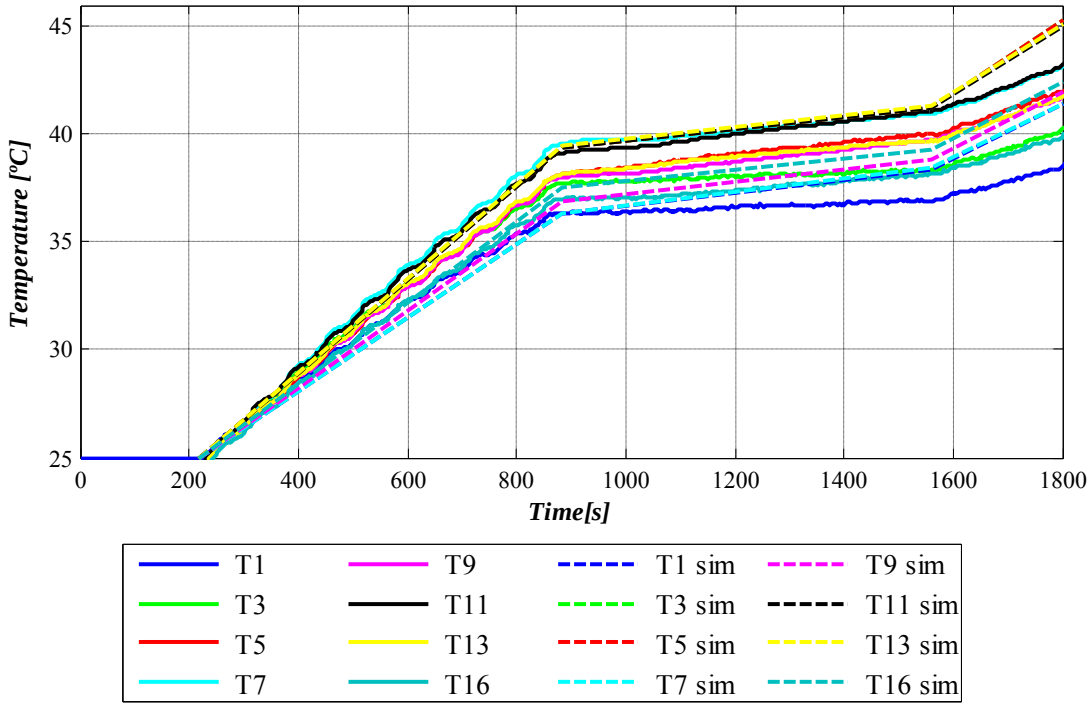

Figure 6.22: Comparison between simulation and experimental results for the final application current profile test.

The transversal forced air cooling system is chosen for this module since the static pressure drop of the longitudinal cooling is higher and the temperature gradient will be improved if the transversal cooling strategy is used. Figure 6.23 a shows the simulation model used to simulate the cylindrical module with the transversal forced air cooling system. The flow channel is increased in this model to get a uniform air velocity distribution at the outlet of the model. It is concluded that an air flow of 0.5 m^3/min is required to reduce the maximum temperature of the module below 45ºC. Figure 6.23 b shows the results of the simulation for the final application current profile. For an air flow of 0.5 m^3/min, this cooling system generates a static pressure drop of 89 Pa according to the results presented in Figure 6.17. Thus, the requirements of the selected fan for this application will be: $v_{fan(min)}$ = 0.5 m^3/min and $p_{fan(min)}$= 89 Pa. Although the requirements are more exigent than the ones for the prismatic module fan, the transversal forced air cooling strategy does not require high air flow values and high

pressure drop values. For the same air flow, the longitudinal forced air cooling strategy requires more than 500 Pa, an important drawback to choose the suitable fan.

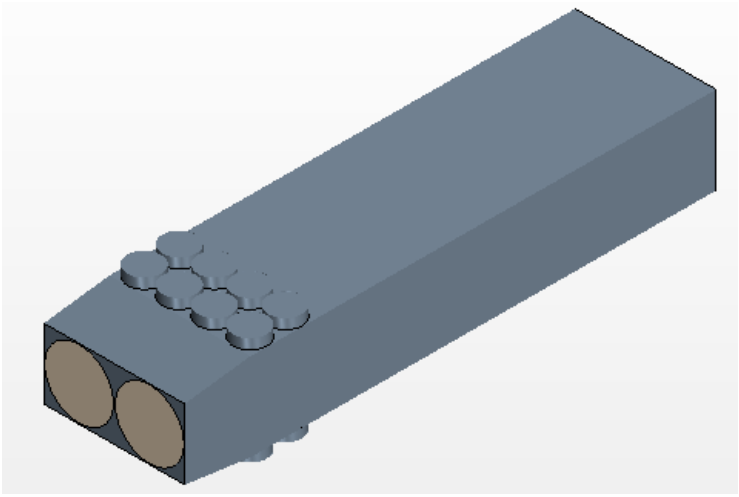

a)

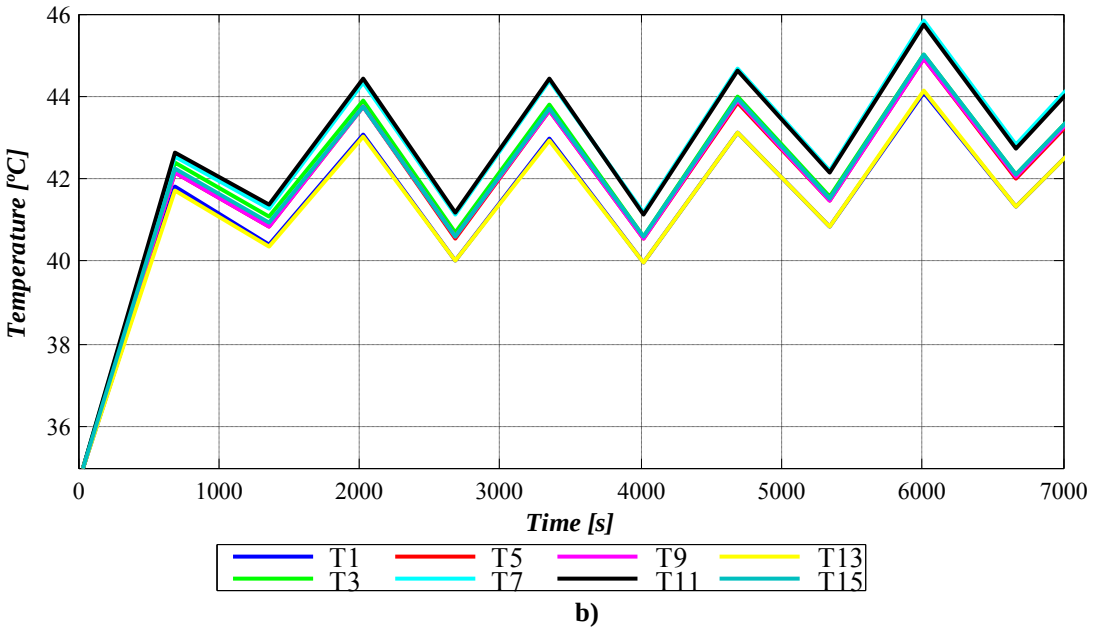

b)

Figure 6.23: Forced convection simulation results at 35ºC of ambient temperature for the cylindrical module; a) Geometry model used to achieve the results; b) Transient simulation results for the cylindrical module.

6.5.3.3 Pouch module

Figure 6.24 shows the comparison between the simulated and the experimental results for the pouch module under the final application current profile and an ambient temperature of 25ºC. The maximum error measured in this simulation is of 2ºC between simulation and experimental results. In the simulation, the temperature gradient estimated is lower than in the experimental tests; the reason is that in the simulation the contact interface between the cell and the aluminium heatsink plate is considered almost ideal, but in the reality a higher thermal resistance appears between these bodies. As a consequence, better temperature distributions are obtained with the simulation tool. If

the ambient temperature is increased to 35ºC in this simulation, the simulation tool estimates temperatures over the maximum temperature permitted, 45ºC.

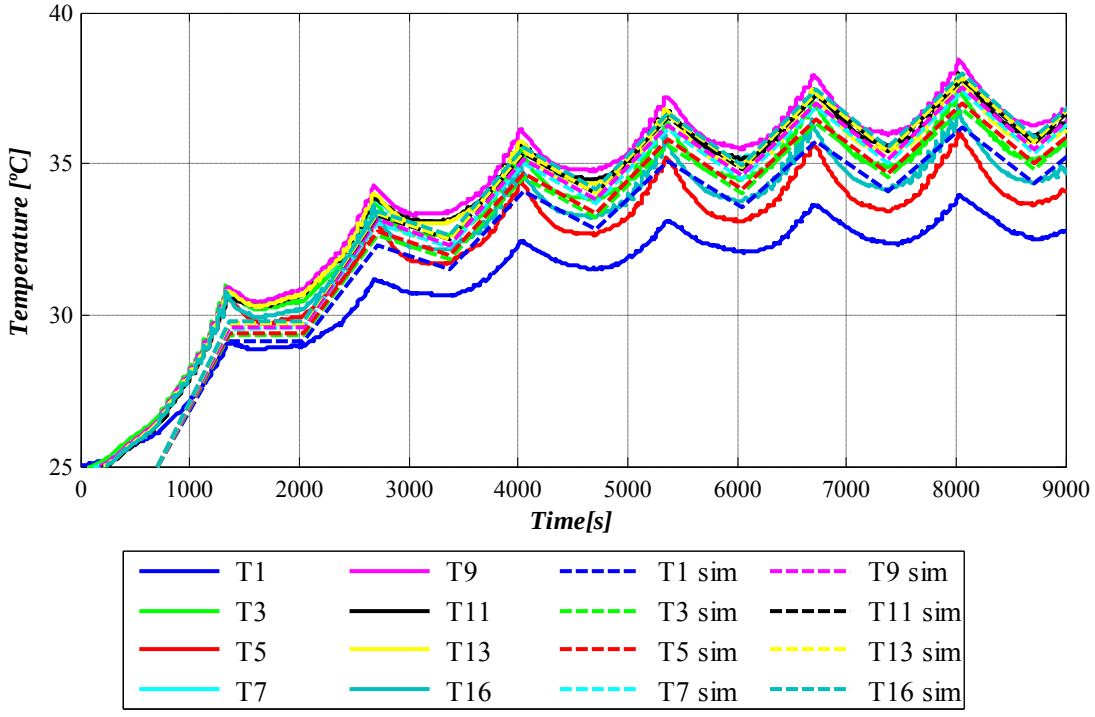

a)

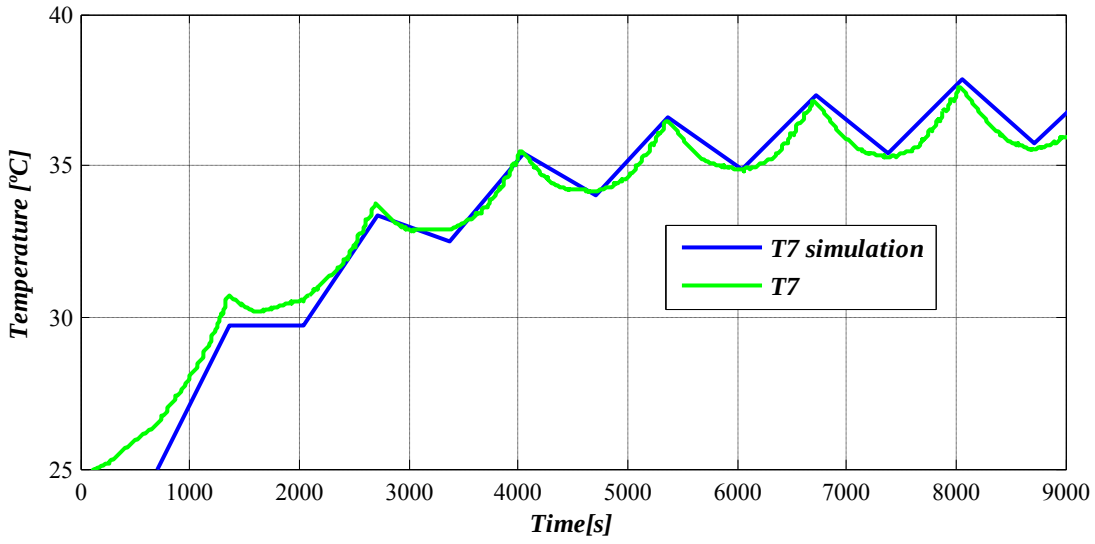

b)

Figure 6.24: Comparison between simulation and experimental results for the final application current profile test; a) One thermocouple per cell; b) Thermocouple T7.

Figure 6.25 shows the model used to simulate the pouch module under forced convection cooling; according to the results presented in this figure, the minimum air flow required by this module to avoid temperatures over 45ºC is 0.45 m^3/min. With this air flow, the maximum temperature reached by the module close to the steady state is 44 ºC for the simulation under the final application current profile and an ambient temperature of 35ºC. Looking at Figure 6.19, the static pressure drop for an air flow of

0.45 m^3/min is 10 Pa. Thus, the fan selected for the cooling system of the pouch module has the following requirements: $v_{fan(min)}$ = 0.45 m^3/min and $p_{fan(min)}$= 2.4 Pa.

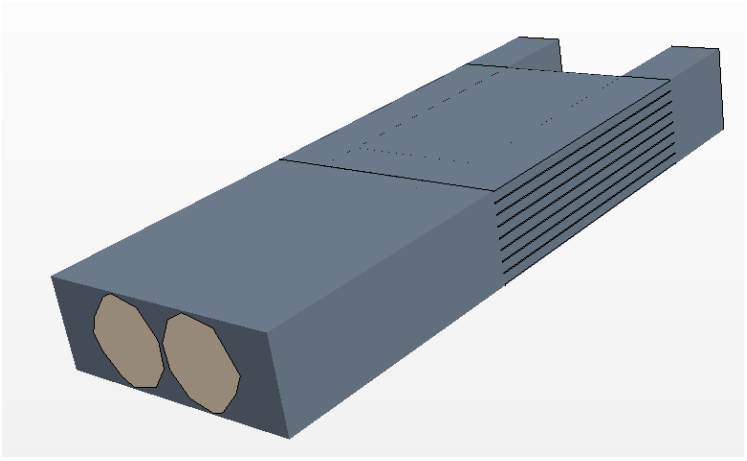

a)

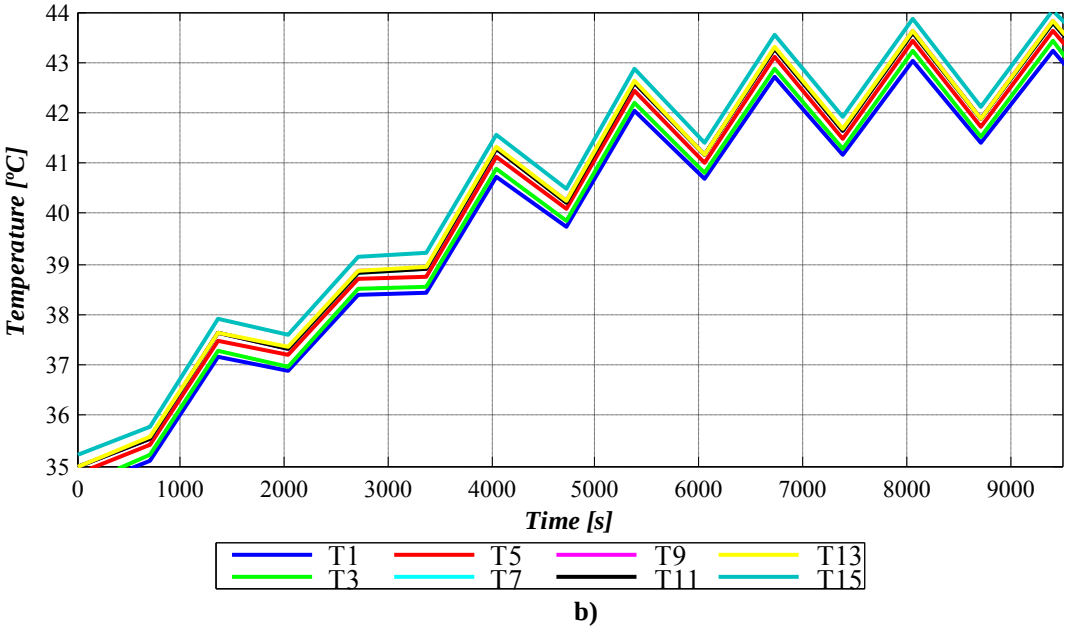

b)

Figure 6.25: Forced convection simulation results at 35ºC of ambient temperature for the pouch module; a) Geometry model used to achieve the results; b) Transient simulation results for the pouch module.

6.6 Validation of the methodology

In order to validate the proposed methodology the designed forced air cooling systems are included into the real modules; static pressure measurements are done in the cooling systems designed with the "Pitot tube" to validate the static pressure curve obtained from simulations. Besides, experimental tests with the three modules under 25ºC and 35ºC ambient temperatures are compared with simulations to evaluate the accuracy of the simulation tool.

6.6.1 Prismatic module

Figure 6.26 shows the final assembly of the prismatic module with the forced air cooling system designed; the fans selected for this module are the sanyo denki 9GA0424P3M0011 axial low power consumption square fans. The dimensions of this fan are 40x40x28 mm and their supply voltage is 24V. The velocity of this fan can be controlled by a *PWM* input and its power consumption for the maximum velocity is 2.64W. Its rated static pressure is 250 Pa and its maximum air volume is 0.46 m^3/min without any load.

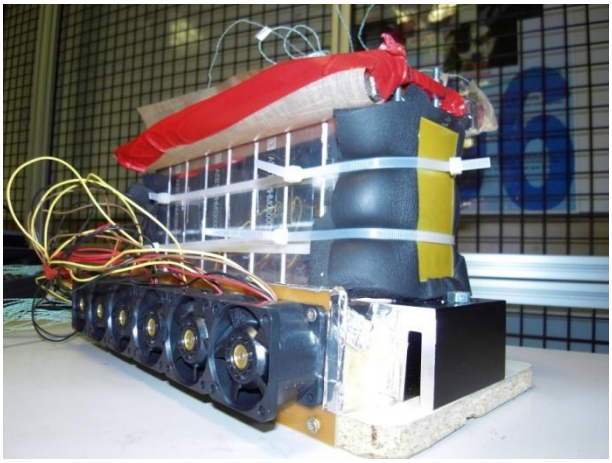

Figure 6.26: Experimental assembly of the prismatic module with the forced air cooling system designed.

The "Pitot tube" has been used to measure the static pressure of the system close to the fans location and to measure the dynamic pressure to calculate the air velocity into the cooling channels of the heatsink for this case. Two different *PWM* values have been applied to measure different working points of the fans: 100% and 50%. Figure 6.27 shows the comparison between the simulation and experimental results; for 50% duty cycle the average dynamic pressure measured into the cooling channels is 19.2 Pa.

$$v = 60\left(\sqrt{\frac{2P_d}{\rho}}\right)S_{cool} \qquad \textbf{(6.2)}$$

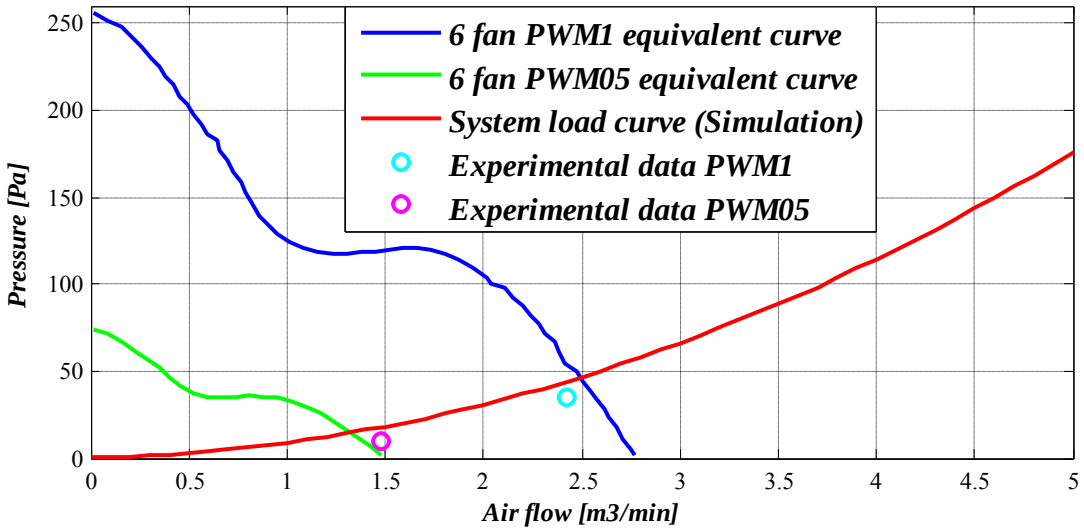

Figure 6.27: Validation of the working points of the fans for the prismatic module.

From equation (6.2) the air flow (v) at the inlet of the cooling system is estimated to be 1.42 m^3/min. P_d is the dynamic pressure measured with the "Pitot tube", ρ is the air density and S_{cool} is the surface of the cooling channels within the heatsink. Afterwards, the static pressure value is directly measured with the "Pitot tube"; for this case the static pressure measured is 12 Pa. When the duty cycle of the *PWM* input is increased to 100% the average dynamic pressure measured is 50.9 Pa that is equivalent to 2.4 m^3/min air flow inlet. For this case the static pressure measured is 30 Pa. Thus, the working points simulated for the cooling system of the prismatic module agree with the results obtained experimentally with the "Pitot tube".

Finally, the real module is exposed to the same conditions as the simulated ones to evaluate the accuracy of the simulation tool. Figure 6.28 b compares the results obtained experimentally and by simulation for the final application current profile at 25ºC of ambient temperature; a maximum error of 2ºC is committed by the simulation tool.

Similar results are obtained when the ambient temperature is increased in the simulation or if the air volume at the inlet of the cooling system is changed. In the case of an ambient temperature of 35ºC the experimental results measured are between 42ºC and 43ºC since the simulation results are between 43ºC and 45ºC. Since the target of the simulation tool is not to estimate accurately the temperatures of the module and taking into account the simplicity of the model utilized for this purpose, it is considered that the simulation tool can help into the design of the cooling system of the modules, although several improvements can be included to improve its accuracy.

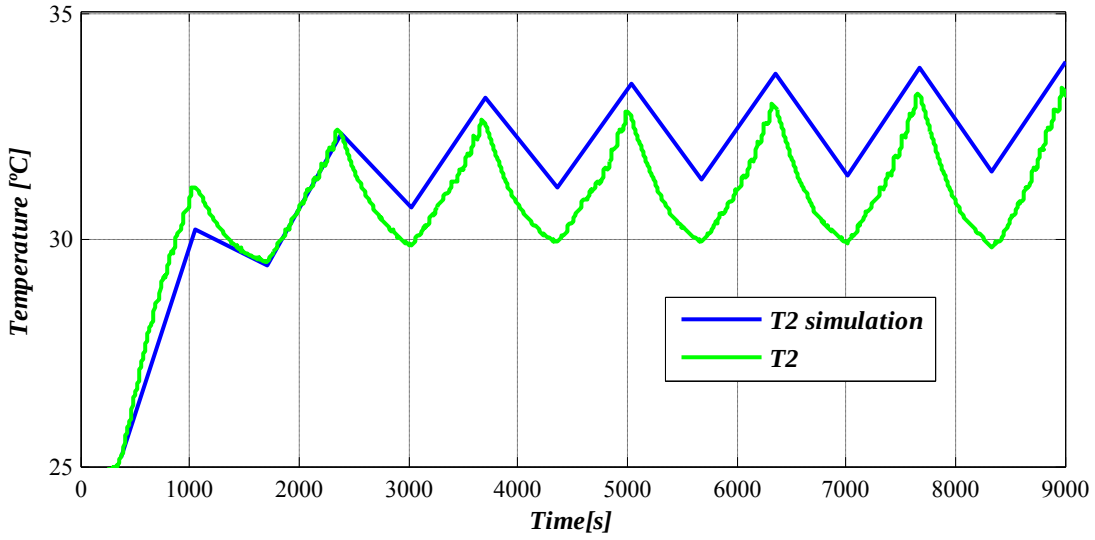

a)

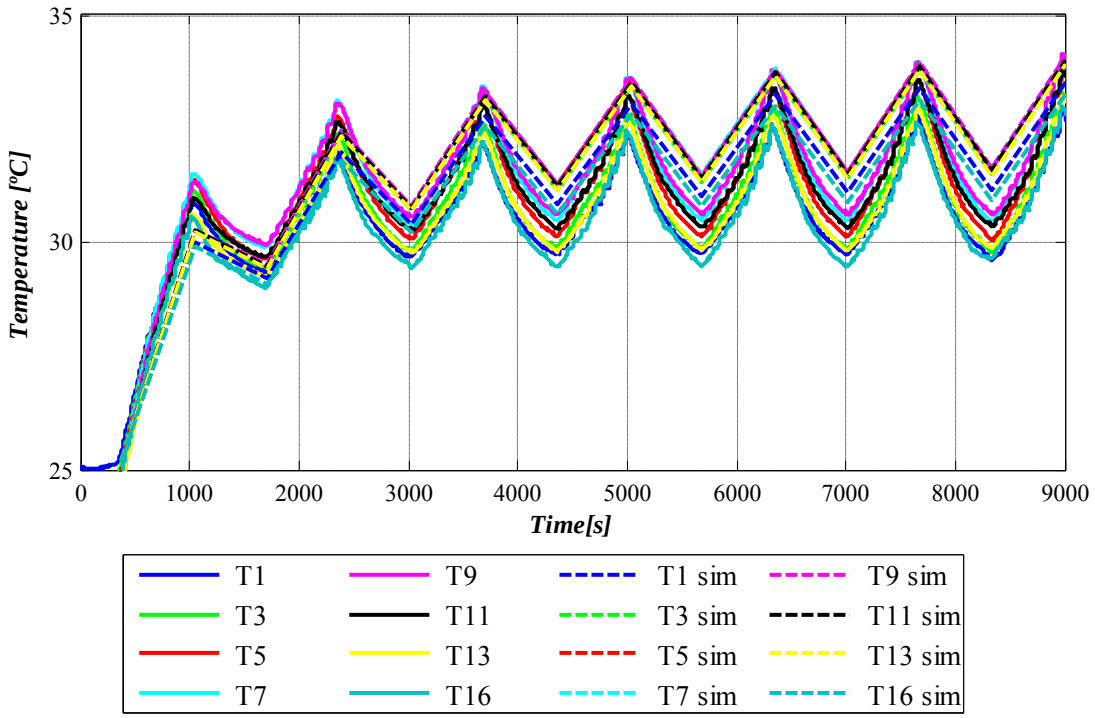

b)

Figure 6.28: Validation of the simulation tool for the final application current profile and 25ºC of ambient temperature; a) Results for T2; b) Results for 8 thermocouples.

6.6.2 Cylindrical module

Figure 6.29 shows the final assembly of the cylindrical module with the transversal forced air cooling system designed; the fans selected for this module are the sanyo denki 9GA0824P2S0011 axial low power consumption square fans. The dimensions of this fan are 80x80x32 mm and their supply voltage is 24V. They have the *PWM* input to control the fan velocity and their power consumption for the maximum velocity is

10.1W. Their rated static pressure is 360 Pa and its maximum air volume is 2.45 m^3/min without any load.

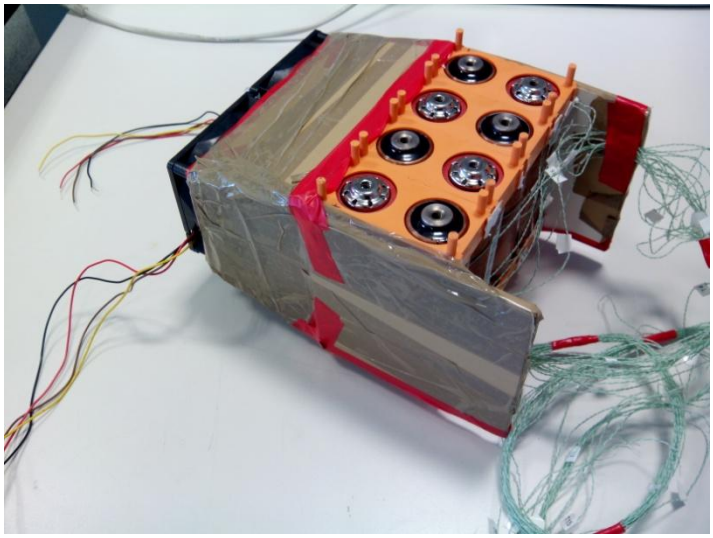

Figure 6.29: Experimental assembly of the cylindrical module with the transversal forced air cooling system.

Following the procedure presented for the prismatic module, the "Pitot tube" has been used with the cylindrical module to validate the methodology. Figure 6.30 shows the validation of the working points of the fans selected for the cylindrical module with a *PWM* input of 100% and with a *PWM* input of a 50%; with an input of 100% the dynamic pressure P_d measured is 150 Pa. According to the equation (6.2) and with an effective surface of 0.00097 m^2, the air flow measured in the cooling system is 0.92 m^3/min. For a *PWM* input of 50% the P_d measured is 72 Pa; the air flow estimated for these working conditions is 0.64 m^3/min. The simulated working points agree with the experimental measurements acquired with the "Pitot tube".

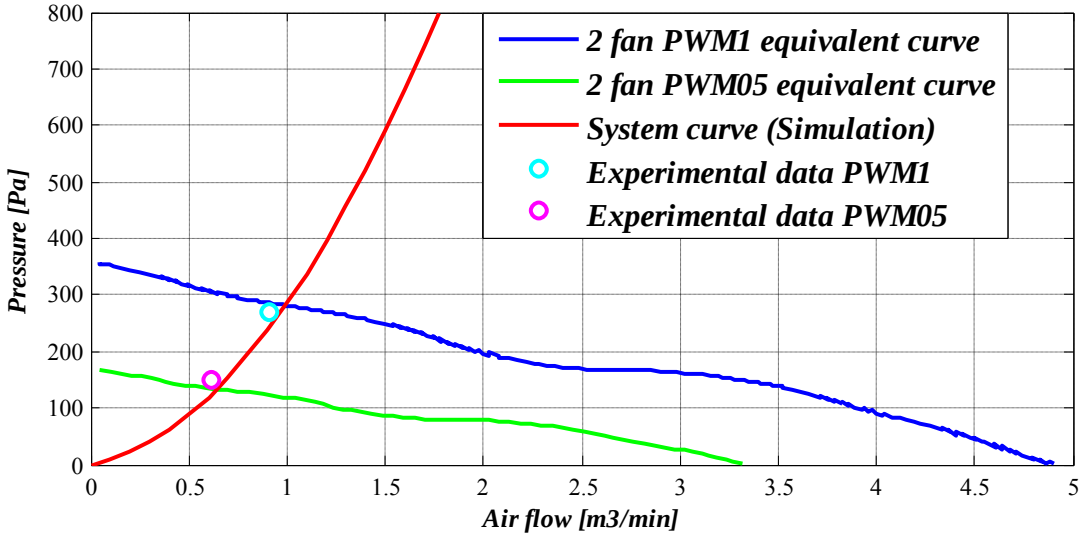

Figure 6.30: Validation of the working points of the fans for the cylindrical module.

Finally, Figure 6.31 shows the validation of the simulation tool for experimental test; the conditions for this experimental test are a *PWM* input of 100% for the fans of the cooling system, 25ºC of ambient temperature and the final application current profile. A maximum error of 2ºC is measured for this simulation; according to the results, the internal heat generation estimated is higher than the real one. However, since the aim of the simulation tool is to help into the design of the cooling system, the results are considered to be suitable for this purpose.

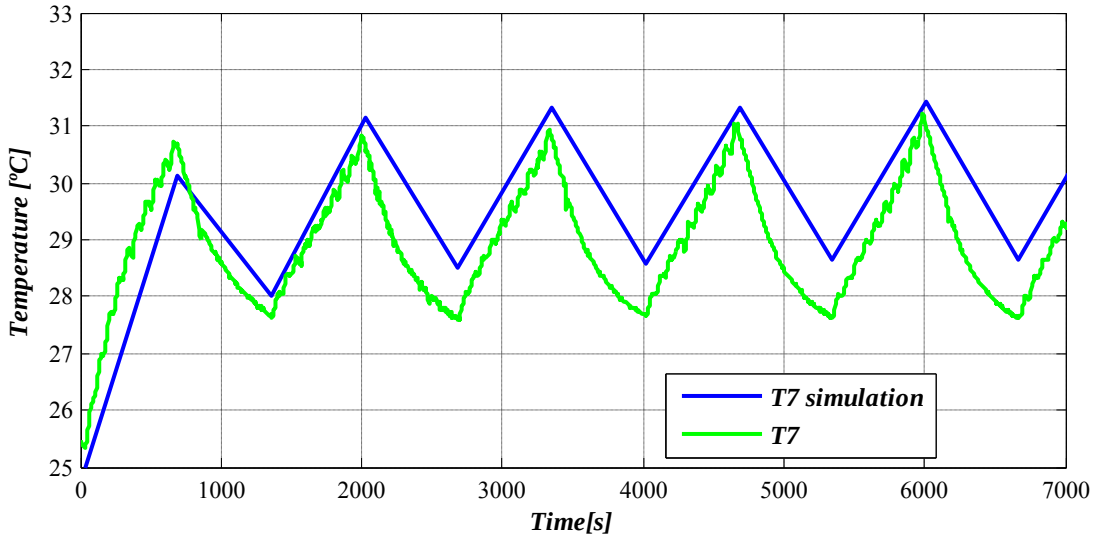

a)

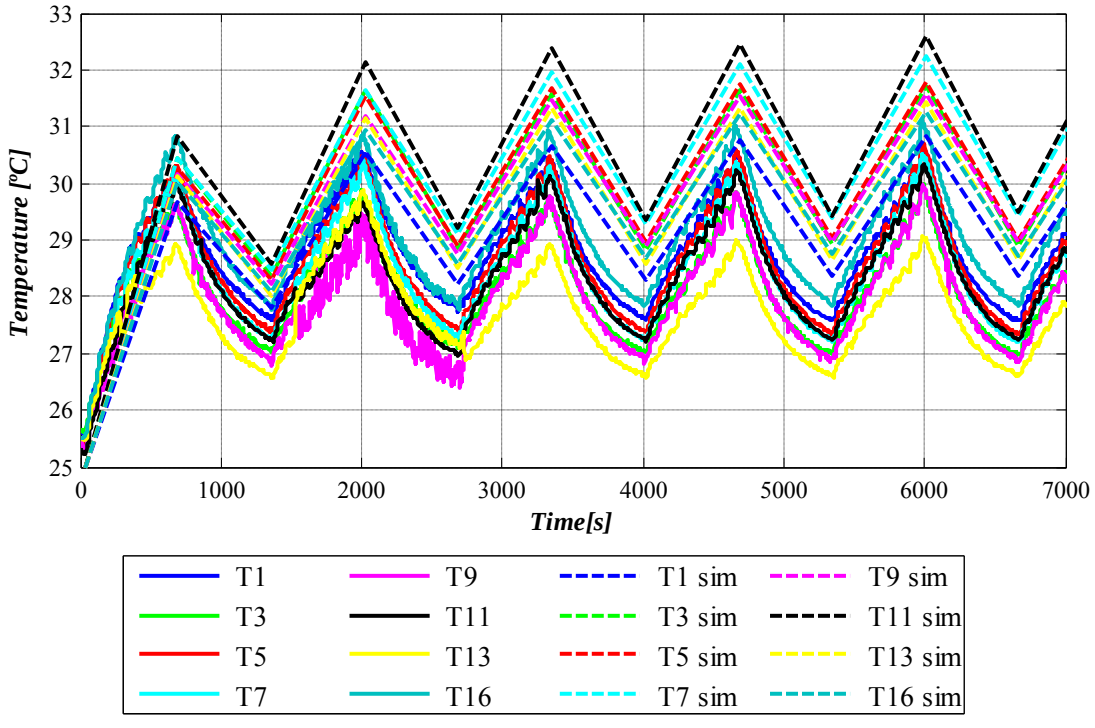

b)

Figure 6.31: Validation of the simulation tool for the final application current profile and 25ºC of ambient temperature; a) Results for T7; b) Results for 8 thermocouples.

6.6.3 Pouch module

Figure 6.32 shows the final assembly for the pouch module in this work; the cooling system designed takes advantage of the chimney effect to blow air through the air channels between the heatsink plates of the cooling system.

Figure 6.32: Experimental assembly of the pouch module with the designed forced air cooling system.

Comparing the final assembly with the other modules, the weight of this module is higher due to the amount of parts required to assemble the cells within the module. The fans selected for the cooling system are the sanyo denki 9GA0824P4G001; the dimensions of the fan are 80x80x25. The rated power is 5W, the rated air flow is 1.91 m^3/min without any load, and the rated static pressure drop is 150 Pa. As in the previous modules, these fans are controllable through a *PWM* regulated input.

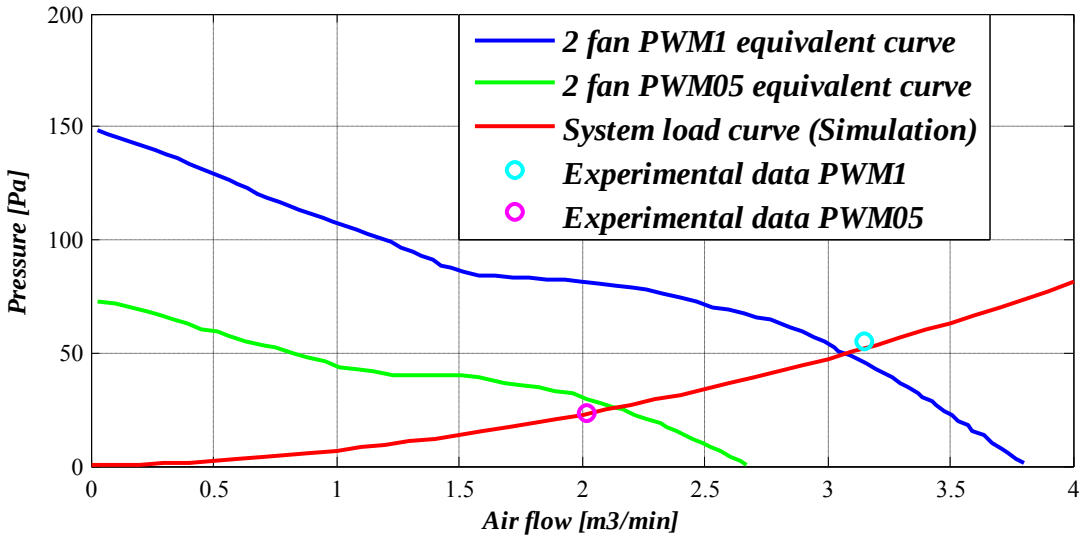

Figure 6.33: Validation of the working points of the fans for the pouch module.

Figure 6.33 shows the validation of the working points of the fans for two different *PWM* values; with a *PWM* of 100%, the simulation tool estimates an air flow 3.05 m^3/min with an static pressure of 50 Pa, and the experimental measurements with the "Pitot tube" measured 3.15 m^3/min with an static pressure of 56 Pa. When the PWM input is reduced to a 50%, the simulation tool estimates an air flow of 2.17 m^3/min with an static pressure drop of 30 Pa; the experimental measurements are 2 m^3/min air flow and an static pressure drop of 28 Pa. Figure 6.34 shows the validation of the simulation tool for the pouch module. The maximum error measured in this case is close to 2ºC between simulation and experimental results.

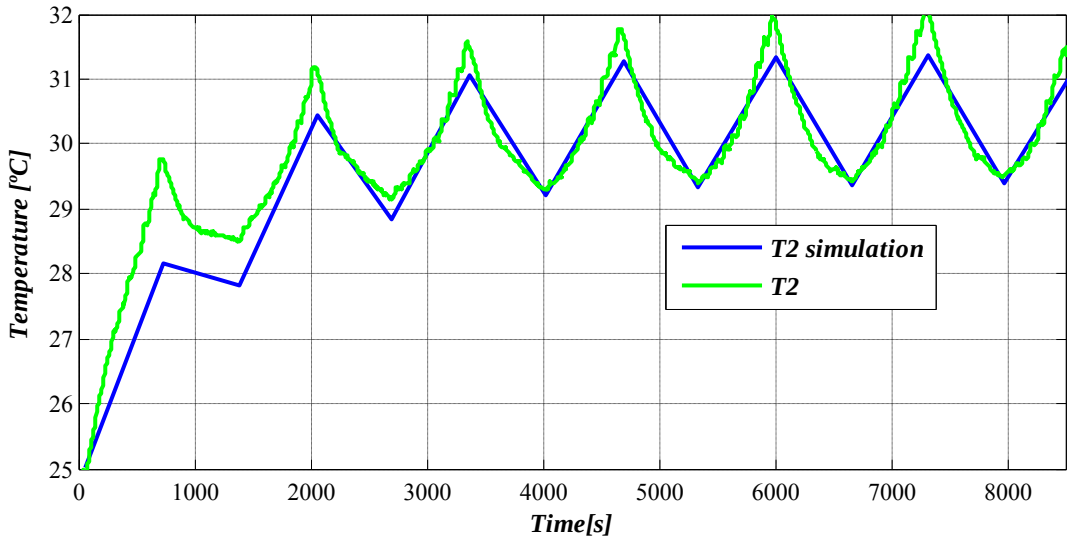

a)

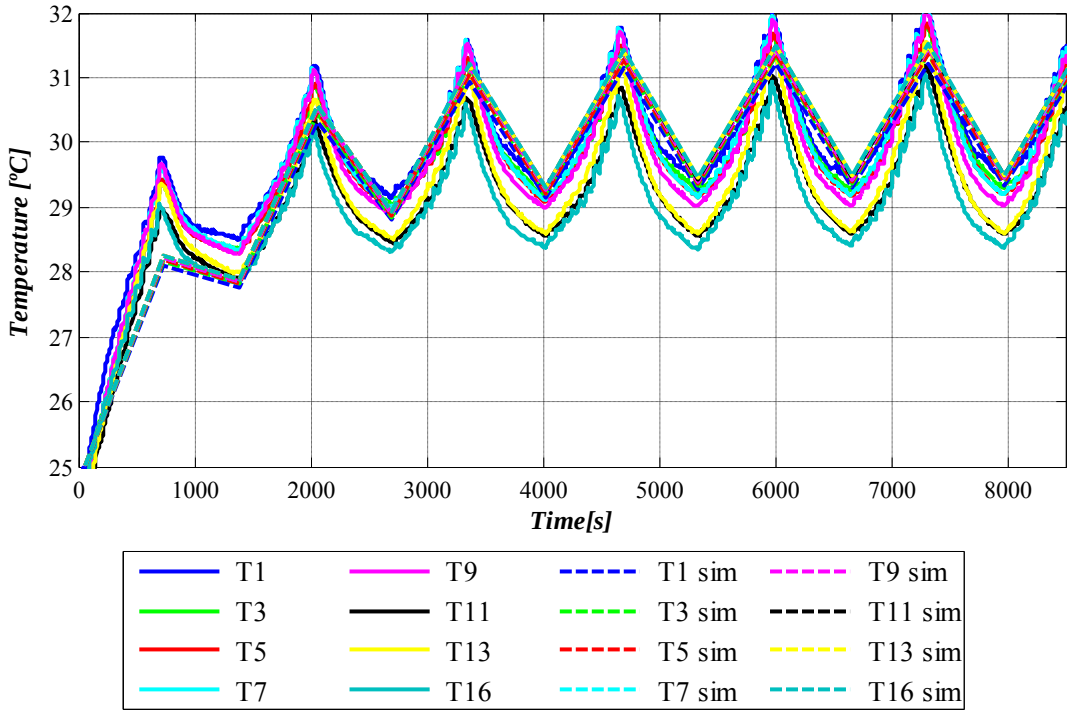

b)

Figure 6.34: Validation of the simulation tool for the final application current profile and 25ºC of ambient temperature; a) Results for T2; b) Results for 8 thermocouples.

6.7 Conclusions

In this chapter a methodology to design forced air cooling systems for battery modules have been presented. A *CFD* simulation tool and a simple 3D model have been used for this purpose. Besides, the requirements for the application analyzed in this work have been presented and different cooling strategies for each battery module are shown.

Talking about the internal heat generation power profile applied in the simulations, it is concluded that the computational time is reduced hugely by applying the partial mean values profile instead of the real profile. In fact, transient simulations with the timestep required for this profile can last more than 8 hours. This simplification can be done since the dynamics of the thermal response of the battery module during the elevator cycles is very slow comparing it with the dynamic of the current during this period.

The strategy to select the suitable fan for each forced air cooling system has been validated with experimental results. The static pressure has been estimated with an error less than 10 Pa for different flow volumes. Besides, the forced air cooling simulations conducted to estimate the air flow required to reach the application requirements have been validated with an error below 0.3 m^3/min. With the developed methodology it is possible to estimate the working point of the fan and apply in simulation the air flow that is being applied during the experimental test.

Regarding to the cooling strategies, including a heatsink to extract heat from the battery module permits a more compact prismatic module. However, it is impossible to improve the behaviour of the cooling system increasing the air flow over 0.024 m^3/min. The reason is that the thermal conductivity of the cell is not high enough to transfer energy from the cells to the heatsink with the current design. Despite this fact, the prismatic module with the forced air cooling system reaches the specifications of the application. The transversal and the longitudinal forced air cooling have been tested with the cylindrical module. The static pressure curve reaches high values if the longitudinal forced air cooling is used; it is possible to use only one fan with this strategy and the cylindrical module, however, the dimensions of this fan are also increased comparing them with the fan of the transversal cooling strategy.

Finally, it is concluded that the developed methodology and the simulation tool are suitable to help in the design of forced air cooling systems for battery modules. The maximum error of 2ºC is acceptable taking into account the simplicity of the model.

Next chapter deals with the analysis of the experimental results obtained comparing the modules with cooling system and without it. Besides, the lifespan of all the modules is estimated taking into account the aging behaviour of a cell from bibliography. The objective of the chapter is to quantify the improvement achieved by including the cooling systems in the battery modules.

Chapter 7. ANALYSIS OF THE PERFORMANCE IMPROVEMENT AFTER THE THERMAL OPTIMIZATION PROCESS.

During the following chapter, a summary of the results obtained in this work for the different modules analyzed is done. The current battery modules with forced air cooling systems are compared with the same modules without the cooling systems; the main variables to analyze are the maximum temperature and temperature distribution, but other parameters like the size of the module or the consumption of the cooling system are also taken into account. After an introduction around the different sections of the chapter, the summary of the results mentioned before is presented. After that the forced air cooling systems designed are analyzed in terms of power consumption and cost. Finally, the deceleration of the aging process of the battery modules due to the thermal optimization is analyzed and quantified. An aging pattern of a li-ion cell is used to calculate the aging process with and without thermal optimization to quantify the total energy delivered by the module during its life. At the end of the chapter, the main conclusions achieved from the chapter are presented.

7.1 Introduction

Three different battery modules have been assembled in this work to fulfil all the requirements of a power application in the field of elevators. Besides, forced air cooling systems have been added to the three modules in order to improve their thermal behaviour. Applying the final application current profile to the modules under test in this work a discharging peak power of almost 1.5 kW is delivered and a charging peak of 500 W is absorbed.

TABLE 7.1 summarizes all the experimental tests done to get the results presented during the chapter. The final application current profile has been applied in all the experimental tests for ambient temperatures of 25ºC and 35ºC.

TABLE 7.1 SUMMARY OF THE EXPERIMENTAL TEST RESULTS PRESENTED IN THIS CHAPTER

	Final application current profile			
	No cooling		*With cooling*	
	25ºC	*35ºC*	*25ºC*	*35ºC*
Prismatic	Yes	No	Yes	Yes
Cylindrical	No	No	Yes	Yes
Pouch	Yes	No	Yes	Yes

The objective of the chapter is to check if the thermally optimized battery modules are able to meet the requirements of the final application. Besides, an analysis of the aging processes of the modules will be done regarding to their working temperatures. Taking into account information from bibliography, a general aging pattern for li-ion cells is defined; this pattern is used to calculate the aging of each cell in each module for the case without cooling system first and after that for the case with cooling system. After the estimation of the aging processes due to temperature the energy delivered by the module during its life will be calculated. The most aged cell will limit this energy amount because of the energy loss and the power capability reduction. The end of life criteria will be previously defined to be the same for all the cases analyzed.

7.2 Results for the final assemblies

Following, several results for the experimental tests previously mentioned are shown; after that a summary of all this tests with information about thermal behaviour is going to be presented. Before showing the results the final assemblies of the battery modules and the improvements in their layout and cooling system will be specified.

7.2.1 Battery modules final assemblies

Figure 7.1 shows the final assemblies of the battery modules tested in this work after including the forced air cooling systems. According to the prismatic module, the layout has been improved including *TIM* between cells to avoid air bubbles between them; besides the differences between the convective heat transfer coefficients of the cells within the module have been compensated including thermal insulation materials in two of these cells. The cooling system of this module is based on a heatsink mounted below the battery module and six fans blowing air through this heatsink. The thermal behaviour of this module will be compared with prismatic module without cooling system and without the insulation materials to compensate the convection heat transfer coefficient.

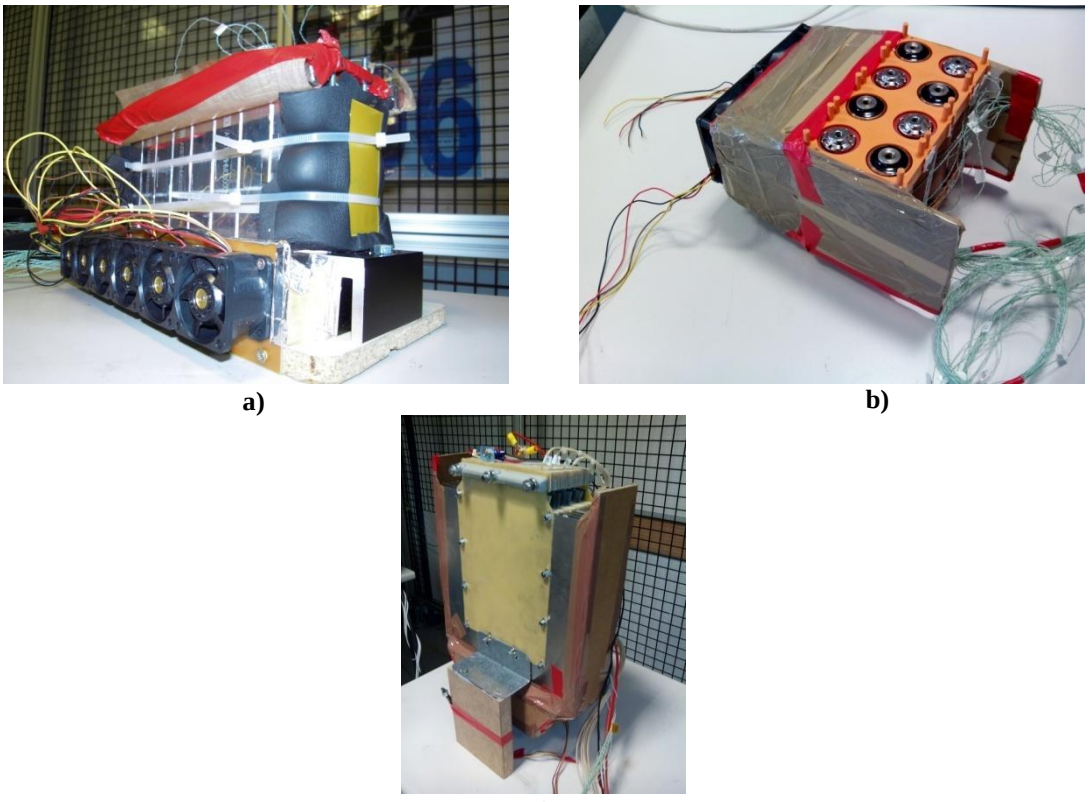

a) **b)** **c)**

Figure 7.1: Final assemblies of the modules with the forced air cooling system included.

The cells of the cylindrical module are mounted between some holders suitable for the size of the cells. The layout of the module is limited due to this mechanical design. The

forced air cooling strategy is a parallel flow forced air cooling, although experimental results for a serial flow forced air cooling will be also presented. This module will be compared with the same module without the cooling system. Finally the pouch cell module assembly is shown in Figure 7.1 c; the layout of the module is similar to the prismatic one because *TIM* are inserted between cells and aluminium layers. These layers are included on the surfaces of the cells to conduct heat to the forced are cooling channels located at both sides of the module. The forced air cooling design blows air from the bottom of the module to take advantage of the chimney effect. This module will be compared with the same module without the forced air cooling system.

7.2.2 Prismatic module results

Figure 7.2 shows the results for the final application current cycle and an ambient temperature of 25ºC; this figure evaluates the influence of the forced air cooling system designed into the overall thermal behaviour of the battery module. A temperature increase of 18ºC can be seen in the case without thermal optimization reaching a temperature of 43ºC; it is close to 45ºC which is the maximum temperature permitted in this work for experimental tests in order to avoid aging of modules. Furthermore, the maximum temperature gradient is 4.27ºC for this case. Comparing it with the prismatic module with thermal optimization and maximum velocity of fans Figure 7.2 b, the temperature increase is reduced to 9ºC reaching a maximum value of 34.2ºC. Temperature distribution is also improved reducing the gradient until 1.4ºC under the same conditions. These results are for the maximum velocity of the fans of the cooling system because the *PWM* input is set to 100%. If the *PWM* input is reduced to a 50% (Figure 7.2 c) the maximum temperature is increased to 35.9ºC and the maximum temperature gradient is also increased to 1.9ºC.The increase of the *PWM* input does not improve the behaviour of the module as much as it was expected.

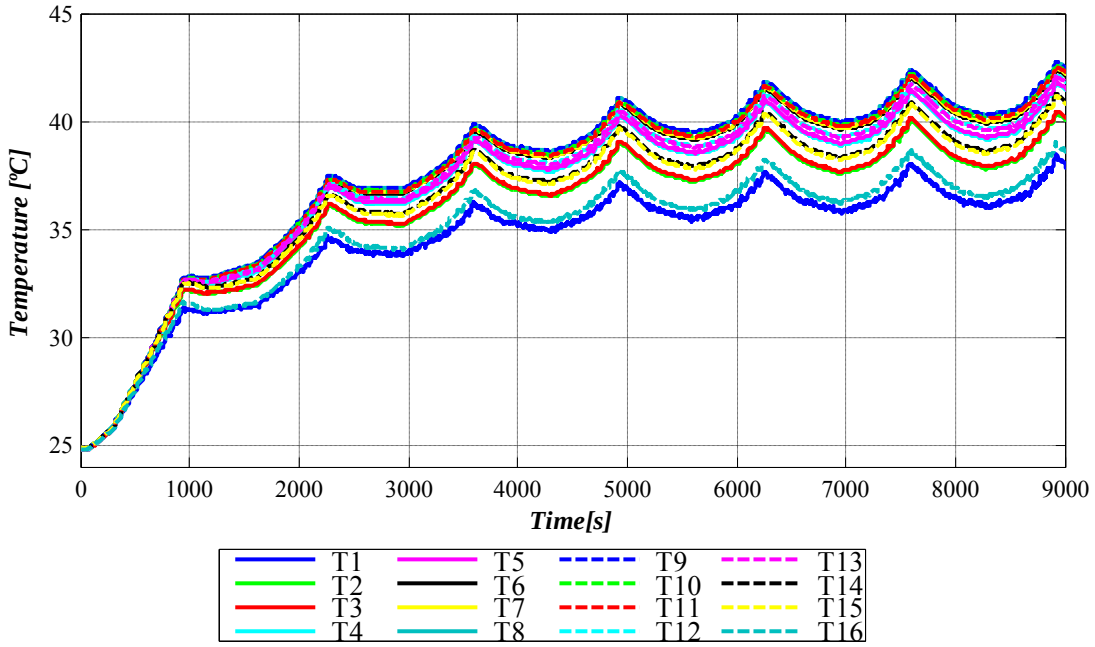

a)

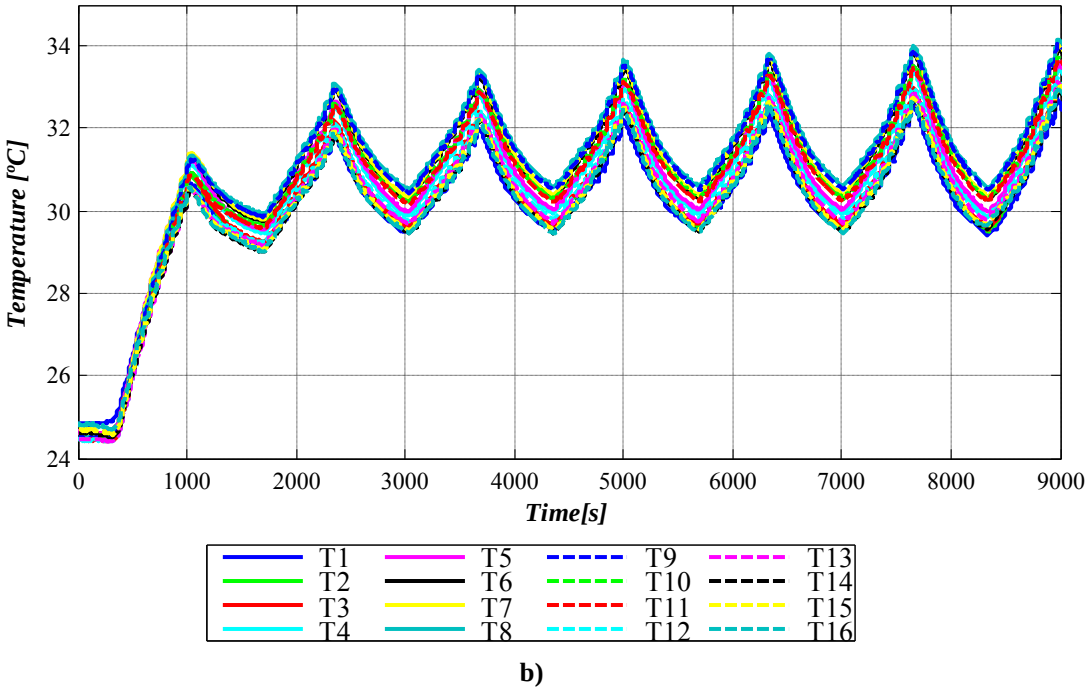

b)

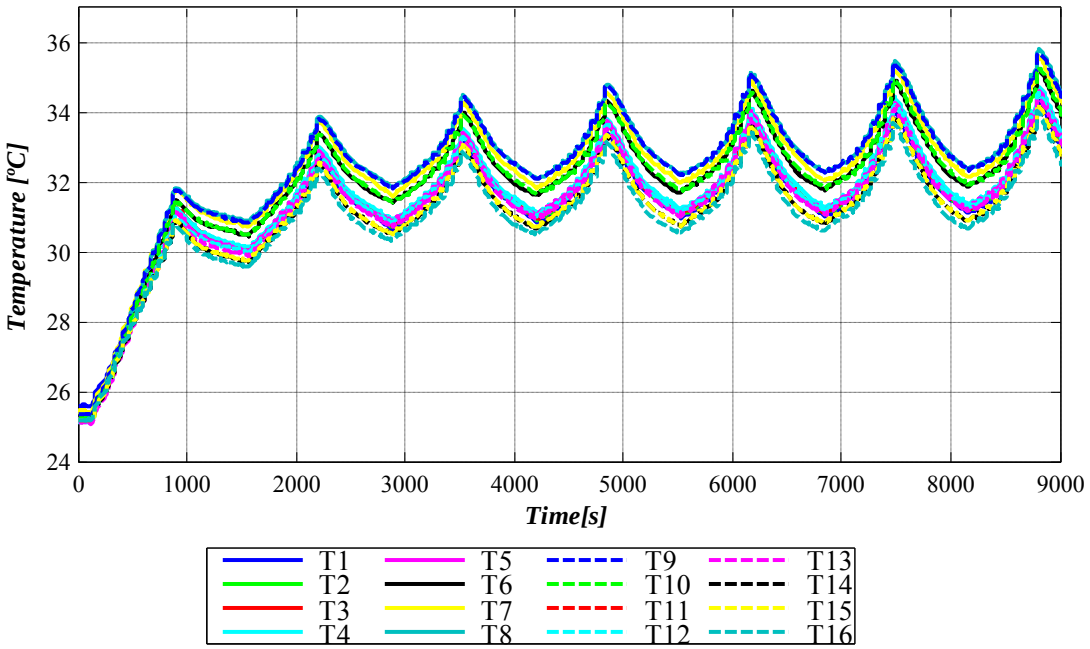

c)

Figure 7.2: Results for the prismatic module during the final application current cycle with an ambient temperature of 25ºC; a) Module without cooling system; b) Module with cooling system *PWM*=100%; c) Module with cooling system *PWM*=50%

As mentioned during Chapter 6, the reason is the low heat transfer rate from the cells to the heatsink for this design. The heatsink is kept cool with lower velocities than the maximum one due to this reason and the consumption of the cooling system can be reduced with lower values than 100% at the *PWM* input.

Figure 7.3 presents the results for 35ºC of ambient; in this case the maximum velocity possible is used in the cooling system. In this experimental test the maximum temperature reached is 43ºC and a maximum gradient of 1.3ºC. Temperature increase is 8ºC in this case; an improvement of the efficiency of the cells due to the increase of the working temperature can be seen comparing these results with the ones at 25ºC of ambient. Before including the cooling system in this module it was impossible to work under 35ºC of ambient and final application profile without reaching 45ºC.

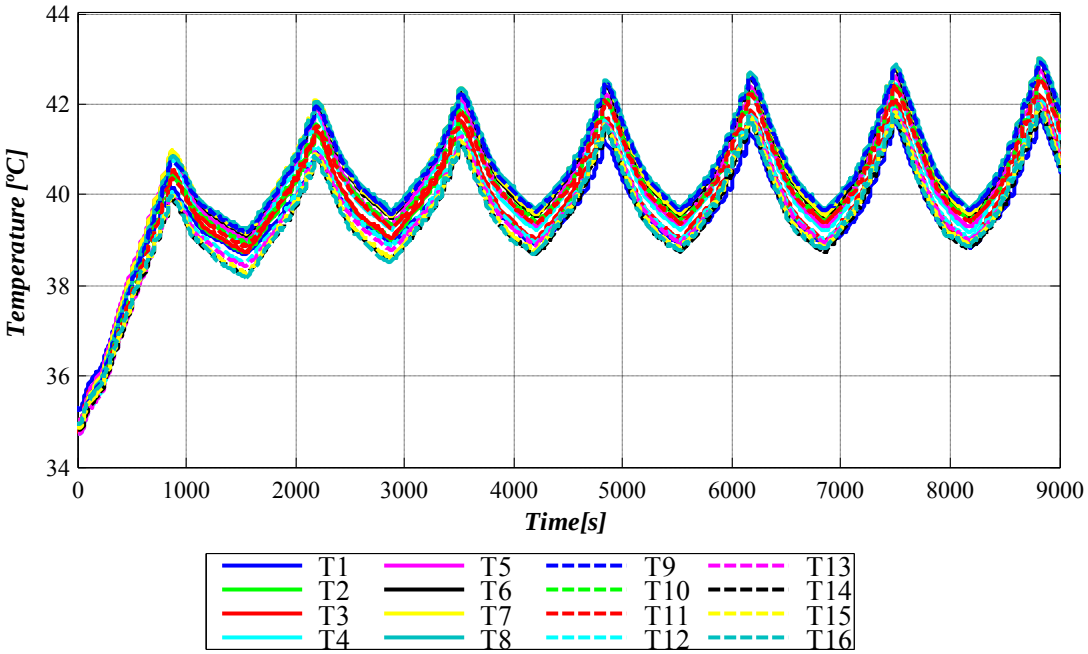

Figure 7.3: Results for the prismatic module with cooling system during the final application current cycle with an ambient temperature of 35ºC.

The power consumption of this cooling system is 14.15W when working at nominal velocity. If the *PWM* input is reduced to 50% the power consumption is also reduced to 4.8W.

7.2.3 Cylindrical module results

For the cylindrical module, it is not possible to apply the final application cycle for any ambient temperature over 25ºC without reaching the alarm temperature of 45ºC. It is compulsory to include the cooling system to be able to test the module. The internal heat generation of these cells is higher than in the prismatic or pouch ones. In this scenario, before choosing the parallel flow air cooling, experimental tests with serial cooling were also done. The reason is that in this case only one fan is used so the power consumption of the cooling system is divided by two. However, the maximum temperature and maximum gradient are hardly affected if a serial flow is utilized. Figure 7.4 shows the comparison between the two different air cooling strategies. For the serial flow cooling the maximum temperature reached is 37.47ºC, value which can be acceptable; the maximum gradient measured in the module instead is 6.62ºC for this strategy, it is an unacceptable value for our requirements.

When parallel flow forced air cooling is used, the air volume of each fan is used for four cells; the drawback is that the power consumption is doubled. According to the results, the maximum temperature is reduced to 31.83ºC, which is a very low value; the maximum gradient is hugely reduced in this case, it is 2.52ºC, a value accepted in the requirements of the work.

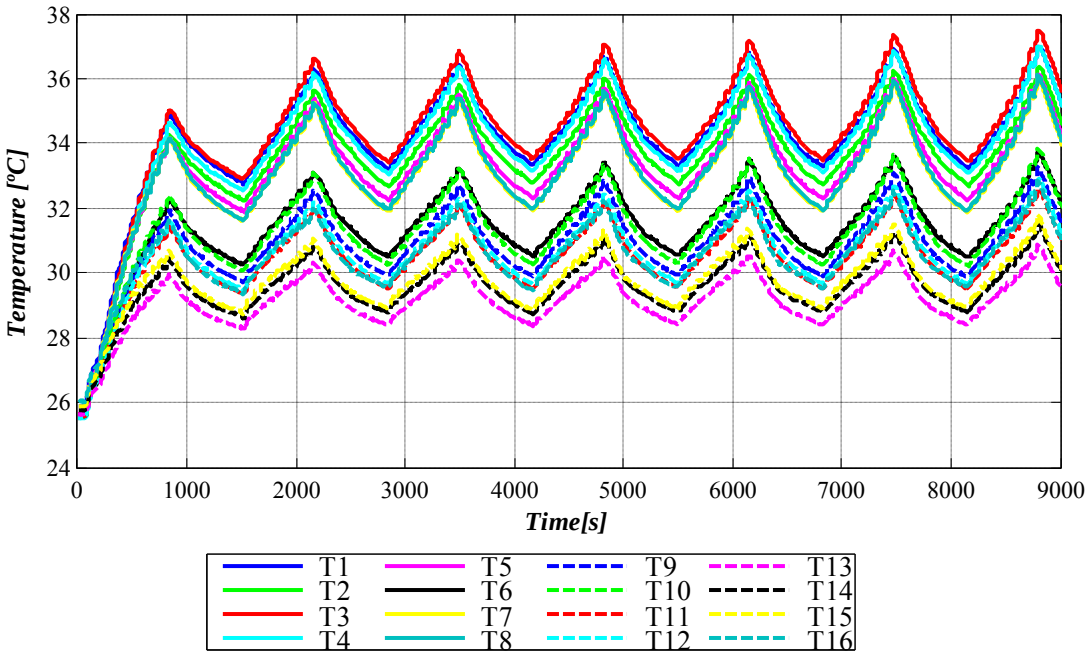

a)

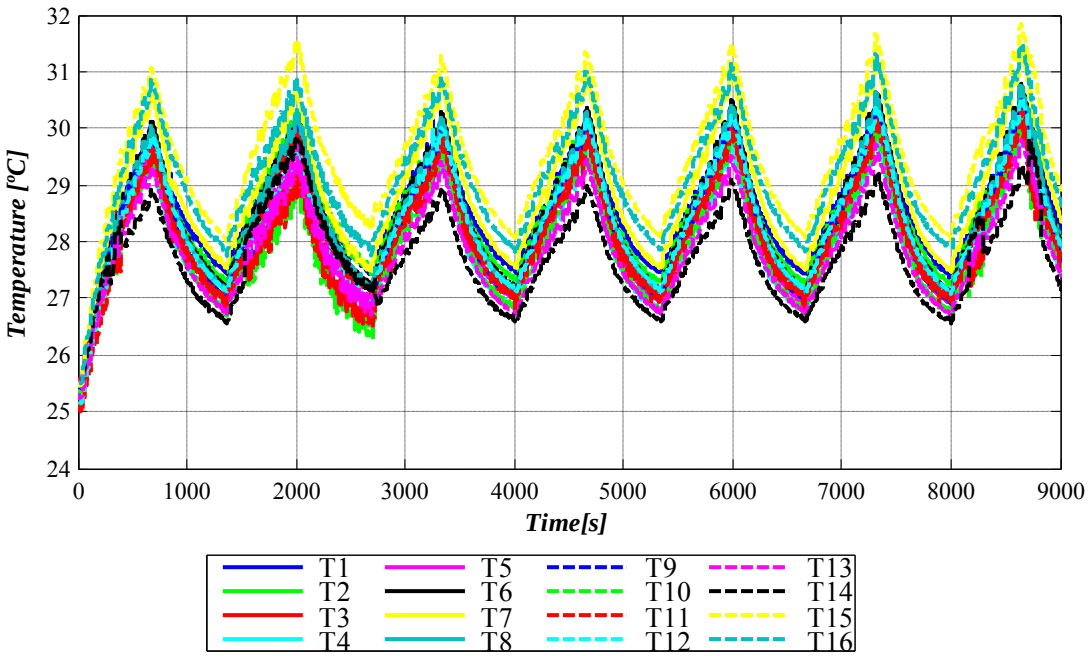

b)

Figure 7.4: Results for the cylindrical module with cooling system during the final application current cycle with an ambient temperature of 25ºC; a) Serial flow air cooling; b) Parallel flow air cooling.

It is possible to think that the air volume is too much for this module but when the ambient temperature is increased to 35ºC it is clearly seen that this air volume is required. However it is possible to reduce the *PWM* input of the fans to reduce the power consumption if the ambient is 25ºC. Maximum temperature reached is 40.6ºC and the maximum temperature gradient is 2.19ºC. The serial flow cooling strategy is not suitable under these conditions to meet the requirements of the application.

The power consumption of the parallel flow cooling system is 24W when working at nominal velocity. If the *PWM* input is reduced to 50% the power consumption is also reduced to 13.92W. In the case of serial flow the consumptions are divided by two.

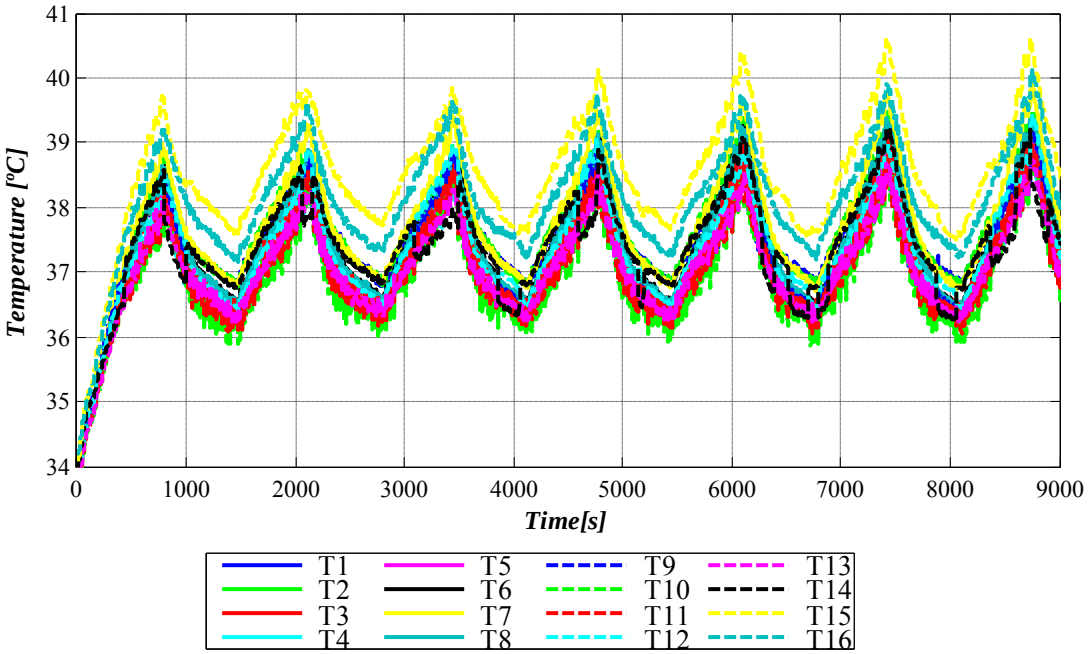

Figure 7.5: Results for the cylindrical module with parallel flow forced air cooling system during the final application current cycle with an ambient temperature of 35ºC.

7.2.4 Pouch module results

According to the pouch module Figure 7.6 shows the results for the final application current profile with an ambient temperature of 25ºC. The module without cooling system reaches a maximum temperature of 38.6ºC which means an increase of 13.6ºC. The maximum gradient in the module is measured between *T8* and *T1* and it is 4.93ºC. When the cooling system is included in the module thermal behaviour is improved reaching a maximum temperature of 32.22ºC and a maximum gradient of 1.1ºC. This improvement is due to the increase of the heat transfer coefficient between the aluminium heatsinks and the ambient. In this case it is clearly seen the effect of this increase not only on the maximum temperature, but in the temperature distribution.

If the ambient temperature is increased to 35ºC the module without cooling system is unable to deliver the energy demanded by the application without reaching the maximum temperature of 45ºC. In the case of the module with cooling system, the

maximum temperature of the module can be limited to 41ºC for the whole experimental test. Besides, the maximum temperature gradient is also reduced to 1.2ºC.

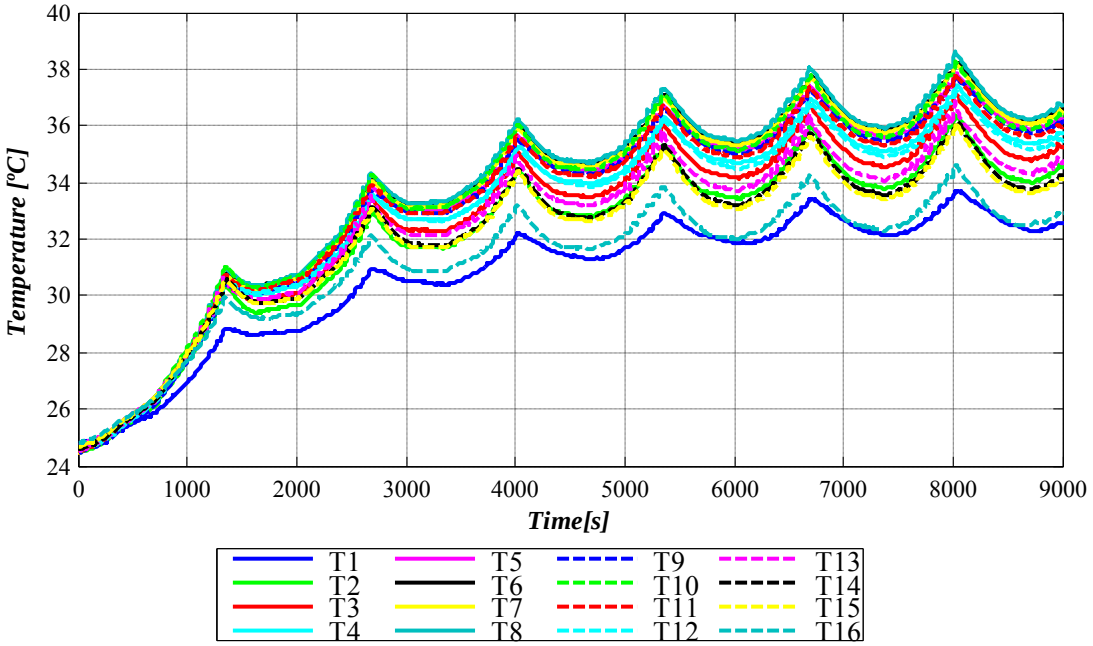

a)

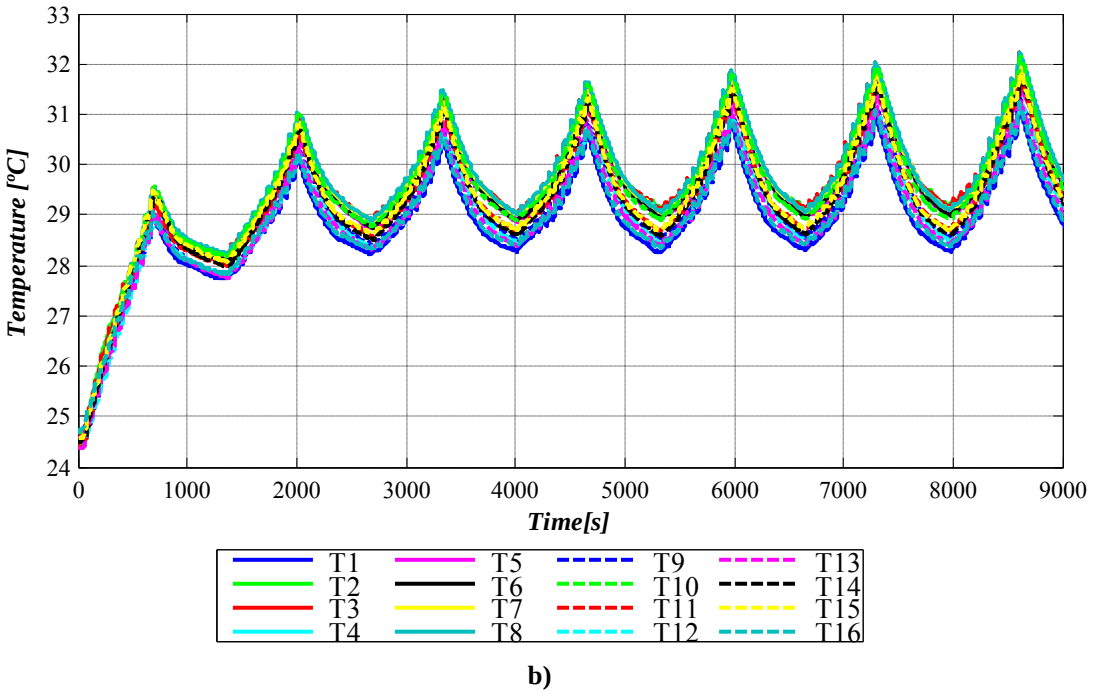

b)

Figure 7.6: Results for the pouch module during the final application current profile with an ambient temperature of 25ºC; a) Module without cooling system; b) Module with cooling system.

As in the case of the previous modules the air volume injected during these experimental tests is 100% of the maximum velocity of the fans. However, it is possible to regulate the *PWM* input of the fans to obtain lower power consumption if necessary. Reducing this velocity the maximum temperature will be increased but also the

maximum gradient, influencing the uneven aging processes for the cells within the module.

The power consumption of this cooling system is 11W working at nominal velocity, and 3.6W working at 50% of the nominal velocity.

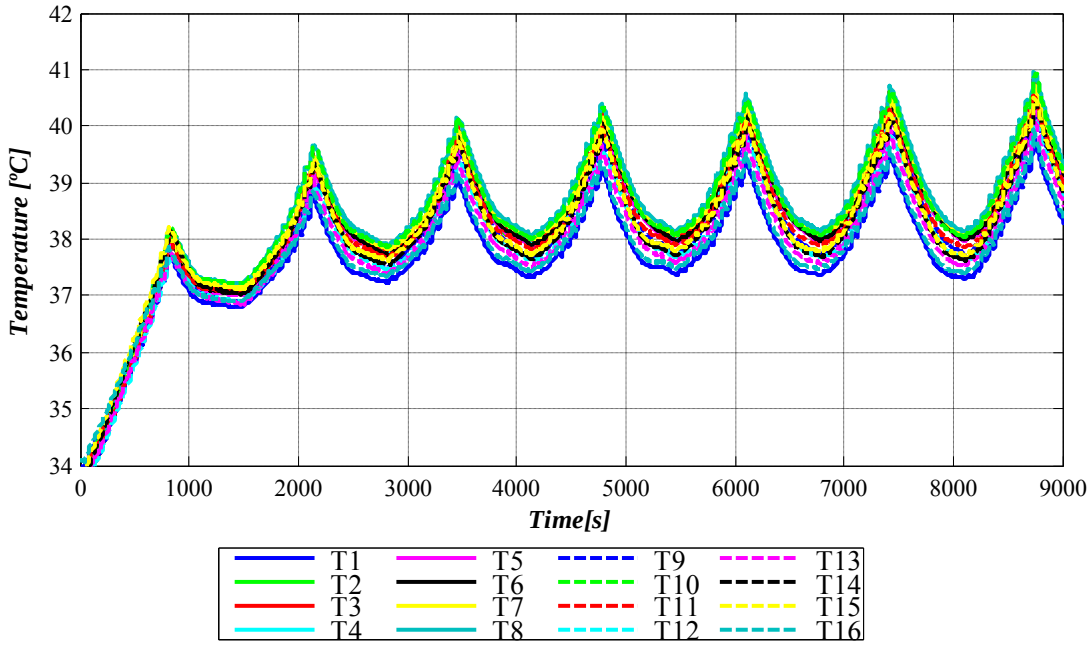

Figure 7.7: Results for the pouch module with forced air cooling system during the final application current cycle with an ambient temperature of 35ºC.

7.2.5 Summary of the results presented

The results presented before are going to be summarized in TABLE 7.2 and TABLE 7.3. The results with the cooling system included in the modules are for *PWM* inputs of 100%. For the cylindrical module with cooling system the results are for parallel flow forced air cooling, the strategy with better results. Important improvements are obtained in all the modules when the cooling system is included. Depending on the optimum working temperature of each cell type, the cooling system can be controlled to increase the working temperature if necessary reducing the velocity of the fans and thus, wasting less energy.

TABLE 7.2 SUMMARY OF THE RESULTS AT 25ºC OF AMBIENT TEMPERATURE

Tamb = 25ºC	**No cooling**		**With cooling**	
	T_{max} [ºC]	$\Delta T_{(max)}$ [ºC]	T_{max} [ºC]	$\Delta T_{(max)}$ [ºC]
PRISMATIC	42.7	4.27	34.2	1.4
CYLINDRICAL	-	-	31.83	2.52
POUCH	38.6	4.93	32.22	1.1

According to the results for 35ºC of ambient temperature, there are no results without cooling systems because it is not possible to reach the requirements of the application

without reaching 45ºC of working temperature. In this case, the cooling system permits applying the current profile keeping the temperatures below 45ºC.

TABLE 7.3 SUMMARY OF THE RESULTS AT 35ºC OF AMBIENT TEMPERATURE

Tamb = 35ºC	**With cooling**	
	T_{max} [ºC]	$\Delta T_{(max)}$ [ºC]
PRISMATIC	43	1.3
CYLINDRICAL	40.6	2.19
POUCH	41	1.2

The three modules meet the requirements of the application since 45ºC are not reached in steady state and the maximum temperature gradient has been reduced below 3ºC. An interesting future line is to optimize the forced air cooling system to continue meeting the requirements but reducing the power consumption of the overall system. Following, the consequences of the improved thermal behaviour will be shown to validate the whole process.

7.3 Analysis of the aging improvement based on an aging pattern

After presenting the results of the battery modules for different working conditions, an analysis of the energy delivered by the modules implemented will be done. As mentioned before, temperature distribution of the modules is improved with the cooling systems for the three modules, and the cooling systems permit to achieve the requirements of the application even if the ambient temperature is quite high (35ºC). The reduction of the average working temperatures of the module slows down the aging processes of the modules, increasing their cycle life and consequently the energy delivered during their whole life. However, the inclusion of the forced air cooling systems into the basic modules produces an amount of power looses in each module. This analysis calculates the energy delivered by each module during its whole life with and without cooling system; in order to do it, the loss of capacity due to the working temperature of the cells within the module is estimated. In the case of modules with cooling system the energy utilized to cool down the module is used for the calculation. The temperatures of the modules for this analysis are taken from the experimental tests with ambient temperatures of 25ºC since modules without cooling systems are unable to work with higher temperatures without reaching 45ºC.

The estimation of the capacity loss due to temperature is estimated with the Arrhenius equation. Arrhenius equation is a simple but accurate formula for the temperature dependence of reaction rates; it describes how the speed of chemical reactions increases with temperature, in this case the rate that the slow deterioration of the active chemicals increases. The Arrhenius relation is commonly used in bibliography for the estimation of the battery aging due to temperature [52], [85]–[87]. In this work an Arrhenius equation has been used for the same purpose based on the work of Wang et al. in [1].

$$Q_{loss} = B exp^{\frac{-E_a}{RT}} (Ah)^z \quad \textbf{(7.1)}$$

Equation (7.1) is a modification for batteries of the most general Arrhenius equation; Q_{loss} is the capacity loss in percentage, B is the pre-exponential factor, E_a is the activation energy [J/mol], R is the gas constant [J/mol K], T is the absolute temperature [K], z is the power law factor and Ah is the Ah-throughput expressed like (*DOD* x Cycle number x nominal capacity of the cell). For a given *C-rate* the pre-exponential factor and the activation energy are constant values, the gas constant is always constant in this work and the equation estimates the percentage of capacity loss that a cell suffers for a working temperature depending on the cycle numbers. B, E_a and z are commonly estimated after a fitting process with experimental aging data. Due to the lack of aging data of the cells under test in this work, the values used for the Arrhenius equation have been taken from [1]. In both works the cell technology is $LiFePO_4$ and so the values of Wang et al. work are considered to be representative also for the cells under test in this work.

TABLE 7.4 shows the Arrhenius equations presented in the work of Wang et al; these equations are constant C-rate dependent. In this work the final application current

profile is an alternative current profile; in order to choose the suitable Arrhenius equation from TABLE 7.4 an average value of the charge and discharge rates of the application will be considered. For the analysis of this work an average value of 6C has been chosen.

TABLE 7.4 ARRHENIUS EQUATION DEPENDING ON THE C-RATE UTILIZED IN [1]

C-rate	Equation
C/2	$Q_{loss} = 30330\ exp(-31500/RT)(Ah)^{0.552}$
2C	$Q_{loss} = 19300\ exp(-31000/RT)(Ah)^{0.554}$
6C	$Q_{loss} = 12000\ exp(-29500/RT)(Ah)^{0.56}$
10C	$Q_{loss} = 11500\ exp(-28000/RT)(Ah)^{0.56}$

Hence, the equation used in this work for the estimation of the aging processes of the three modules is equation

$$Q_{loss} = 12000exp^{\frac{-29500}{RT}}(Ah)^{0.56} \quad \textbf{(7.2)}$$

Figure 7.8 shows the current profile for the elevator application; it consists of 10 elevator cycles and a recharge process. During 10 elevator cycles 2.93 Ah are discharged from the energy storage system; after that a recharge process with 15A is done to recover this energy. The Arrhenius equation requires the value of *DOD* of the application to estimate the aging processes; 2.93 Ah are equivalent to a 45% of *DOD* for the prismatic cell; 36% of *DOD* for the cylindrical cell and 42% of *DOD* for pouch cell. The increase of the *DOD* due to the cooling system consumption is neglected in this work for the cooled modules because this energy consumption is neglectable comparing it with the overall energy flow of the modules. For the results of the following sections, 1 cycle is equivalent to 10 elevator cycles plus one recharge process. For this analysis, the battery modules will reach their *EOL* if one of the cells within the module looses 20% of their initial capacity.

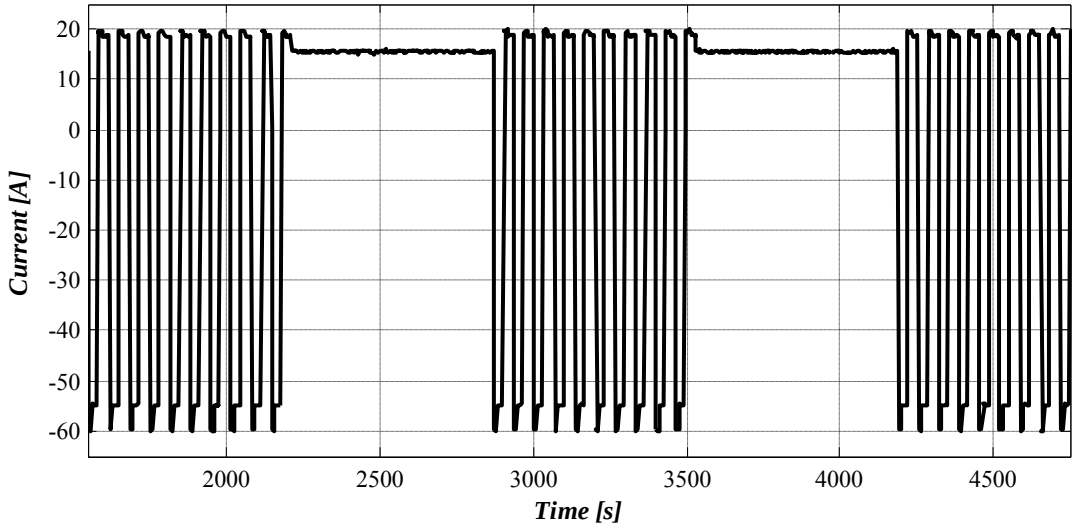

Figure 7.8: Final application current profile.

7.3.1 Prismatic module

Applying the Arrhenius equation previously presented to the prismatic cell the influence of temperature in the cell during the cycle life is estimated. Figure 7.9 shows the capacity loss of the prismatic cell for the final application current profile and different temperatures. For 25ºC more than 6000 application cycles are done before losing 20% of its capacity, but for 45ºC of working temperature this value is reduced to 1700 cycles. Thus, it is important to keep the working temperature closer to 25ºC to improve the lifespan of the battery.

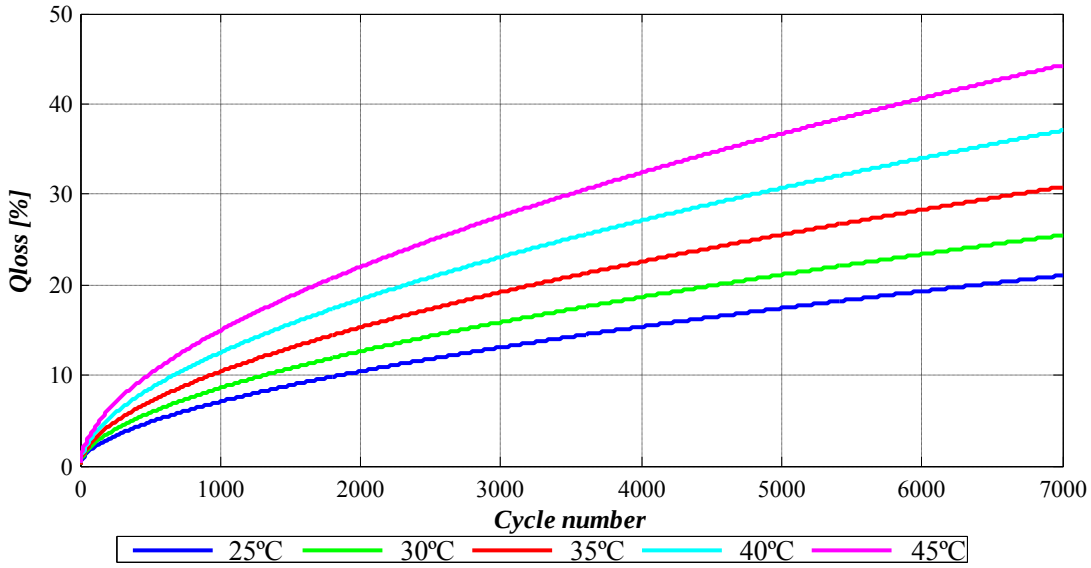

Figure 7.9: Capacity loss of the prismatic cell for the final application current profile.

The steady state temperatures of each cell of the prismatic modules with and without cooling system are used for the following analysis. These temperatures are obtained from the experimental test applying the application current profile and 25ºC of ambient temperature. Figure 7.10 shows the results for both modules; results show uneven aging processes of the cells without cooling system due to non uniform temperature distribution comparing it with the cooled module. Besides, the cooling system permits lower working temperatures of the modules and a longer lifespan. After 1960 application cycles cell number 5 of the non-cooled module reaches the *EOL*; however, with the cooled system, cell number 4 looses 20% of its initial capacity after 3420 cycles.

$$E_{cyc} = \left(\frac{10(I_1 t_1 + I_2 t_2 + I_3 t_3 + I_4 t_4) + \left(I_{recharge}\, t_{recharge} \right)}{3600} \right) V_{battery} \quad \textbf{(7.3)}$$

$$E_{cool} = \frac{P_{cool}\left(I_1 + I_2 + I_3 + I_4 + I_{recharge} \right)}{3600} \quad \textbf{(7.4)}$$

The absolute energy flow for the application profile during 10 elevator cycles and a recharge process is calculated with equation (7.3) and its value is 238.5 Wh; thus, after 1960 cycles the absolute energy flow of the module without cooling system during its life is 467.5 kWh. The power consumption of the cooling system of this module during

one application cycle is calculated with equation (7.4) and its value is 5.2 Wh. After 3420 cycles and taking into account the constant power consumption of the cooling system, the absolute energy flow of the prismatic module with cooling system is 798 kWh. The energy consumed by the cooling system is subtracted to the total energy flow of the module during its whole life to reach this result. The difference means an improvement of 41% in the absolute energy flow when the cooling system is included. The conclusion is that although the power consumption of the cooling system, the overall energy flow is improved because of the improvement of the lifespan. TABLE 7.5 summarizes the energy analysis for the prismatic module with and without cooling system.

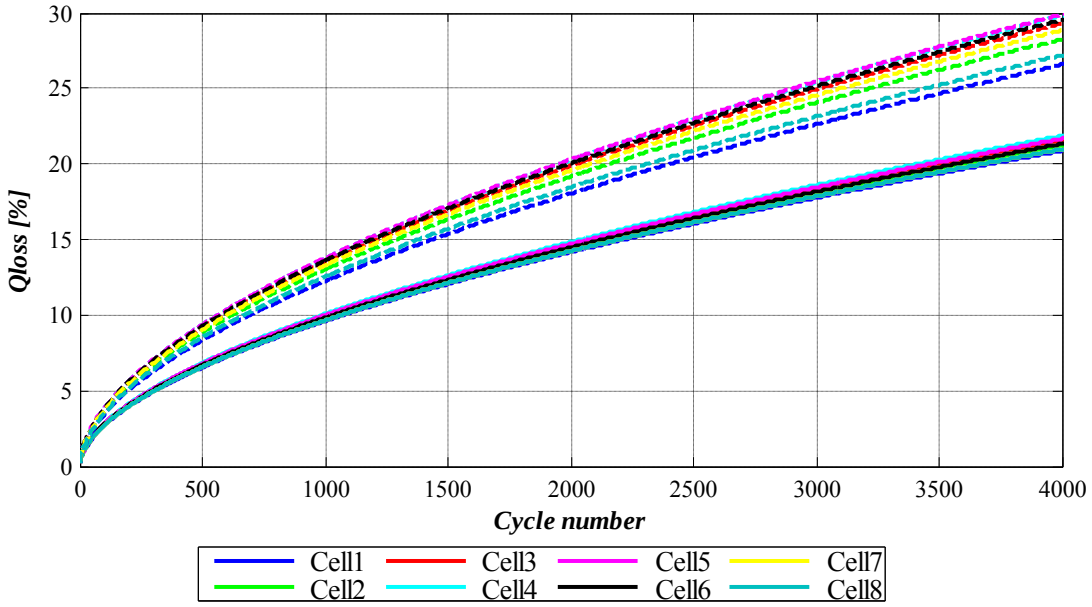

Figure 7.10: Capacity loss of the cells of the prismatic modules for the application current profile and 25ºC of ambient. Dashed: Module without cooling system; Continuous: Module with forced air cooling system.

TABLE 7.5: SUMMARY OF THE ENERGY ANALYSIS FOR THE PRISMATIC MODULE WITH AND WITHOUT COOLING SYSTEM

	Nº of cycles	**Nº of cycles x Energy/cycle [kWh]**	**Cooling system consumption [kWh]**	**Total energy flow [kWh]**
Without cooling	1960	467.54	-	467.54
Cooled module	3420	815.81	17.78	798.03

7.3.2 Cylindrical module

According to the cylindrical module the same Arrhenius equation is applied to estimate the aging process of the cells. In this module there is no experimental result with the module without cooling system because 45ºC where reached if the final application current profile was applied under any ambient temperature over 25ºC. The steady state temperatures for the comparison are obtained from a 3D *CFD* simulation for this case.

For the cylindrical cell in general, a working temperature of 45ºC permits 1721 application cycles. If the working temperature is 25ºC this value is increased until 6509. It is important to reduce the working temperature of the module to improve its cycle life.

Figure 7.11 shows the results for the cylindrical module; in this case the temperatures for the module without cooling system are very close to 45ºC, even over this value. For this module 1610 complete application cycles can be done before reaching the *EOL*. When the parallel flow forced air cooling system is included the cycle life is increased to 4060 cycles in this module. 1610 cycles implies an absolute energy flow of 384 kWh.

The cooling system of this module has a constant power consumption of 24 W that means 8.82 Wh per application cycle (equation (7.4)). This consumption is taken into account for the calculation of the absolute energy of the cooled module. For a cycle life of 4060 the absolute energy flow of this energy storage system is 932.7 kWh (TABLE 7.6). The improvement due to the inclusion of the cooling system represents a 58.8% of the overall energy.

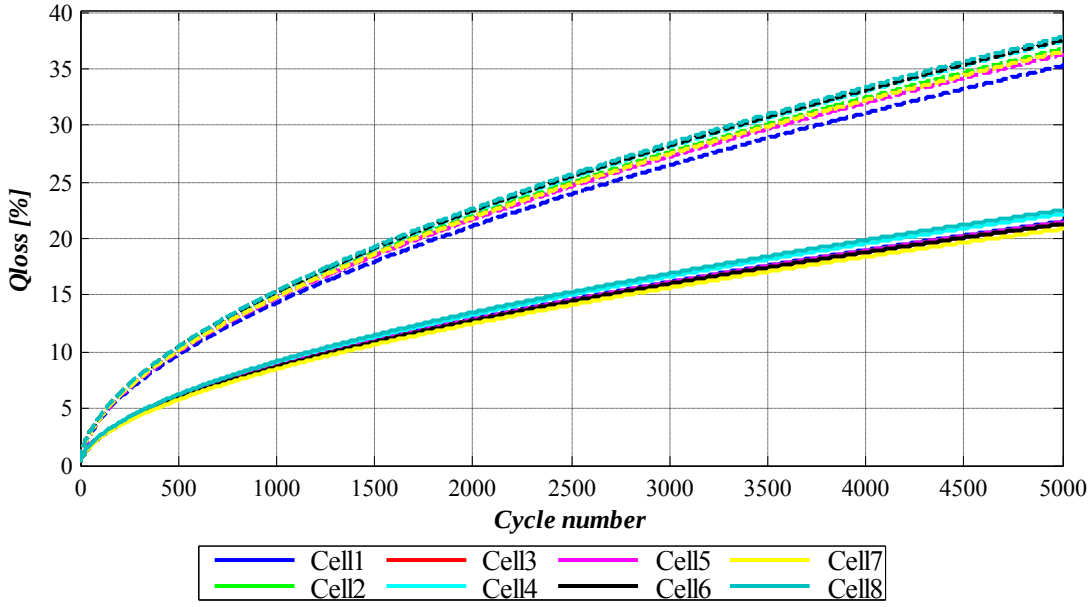

Figure 7.11: Capacity loss of the cells of the cylindrical modules for the application current profile and 25ºC of ambient. Dashed: Module without cooling system simulated with the finite element model; Continuous: Module with forced air cooling system.

TABLE 7.6: SUMMARY OF THE ENERGY ANALYSIS FOR THE CYLINDRICAL MODULE WITH AND WITHOUT COOLING SYSTEM

	Nº of cycles	**Nº of cycles x Energy/cycle [kWh]**	**Cooling system consumption [kWh]**	**Total energy flow [kWh]**
Without cooling	1610	384.05	-	384.05
Cooled module	4060	968.48	35.8	932.67

7.3.3 Pouch module

The same procedure is applied to the pouch module to estimate the aging process of the cells. With this cell working at 45ºC, 1685 application cycles can be done before reaching the *EOL*; if a working temperature of 25ºC is considered, this cell can reach an amount of 6376 cycles.

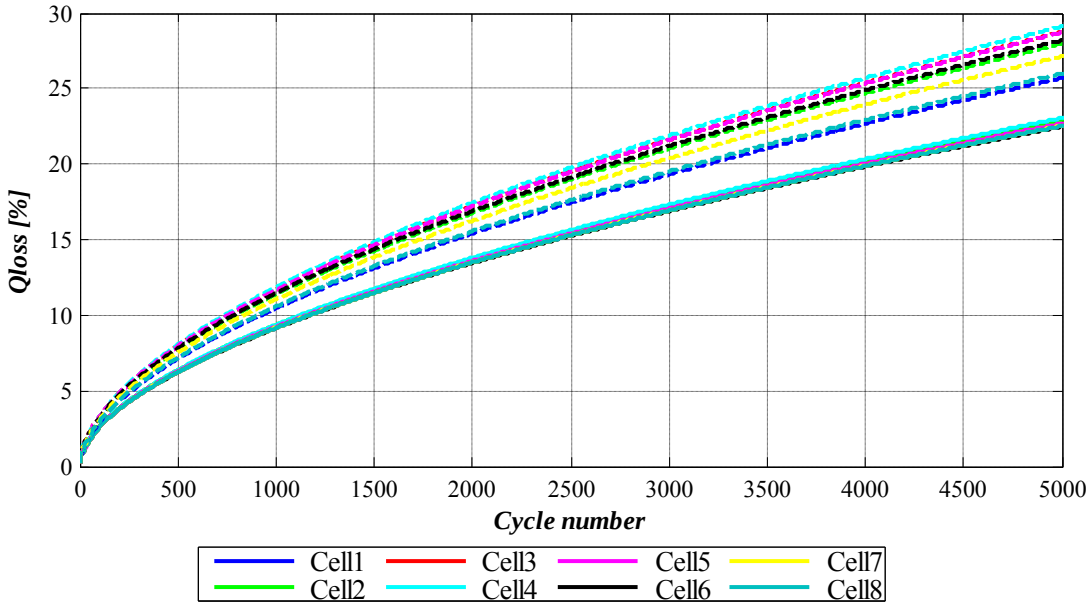

Figure 7.12: Capacity loss of the cells of the pouch modules for the application current profile and 25ºC of ambient. Dashed: Module without cooling system; Continuous: Module with forced air cooling system.

Figure 7.12 shows the comparison between pouch modules; the small temperature gradient obtained with this module can be clearly seen in this figure since very similar aging processes of the cells are achieved. The module without cooling system is able to reach 2559 cycles. The absolute energy delivered by the module after these cycles is 602.1 kWh. The power consumption of the cooling system of this module during one application cycle is 4 Wh. When this cooling system is included the cycle life is improved until 3887 before cell number 4 reaches the 20% of its capacity loss. After 3887 cycles and taking into account the constant power consumption of the cooling system, the absolute energy flow of the prismatic module with cooling system is 911.5 kWh (TABLE 7.7). The difference means an improvement of 33% in the absolute energy flow when the cooling system is included.

TABLE 7.7: SUMMARY OF THE ENERGY ANALYSIS FOR THE POUCH MODULE WITH AND WITHOUT COOLING SYSTEM

	Nº of cycles	**Nº of cycles x Energy/cycle [kWh]**	**Cooling system consumption [kWh]**	**Total energy flow [kWh]**
Without cooling	2559	610.19	-	610.19
Cooled module	3887	927.21	15.71	911.5

7.3.4 Summary of the results obtained with the analysis

TABLE 7.8 shows a summary of the results obtained with the previous analysis. According to the modules without cooling systems, the cylindrical module delivers less energy because the working temperature is too high in this module comparing it with the other ones. Pouch module instead is the module with the lowest working temperatures and delivers more energy before including the cooling systems.

After including the cooling system, the cylindrical module suffers the most important improvement of the three modules with a 58.8%. It delivers more energy than the other modules during its life although the cooling system is the most consuming one. However, the cylindrical cell is also the cell with highest initial capacity, 8 Ah, thus, the cell with lowest *DOD* due to the application current profile. The prismatic module improves its absolute energy amount until 798 kWh and the pouch module suffers an improvement of 33%. This lower improvement is due to the better performance of the pouch module without cooling system and because it has the cooling system with less air velocity and hence, the one with the lowest power consumption.

TABLE 7.8 SUMMARY OF THE RESULTS OBTAINED FROM THE PREVIOUS ANALYSIS

	Energy flow [kWh]		*Energy Improvement [%]*	*CSPC/cycle [Wh]*
	No cooling	*Cooling*		
PRISMATIC	467.5	798	41	5.2
CYLINDRICAL	384	932.7	58.8	8.82
POUCH	602.1	911.5	33	4

7.4 Conclusions

This chapter presents the final results of the modules with cooling systems developed during this work. Besides, an analysis of the energy delivered by these modules and by the same modules without cooling systems is also presented. This analysis is based on the Arrhenius equation obtained from bibliography in a work with the same lithium technology cells.

The cooling systems of the three modules improve their overall thermal behaviour; in the case of an ambient temperature of 25ºC, the average working temperature of the module is reduced and the maximum temperature gradient is also smaller. The prismatic module reduces its maximum temperature from 42.7ºC to 34.2ºC and the maximum gradient from 4.27ºC to 1.4ºC. The cylindrical module instead was not able to work with the final application without cooling system at 25ºC. After including the cooling system a maximum temperature of 31.83ºC and a maximum gradient of 2.52ºC are reached. Finally the pouch module reduces the maximum temperature from 38.6ºC to 32.22ºC and the maximum gradient from 4.93ºC to 1.1ºC.

When the ambient temperature is increased to 35ºC the modules can work under the final application current profile reaching the requirements defined. The prismatic module works with an average maximum temperature of 43ºC and a maximum gradient of 1.3ºC. The cylindrical module reaches a maximum temperature of 40.6ºC and a maximum gradient of 2.19ºC. The pouch module reaches 41ºC with a gradient of 1.2ºC.

The forced air cooling designs permit the use of the three modules under the final application current profile and an ambient of 35ºC reaching the requirements of T_{max}<45ºC and $\Delta T_{(max)}$<3ºC. The extraction of heat through a heatsink is less efficient than blowing air directly to the cells because the low thermal conductivity of the li-ion cells to the heatsink reduces the performance of the overall cooling system; however the designed cooling systems with heatsinks for the prismatic and pouch modules reach the requirements of the application perfectly. The longitudinal forced air cooling systems provokes big temperature gradients in the cylindrical module (6.62ºC) comparing it with the transversal cooling system (2.52ºC).

Taking advantage of the Arrhenius equation, the forced air cooling systems designed have been validated; the lifespan of the modules is enlarged in the three cases due to the cooling system. The absolute energy delivered by the modules during their whole life is increased although the cooling system consumes energy. The prismatic, cylindrical and pouch modules obtain an improvement of 41%, 58.8% and 33% respectively.

Chapter 8. CONCLUSIONS AND FUTURE LINES

This chapter presents the main conclusions obtained during the thesis work. The main conclusions presented during the chapters are summarized in this one. After the conclusions, a section with some future suggestions is also presented.

8.1 Conclusions

The main objective of this thesis work is to enlarge the lifespan of lithium ion battery modules for power applications through their electro-thermal optimization. According to the results presented during Chapter 7 the electro thermal optimization applied to the battery modules developed in this work enlarges their lifespan hugely due to the reduction of the working temperature of the modules and the reduction of the temperature gradient principally. The absolute energy delivered by the modules during their whole life is increased although the cooling system consumes energy. The prismatic, cylindrical and pouch modules obtain an improvement of 41%, 58.8% and 33% respectively comparing the absolute energies between the non-cooled and the cooled modules. The overall cycle life of the module is increased because the working temperature of the module is reduced closer to its optimum temperature.

The three modules reach the requirements of a temperature gradient below 3ºC and a maximum working temperature of 45ºC for the final application current profile and an ambient temperature of 35ºC. Hence, the methodology developed in this thesis to design forced air cooling systems for battery modules is also validated.

According to the thermal characterization and modelling of lithium ion single cells, the main concerns of Chapter 3 are the modelling of the internal heat generation with the equation of Bernardi, modelling the surface temperature response of the cell with *Cauer* 1st and 2nd order models and with a 3D numerical model, and the methodology to thermally characterize the cell under test.

The equation of Bernardi to calculate the internal heat generation of the cell is not validated directly measuring this parameter since the suitable equipment is not available at the moment. However, an indirect validation is done measuring the temperature response of the cell under test for different current profiles: discharge, charge, charge/discharge. An accurate *SOC* estimation is required to calculate the internal heat generation with this equation due to the strong influence of the initial *SOC* to estimate this parameter during complete discharge and complete charge processes. The thermal characterization methodology and the calculation of the parameters of the models have been validated with the same thermal response results. It is very important to measure accurately the value of the impedance R_0 during the constant power pulse test and the heat capacity test.

Results for discharge, charge and charge/discharge processes are presented in this work for the *Cauer* 1st and 2nd order models and for 3D numerical model; *Cauer* 1st order model estimates accurately the thermal response of the cell under test, with less than 1ºC of error for all the tests. However, the real behaviour of the cell is closer to the *Cauer* 2nd order model; this effect is clearly seen when the internal heat generation begins and finishes because the 1st order model instantaneously reacts to the change of the internal heat generation, and the real cell reacts after a delay. The accuracy of the *Cauer* 2nd order model is similar to the 1st order one, the error is below 1ºC for all the experimental tests. The 3D numerical model commits bigger errors; the maximum error committed by this model for the analyzed tests is almost 2ºC. Besides, this model

requires larger computational times than the *Cauer* behavioural models. The conclusion is that the *Cauer* 2nd order model is the best model in terms of accuracy and computational time for single cell thermal models.

The main contribution of this chapter is the methodology presented to develop thermal models for li.ion single cells. The experimental tests presented to estimate the parameters of the thermal models and of the internal heat generation model, do not require expensive devices for thermal purposes.

The main conclusion obtained from Chapter 4 is that the maximum temperature and the maximum temperature gradient of a li-ion battery module have to be controlled to enlarge the lifespan and to obtain the maximum efficiency of the energy storage system. The high current demanded in power applications lead to high internal heat generation rates. If these rates are different between cells and are not compensated, temperature gradients will increase reducing the performance of the battery modules.

Chapter 5 deals with the minimization of the temperature gradients in three different battery modules; the influence of the air gap between cells has been analyzed with a prismatic module. Bigger air gaps increase the maximum temperature gradient of the prismatic module; however, bigger air gaps are suitable to include a forced air cooling system blowing directly to the cells since the static pressure of the system is reduced leading to lower power consumptions of the *BTMS*. When the air gaps are reduced, the static pressure that the cooling system has to overcome and the power consumption of the cooling system are bigger. In the case of avoiding air gaps, the maximum temperature gradient is reduced but the forced air cooling will not blow directly the cells because of the absence of cooling channels. A module without cooling channels between cells and with *TIM* is considered to be the best option to reduce the gradients. Concretely, during the constant current discharge the maximum temperature gradient for 5mm air gap module is 2.8ºC, 2.4ºC for 1.5mm air gap and 1.8ºC for the case without air gaps; with the alternative charge/discharge cycle 5.3ºC for 5mm air gap module, 4ºC for 1.5mm air gap and 3ºC for the case without air gap.

Besides, a compensation of the convective heat transfer coefficient is done to the 1st and 8th cells permits reducing even more this gradient. *T1* and *T16* measure temperatures closer to the maximum temperature improving module average temperature distribution.

In the case of cylindrical module, a novel procedure to reduce temperature gradient is proposed taking advantage of voltage balancing systems. Voltage balancing systems are commonly used to avoid *SOC* mismatches between cells within the same module improving their voltage distribution. However, if higher balancing currents are reached for these systems, an important improvement in the temperature distribution can be also obtained in applications where the depth of discharge is high due to the internal heat generation compensation. Actually, temperature gradient has been improved in more than 54% for 1C rates and 45% for 2C rates with a passive balancing system. However, the passive balancing systems reduce the efficiency of the overall energy storage system; an active balancing system mitigates this problem or even improves the available energy for certain working conditions. With a 1C rate scenario the energy is improved in a 2% and when 2C discharge rate is applied the available energy is reduced

but only in a 0.66%. However, the improvement in the temperature distribution is not as notable as with passive balancing. Whit 1C rate an improvement of a 33% is reached and with 2C rate of discharge the improvement is a 31%.

$LiFePO_4$ cells have a very flat voltage profile in a big range of their *SOC*, from 90% to 20%; hence, this strategy based on voltage differences between cells is hardly applicable if all the cells have similar *SOC*. However, it is considered an important contribution in applications reaching low and high *SOC*, because if the current rate is below 1C, the temperature gradient can be minimized without any cooling system. It should be pointed out that during the search in bibliography, similar proposals have not been found.

Pouch module conclusions are related to advantages and disadvantages of these cells to be assembled into a battery module. The main advantage of these cells is that more energy can be available in a smaller space, a very important issue in electro mobility applications. However, after the assembly process of this work, several drawbacks have been detected; the non rigid case of these cells forces to include additional parts to build up a rigid structure for the module unlike the cases with cylindrical and prismatic cells. Besides, it is not possible to press one cell against the other to erase air bubbles since the case is not rigid and cell can be damaged. Furthermore, the interconnection of the tabs can lead to high contact resistances leading to higher temperatures close to the power terminals. Special ultrasonic welding equipment can be required in these cases to mitigate this problem.

Chapter 6 deals with the partial objective of defining a methodology to design a forced air cooling system for battery modules. The main purposes of the chapter are to choose the cooling strategy, the suitable fan for the application and validating the simulation tool used for the previous purposes.

The cooling strategy mainly depends on the mechanical assembly of the battery modules. For the prismatic module, an assembly with the cells mounted on a heatsink and 6 fans blowing the heatsink is selected; for the cylindrical module, a transversal forced air cooling strategy is defined trying to reduce the cooling channel of the cooling system to reduce the static pressure drop and the consumption of the fan. Finally, for the pouch module, heat is conducted to the outside of the battery module through several heatsink plates and two fans blow these heatsink plates to increase the heat transfer between them and the ambient.

In order to choose the suitable fan for each module, simulations to estimate the static pressure curve and the minimum air flow required for the application are conducted. With the developed simulation tool it is possible to estimate the working point of the fan selected to validate it with experimental measurements. In this work, the experimental measurements have been done with a "Pitot tube". Results show an error below 10 Pa in the static pressure estimation, and below 0.3 m^3/min in the estimation of the air flow.

Finally, the simulation tool is compared with experimental results estimating the temperature distribution of the battery modules. The error committed by the simulation tool is less than 2ºC all the cases so it is considered a suitable tool for the purpose of this thesis work.

8.2 Future lines

According to the thermal characterization of li-ion single cells, the measurement of the thermal conductivity of the cell is considered an important improvement. This parameter is normally obtained conducting an experimental test, applying a certain amount of heat on one surface of the cell and measuring the evolution of the temperature on another surface.

Besides, a system to measure the impedance of the single cell during the constant power pulse test and heat capacity test is considered another good improvement. This system has to measure the voltage of the cell and the sinusoidal current applied. The frequency of these signals is sometimes over 1 kHz so the sampling frequency has to be over 10 kHz to get good results. Furthermore, the internal impedance of the cells utilized in this work is less than 5 mΩ so the measurement system has to be able to measure very small voltages accurately.

Regarding to the voltage balancing to reduce temperature gradients, it can be very interesting to design active balancing systems able to deliver higher currents. This way, it will be possible to test the proposal under higher current profiles.

According to the methodology to design forced air cooling systems for battery modules, a good improvement can be to avoid the use of *CFD* simulation tools without losing precision in the estimation. A simulation tool able to calculate average flow velocities and static pressures of cooling systems with less simulation time would be an important contribution for this methodology.

Finally, the Arrhenius equation proposed is considered a good tool to compare different modules and their performance. However, including experimental aging data instead of bibliography aging data can lead to an accurate temperature dependent aging process estimation.

REFERENCES

[1] J. Wang, P. Liu, J. Hicks-Garner, E. Sherman, S. Soukiazian, M. Verbrugge, H. Tataria, J. Musser, and P. Finamore, "Cycle-life model for graphite-LiFePO4 cells," *J. Power Sources*, vol. 196, no. 8, pp. 3942–3948, Apr. 2011.

[2] T. M. Bandhauer, S. Garimella, and T. F. Fuller, "A Critical Review of Thermal Issues in Lithium-Ion Batteries," *J. Electrochem. Soc.*, vol. 158, no. 3, p. R1, 2011.

[3] Y. Ji and C. Y. Wang, "Heating strategies for Li-ion batteries operated from subzero temperatures," *Electrochim. Acta*, Apr. 2013.

[4] A. Pesaran, S. Burch, and M. Keyser, "An approach for designing thermal management systems for electric and hybrid vehicle battery packs," *Fourth Veh. Therm. Manag. Syst. Conf. Exhib.*, no. January, 1999.

[5] H. Ibrahim, a Ilinca, and J. Perron, "Energy storage systems—Characteristics and comparisons," *Renew. Sustain. Energy Rev.*, vol. 12, no. 5, pp. 1221–1250, Jun. 2008.

[6] D. Linden and T. B. Reddy, *Handbook of batteries*. McGraw-Hill, 2002.

[7] "Battery university." [Online]. Available: http://batteryuniversity.com.

[8] B. W. Williams, *Power Electronics: Devices, Drivers, Applications, and Passive Components*. McGraw-Hill, 1992.

[9] F. P. Tredeau, B. G. Kim, and Z. M. Salameh, "Performance evaluation of Lithium Cobalt cells and the suitability for use in electric vehicles," *2008 IEEE Veh. Power Propuls. Conf.*, pp. 1–5, Sep. 2008.

[10] F. P. Tredeau and Z. M. Salameh, "Evaluation of Lithium iron phosphate batteries for electric vehicles application," *2009 IEEE Veh. Power Propuls. Conf.*, pp. 1266–1270, Sep. 2009.

[11] J. W. Fergus, "Recent developments in cathode materials for lithium ion batteries," *J. Power Sources*, vol. 195, no. 4, pp. 939–954, Feb. 2010.

[12] T. Horiba, K. Hironaka, T. Matsumura, T. Kai, M. Koseki, and Y. Muranaka, "Manganese-based lithium batteries for hybrid electric vehicle applications," *J. Power Sources*, vol. 119–121, pp. 893–896, Jun. 2003.

[13] J. Vetter, P. Novák, M. R. Wagner, C. Veit, K.-C. Möller, J. O. Besenhard, M. Winter, M. Wohlfahrt-Mehrens, C. Vogler, and a. Hammouche, "Ageing mechanisms in lithium-ion batteries," *J. Power Sources*, vol. 147, no. 1–2, pp. 269–281, Sep. 2005.

[14] M. Wohlfahrt-Mehrens, C. Vogler, and J. Garche, "Aging mechanisms of lithium cathode materials," *J. Power Sources*, vol. 127, no. 1–2, pp. 58–64, Mar. 2004.

[15] L. Lu, X. Han, J. Li, J. Hua, and M. Ouyang, "A review on the key issues for lithium-ion battery management in electric vehicles," *J. Power Sources*, vol. 226, pp. 272–288, Mar. 2013.

[16] E. P. Roth, D. H. Doughty, and D. L. Pile, "Effects of separator breakdown on abuse response of 18650 Li-ion cells," *J. Power Sources*, vol. 174, no. 2, pp. 579–583, Dec. 2007.

[17] U. S. Kim, J. Yi, C. B. Shin, T. Han, and S. Park, *Modelling the thermal behaviour of a lithium-ion battery during charge*, vol. 196, no. 11. 2011, pp. 5115–5121.

[18] D. Bernardi, E. Pawlikowski, and J. Newman, "A general energy balance for battery systems," *J. Electrochem. Soc.*, vol. 132, no. 1, 1985.

[19] S. Al Hallaj, H. Maleki, J. S. Hong, and J. R. Selman, "Thermal modeling and design considerations of lithium-ion batteries," *J. Power Sources*, vol. 83, no. 1–2, pp. 1–8, Oct. 1999.

[20] S. Chen, Y. Wang, and C. Wan, "Thermal analysis of spirally wound lithium batteries," *J. Electrochem. Soc.*, vol. 153, no. 4, 2006.

[21] K. Onda, T. Ohshima, M. Nakayama, K. Fukuda, and T. Araki, "Thermal behavior of small lithium-ion battery during rapid charge and discharge cycles," *J. Power Sources*, vol. 158, no. 1, pp. 535–542, Jul. 2006.

[22] S. C. Chen, C. C. Wan, and Y. Y. Wang, "Thermal analysis of lithium-ion batteries," *J. Power Sources*, vol. 140, no. 1, pp. 111–124, Jan. 2005.

[23] W. B. Gu and C. Y. Wang, "Thermal-Electrochemical Modeling of Battery Systems," *J. Electrochem. Soc.*, vol. 147, no. 8, p. 2910, 2000.

[24] M. Doyle, T. Fuller, and J. Newman, "Modeling of galvanostatic charge and discharge of the lithium/polymer/insertion cell," *J. Electrochem. Soc.*, vol. 140, no. 6, pp. 1526–1533, 1993.

[25] G. G. Botte, V. R. Subramanian, and R. E. White, “Mathematical modeling of secondary lithium batteries,” *Electrochim. Acta*, vol. 45, no. 15–16, pp. 2595–2609, May 2000.

[26] K. E. Thomas and J. Newman, “Thermal Modeling of Porous Insertion Electrodes,” *J. Electrochem. Soc.* , vol. 150 , no. 2 , pp. A176–A192, Feb. 2003.

[27] P. M. Gomadam, R. E. White, and J. W. Weidner, “Modeling Heat Conduction in Spiral Geometries,” *J. Electrochem. Soc.*, vol. 150, no. 10, p. A1339, 2003.

[28] K. Kumaresan, G. Sikha, and R. White, “Thermal model for a Li-ion cell,” *J. Electrochem. Soc.*, vol. 155, no. 2, pp. A164–A171, 2008.

[29] M. W. Verbrugge, “Three-dimensional temperature and current distribution in a battery module,” *AIChE J.*, vol. 41, no. 6, pp. 1550–1562, 1995.

[30] L. Song and J. Evans, “Electrochemical- • Thermal Model of Lithium Polymer Batteries,” *J. Electrochem. Soc.*, vol. 147, no. 6, pp. 2086–2095, 2000.

[31] M. Muratori, “THERMAL CHARACTERIZATION OF LITHIUM-ION BATTERY CELL,” Politecnico di Milano, 2009.

[32] I. Power, “AN2008-03 Thermal equivalent circuit models.application note,” pp. 1–10, 2008.

[33] X. Hu, S. Lin, S. Stanton, and W. Lian, “A Foster Network Thermal Model for HEV/EV Battery Modeling,” *Ind. Appl. IEEE Trans.*, vol. 47, no. 4, pp. 1692–1699, 2011.

[34] C. Forgez, D. Vinh Do, G. Friedrich, M. Morcrette, and C. Delacourt, “Thermal modeling of a cylindrical LiFePO4/graphite lithium-ion battery,” *J. Power Sources*, vol. 195, no. 9, pp. 2961–2968, May 2010.

[35] J. P. Schmidt, D. Manka, D. Klotz, and E. Ivers-Tiffée, “Investigation of the thermal properties of a Li-ion pouch-cell by electrothermal impedance spectroscopy,” *J. Power Sources*, vol. 196, no. 19, pp. 8140–8146, Oct. 2011.

[36] K. H. Kwon, C. B. Shin, T. H. Kang, and C.-S. Kim, “A two-dimensional modeling of a lithium-polymer battery,” *J. Power Sources*, vol. 163, no. 1, pp. 151–157, Dec. 2006.

[37] V. Pop, H. J. Bergveld, D. Danilov, P. P. L. Regtien, and P. H. L. Notten, *Battery Management Systems: Accurate State-of-Charge Indication for Battery-Powered Applications (Philips Research Book Series) (Philips Research Book Series)*, 1st ed. Springer Publishing Company, Incorporated, 2008.

[38] V. V. Viswanathan, D. Choi, D. Wang, W. Xu, S. Towne, R. E. Williford, J.-G. Zhang, J. Liu, and Z. Yang, “Effect of entropy change of lithium intercalation in

cathodes and anodes on Li-ion battery thermal management," *J. Power Sources*, vol. 195, no. 11, pp. 3720–3729, Jun. 2010.

[39] K. Thomas, C. Bogatu, and J. Newman, "Measurement of the entropy of reaction as a function of state of charge in doped and undoped lithium manganese oxide," *J. Electrochem. Soc.*, vol. 148, no. 6, 2001.

[40] S. Al Hallaj and R. Venkatachalapathy, "Entropy changes due to structural transformation in the graphite anode and phase change of the LiCoO2 cathode," *J. Electrochem. Soc.*, vol. 147, no. 7, pp. 2432–2436, 2000.

[41] M. Keyser, A. Pesaran, M. Mihalic, and J. Yu, "Thermal characterization of advanced lithium-ion polymer cells," in *Third Advanced Automotive Battery Conference*, 2003.

[42] U. Iraola, I. Aizpuru, J. M. Canales, A. Etxeberria, and I. Gil, "Methodology for thermal modelling of lithium-ion batteries," in *Industrial Electronics Society, IECON 2013 - 39th Annual Conference of the IEEE*, 2013, pp. 6752–6757.

[43] S. Chen, C. Wan, and Y. Wang, "Thermal analysis of lithium-ion batteries," *J. Power Sources*, vol. 143, no. 9, 2005.

[44] D. Neumeister, "Cooling solutions for Li-Ion batteries to improve range and lifecycle," in *IQPC: 2nd International Conference Thermal Management for EV/HEV*, 2012, no. June.

[45] F. Ren, T. Cox, and H. Wang, "Thermal runaway risk evaluation of Li-ion cells using a pinch–torsion test," *J. Power Sources*, vol. 249, pp. 156–162, Mar. 2014.

[46] P. Ramadass, W. Fang, and Z. (John) Zhang, "Study of internal short in a Li-ion cell I. Test method development using infra-red imaging technique," *J. Power Sources*, vol. 248, pp. 769–776, Feb. 2014.

[47] G. K. Prasad and C. D. Rahn, "Model based identification of aging parameters in lithium ion batteries," *J. Power Sources*, vol. 232, pp. 79–85, Jun. 2013.

[48] S. Paul, C. Diegelmann, H. Kabza, and W. Tillmetz, "Analysis of ageing inhomogeneities in lithium-ion battery systems," *J. Power Sources*, vol. 239, pp. 642–650, Oct. 2013.

[49] B. Eberleh, F. von Borck, and S. Raiser, "A highly integrated, mass produced battery module as basis for various EV and HEV systems.," *2010 Emobility - Electr. Power Train*, pp. 1–6, Nov. 2010.

[50] Q. Zhang and R. E. White, "Calendar life study of Li-ion pouch cells," *J. Power Sources*, vol. 173, no. 2, pp. 990–997, Nov. 2007.

[51] a. Eddahech, O. Briat, E. Woirgard, and J. M. Vinassa, “Remaining useful life prediction of lithium batteries in calendar ageing for automotive applications,” *Microelectron. Reliab.*, vol. 52, no. 9–10, pp. 2438–2442, Sep. 2012.

[52] S. Käbitz, J. B. Gerschler, M. Ecker, Y. Yurdagel, B. Emmermacher, D. André, T. Mitsch, and D. U. Sauer, “Cycle and calendar life study of a graphite|LiNi1/3Mn1/3Co1/3O2 Li-ion high energy system. Part A: Full cell characterization,” *J. Power Sources*, vol. 239, pp. 572–583, Oct. 2013.

[53] R. B. Wright, C. G. Motloch, J. R. Belt, J. P. Christophersen, C. D. Ho, R. A. Richardson, I. Bloom, S. A. Jones, V. S. Battaglia, G. L. Henriksen, T. Unkelhaeuser, D. Ingersoll, H. L. Case, S. A. Rogers, and R. A. Sutula, “Calendar- and cycle-life studies of advanced technology development program generation 1 lithium-ion batteries,” *J. Power Sources*, vol. 110, no. 2, pp. 445–470, Aug. 2002.

[54] I. Bloom, B. W. Cole, J. J. Sohn, S. A. Jones, E. G. Polzin, V. S. Battaglia, G. L. Henriksen, C. Motloch, R. Richardson, T. Unkelhaeuser, D. Ingersoll, and H. L. Case, “An accelerated calendar and cycle life study of Li-ion cells,” *J. Power Sources*, vol. 101, no. 2, pp. 238–247, Oct. 2001.

[55] Björn Eberleh, “Thermal Management of battery systems – issues and solutions for the heart of the future drive train,” in *IQPC: 2nd International Conference Thermal Management for EV/HEV*, 2012.

[56] K. Amine, J. Liu, and I. Belharouak, “High-temperature storage and cycling of C-LiFePO4/graphite Li-ion cells,” *Electrochem. commun.*, vol. 7, no. 7, pp. 669–673, Jul. 2005.

[57] B. G. Potter, T. Q. Duong, and I. Bloom, “Performance and cycle life test results of a PEVE first-generation prismatic nickel/metal-hydride battery pack,” *J. Power Sources*, vol. 158, no. 1, pp. 760–764, Jul. 2006.

[58] L. Fan, J. M. Khodadadi, and a. a. Pesaran, “A parametric study on thermal management of an air-cooled lithium-ion battery module for plug-in hybrid electric vehicles,” *J. Power Sources*, vol. 238, pp. 301–312, Sep. 2013.

[59] H. Fathabadi, “A novel design including cooling media for Lithium-ion batteries pack used in hybrid and electric vehicles,” *J. Power Sources*, vol. 245, pp. 495–500, Jan. 2014.

[60] H. Park, “A design of air flow configuration for cooling lithium ion battery in hybrid electric vehicles,” *J. Power Sources*, vol. 239, pp. 30–36, Oct. 2013.

[61] J. Xun, R. Liu, and K. Jiao, “Numerical and analytical modeling of lithium ion battery thermal behaviors with different cooling designs,” *J. Power Sources*, vol. 233, pp. 47–61, Jul. 2013.

[62] X. Li, F. He, and L. Ma, “Thermal management of cylindrical batteries investigated using wind tunnel testing and computational fluid dynamics simulation,” *J. Power Sources*, vol. 238, pp. 395–402, Sep. 2013.

[63] M. R. Giuliano, A. K. Prasad, and S. G. Advani, “Experimental study of an air-cooled thermal management system for high capacity lithium–titanate batteries,” *J. Power Sources*, vol. 216, pp. 345–352, Oct. 2012.

[64] S. Park and D. Jung, “Battery Cell Arrangement and Heat Transfer Fluid Effects on the Parasitic Power Consumption and the Cell Temperature Distribution in a HEV,” *J. Power Sources*, 2012.

[65] X. M. Xu and R. He, “Research on the heat dissipation performance of battery pack based on forced air cooling,” *J. Power Sources*, vol. 240, pp. 33–41, Oct. 2013.

[66] Y. Yang, X. Hu, D. Qing, and F. Chen, “Arrhenius Equation-Based Cell-Health Assessment: Application to Thermal Energy Management Design of a HEV NiMH Battery Pack,” *Energies*, vol. 6, no. 5, pp. 2709–2725, May 2013.

[67] M. Mousavi, S. Hoque, S. Rahnamayan, I. Dincer, and G. F. Naterer, “Optimal design of an air-cooling system for a Li-Ion battery pack in Electric Vehicles with a genetic algorithm,” *2011 IEEE Congr. Evol. Comput.*, pp. 1848–1855, Jun. 2011.

[68] U. Rohatgi, “Thermal Characteristics of Air Flow Cooling in the Lithium Ion Batteries Experimental Chamber,” in *ASME 2012 Summer Heat Transfer Conference*, 2012.

[69] R. Mahamud and C. Park, “Reciprocating air flow for Li-ion battery thermal management to improve temperature uniformity,” *J. Power Sources*, vol. 196, no. 13, pp. 5685–5696, 2011.

[70] A. Pesaran, “Battery Thermal Management In Ev And Hevs: Issues And Solutions,” in *Advanced Automotive Battery Conference*, 2001.

[71] A. Jarrett and I. Y. Kim, “Influence of operating conditions on the optimum design of electric vehicle battery cooling plates,” *J. Power Sources*, vol. 245, pp. 644–655, Jan. 2014.

[72] Behr, “Technical Press Day 2009.” 2009.

[73] Z. Ling, Z. Zhang, G. Shi, X. Fang, L. Wang, X. Gao, Y. Fang, T. Xu, S. Wang, and X. Liu, “Review on thermal management systems using phase change materials for electronic components, Li-ion batteries and photovoltaic modules,” *Renew. Sustain. Energy Rev.*, vol. 31, pp. 427–438, Mar. 2014.

[74] R. Kizilel, R. Sabbah, J. R. Selman, and S. Al-Hallaj, “An alternative cooling system to enhance the safety of Li-ion battery packs,” *J. Power Sources*, vol. 194, no. 2, pp. 1105–1112, Dec. 2009.

[75] P. Tamburrino, A. ElShafei, R. Kizilel, and A. Lateef, “Novel PCM Thermal Management Makes Li-ion Batteries a Viable Option for High Power and High Temperature Applications,” *bioage.typepad.com*, vol. 60616, no. 6.

[76] R. Sabbah, R. Kizilel, J. R. Selman, and S. Al-Hallaj, “Active (air-cooled) vs. passive (phase change material) thermal management of high power lithium-ion packs: Limitation of temperature rise and uniformity of temperature distribution,” *J. Power Sources*, vol. 182, no. 2, pp. 630–638, Aug. 2008.

[77] R. Kizilel, a. Lateef, R. Sabbah, M. M. Farid, J. R. Selman, and S. Al-Hallaj, “Passive control of temperature excursion and uniformity in high-energy Li-ion battery packs at high current and ambient temperature,” *J. Power Sources*, vol. 183, no. 1, pp. 370–375, Aug. 2008.

[78] V. V. Tyagi, D. Buddhi, R. Kothari, and S. K. Tyagi, “Phase change material (PCM) based thermal management system for cool energy storage application in building: An experimental study,” *Energy Build.*, vol. 51, pp. 248–254, Aug. 2012.

[79] C. Alaoui and Z. Salameh, “A novel thermal management for electric and hybrid vehicles,” *Veh. Technol. IEEE Trans.*, vol. 54, no. 2, pp. 468–476, 2005.

[80] C. Alaoui, “Solid-State Thermal Management for Lithium-Ion EV Batteries,” *Veh. Technol. IEEE Trans.*, vol. 62, no. 1, pp. 98–107, 2013.

[81] T.-H. Tran, S. Harmand, B. Desmet, and S. Filangi, “Experimental investigation on the feasibility of heat pipe cooling for HEV/EV lithium-ion battery,” *Appl. Therm. Eng.*, vol. 63, no. 2, pp. 551–558, Feb. 2014.

[82] Z. Rao, S. Wang, M. Wu, Z. Lin, and F. Li, “Experimental investigation on thermal management of electric vehicle battery with heat pipe,” *Energy Convers. Manag.*, vol. 65, pp. 92–97, Jan. 2013.

[83] M. Uno and K. Tanaka, “Single-Switch Cell Voltage Equalizer Using Multistacked Buck-Boost Converters Operating in Discontinuous Conduction Mode for Series-Connected Energy Storage Cells,” *Veh. Technol. IEEE Trans.*, vol. 60, no. 8, pp. 3635–3645, 2011.

[84] G. N. Ellison, *Thermal Computations for Electronics: Conductive, Radiative, and Convective Air Cooling*. CRC PressINC, 2011.

[85] T. Yuksel and J. Michalek, “Development of a Simulation Model to Analyze the Effect of Thermal Management on Battery Life,” *SAE Int.*, Apr. 2012.

[86] M. Ecker, N. Nieto, S. Käbitz, J. Schmalstieg, H. Blanke, A. Warnecke, and D. U. Sauer, "Calendar and cycle life study of Li(NiMnCo)O2-based 18650 lithium-ion batteries," *J. Power Sources*, vol. 248, pp. 839–851, Feb. 2014.

[87] Y. Yang, X. Hu, D. Qing, and F. Chen, "Arrhenius Equation-Based Cell-Health Assessment: Application to Thermal Energy Management Design of a HEV NiMH Battery Pack," *Energies*, vol. 6, no. 5, pp. 2709–2725, May 2013.